UNIVERSITY OF SIENA

DEPARTMENT OF BIOTECHNOLOGY,
CHEMISTRY AND PHARMACY

DOCTORAL THESIS IN
BIOCHEMISTRY AND MOLECULAR BIOLOGY
Cycle XXXVI

Coordinator: Prof. Lorenza Trabalzini

Endocannabinoids and Sphingosine 1-Phosphate: a crosstalk between two lipid systems in the regulation of myoblasts metabolism and differentiation

SCIENTIFIC-DISCIPLINARY SECTOR:

Biochemistry and Molecular Biology

Tutor
Prof. Chiara Donati

PhD Student
Sara Pecchioli

Co-Tutor
Prof. Francesca Cencetti

Sara Pecchioli Firmato il 15-04-2024

2022/2023

INDEX

Section 1

1 Introduction

1.1 Muscle tissue

Muscle tissue is one of the four types of animal tissues. It is composed of cells that have the special ability to shorten or contract to produce movement of the body's components. The muscle tissue is highly specialised and has four main functional properties: contractility, excitability, extensibility, and elasticity. Contractility is the ability of the tissue to shorten by exercising a pulling force; excitability is the ability to respond to an electrical stimulus; extensibility is the ability of the muscle to stretch beyond the normal length of rest; and elasticity is the ability of the muscle tissue to return to its original length after it is stretched. The muscle tissue is highly cellular and well supplied with blood vessels. Muscular cells are long and slender and usually arranged in bundles or layers that are surrounded by connective tissue. Three types of muscle tissue are present in mammals and can be differentiated based on their morphology and function: skeletal or striated muscle tissue, smooth muscle tissue, and cardiac muscle tissue.

1.1.1 Skeletal muscle

The skeletal muscle, with its associated connective tissue, makes up about 40% of the body weight and is responsible for locomotion, facial expressions, posture, respiratory movements, and many other body movements. The functionality of this type of tissue is controlled voluntarily by the nervous system. Each skeletal muscle is a complete organ composed of cells, named skeletal muscle fibers, associated with connective tissue, blood vessels, and nerve fibers. Each skeletal muscle has three layers of connective tissue that enclose it, and the collagen in the three layers intertwines with the collagen of a tendon that connects the muscle

to the bone. Each muscle fiber is enclosed within a thin layer of collagen connective tissue and reticular fibers called endomysium. Within each skeletal muscle, muscle fibers are organised into clusters called fascicles and surrounded by a medium layer of connective tissue called perimysium. Moreover, every muscle is composed of many fascicles and surrounded by a third layer of dense irregular connective tissue called epimysium (fig. 1). The epimysium separates the muscle from other tissues and organs within the region, enabling the muscle to move independently. The connective tissue of the muscle has the function of holding together the muscle fibres; it allows the passage of blood vessels and nerves; and it connects the muscle to the tendons and bones.

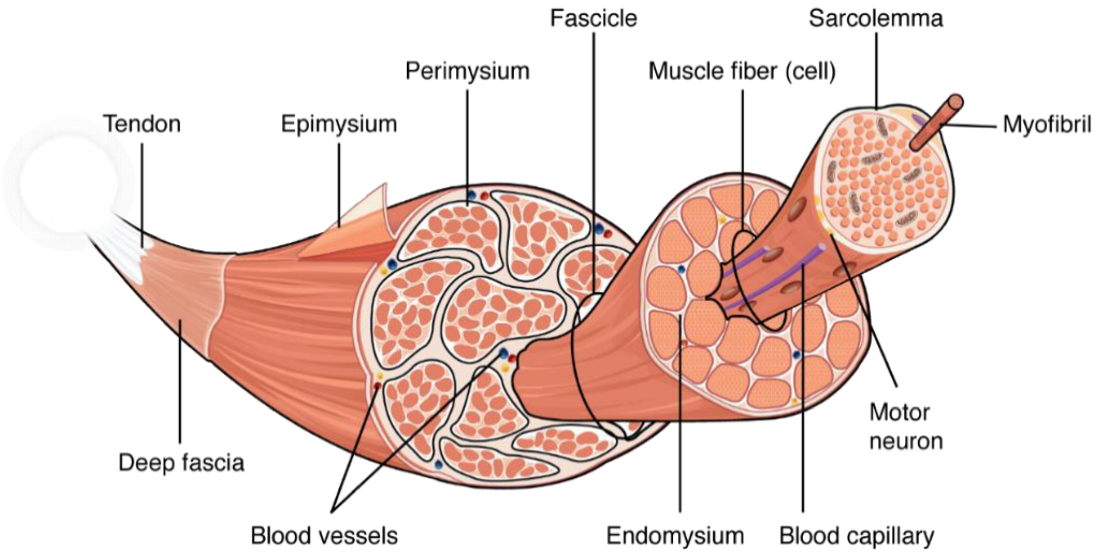

Figure 1. The Three Connective Tissue Layers (Biga et al., 2017)

Cells of the skeletal muscle are commonly named muscle fibers (or myofibers) because of their long and cylindrical shape, with diameters up to 100 µM and lengths up to 30 cm. Muscle fibers have many nuclei localized under the plasma membrane, in fact they are formed by the differentiation of embryonic cells into myoblast and their fusion, during the embryonic development. Therefore, muscle fibers are a syncytium. Besides nuclei, skeletal fibers also contain common organelles such as mitochondria and endoplasmic reticulum (ER), which is specialized and referred as the sarcoplasmic reticulum (SR). Muscle fibers are surrounded by the plasma membrane called sarcolemma (from the Greek sarco, which means "flesh") and their cytoplasm is known as sarcoplasm. The sarcolemma invaginates into the sarcoplasm of

the muscle cell, forming membranous tubules radially and longitudinally within the fibre called T-tubules or transverse tubules. On either side of the T-tubules are terminal cisternae, enlargements of the SR. A T-tubule surrounded by two SR cisternae is known as a triad. The SR forms a network around each myofibril of the muscle fiber and serves as a reservoir for calcium ions (Ca^{2+}), so when an action potential spreads over the T-tubule, the SR releases calcium ions from the gated membrane channels to stimulate a muscle contraction.

Myofibrils are structures of proteins that run the length of the cell within a muscle fiber and consist of sarcomeres connected in series. Myofibrils have a diameter of approximately 1.2 µm, and each muscle fibre is composed of a hundred to a thousand of them (fig. 2).

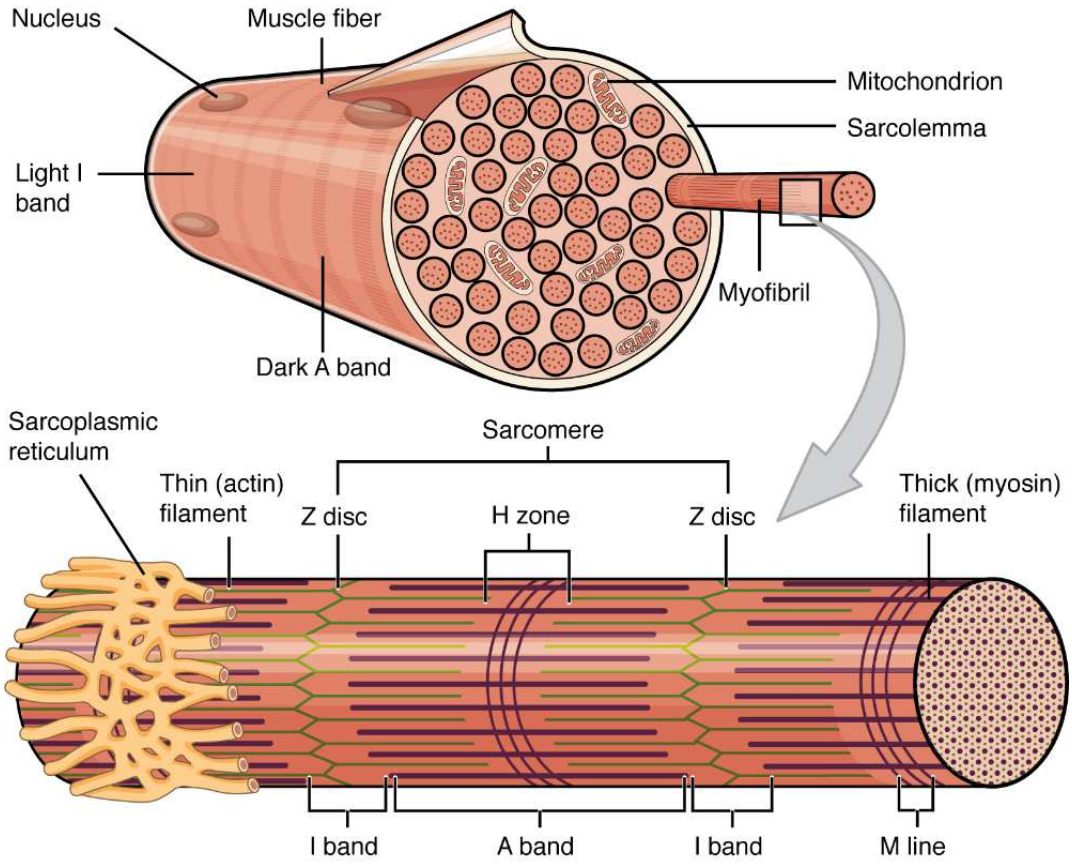

Figure 2. Muscle Fiber (Biga et al., 2017)

Sarcomeres are the smallest functional units of skeletal muscle fibers. It is organised into structural, regulatory, and contractile proteins, and its shortening propriety enables the contraction of the single fiber and, consequently, of the whole muscle.

A sarcomere is defined as the region of the myofibril contained between two Z-discs or Z-lines, made up of a weave of protein filaments forming a discoid structure bound to the actin filaments. The striated appearance of skeletal muscle fibres is due to the placement of thick and thin myofilaments in each sarcomere. In fact, the sarcomere is constituted by two lighter bands separated by a dark band. In particular, lighter bands are called isotropic or I bands, and the dark ones are called anisotropic or A bands. A thick filament containing myosin, which spreads from the centre of the sarcomere towards the Z-discs, forms the A band. Myosin filaments are bound to the middle of the sarcomere (the M line) by myomesin. Thin actin filaments, on the other hand, are anchored at the Z-discs by a protein called α-actinin, which forms the I band. The thin filaments extend into the A band toward the M-line and partially overlap with the thick filaments. The thicker myosin filaments overlapped with the actin filaments make the A band appear dark. The H zone in the middle of the A band is lighter because there are no thin filaments in this region (fig. 3).

The sliding of the myofilaments across each other allows the approach of the two Z-discs and therefore the contraction of the muscle. The A band and the myofilaments themselves do not change in length, but since the I band and the H zone are regions without overlapping filaments and the filaments' overlap increases during contraction, these regions decrease.

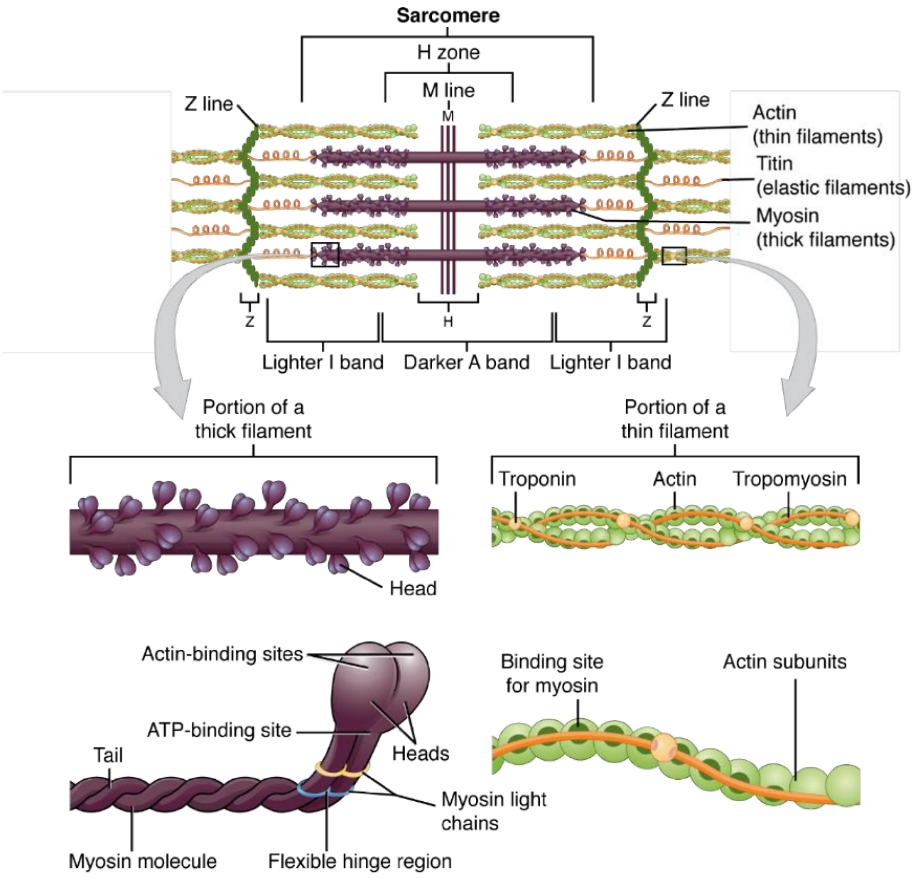

Figure 3. The Sarcomere (Biga et al., 2017)

The thin filaments present two filamentous actin chains (F-actin), composed of many globular actin monomers (G-actin) in a row, containing the myosin-binding site. Along the thin filaments run regulatory proteins, troponin and tropomyosin, which control the state of exposition of the myosin-binding site. Tropomyosin is a two-stranded alpha-helical, coiled coil protein associated with the actin chains, while Troponin is a protein complex consisting of three polypeptides: troponin I (TnI) binding actin, troponin T (TnT) binding tropomyosin, and troponin C (TnC) binding Ca^{2+}. In addition, thin filaments contain a stabilising protein called nebulin.

The thick filaments, instead, are composed of myosin protein complexes: two myosin heavy chains and four light chain molecules. The heavy chains are divided into a tail region, a flexible hinge region, and a globular head. This last region contains an actin-binding site and an ATP-binding site. Each thick filament contains hundreds of myosin proteins with tails toward the

M-line and heads toward the Z-discs. Thick filaments are also connected to a structural elastic protein called titin. Titin is anchored at the M-line and runs the length of myosin, connecting the filaments to the Z discs, helping their alignment.

This peculiar structure of the sarcomere allows muscle contraction. In fact, after the signal given by a motor neuron, Ca^{2+} released by the SR in the sarcoplasm allows the cross-bridge cycling. The cross-bridge is the projection of the two myosin heads from the thick filament. The binding of ATP to myosin causes the myosin head to detach from actin. Myosin hydrolyses ATP and this release of energy drives the myosin head to move closer to another binding site on actin. However, this site is hidden by tropomyosin. The Ca^{2+} free in the sarcoplasm binds to the TnC, which causes tropomyosin to slide over and unblock the myosin binding site on actin. This enables the myosin heads to bind to the actin. During the power stroke, myosin releases the inorganic phosphate and moves the actin filament inwards, shortening the sarcomere. At last, ADP is released from the myosin heads and myosin remains tight to actin until another ATP binds to myosin.

In skeletal muscle, two types of muscle fibre exist: Type I slow-twitch and Type II fast-twitch. Type I, also known as slow-twitch, slow oxidative or red muscle, is dense with blood vessels, mitochondria and myoglobin, therefore has a characteristic red colour, can carry more oxygen and sustain aerobic activity. These types of fibers present a smaller diameter, a slower contraction, and better fatigue endurance. Type II, or fast-twitch muscle, has three major types of fibers: Type IIa are fast oxidative fibers, rich in mitochondria and capillaries; Type IIx are less dense in mitochondria and myoglobin and can contract more quickly and with greater force but can only sustain short anaerobic bursts; and Type IIb are anaerobic, glycolytic, and referred to as "white" because it has a low concentration of mitochondria and myoglobin.

1.1.1 Myogenic differentiation and tissue repair in skeletal muscle

Skeletal muscle is a dynamic tissue whose mass depends on the balance between protein synthesis and degradation (Frontera & Ochala, 2015). It can grow after physical exercise and be repaired after injuries. Satellite cells are essential for tissue regeneration, a process controlled by the sequential expression of transcriptional factors, as indeed is the

differentiation programme of embryonic myogenesis (Schmidt et al., 2019). The repair of skeletal muscle can be divided into three phases. During the first phase, after injury, damaged myofibers undergo necrosis, accompanied by an increase in calcium influx that leads to proteolysis and degeneration of the tissue. Here begins an inflammatory response that recruits neutrophils and macrophages, infiltrating the damaged tissue and secreting, first, pro-inflammatory cytokines, and then anti-inflammatory cytokines, which facilitate the proliferation and differentiation of satellite cells. The activation and differentiation of satellite cells characterise the second phase. The expression of Pax7 is necessary for the maintenance of the quiescent status of satellite cells, but when activated, satellite cells start to express another marker, MyoD, an early marker for myogenic commitment, begin to migrate to the site of damage and here fuse with the impaired myofibers (Schmidt et al., 2019). These cells, characterised by the expression of MyoD and Myf5, are highly proliferative cells and are called myoblasts. Myf5, MyoD, Myogenin, and MRF4 are myogenic regulatory factors (MRFs) sequentially expressed in tissue regeneration as downstream of Pax7 and Pax3, in order to promote myogenic differentiation (K. Singh & Dilworth, 2013; Soleimani et al., 2012). Once Myogenin starts to be expressed, myoblasts begin their terminal differentiation, becoming elongated myocytes that fuse to form multinucleated myotubes. Here starts the third phase of regeneration in which myotubes mature into myofibers characterised by the expression of devMHC (developmental myosin heavy chain) (Schmidt et al., 2019). These isoforms, transiently expressed during muscle regeneration, have a fundamental role in the muscle development during embryogenesis. All skeletal muscles derive from mesodermal precursor cells, originated from the somites (epithelial spheres of paraxial mesoderm). The myotomal cells express PAX3, essential for the migration of muscle precursors from the somite during development, and Pax7, required for satellite cell specification. Signals from surrounding tissues induce the expression of the MRFs such as Myf5 and MyoD, which commit mesodermal cells into myoblasts. Myf5 and MyoD regulate the expression of Myogenin, a secondary MRF, which, together with MFR4 (regulated by Myogenin itself) induce terminal differentiation of myoblasts into myocytes. Mononucleated myocytes fuse to form multinucleated syncytium, which finally mature into contracting muscle fibers, which express not only Myogenin and MRF4 but also important genes for muscle cells such as myosin heavy chain (MHC).

1.1.2 Satellite cells

Myosatellite cells, also known as satellite cells, are located between the basement membrane and the sarcolemma of muscle fibers. Myosatellite cells are small multipotent cells with little cytoplasm and form niches parallel or transversely to the longitudinal axis of the muscle fibers. Upon muscle tissue damage, these cells have the ability to activate, proliferate, and differentiate in order to create new muscle fibers that will substitute the impaired ones. Myosatellite cells not only re-enter the cell cycle, proliferate and undergo differentiation forming new myotubes, but they can also fuse with the existing injured myofibers to increase growth and repair of the tissue. Moreover, the asymmetrical division that characterises myosatellite cells leads to the creation of new quiescent satellite cells, so that the staminal niche will not be depleted. The specialised local environment, where satellite cells reside, is characterized by a remarkable plasticity thus changes during tissue regeneration thanks to the action of a multitude of functionally diverse cell types, among them, immune cells, vessel-associated cells, fibrogenic cells and differentiated cells of the myogenic lineage, besides stem cells themselves (Bentzinger et al., 2013). The main function of satellite cells in the adult actually appears to be the regeneration of the tissue after damage, since the ablation of these cells under homeostatic conditions does not lead to myopathies or muscle atrophy (Fry et al., 2015; Mccarthy et al., 2011).

1.1.3 Mitochondria and Myogenesis

Mitochondria are essential for the maintenance of skeletal muscle metabolic plasticity and function. Besides harvesting energy, mitochondria have important functions linked to the Ca^{2+} signalling and the cell fate. Mitochondrial quality control is provided by the constant fission (division) and fusion (elongation) of mitochondria in response to metabolic stressors (Nakano & Machida, 2022). Recent studies have identified mitophagy as a process that governs cell fate through metabolic reprogramming (Naik et al., 2019). The remodelling of the mitochondrial network via mitophagy facilitates the cellular metabolic shift, either into a glycolytic phenotype or into an OXPHOS phenotype. This change in the bioenergetic profile is

accompanied by altered levels of metabolic intermediates which are required for transcriptional regulation of cell fate (Rahman & Quadrilatero, 2023). In skeletal muscle, mitophagy plays an important role in initiating myogenesis and it has been shown to govern skeletal muscle regeneration in adulthood by regulating cell fate. On one hand Myogenin seems to induce the shift from glycolytic metabolism to oxidative metabolism both *in vivo* (Hughes et al., 1999) and *in vitro* (Zhu et al., 2013). On the other hand, myoblasts, presenting mitochondrial alterations, fail to differentiate into myotubes (Herzberg et al., 1993; Rochard et al., 2000), demonstrating that the two processes influence each other. During myogenic differentiation, mitochondrial enzyme activity is drastically increased. In proliferating myoblasts, oxidative phosphorylation (OXPHOS) provides only 30% of the ATP used by the cells, increasing up to 60% in terminally differentiated myotubes. Therefore, during myogenesis a metabolic shift occurs from glycolysis to oxidative phosphorylation, which becomes the major energy source in differentiated myotubes (Wagatsuma, 2013). Skeletal muscle fibers have higher bioenergetic needs than myoblasts, hence it is not surprising that there is a unique change in the metabolic phenotype that occurs during myoblast differentiation. Moreover, the skeletal muscle's mitochondria are characteristically different from the mitochondria found in myoblasts. Indeed, the differentiation of myoblast to myotubes is accompanied by greater development of the mitochondrial network (Rahman & Quadrilatero, 2023). The number of mitochondria within a cell is determined by two opposing processes: biogenesis, which creates new mitochondria, and mitophagy, which eliminates the unneeded ones. Dynamic fission and fusion of mitochondria are necessary to their function: optimize OXPHOS, minimize the generation of reactive oxygen species (ROS), and maintain membrane potential. Mitochondrial fusion produces elongated mitochondria that are associated with increased OXPHOS activity mainly through the regulation of mtDNA. Conversely, fission results in augmented mitochondrial fragmentation leading to increased oxidative stress and reduced ATP production (Bhattacharya & Scimè, 2020). It is known that Ca^{2+} plays a role in mitochondrial function. Ca^{2+} can enter the mitochondria through voltage-dependent anion channels (VDACs), on the outer mitochondrial membrane, and the mitochondrial Ca^{2+} uniporter (MCU) complex, which accumulate the ion in the mitochondrial matrix (Morciano et al., 2018). In skeletal muscle cells, during contraction, Ca^{2+} enters mitochondria and activates the oxidative metabolism enzymes, resulting in increased ATP

synthesis to satisfy the energy demand (Mosqueira et al., 2021). Ca^{2+} levels inside the mitochondria are also maintained thanks to mitochondria-associated membrane (MAM), highly specialised subcellular compartments, which structurally and functionally connect the ER with the mitochondria. MAMs are enriched in enzymes for lipid synthesis and transport and Ca^{2+} channels for the transport of the ion from the ER to the mitochondria. A reduction of the number of MAMs has been found in muscular dystrophy, ageing and insulin resistance highlighting their important role in a correct skeletal muscle function (Zhang et al., 2021). Elevated intracellular Ca^{2+} concentration leads to an increased expression of mitochondrial enzymes at mRNA and protein level. Indeed, increased concentration of intracellular Ca^{2+} activates the calcium- and calmodulin-dependent phosphatase (CaN), which dephosphorylates and activates the nuclear factor of activated T-cells (NFAT). NFAT-dependent transcriptional pathway regulates the transformation of skeletal fibers from fast-twitch to slow-twitch (Shen et al., 2006)

1.1.4 C2C12 cell line

The immortalised mouse myoblast cell line C2C12, which was generated from satellite cells, is typically regarded as a lineage of muscle progenitors (Burattini et al., 2004; Curci et al., 2008). C2C12 cells are a subclone of C2 myoblast (Yaffe D. & Saxel O., 1977), which naturally undergoes differentiation in culture following serum removal (Blau et al., 1983). Over the past 20 years, myoblast cell lines have been used as useful *in vitro* models in studying physiological and pathological conditions of skeletal muscle. C2C12 cells are displayed as mononucleated and spindle-shaped myoblasts (Wong et al., 2020). The differentiation process can be triggered in confluent cells by the deprivation of the serum in the culture medium, substituted by 0.1% BSA (bovine serum albumin) or 2% HS (horse serum). Within 3-5 days of differentiation, C2C12 cells fuse forming multinucleated and elongated fiber-shaped myotubes (Wong et al., 2020). Only 50% of the cultured cells actually begin to express differentiation markers and complete the differentiation process, the other 50% (the MyoD-negative population) remain undifferentiated, designated by Yoshida and colleagues as “reserve cells” (Yoshida N. et al., 1998). Interestingly, ectopic expression of MyoD triggered

the differentiation process in the “reserve cells”, pointing out that down-regulation of this marker is a causal event during differentiation (Yoshida N. et al., 1998). Muscle differentiation in vitro mimics in vivo development: along with the differentiation, the activation of MRFs occurs, leading to the expression of Myogenin in the first 24h of starvation; Caveolin 3 (a structure protein of the vesicular invaginations of the striated skeletal muscle sarcolemma) required for myoblast fusion (Galbiati et al., 1999); and myosin heavy chain (MHC) in nascent myotubes (Jiwlawat et al., 2018). Moreover, during the early stages of differentiation, precisely coinciding with cell elongation and myotubes formation, myoblasts start to express an adhesion molecule, M-cadherin, taking part in the assembly of muscle syncytia (Curci et al., 2008).

1.2 Endocannabinoid system

In 1988, after the discovery of membrane receptors for Δ9-tetrahydrocannabinol (Δ9-THC or simply "THC"), the word "Endocannabinoid" was coined, and the term "Endocannabinoid System (ECS)" was then used to describe a complex molecular/biological system discovered by scientists Allyn Howlett and W.A. Devane (Lowe et al., 2021). THC is the main psychoactive component of the plant *Cannabis sativa*, better known as marijuana, a plant used for centuries for its anti-nociception, anti-inflammatory, anticonvulsant, and anti-emetic effects. THC's discovery led to the generation of many synthetic cannabinoids and finally to the identification and cloning of the cannabinoid receptor 1 (CB1) and, shortly afterward, the cannabinoid receptor 2 (CB2) (Zou & Kumar, 2018). The endogenous agonists of the cannabinoid receptors (CBRs) have been identified in the 1990s to be arachidonic acid (AA)-derivates: *N*-arachidonoyl-ethanolamine (AEA; anandamide from a Sanskrit word "ananda" meaning "bliss or happiness"), and 2-arachidonoylglycerol (2-AG). Nowadays they are the two most studied endocannabinoids (eCBs), which belong to the large families of *N*-acylethanolamines (NAEs) and 2-monoacylglycerols (MAG), respectively. Both molecules are metabolised by different enzymes and transported through the plasma membrane and intracellularly by specific carriers (Maccarrone, 2021). Besides AEA and 2-AG other ω-6 (n-6) fatty acid compounds joined the endocannabinoid family, such as *N*-arachidonoyldopamine (NADA), 2-arachidonoylglycerylether (noladin ether) and *O*-arachidonoylethanolamine (virodhamine) (Maccarrone, 2017). In addition, ω-3 (n-3) fatty acid derivates as *N*-docosahexaenoylethsanolamine (DHEA) and *N*-eicosapentaenoylethanolamine (EPEA) were found to be CBRs agonist (Fezza et al., 2014). Interesting is the existence of eCB-like compounds, which are metabolized by the same enzymes as eCBs but lack of affinity for CBRs (Fezza et al., 2014).

The endocannabinoid are bioactive lipids capable of binding the two CBRs with a different affinity: 2-AG act as a full agonist at both CBRs, while AEA act as a partial agonist of CB1 and a weak partial agonist of CB2 (Pertwee et al., 2010). ECBs can also interact with non-CB receptors: GPR55, an orphan G-protein-coupled receptor; PPARs, peroxisome proliferator activated receptors, α and γ; and TRPV1, transient receptor potential vanilloid-1 channel, activated by both AEA (Di Marzo & De Petrocellis, 2010) and 2-AG (Zygmunt et al., 2013).

In summary, the whole set of receptors, enzymes, transporters for endocannabinoids and the endocannabinoids themselves form the ECS. The ECS plays a meaningful role in the central nervous system (CNS) regulating a variety of processes such as anxiety, appetite, memory, pain, and emotional behaviour, and it has also peripheral effects at respiratory, cardiovascular and metabolic level. The ECS's involvement in a variety of pathophysiological processes is a significant opportunity for the development of new cannabinoid-based therapeutic medicines that could be personalised to target specific ECS components and/or cell-signalling pathways (Lowe et al., 2021).

1.2.1 Anandamide

N-arachidonoyl-ethanolamine (AEA) was identified some 25 years ago as a brain constituent that binds to the cannabinoid receptors, CB1 and CB2. It is produced by almost all cells and body tissues, which triggers different signalling pathways by binding to different receptors. AEA activates CBs at nanomolar/submicromolar concentrations by binding to an extracellular binding site, whereas micromolar concentrations are required to activate TRPV1, which AEA binds intracellularly, or PPARs, located in the nucleus (Maccarrone et al., 2010). AEA biological activity is related to the metabolic control of its biosynthetic, catabolic, and oxidative pathways, which are described below (fig. 4).

AEA in vivo synthesis begins with the Ca^{2+}-dependent synthesis of N-arachidonylethanolamide (NAPE) from phosphatidylethanolamine and phosphoglyceride catalysed by N-acyltransferase (NAT) (Reddy et al., 1983). NAPE will then be transformed in AEA following three different pathways. First of all, NAPE can be hydrolysed (Di Marzo et al., 1994) by a NAPE specific phosphatase D (NAPE-PLD) (Okamoto et al., 2004) to AEA and phosphatidic acid. In addition, phospholipase C (PLC) may hydrolise NAPE to phosphoethanolamide, which is subsequently dephosphorylated to AEA by tyrosine phosphatase PTPN2 or by inositol phosphatase SHIP1 (Liu et al., 2008). Alternatively, NAPE can be deacylated in phosphatidylethanolamine by α, β-hydrolase 4 (Abhd4), which is then cleaved of glycerophosphate to yield AEA (Simon & Cravatt, 2006). It is noted that these three pathways are metabolising NAPE, which is a minor membrane component. Therefore, its synthesis may be the limiting step in AEA synthesis

(Tóth et al., 2009). Interestingly, NAPE-PLD knockout mice did not show a decrease in AEA levels compared to wild-type animals, suggesting the occurrence of additional pathways for *in vivo* synthesis of anandamide (Leung et al., 2006).

For many years, in contrast to classic neurotransmitters, endocannabinoids were thought to be synthesized and released "on demand" after specific signals, and not stored in vesicles. The discovery of AEA intracellular stores (adiposomes) (Oddi et al., 2008) and its intracellular binding to proteins (Kaczocha et al., 2009; Oddi et al., 2009), led to a reconsideration of this dogma and the addition of one more level of complexity to the AEA metabolic control and its regulatory mechanism (Maccarrone et al., 2010). The mechanism by which AEA is transported across the plasma membrane remains poorly understood. Different hypotheses have been postulated over the years leading to two prevailing models: simple diffusion (Fasia et al., 2003; Glaser et al., 2003), or facilitated diffusion by a putative anandamide membrane transporter (AMT) (Beltramo et al., 1997; Chicca et al., 2012). In addition, caveolae-related endocytosis has been proposed as a third mechanism of transport (McFarland & Barker, 2004).

Even less understood is the intracellular trafficking of AEA, i.e., the movement inside the cell to reach its targets. Since AEA has a lipid nature, it cannot quickly diffuse in the cytoplasm, moreover, AEA is a small molecule that does not contain the appropriate sorting signals for specific targeting (Maccarrone et al., 2010). Therefore, for AEA to be efficiently and quickly dispersed throughout its intracellular locations, it must interact with soluble transporters. Several classes of proteins have been identified as intracellular targets for AEA, as for 2-AG. First of all, Fatty acid binding proteins (FABPs) (Kaczocha et al., 2009), which are expressed in the mammalian brain and bind to AEA with different affinity: FABP7 first, followed by FABP5 and FABP3 (Kaczocha & Haj-Dahmane, 2021). When upregulated, FABP5 and FABP7, but not FABP3, enhance the cellular uptake of AEA (Kaczocha & Haj-Dahmane, 2021) and since only FABP5 is expressed in the adult brain, while FABP7 is downregulated after birth (Owada et al., 1996), it is the most important FABP that regulates brain AEA diffusion. Other two AEA-interacting proteins have been identified: heat shock protein 70 (Hsp70) and serum albumin (Oddi et al., 2009). Albumin is differently expressed in tissue and cell lines; particularly high levels of this protein can be found in actively metabolising or developing tissue. The interaction between albumin and AEA has already been demonstrated in the extracellular milieu (Bojesen & Hansen, 2003; Giuffrida et al., 2000). Therefore, albumin is an AEA

bioavailability regulator in multiple functional contexts (Oddi et al., 2009). Hsp70 is constitutively expressed in the cell cytoplasm of various tissues and in association with membrane lipids (Gehrmann et al., 2008), but, compared to albumin, AEA binds to Hps70 with approximately fivefold lower affinity (Oddi et al., 2009). Others intracellular AEA interacting proteins have been identified, such as FAAH-like anandamide transporter (FLAT) (Fu et al., 2012), Sterol carrier protein-2 (Liedhegner et al., 2014) and nucleobindin-1 (NUCB1) (Niphakis et al., 2015), although their influence upon AEA metabolism *in vivo* is unknown. Adiposomes, ubiquitous organelles which are described as intracellular stores for neutral lipids, participate as well in the trafficking, accumulation, and signals of AEA (Maccarrone et al., 2010). It is still unclear the mechanism by which AEA reaches the adiposomes, but, since Hsp70 and albumin are associated with adiposomes in several cell types, it is likely that AEA transport into adiposomes is mediated by proteins (Maccarrone et al., 2010). Adiposomes are indeed intracellular AEA reservoirs that can move within the cell, establishing close contacts with multiple organelles: ER, mitochondria, and peroxisomes (Martin & Parton, 2006). Moreover, adiposomes are associated with AEA-metabolising enzymes, acting as the starting point for several metabolic pathways.

AEA breakdown is predominantly catalysed by the fatty acid amide hydrolase (FAAH), cloned in 1996 (Cravatt et al., 1996), which catalyses AEA into ethanolamide and arachidonic acid. In fact, *faah* knockout mice have ~15-fold higher levels of AEA than wild types (Cravatt et al., 2001, 2004) confirming a pivotal role of FAAH in monitoring AEA tone *in vivo*. Human tissues contain two FAAH isoforms: FAAH-1 (the main AEA-hydrolase), which is predominant in the brain, and FAAH-2, which is expressed in heart and ovary. In some tissues, the two FAAHs can be co-expressed, regulating distinct or overlapping AEA pools (Maccarrone et al., 2010). Additionally, AEA can be subjected to oxygenation by cyclooxygenase-2 (COX-2), 5-, 12- and 15-lipoxygenase (5-/12-/15-LOX) and cytochrome P450 monooxygenases (CYP450s). The degradation of AEA by COX-2 results in the formation of prostaglandin-ethanolamides, LOXs form hydroxy-anandamide or hydroxyeicosatetraenoyl-ethanolamides, while P450s create epoxyeicosatrienoyl-ethanolamides (Maccarrone, 2017).

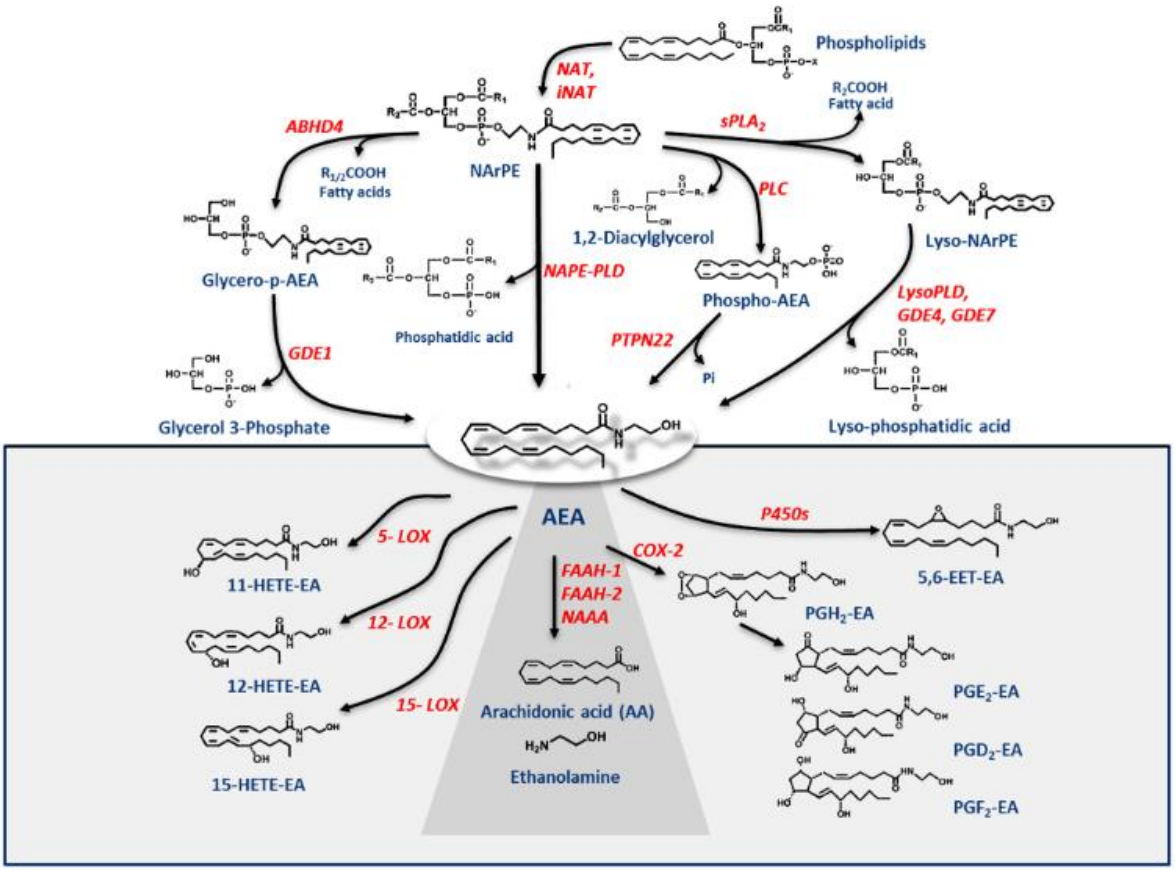

Figure 4. Schematic representation of AEA metabolism (Maccarrone, 2017)

1.2.2 2-AG

2-AG was first isolated in 1995 from canine gut (El Mechoulam et al., 1995) and it is a full agonist of CB1 and CB2 receptors (Savinainen et al., 2001). As with AEA, 2-AG acts as a retrograde neurotransmitter in both inhibitory and excitatory synapses (Baggelaar et al., 2018), although 2-AG levels in the brain are roughly 170 times greater than AEA levels (Stella et al., 1997). Phosphatidylinositol-4, 5-bisphosphate (PIP_2) and sn2-arachidonate containing triglycerides are 2-AG precursors (fig. 5). Both can be converted by specific enzymes in diacylglycerol (DAG), which is further processed by diacylglycerol lipase-α and –β (DAGL-α and -β) and generates 2-AG (Bisogno et al., 2003). Both human genes of DAGLs shear a high homology with the mouse ones, 97% for DAGL- α and 79% for DAGL-β. DAGLs expressed in

the brain, DAGL-α mainly in neurons while DAGL-β is more active in microglia, as well as in other tissues, differently contributing to the 2-AG creation (Baggelaar et al., 2018). DAGLs are considered the most important enzymes for 2-AG biosynthesis, although two other alternative pathways have been discovered. The first one includes lysophospholipase C (lysoPLC) (Ueda et al., 1993), which creates 2-AG removing the phosphate of 2-arachidonoyl-LPI generated from the phosphorylation and hydrolysis of PIP_2. In the second one, 2-arachidonoyl lysophosphatidic acid (2-arachidonoyl LPA) is converted into 2-AG by 2-LPA phosphatases (Nakane et al., 2002). Monoacylglycerol lipase (MAGL) is the principal enzyme in 2-AG catabolism, hydrolysing ~85% of 2-AG in the mouse brain into arachidonic acid and glycerol (Blankman et al., 2007). The same hydrolysis reaction can be catalysed by α, β-hydrolasedomain-containing protein 12, 6 and 2 (ABHD12, ABHD6 and ABHD2), albeit to a lesser extent. However, MAGL, ABHD12 and ABDH6 are differently distributed in the central nervous system, suggesting a different physiological function of these enzymes (Fezza et al., 2014). Moreover, resembling AEA catabolism, 2-AG breakdown can be carried out by COX-2, LOXs and CYP450 (Baggelaar et al., 2018).

Since the investigation of the transport mechanisms is complicated by 2-AG's metabolism, less research has been done on this process (Baggelaar et al., 2018). 2-AG uptake could be inhibited by inhibitors of AEA transport, therefore it was proposed a common carrier mechanism (Bisogno et al., 2001; Chicca et al., 2012; Hermann et al., 2006). Intracellularly, 2-AG was shown to bind FABP5 (Sanson et al., 2014), although it is not known how FABP5 or other putative 2-AG targeting proteins could regulate the physiological role of this endocannabinoid so far.

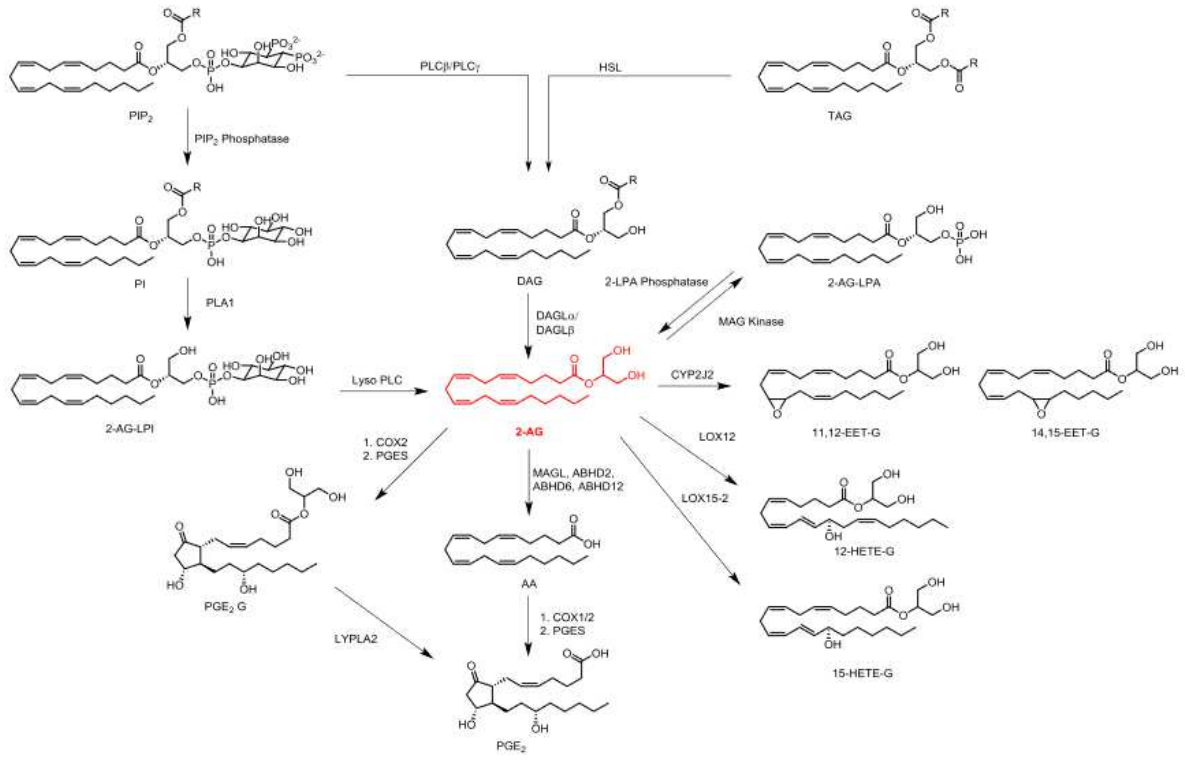

Figure 5. Schematic representation of 2-AG metabolism (Baggelaar et al., 2018)

1.2.3 CB1

CB1 is the first cannabinoid receptor to be identified and cloned in 1990 by Matsuda and colleagues (Matsuda et al., 1990). The human protein CB1 is produced by *CNR1* gene, and consists of 472 amino acids (473 in rat and mice), with 97-99% amino acid sequence identity between these species (Zou & Kumar, 2018). A few years ago, other two isoforms, besides the canonical long form of CB1, have been reported as the result of alternative splicing of the N-terminus region (Ryberg et al., 2005; Shire et al., 1995). In addition, it seems that the full-length CB1 localized in the brain and skeletal muscle, whereas the shorter form dominates in liver and pancreatic islets, showing a different expression pattern in the human body (González-Mariscal et al., 2016). Indeed, CB1 is highly expressed in the brain, mainly in the olfactory bulb, hippocampus, basal ganglia, and cerebellum (Mackie, 2005), but it can be also abundantly found in the peripheral nervous system (PNS), mostly in the dorsal root ganglia,

as well as in other body regions, such as the gastrointestinal tract, adipose tissue, skeletal muscle, bone, skin, eye, and reproductive system. Interestingly, CB1 levels in the liver and in the cardiovascular system are usually low, and its upregulation promotes pathological conditions (Zou & Kumar, 2018). CB1's structure, as all G-protein-coupled receptors, consists of seven transmembrane domains connected by three extracellular and three intracellular loops, an extracellular N-terminal tail, and an intracellular C-terminal tail. At cellular levels, CB1 mainly localizes in the cell membrane, even if intracellular compartments of CB1 located in acid-filled endo/lysosomes have been identified. These intracellular CB1 counterparts, upon intracellular agonist administration performed by cell microinjection, increase the release of calcium from the ER and lysosomes (Brailoiu et al., 2011). Moreover, another subpopulation of CB1 in mitochondria has been reported (Hebert-Chatelain et al., 2014). Both CBs can couple to pertussis toxin (PTX)-sensitive G-protein (G_i/o) to inhibit adenylate cyclase (AC) and therefore suppress the formation of cAMP (Felder et al., 1995). Indeed, 2AG as well as AEA act as full agonists in the inhibition of cAMP formation through CB1 (Felder et al., 1995), while only 2AG is a full agonist for the inhibition of cAMP via CB2 (Gonsiorek et al., 2000). However, besides the coupling to PTX-sensitive G-proteins, CB1 and CB2 do not couple to the same signal transduction pathways (Roger G Pertwee, 1997). Moreover, CB1 can act via $G_{\beta\gamma}$ subunits stimulation of specific AC isoforms (Rhee et al., 1998), and it is able to stimulate cAMP formation via coupling to G_s in determined conditions in different cell types (Zou & Kumar, 2018). Numerous studies have shown an activation of mitogen-activated protein kinase (MAPK) signalling upon CB1 stimulation. The MAPK family includes the extracellular signal-regulated kinase 1/2 (ERK1/2), C-Jun N-terminal kinase (JNK) and p38, which are involved in the regulation of cell proliferation, cell cycle control, and cell death (Demuth & Molleman, 2006; Allyn C Howlett et al., 2010; Turu & Hunyady, 2010). In addition, CB1 can act through a G protein-independent signal pathway in association with β-arrestin (Howlett et al., 2010), the key mediator of G-protein coupled receptors desensitization. After CB1 phosphorylation, β-arrestin binds to the receptor and starts the internalization process, during which it could mediate biased signalling pathways (McCudden et al., 2005). Moreover, CB1 signalling has been associated with the activation of the PI3K/Akt pathway, responsible for the protective effects of CB1 on cell survival aside from MAPK (Zou & Kumar, 2018). Indeed, in primary cultured neurons a CB agonist triggered the activation of Akt, through its phosphorylation on

serine 473. This effect was reduced by both CB1 and CB2 antagonists, and by the inhibition of PI3K, which blocked the phosphorylation of Akt and prevented the neuroprotective effects of the CB agonist(Molina-Holgado et al., 2005) .

1.2.4 CB2

Soon after the identification of CB1, in 1993, a second cannabinoid receptor was identified and named CB2 (Munro et al., 1993). The human protein CB2 is produced by the *CNR2* gene and consists of 360 amino acids. Unlike CB1, CB2 has a great species difference. The sequence homology is indeed about only 80% between humans and rodents (Liu et al., 2009; Zhang et al., 2015). Moreover, in humans and mice two CB2 isoforms have been discovered, while in rats four isoforms have been identified so far (Liu et al., 2009; Zhang et al., 2015). Finally, at the protein level, in humans, CB2 and CB1 share only 44% sequence homology (Zou & Kumar, 2018). CB2 is predominantly expressed in immune cells, where it can modulate cell migration and cytokine release (Pertwee et al., 2010). However, it can also be found in other peripheral tissues such as the cardiovascular system, the gastrointestinal tract, liver, bone, adipose tissue, and reproductive system (Howlett et al., 2002). Although CB2 expression in the CNS is limited, it plays a role in neurological activities, including nociception, neuroinflammation, and drug addiction (Atwood & MacKie, 2010; Dhopeshwarkar & Mackie, 2014). As with CB1, CB2 shares the same G-protein coupled receptors' typical structure, and it couples primarily to $G_{i}/_{o}$ protein to inhibit AC as well as to modulate other signalling pathways, among them MAPK (ERK1/2 and p38), and PI3K/Akt (Dhopeshwarkar & Mackie, 2014). Mice lacking the CB2 receptor have exacerbated inflammation, thus highlighting the possible employment of therapies targeting CB2 to treat inflammatory diseases.

1.2.5 GPR55

GPR55 is an orphan G-protein coupled receptor first isolated in 1999 in the human striatum, where it is present at high levels of expression (Sawzdargo et al., 1999). It is a protein located in the cell membrane and is composed of 319 amino acids. GPR55 shows few similarities with CB1 and 2, with which it shares a sequence identity of 13.5% and 14.4%, respectively (Pertwee et al., 2010). Nonetheless, some studies suggest GPR55 as a novel "CB3" receptor. Indeed, nanomolar concentrations of AEA and 2AG activate the G protein coupled to GPR55, increasing their GDP/GTP exchange (Gasperi et al., 2013). Besides the CNS, GPR55 is expressed in bone, liver, kidney, and adipose tissue. It has been reported that GPR55 induces calcium exit from intracellular stores via PLC activation, causing neuronal excitation and the increase of neurotransmitter release such as glutamate, in contrast to CB1/CB2 suggesting potential pharmacological effects of modulating GPR55 in CNS (A. Marichal-Cancino et al., 2016).

1.2.6 PPARs

PPARs are ligand-activated transcription factors within the nuclear hormone receptor superfamily (Michalik et al., 2006) PPARs are characterised by three isoforms, which each present specific tissue distribution and functional roles. PPARα was the first discovered and it is expressed in organs with high levels of fatty acid catabolism (Mandard et al., 2004) such as liver and brown adipose tissue, but also in the heart, kidney, and skeletal muscle (Gasperi et al., 2013). PPARγ is highly expressed in the adipose tissue and less in the colon, immune system, and brain. PPARδ has the broadest expression pattern, with the highest expression in the gut, kidney and heart (Desvergne et al., 1999). PPARs control many physiological and pathological processes through a specific heterodimerization with the receptor *9-cis*-retinoic acid. In fact, this heterodimer, activated by a ligand, binds to a specific DNA sequence element (peroxisome proliferator response element) modulating the transcription of targeted genes (Michalik et al., 2006). However, since AEA and 2-AG are able to directly bind to and activate PPARα and PPARγ (Bouaboula et al., 2005; Gasperi et al., 2007; Rockwell et al., 2006), PPARs

can be counted among the endocannabinoid receptors. Indeed, AEA binding to PPARγ induces 3T3-L1 fibroblast differentiation into adipocytes (Bouaboula et al., 2005) , while in in Jurkat T cells 2-AG via PPARγ activation promotes the suppression of interleukin (IL-2) (Rockwell et al., 2006). Moreover, synthetic and plant-derived cannabinoids attenuate neuroinflammation and neurodegeneration in animal models of acute or chronic neurodegenerative disorders through activation of cannabinoid receptors and PPARγ pathway (Iannotti & Vitale, 2021).

1.2.7 TRPV1

TRPV1 is a member of the TRPV subfamily of the large TRP ion channel superfamily (Tominaga & Tominaga, 2005). Like others TRP, it is assembled as a homotetramer: each subunit contains six-transmembrane domains, with a nonselective cation-permeable pore region between the fifth and the sixth domain, a relatively short cytosolic C- terminal region and a long intracellular N-terminus with multiple ankyrin repeats (Benítez-Angeles et al., 2020). In the sixth transmembrane domain, cysteine residues appear to contribute to the formation of an activation gate (Salazar et al., 2009). Moreover, some amino acids influencing the agonist responses have been shown to be located in the pore loop, and, in the intracellular loops and in the terminal domains, different phosphorylation sites have been discovered (Bevan et al., 2014). Initially known as VR1, it was discovered and cloned in 1997 as the first receptor for capsaicin, the main pungent ingredient in hot chilli peppers (Caterina et al., 1997). It is also activated by heat (>42°C), protons (pH<6.9) and endogenous (endocannabinoid) as well as exogenous (vanillotoxins) molecules (Pertwee et al., 2010). At last, lacking any other stimulus, also membrane depolarization can activate TRPV1 (Vlachová et al., 2003). The *Trpv1* gene located on chromosome 17p13 encodes the human TRPV1 protein, which consists of 839 amino acids (Birnbaumer et al., 2003). TRPV1 is a non-selective cation channel, which, upon capsaicin activation, shows a higher permeability to divalent cations (i.e. Ca^{2+} and Mg^{2+}) than to monovalent cations (i.e. Na^{+}) (Ahern et al., 2005) TRPV1 is prevalently located in the PNS where it is expressed in half of all somatic and visceral sensory neurons of dorsal root ganglia (DRG) and trigeminal ganglia (TG) (Pertwee et al., 2010). TRPV1 expression is regulated by the nerve growth factor (NGF), which acts as a trophic signal to keep TRPV1 expressed. TRPV1 is

also present in the CNS at the hypothalamus level, where it has a role in thermoregulation, and in some brain nuclei or regions (Bevan et al., 2014). In addition to the location of TRPV1 in the nervous system, TRPV1 also presents a non-neuronal expression. It is indeed found in a variety of cell types such as epithelial, endothelial, glial, mast, dendritic, smooth and skeletal muscle cells, hepatocytes, lymphocyte and others (Pertwee et al., 2010).

The prominent role of TRPV1 is its thermosensor activity. The typical sensation of "burning" heat is perceived when TRPV1 of sensory neurons is activated by either high temperatures or chemical agonists, like capsaicin (Bevan et al., 2014). Interesting is TRPV1's role as a thermosensor in inflammation: inflammatory mediators can sensitise TRPV1, lowering its temperature threshold and, therefore, eliciting a painful sensation. The regulation of TRPV1 is carried out by the phosphorylation of several key residues by different kinases, among them protein kinase A (PKA) and protein kinase C (PKC), known to be activated during the inflammatory response, but also calcium-calmodulin kinase II (CaMKII) and MAPK. Phosphorylation can also lead to TRPV1 trafficking to the plasma membrane, as shown by Zhang and colleagues (Zhang et al., 2005) NGF, ATP, and IGF-1 are examples of mediators which can promote the membrane insertion of TRPV1, and therefore its response, via SNARE-dependent Ca^{2+}-mediated exocytosis (Camprubí-Robles et al., 2009). Another characteristic of TRPV1 is its calcium-mediated inactivation or desensitisation, which causes the loss of sensitivity to chemical agonists. In order to explain the desensitisation effect, more than one mechanism has been suggested. One of them sees the desensitisation as the result of the dephosphorylation of TRPV1 by Ca^{2+}-dependent phosphatases, activated by the calcium influx through TRPV1 itself (Docherty et al., 1996).

1.2.8 Endocannabinoid system and skeletal muscle

The endocannabinoid system is expressed and its members are active in regulating numerous biological processes in skeletal muscle (Ruiz de Azua & Lutz, 2019). CB1 is known to be involved in metabolic dysregulation and glucose maintenance in skeletal muscle. CB1 activation, decreased mitochondrial and oxidative markers (peroxisome proliferator-activated receptor gamma coactivator 1 alpha, PGC1α, and nuclear respiratory factor 1, NRF-1), and

mitochondrial biogenesis in white adipose, muscle and liver tissues from high fat diet-fed mice (Tedesco et al., 2010). On the other hand, in murine skeletal muscle, pharmacological CB1 antagonism and CB1 knockout prevented insulin-induced resistance, leading to an increase in muscle mass, physical endurance, mitochondrial performance, and an upregulation of metabolic regulators (González-Mariscal et al., 2019; Liu et al., 2005). Recently, it has been discovered that CB1 expression is higher in slow compared to fast human muscle fibers, and CB1 levels vary depending on the muscle type (Dalle et al., 2022). Not only, with a decrease in metabolic health with aging, CB1 protein expression was found to be increased in the muscle of old compared to young human adults (Dalle & Koppo, 2021). However, whether alterations in the cannabinoid tone are a result or a cause of metabolic dysfunction should be clarified. A recent study pointed out the role of CB2 in metabolic regulation: in C2C12 myotubes, CB2 activation enhanced glucose uptake, glycolytic and oxidative pathways, and ATP production (Geddo et al., 2021). Among canonical cannabinoid receptors, non-classic cannabinoid receptors have a role in metabolic processes (Dalle et al., 2022). GPR55 activation appears to improve muscle insulin sensitivity (Lipina et al., 2019), while TRPV1 promotes oxidative metabolism, shifting the mice muscle fibres toward a slow phenotype (Luo et al., 2012). Besides the involvement of ECS in muscle metabolic regulation, it also plays a role in myogenesis, muscle differentiation and regeneration. 2-AG, but not AEA, levels decreased during differentiation both *in vitro* and *in vivo*, while CB1 and CB2 expression were found to significantly increase (Iannotti et al., 2014). The same study confirmed the role of 2-AG in the control of myoblast differentiation. In fact, 2-AG treatment reduced myotubes formation via CB1-induced K_v7 channel inhibition (Iannotti et al., 2014). A previous study showed the permissive role of Kv7 channel in skeletal myogenesis (Iannotti et al., 2013). CB1 couples to $G_{q/11}$, which upon PLC activation, leads to PIP_2 hydrolysis. Low PIP_2 concentration correlates with a decrease of the open state probability of K_v7 channel, reducing K_v7-mediated K^+ current and therefore the differentiation process. In C2C12, TRPV1 activation was also shown to promote myoblasts differentiation by increasing Ca^{2+} concentration (Iannotti et al., 2019). Moreover, CB1 antagonism enhanced the expression of myogenic markers (Myogenin and MHC) promoting differentiation in human satellite cells, whereas, in dystrophic mice, it increased the number of healthy/regenerating myofibers, and decreased inflammatory markers (Iannotti et al., 2018). Both *in vivo* and *in vitro* experiments show the involvement of

CB2 in muscle cell growth and regeneration. Indeed, CB2 agonism attenuated the inflammatory response and ameliorated muscle repair after skeletal muscle injury (M. Zhang et al., 2019), while CB2 knockout mice showed myofiber necrosis, decreased MyoD and Myogenin expression, and increased fibrosis and inflammatory cell infiltration (Jiang et al., 2020).

1.3 Sphingosine 1-phosphate system

Sphingolipids are a class of polar lipids whose backbone is a molecule of sphingosine. Initially considered mere structural components of the eukaryotic membrane, they have been discovered to be bioactive molecules involved in a variety of different biological processes, such as proliferation, cell migration, differentiation, survival, inflammation, and much more (Hannun & Obeid, 2008; Maceyka et al., 2012). Among the sphingolipids, ceramide and sphingosine 1-phosphate (S1P) have gained more and more interest for their opposing effects in the organism: apoptosis on one hand and cell survival on the other. Therefore, the relative levels of these two sphingolipids, the so-called "Sphingolipid rheostat", are essential to determine cell fate (Spiegel & Milstien, 2003). S1P was discovered in the 1960s, when the prevailing notion was that S1P was more similar to traditional second messengers (i.e. diacylglycerol and Ca^{2+}), although *in vitro* studies suggested its bioactive nature (Cartier & Hla, 2019). Over the years, five S1P receptors ($S1P_{1-5}$), which respond to extracellular S1P, have been identified in vertebrates (Cartier & Hla, 2019). S1P receptors couple to multiple α subunits of heterotrimeric G proteins, are differently expressed in the human body, and induce the activation of different downstream pathways, therefore resulting in involvement in distinct biological processes (Donati et al., 2013). S1P production starts with the synthesis of its precursor ceramide. In the *de novo* pathway (fig. 6), the enzyme serine palmitoyl transferase uses palmitoyl-CoA and serine to form dihydrosphingosine, which is then acylated by ceramide synthase to dihydroceramide and desaturated to ceramide by ceramide desaturase enzyme. Ceramide is also obtained by the breakdown of membrane sphingolmyelins and glycosphpingolipids. Once ceramide is produced, ceramidases cut the acyl chain of ceramide to create sphingosine, which can be converted back to ceramide by ceramide synthase. Sphingosine can be phosphorylated in an ATP-dependent manner by two isoforms of sphingosine kinase (SK1 and SK2) to produce S1P. S1P, in turn, can be dephosphorylated to sphingosine by two specific sphingosine phosphatases (SPP1 and SPP2) or it can be degraded by sphingosine lyase (SPL) into hexadecenal and phosphoethanolamine. S1P's fate depends on the site of its production. SK1 is a cytosolic enzyme, which can be activated by growth factors, hormones, cytokines, and ligands of G protein-coupled receptors. When SK1 is phosphorylated by ERK at serine 225, it translocates to the plasma membrane,

where resides its substrate, sphingosine (Pitson et al., 2003). S1P, produced by SK1, is then released out of the cells through ATP-binding cassette transporters or the specific spinster 2 (SPNS2), acting in an autocrine or paracrine manner and, therefore, beginning the "inside-out" signalling (Donati et al., 2013). Recently, lipid transporter MFSD2B was found to mediate specific export of S1P in erythrocytes and platelets (Vu et al., 2017). SK2 localises in intracellular compartments such as the ER, nucleus, and mitochondria. S1P produced by this kinase is far from the plasma membrane but close to its degrading enzymes, SPL and SPPs, which can recycle sphingosine for ceramide production (Le Stunff et al., 2007). Nuclear SK2 forms a complex with histone H3 and histone deacetylases (HDACs), and S1P, binding to and inhibiting HDAC1/2, can control the epigenetic regulation of gene expression (Hait et al., 2009). In the mitochondria, S1P was found to interact with a conserved protein able to regulate mitochondrial assembly and function, prohibitin 2. This interaction appears to be important for cytochrome-*c* oxidase assembly and mitochondrial respiration (Strub et al., 2011). S1P is mainly produced by erythrocytes and platelets (Cordeiro et al., 2019) but, due to its poor aqueous solubility, S1P transport in blood and lymphatic circulation needs chaperon proteins, whose interaction with S1P results in the formation a spatial gradient allowing different biological activities of this bioactive sphingolipid (Cartier & Hla, 2019). The specific S1P-binding protein in blood is apolipoprotein M (ApoM), a component of high-density lipoprotein (HDL). Its binding to S1P is stable and promotes endothelial cells' S1PRs activation, leading to an inhibition of inflammation and a promotion of barrier function. S1P can also associate with albumin, but with a lower affinity and a less stable binding (Cartier & Hla, 2019).

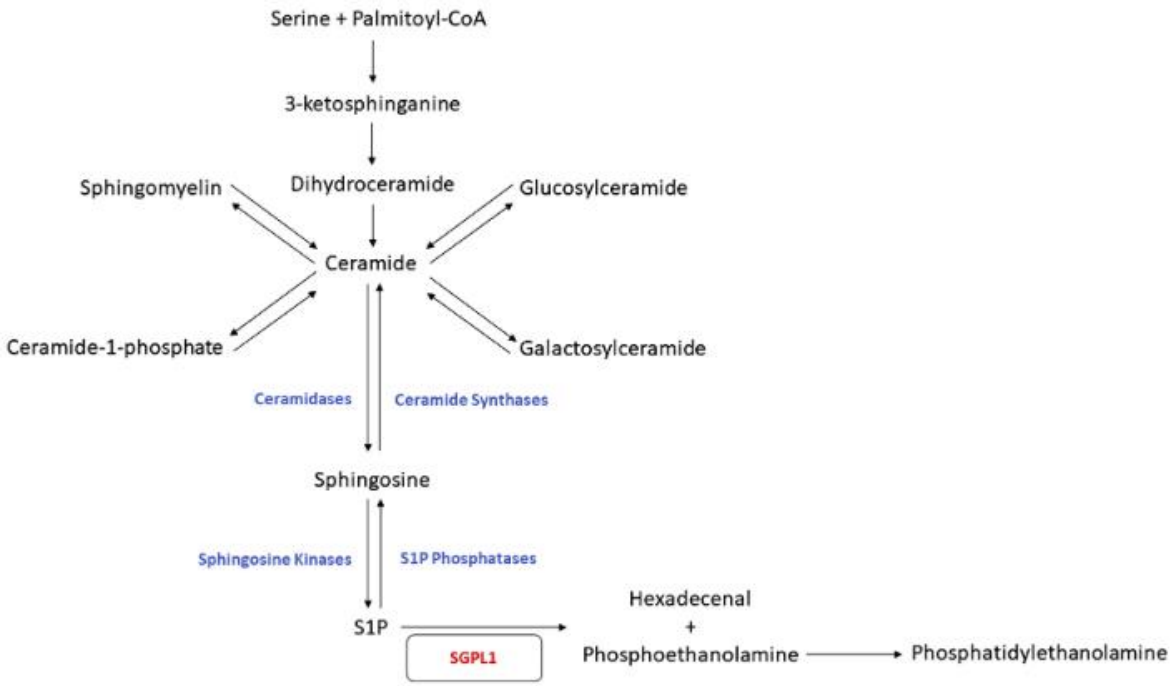

Figure 6. Sphingolipid metabolism (Taylor et al., 2019)

1.3.1 S1P Receptors

The five G protein coupled receptors specific for S1P share some structural and functional similarities with both cannabinoid and lysophosphatidic acid receptors (Rosen et al., 2009). $S1P_{1-3}$ are ubiquitously expressed, whereas $S1P_4$ and $S1P_5$ are tissue specific, being found in the lymphoid and nervous system, respectively (Spiegel & Milstien, 2003).

$S1P_1$, once called Edg-1, was the first S1P receptor to be cloned. It is ubiquitous expressed, and its wide distribution leads to multiple biological effects in different organs (Bravo et al., 2022). $S1P_1$ is coupled to G_i alone, leading to the inhibition of AC, as demonstrated in overexpressed HEK cells, where constitutively active $S1P_1$ leads to the activation of ERK2, which is sensitive to PTX. However, in some cells, $S1P_1$-mediated actions are not sensitive to PTX, such as the S1P-induced cell-cell aggregation and up-regulation of P and E cadherins in HEK overexpressing human $S1P_1$ (Siehler & Manning, 2002). Of all the S1P receptors, the deletion of $S1P_1$ alone is embryonic lethal. Failure of the arterial smooth muscle to migrate dorsally to form the media prevents arterial pressure resistance and results in catastrophic

artery rupture. This phenotype, which shows one clear, nonredundant function of S1P during development, is mimicked by the dual loss of sphingosine kinases 1 and 2 (Rosen et al., 2009). As a result, there are no $S1P_1$ knockout mice available. On the other hand, the fact that $S1P_2$ and $S1P_3$ deletions produce healthy offspring with a range of phenotypes raises the possibility that compensatory changes in receptor expression and signalling may take place (Rosen et al., 2009). In fact, many cell types express multiple S1P receptor subtypes. For example, skeletal muscle cells express $S1P_{1-4}$.

$S1P_2$ and $S1P_3$ share 92% sequence identity, therefore are closely related (Toman & Spiegel, 2002), and couple, not only to G_i, but also to G_q and $G_{12/13}$, while $S1P_{4-5}$ couple to G_i and $G_{12/13}$. These G proteins can trigger a variety of downstream signals, including small GTPase modulation (Rac and Rho), AC inhibition or upregulation, PLC activation and intracellular calcium mobilisation, and Akt and ERK 1/2 phosphorylation (Rosen et al., 2009).

1.3.2 S1P in skeletal muscle

Myoblasts express four out of five S1P receptors ($S1P_{1-4}$), with the highest prevalence of $S1P_1$. In C2C12 cell line, the differentiation of myoblasts into myotubes is followed by a change in S1PR expression, revealing the important role of the S1P system in myogenic differentiation. Indeed, during this process, $S1P_2$ is downregulated while $S1P_3$ is upregulated (Meacci et al., 2003). The involvement of the $S1P_2$ subtype in C2C12 differentiation is undeniable since S1P acting via $S1P_2$ is able to revert the serum-induced proliferation and stimulate myoblast differentiation (Bernacchioni et al., 2011; Donati et al., 2005b). Additionally, SK1 expression was found to be increased in differentiating myoblasts (Meacci et al., 2008). SK1 over-expression leads to a reduction in the myoblast proliferation rate and the induction of myogenic marker expression. This pro-myogenic action was abolished in $S1P_2$ silenced cells, highlighting the crucial role of S1P/$S1P_2$/SK1 axis in the differentiation process. SK1 activation, and therefore its translocation to the membrane, is under the control of a number of growth factors, cytokines and hormones (Maceyka et al., 2012). Low doses of TNFα leads to SK1 translocation to membrane, its activation and S1P production, which acting on $S1P_2$ stimulates C2C12 myoblast differentiation (Donati et al., 2007). IGF-1 can activate both SK1 and SK2 and

via $S1P_2$ transactivation exerts its myogenic action, while the transactivation of $S1P_1$ and $S1P_3$ reduces cell proliferation (Bernacchioni et al., 2012). Another growth factor (platelet derived growth factor or PDGF) has a negative role on myoblast proliferation inducing the activation of SK1 and the selective transactivation of $S1P_1$ (Donati et al., 2013).

The role of S1P is not limited to the regulation of the myogenic differentiation of myoblast into myotubes. This bioactive sphingolipid can also activate a normally quiescent population of cells, the satellite cells, participating in the process of muscle repair after injury. During muscle regeneration, S1P can activate satellite cells and promote their proliferation and migration to the site of the lesion (Calise et al., 2012). Indeed, in satellite cells the pro-mitogenic action is due to S1P increased levels by SK1 (and SPL activity reduction) and $S1P_2$/STAT3 signalling (Loh et al., 2012). While the S1P migratory effect on satellite cells is exerted by $S1P_1$ activation (Cordeiro et al., 2019). Once reached the injured fibers, the differentiation process takes place: cells stop proliferating and start to form myotubes. Interestingly, $S1P_2$ was shown to inhibit myoblast mobility, which is induced by S1P in activated satellite cells, revealing a dual role of the sphingolipid on cell migration.

As already said, during differentiation, a small reservoir of cells remains undifferentiated. S1P acting via $S1P_1$ stimulates “reserve cells” proliferation, renewing the cellular pool (Rapizzi et al., 2008).

1.4 ECS and S1P system functional interaction

S1P receptors and endocannabinoid CB1 and CB2 receptors belong to the lysolipid superfamily of GPCRs (G-Protein Coupled Receptors) and phylogenetic analysis indicate ~20% of amino acid sequence homology (Sanchez & Hla, 2004). These structural similarities open the possibility to the ligands to bind to the receptors of both systems. In fact, it has already been demonstrated an interaction between FTY720 and sphingosine and CB1 receptor (Paugh et al., 2006). FTY720 (Fingolimod) is an analogue of sphingosine and an immunomodulatory drug which, following its phosphorylation by SK2, can bind to the S1P receptors, except for $S1P_2$, and prevent kidney transplantation development, autoimmune diseases, and multiple sclerosis. Both Fingolimod and sphingosine act as competitive CB1 antagonists without interfering with CB2 (Paugh et al., 2006).

Other significant interactions between the two systems have been found in the regulation of the vascular tone. In fact, both S1P and endocannabinoids are cardioprotective and have a role in the regulation of the cardiovascular system. S1P's impact on vascular tone appears to be influenced by the receptor subtypes expressed in that vessel and their distribution (Coussin et al., 2002). Indeed, similar concentration of S1P induces different responses in rat mesenteric arteries and in rat aorta: while in the first case it constricts the vessels, in the second case it dilates the aorta (Hemmings et al., 2004; Roviezzo et al., 2006). In rat coronary artery, S1P and AEA induce vascular relaxation involving both CB2 and $S1P_3$ receptors. CB2 antagonists attenuated AEA-induced relaxation, and $S1P_3$ was required for AEA-mediated vasorelaxation. Also, S1P-mediated relaxation was dependent on $S1P_3$ and reduced by CB2 antagonists. Interestingly, AEA treatment stimulates SK1 phosphorylation and the inhibition of SK1 abolished the AEA-mediated relaxation (Mair et al., 2010). Previous studies have shown the possibility of CBs to regulate the sphingolipid metabolism: CB1 activation results in an accumulation of ceramide in different cell types (Blázquez et al., 1999; Galve-Rophert et al., 2000).

1.5 Calcium

Calcium (Ca^{2+}) is a ubiquitous intracellular signal responsible for controlling a variety of cellular processes: ranging from muscle excitability and contraction to gene expression, invasion migration and cell apoptosis. This versatility results from the utilization of a wide range of molecular signalling elements that together make up a Ca^{2+} signalling toolkit that may be used to produce signals with a wide range of spatial and temporal patterns (Berridge et al., 2000). Briefly, a stimulus generates Ca^{2+} mobilization signal, Ca^{2+} is released into the cytoplasm and acts as a messenger to stimulate Ca^{2+}-sensitive processes. Finally, to restore the resting state, a series of pumps and exchangers remove Ca^{2+} from the cytoplasm. The source of calcium can be both external and internal to the cells (i.e., the ER) and the release from the internal storage of Ca^{2+} is controlled by different channels, of which the inositol-1,4,5-trisphosphate receptor (InsP3R) and ryanodine receptor (RYR) families are the most studied. Several families of Ca^{2+} entry channels exist and are defined by how they are activated: Voltage-Operated Channels (VOCs), Receptor-Operated Channels (ROCs), and Store-Operated Channels (SOCs). Once the mechanism of release of calcium is turned on, intracellular concentration of Ca^{2+} rises from 100 nM up to 1000 nM, leading to Ca^{2+}-activated processes. Once Ca^{2+} has exerted its action, it is rapidly removed from the cytoplasm by the plasma membrane Ca^{2+}-ATPase (PMCA) pumps and Na^{+}/ Ca^{2+} exchangers, which extrude Ca^{2+} to the outside, and the sarco-endoplasmic reticulum ATPase (SERCA), which returns Ca^{2+} into the ER. The mitochondrion can also sequester Ca^{2+}.

Among other signals that participate in the generation of intracellular Ca^{2+} spikes, S1P can be mentioned. S1P-induced Ca^{2+} increase mainly couples to the phospholipase C (PLC) pathway, through $S1P_{2\text{-}3}$, leading to the hydrolysis of phosphatidylinositol 4,5-bisphosphate (PIP2) to inositol 1,4,5-trisphosphate (IP3) and diacylglycerol (DAG) (Berridge et al., 2000; Rapizzi et al., 2007; Young & Nahorski, 2002). IP3 binds to the IP3 receptor provoking the calcium release from the intracellular stores, while DAG may activate the calcium permeable ion channels in the plasma membrane (Berridge et al., 2000). Noteworthy, there are studies suggesting the direct activation of Ca^{2+} release from intracellular stores by intracellular S1P via IP3-

independent manner (Ghosh et al., 1994; Meyer Zu Heringdorf et al., 2003). However, no intracellular S1P-Ca^{2+} releasing target protein has been identified yet (Pulli et al., 2018).

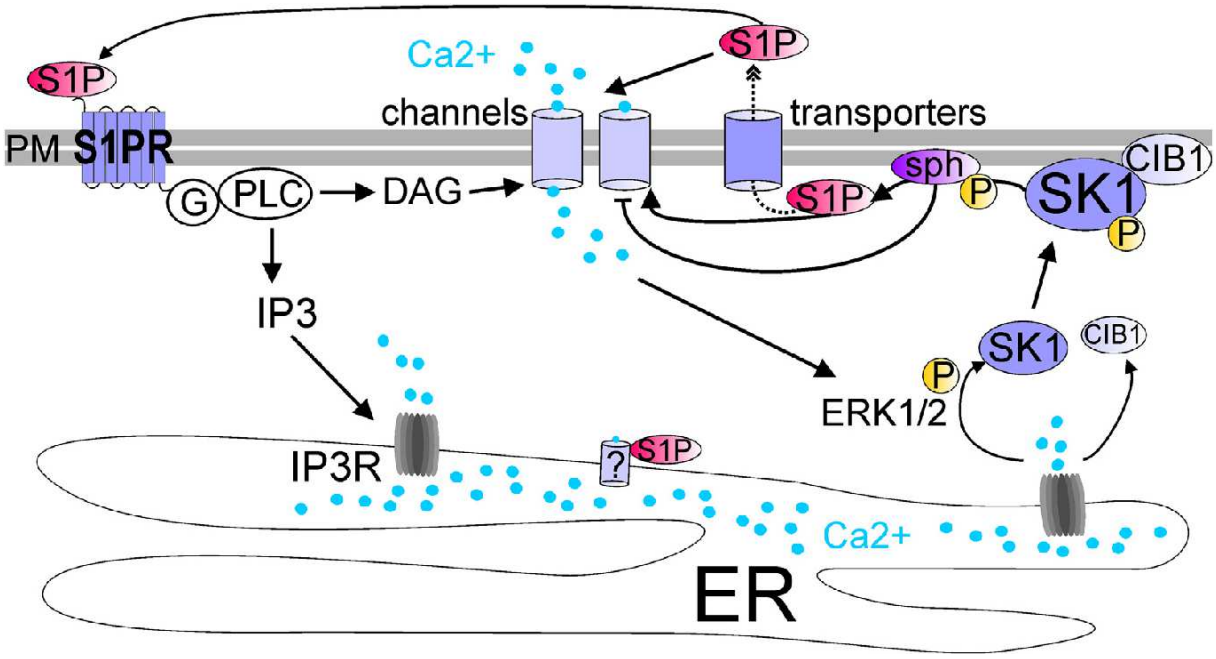

Figure 7. General schematics of sphingosine kinase 1 (SK1), sphingosine 1-phosphate (S1P) and calcium signaling (Pulli et al., 2018).

As shown in figure 7, SK1 phosphorylation and its translocation to the plasma membrane resulting in S1P production are regulated by ERK 1/2 and by the calcium and integrin binding protein (CIB1), which in turn are both regulated by Ca^{2+}. Together, S1P synthesis and transport may be positively regulated by intracellular Ca^{2+}, which may then modify calcium signalling through the S1PRs in an auto/paracrine manner as well as by unknown intracellular mechanisms (Pulli et al., 2018).

Besides S1P, also endocannabinoids can influence Ca^{2+} signalling. In fact, CB1 agonists, including AEA, acting via G_i and G_q, can induce the hydrolysis of PIP2 into IP3 and therefore the Ca^{2+} mobilization from the ER. TRPV1 activity can be also regulated by GPCRs, including CBs, that by activating PLC, induce the release of TRPV1 from the inhibitory effect of PIP2 (Nilius et al., 2008). At the same time, DAG-induced activation of PKC, and the activation of PKA, are two other mechanisms of sensitization of TRPV1. On the other hand, both GPCRs and TRPV1-mediated Ca^{2+} increase can stimulate AEA biosynthesis (De Petrocellis & Di Marzo, 2009).

2 Materials and Methods

2.1 C2C12 cell culture

Murine C2C12 myoblast cell line was obtained from the American Type Culture Collection (ATCC® CRL-1772™ Manassas, VA, USA). C2C12 were grown in a complete medium consisting of Dulbecco's Modified Eagle Medium (DMEM) supplemented with 10% Fetal Bovine Serum (FBS), 100 U/mL penicillin/streptomycin, 2 mM L-glutamine, and 0.5% Ciprofloxacin. The cell line was maintained in a 5% CO_2 atmosphere at 37°C. Thanks to the ability to differentiate in myotubes depending on the culture conditions, C2C12 myoblast cell line is the most common *in vitro* model used to study skeletal muscle biology. The myogenic differentiation of C2C12 myoblast was performed as previously described in (Donati et al., 2005). To induce differentiation, confluent cells were washed twice with PBS (Phosphate Buffer Saline) and starvation medium was added 30 minutes before treating the cells with different molecules depending on the experiment's conditions. The starvation medium consisted of DMEM with 0.1% Bovine Serum Albumin (BSA), 100 U/mL penicillin/streptomycin and 2 mM L-glutamine. DMEM, FBS, PBS, and BSA were purchased from Sigma-Aldrich (St. Louis, MO, USA).

2.2 Cell treatments and collection

C2C12 cells were pre-treated with endocannabinoids receptors antagonists SR1, SR2 and I-RTX for 30 minutes in serum free media, before adding 10 µM metanandamide (mAEA, AEA stable analogue) or 1 µM S1P, or 1 µM capsaicin (CAP). SR141716A (SR1) and SR144528 (SR2) (Sigma-Aldrich St. Louis, MO, USA) are CB1 and CB2 antagonists respectively, while I-RTX (Tocris Bio-Techne SRL, Milan, Italy) is a TRPV1 antagonist. mAEA was purchased from Sigma-Aldrich (St. Louis, MO, USA), S1P from Calbiochem (Darmstadt, Germany) and CAP from Sigma-Aldrich (St. Louis, MO, USA). Cells were washed twice in cold PBS after 24-48h treatment and collected in lysis buffer containing 50 mM Tris-HCl pH 7.5, 1 mM EDTA, 6 mM EGTA, 120 mM

NaCl, 20 mM NaF, 1% Nonidet, and proteases and phosphatases inhibitors mix purchased from St. Louis, MO, USA. After 30 minutes on ice, the samples were centrifuged at 1x10^4 x g for 15 minutes at 4 °C. After centrifugation the soluble molecules-containing supernatant was collected, while the pellet containing nucleic acids and cell membranes was discarded. Supernatants were subjected to protein quantification.

2.3 Protein quantification

Protein concentration quantification of each sample was performed in total cell lysates by Bradford protein assay. This quantification method is based on the employment of the dye Coomasie brilliant blue G-250, which can form strong non-covalent complexes with proteins, causing a shift from 465 nm to 595 nm (wavelength of the absorbance readings taken by the spectrophotometer). The absorbance at 595 nm and the amount of bound dye are proportional, therefore the absorbance reflects the amount of protein present in each sample. To calculate the sample's protein concentration, the spectrophotometer compares the absorbance of the samples to a standard curve previously calculated by the instrument by using known concentrations of BSA and measuring the corresponding absorbance values. The measurements were performed in duplicate using 2 µL of protein sample, 798 µL of deionized H_2O and 200 µL of Bradford dye. By interpolation of the absorbance of cell lysates with the standard curve, the spectrophotometer calculates the exact concentration of each sample in µg/µL. Bradford dye was purchased by BioRad (Hercules,CA,USA).

2.4 SDS-PAGE

The volume needed to obtain a certain amount of protein for each sample was estimated, then collected and diluted in Laemmli Sample Buffer 4X, which denatures protein and reduces disulphide bonds. Samples were then boiled for 5 minutes, to increase the denaturation process, and centrifuged 1 minute at 1.6x10^4 xg. SDS-PAGE is an electrophoresis method

that allows protein separation by molecular mass. The polyacrylamide gel consists of two phases: the Stacking gel, above, and the Separating gel, below. Samples are charged into the first gel, where they can alienate and start running all together in the second gel, where the proteins are separated by their molecular mass. Different concentrations of acrylamide in the Separating gel allow better separation of high (8%) or low (14%) molecular weight proteins. The SDS-PAGE was performed in a Running Buffer consisting of 192 mM Glycine, 25 mM Tris HCl, and 1% SDS pH 8.3, and a current of 130 V and 400 mA was applied for about 90 minutes.

2.5 Western Blot analysis

After the SDS-PAGE, proteins were transferred from the gel to a PVDF (polyvinylidene fluoride) membrane using the Trans-Blot Turbo instrument, purchased from BioRad (Hercules,CA,USA). This method consists of placing the electrophoretic gel on top of the PVDF membrane and between two filter papers dipped in a buffer containing glycine and 20% methanol. This sandwich is located between the two plates of the instrument (the cathode and the anode), which, thanks to an electric current, allows the negatively charged protein to be transferred from the gel to the membrane. The membrane was then incubated for 5 minutes at room temperature with EveryBlot Blocking Buffer (BioRad,Hercules,CA,USA), in order to avoid the non-specific interactions between the membrane and the primary antibody. Subsequently, the primary antibody, specific for the protein of interest, was diluted in TTBS (20 mM Tris-HCl, 150 mM NaCl, pH 7.5 with 0.1% Tween 20) and incubated with the membrane at 4°C overnight. The morning after, the membrane was washed three times for 5 minutes with TTBS and incubated with the secondary antibody, diluted in TTBS, for one hour at room temperature. The secondary antibody, conjugated to horseradish peroxidase, recognises and specifically binds to the primary antibody. The anti-mouse and anti-rabbit secondary antibodies were purchased from Santa Cruz Biotechnology Inc. (Santa Cruz, CA, USA). The membrane was washed three times for 5 minutes with TTBS and once with TBS. The membrane was incubated with ECL chemiluminescence reagent (GE Healthcare Europe GmbH, Milano, Italy) containing the horseradish peroxidase's substrate. The enzyme cathalyses the cleavage of the substrate, causing chemiluminescence detected by the

Amersham Imager 600 GE Healthcare®. After the detection of the protein band of interest the image analysis was performed through Image J software, which allows a quantitative densitometric analysis of the bands. The proteins of interest were normalised to a housekeeping protein, which does not vary under any experimental condition.

Antibodies against housekeeping proteins, anti-βactin and anti-GAPDH were purchased from (Santa Cruz, CA, USA). To detect proteins of interest, different specific primary antibodies were used: anti-Myogenin (Santa Cruz, CA, USA), anti-Caveolin 3 (BD Biosciences, New Jersey, USA), anti-MHC (Sigma-Aldrich, St. Louis, MO, USA), anti-SPL (Invitrogen, Life Technologies Corp., Carlsbad, CA, USA), and anti-SK1 anti-SK2, anti-PSK1, anti-PSK2 (ECM Biosciences LLC, Versailles, KY USA).

2.6 Stripping of PVDF membrane

The PVDF membrane holding the proteins can be probed multiple times by incubating with stripping solution that enables the detachment of the antibodies from the membrane. The membrane was washed with TTBS, the stripping solution (Termo Scientific, Rockford, IL, USA) was warmed to 50°C and applied to the membrane for 20 minutes at room temperature. The membrane was then washed three times for 5 minutes with TTBS and incubated with primary antibodies to detect new proteins of interest.

2.7 Real-Time PCR

C2C12 cells were washed twice in PBS and collected in Tri Reagent solution (Sigma-Aldrich, St. Louis, MO, USA) under a chemical hood. Samples were frozen and maintained at -80°C until the RNA extraction procedure. Once RNA was obtained, the concentration of total RNA for each sample was determined with a spectrophotometer ND-1000 and 1.5 µg of RNA was subjected to retrotranscription with High-Capacity cDNA Reverse Transcription Kit (Thermo Fisher Scientific INC, MA, USA). The cDNA formed by the reverse transcriptase was maintained

at -20°C. Real-time PCR analysis was then performed to quantify the mRNA expression of genes involved in S1P metabolism and in the C2C12 differentiation process. In this study, the instrument ABI 7700 SDS (Sequence Detection System Applied Biosystem, Foster city, USA) and TaqMan probes were used. TaqMan probes are able to identify and bind one specific region of the cDNA strand and consist of a fluorescent reporter and a quencher at the opposite site of the probe. The proximity of the quencher prevents the detection of the fluorescence emitted by the reporter. The Real-Time PCR method was carried out in a thermal cycler, which repeats a series of temperature changes 40 times. Each cycle consists of three phases: the first, at 95°C, allows the separation of the nucleic acid's double chain; the second, at 50-60°C, allows the specific binding of the primers with the cDNA; and in the third, at 68-72°C, the polymerization is catalysed by DNA polymerase while degrading the probe that binds the cDNA. This way, the quencher moves away from the fluorophore, whose fluorescence is captured by the instrument after excitation with a laser. The fluorescence increase is proportional to the breakdown of the probe and therefore to the amount of cDNA binding the probe. The threshold cycle (C_t) is the cycle of the reaction that is above the chosen threshold, and it is useful for the quantity analysis carried out with the ΔΔCt comparative method (Livak & Schmittgen, 2001).

The thermal cycler was provided by BioRad (Hercules, CA, USA) the retro-transcription kit, Real Time PCR kit and probes were obtained from Life Technologies (Carlsbad, CA, USA). For the quantitative analysis, β-Actin was employed as housekeeping gene.

2.8 Immunofluorescence Assay

C2C12 cells were seeded on microscope slides (22 mm x 22 mm) (1x10^5 cells/slide), and let them grow, for at least two days, until the 80% confluency was reached. Then, the growth medium was removed and replaced with serum-deprived medium in the presence of 0.1% BSA, treated or not with 0.1 µM I-RTX for 30 minutes before adding the stimulus. Cells were incubated at 37°C for 4 days and then were washed twice with PBS and fixed with paraformaldehyde solution 3%. A permeabilization and quenching solution (0.1% Triton X-100 and ethanolamine (1:165) in PBS) was added for 30 minutes at room temperature, and 3%

BSA was then used as a blocking solution. Cells were then incubated with the primary antibody anti-MHC, diluted 1:200 in 1% BSA for two hours and another hour with the secondary antibody, Texas Red anti-mouse IgG (H+L) (TI-200, Vector Burlingame, CA) diluted 1:200 in 1% BSA. A DAPI solution 1000X (#MBD0015, Sigma-Aldrich, MA, USA) was incubated with cells for 20 minutes in the dark to stain cell nuclei. Fluoromount Aqueous Mounting Medium (Sigma-Aldrich, MA, USA) was used to mount the slides, and a Leica SP8 laser scanning confocal microscope (Leica Microsystems GmbH, Wetzlar, Germany) was used to capture the pictures while using a 40X or 63X oil-immersion objective.

2.9 Mitochondrial membrane potential assay

The mitochondrial membrane potential status of C2C12 cells was assessed by Mito-Tracker CMXRos (#M7512) probe (Thermo Fisher Scientific INC, MA, USA) and Laser scanning confocal microscopy. The amount of dye accumulated in the mitochondria is proportional to its membrane potential. Cells were seeded on microscope slides the day after they were shifted in starvation medium and treated with 1 µM of SR1, SR2 and I-RTX for 30 minutes before being challenged with 5 µM mAEA. After 24h treatment, the probe was diluted in DMEM medium without phenol red at a concentration of 50 nM, incubated 30 min at 37°C and 5% CO_2 in the dark. Then, cells were fixed in 3% paraformaldehyde, washed twice, and incubated with a permeabilization and quenching solution. A DAPI solution was used to detect nuclei. Fluoromount Aqueous Mounting Medium (Sigma-Aldrich, MA, USA) was used to mount the slides, and a Leica SP8 laser scanning confocal microscope (Leica Microsystems GmbH, Wetzlar, Germany) was used to capture the pictures while using a 40X or 63X oil immersion objective.

2.10 High-Resolution Respirometry analysis

The Oroboros oxygraph-2K high-resolution respirometer (Oroboros Instruments, Innsbruck, Austria) and substrate, uncoupler, inhibitor, titration (SUIT) protocols were used to measure oxygen consumption in 2 mL glass chambers at 37°C as described by Ye & Hoppel (Ye & Hoppel, 2013). The oxygen flux normalized on the cell number is calculated as the negative time derivative of the oxygen concentration, measured in sealed chambers, and normalised on the instrumental background (assessed in a dedicated experiment prior to cell assaying). Analyses of respirometry were performed on C2C12 myoblasts treated for 24 hours with 5 µM mAEA or the control vehicle (ethanol). 3x10^5 cells resuspended in DMEM with 1 mg/mL BSA were added to the chambers after the instrument's air calibration, and the baseline respiratory activity was evaluated as routine respiration (R). After the administration of oligomycin (5 nM), which inhibits ATP synthase, it was possible to evaluate the LEAK state (L), which represents the non-phosphorylating state of uncoupled respiration caused by proton leak, proton and electron slip, and cation cycling (Pesta & Gnaiger, 2012). Uncoupler titrations were used to determine the capacity of the electron transfer system (ETS) using the uncoupler CCCP (1.5 µM/titration steps) as the readout of the maximum oxygen usage capacity (E). Antimycin A (2.5 µM) injection was used to measure the residual oxygen consumption (ROX) that remained after ETS inhibition. Data collection and analysis were carried out using the DatLab software (version 7.4, Oroboros Instrument, Innsbruck, Austria). The oxygen fluxes recorded in the individual titration steps were corrected for ROX.

2.11 Calcium Measurement

Calcium influx concentration was measured by the Fura2 fluorescence dual-wavelength method. C2C12 cells were seeded in 143 cm^2 plates and, when 80% confluent, treated with 1µM S1P. After 24 hours, cells were washed twice with PBS and detached with Trypsin-EDTA. To dilute Trypsin, serum free medium was added, and cells were centrifuged at 1000 x g for 5 minutes. Pellets were rinsed with HBSS and centrifuged again. Cells were incubated with 1µM

Fura-2, AM ester (Biotium, Fremont, CA, USA), diluted in HBSS, for 45 minutes at room temperature in the dark. Cells were centrifuged and washed with HBSS twice to remove the probe. Cells were diluted 6 x 10^5/mL in HBSS, 2 mL of cell suspension was added to each cuvette, and the excitation-to-emission fluorescence ratio was measured with constant stirring using an F-2500 fluorescence spectrophotometer (Hitachi - Science & Technology). The use of Fura2-AM allows accurate measurement of the intracellular Ca^{2+} concentration (Moriello & De Petrocellis, 2016). This probe changes its excitation wavelength whether it is bound to calcium (340 nm) or not (380 nm), while the emission remains at 510 nm. The ratio of fluorescence intensities at 340 and 380 nm is calculated while the agonist/antagonist are added to the cell suspension. With the use of the Grykiewicz equation, the intensity data can be converted to calcium concentration (Iredale & Dickenson, n.d.).

2.12 siRNA TRPV1 transfection

Small interfering or short interfering RNA (siRNA) are common tools to knock-down specific target genes. In order to silence the expression of TRPV1, 1.5 x10^5 C2C12 cells were seeded on each well of 6-multiwell plate and the day after cells were transfected using the Lipofectamine® RNAiMAX Reagent (Invitrogen, Life Technologies Corp., Carlsbad, CA, USA). 1.2 µL siTRPV1 (or siSCR used as a control) 50 µM were dissolved in 100 µL of serum free medium, meanwhile 3 µL of RNAiMAX Reagent were dissolved in 100 µL of serum free medium. Then 100 µL of the RNAiMAX mix were added to the eppendorf containing the siRNA mix and left for 20 minutes at room temperature. In the meantime, cells were washed twice with PBS and 0.8 mL of complete medium, without antibiotics and ciprofloxacin, were added to each well. Shortly afterwards, 200 µL of the mix containing RNAiMAX and siRNA were added to the cells for 24h. The next day cells were washed with PBS and shifted in starvation medium. After 30 minutes cells were then treated with 5 µM mAEA or1 µM S1P or 1 µM CAP for 24h.

2.13 LC/MS Analysis

The lipid fractions from control and S1P-treated C2C12 cells were extracted with chloroform/methanol (2:1 v/v) in the presence of internal standards (1 ng mL-1 AEA-d8, 200 ng mL-1 2-AG-d8). Then, a clean-up step was performed as previously reported (Sergi et al., 2012). Briefly, the organic phase was dried and then subjected to micro-solid phase extraction (μSPE) for a rapid clean-up, by using OMIX C18 tips from Agilent Technologies (Santa Clara, CA, USA). All analyses were performed on a Nexera LC 20 AD XR UHPLC system (Shimadzu Scientific Instruments, Columbia, MD, USA) with NUCLEODUR® C18 Isis column from Macherey-Nagel GmbH and Co. (Neumann, Germany), coupled with a 4500 Qtrap mass spectrometer from Sciex (Concord, ON, Canada) equipped with a Turbo V electrospray ionization (ESI) source, operating in positive mode. The levels of AEA and 2-AG were then calculated on the basis of their area ratios with the internal deuterated standard signal areas, and their amounts in pmoles were normalized to the number of cells, as reported (Pucci et al., 2012).

2.14 Statistical analysis

In order to obtain a statistical analysis of the experimental results, Student's *t*-test and one-way or two-way analysis of variance (ANOVA), followed by Bonferroni post-hoc analysis, were performed. A level of $p<0.05$ was considered statistically significant.
Densitometry analysis of Western Blot images was carried out with imageJ software and for all the graphical images, GraphPad Prism v8.4.3 (GraphPad Software, La Jolla, CA, USA) was used.

3 Results

Many studies in the literature show the involvement of S1P metabolism and signalling in skeletal muscle biology (Bernacchioni et al., 2012, 2021; Cencetti et al., 2010; Donati et al., 2005a), along with the regulation of skeletal muscle differentiation driven by the eCB system (Iannotti et al., 2014). Even if both systems are expressed in skeletal muscle, the literature lacks evidence for the interaction between eCBs and S1P systems in the regulation of skeletal muscle metabolism and differentiation. Therefore, in collaboration with the University of Teramo, we employed C2C12 myoblast cell line as cellular model to elucidate whether the hypothesized functional crosstalk occurred and was responsible for the regulation of skeletal muscle cell biology. This chapter reports data from a published article entitled "The TRPV1 Receptor Is Up-Regulated by Sphingosine 1-Phosphate and Is Implicated in the Anandamide-Dependent Regulation of Mitochondrial Activity in C2C12 Myoblasts". The candidate of this thesis is a co-author of the above-mentioned article (see appendix).

First of all, we evaluated the mRNA expression of eCB-binding receptors (CB1, CB2, GPR55, TRPV1) and AEA and 2-AG metabolic enzymes (NAPE-PLD, FAAH, DAGLα, DAGLβ, and MAGL) by qRT-PCR in C2C12 cells treated for 24 and 48 h with 1 µM S1P, a dose that was shown to be effective to induce myogenic differentiation (Donati et al., 2005b). Upon exposure to S1P for 24 h, GPR55, TRPV1, FAAH, DAGLβ ($p < 0.01$ vs. control) and DAGLα ($p < 0.05$ vs. control) mRNA levels were significantly enhanced but returned to control levels at 48 h treatment with S1P, except for GPR55 which levels of expression decreased significantly ($p < 0.01$ vs. control). Then, the protein expression of eCB-binding receptors, AEA and 2-AG metabolic enzymes was evaluated by Western blot in C2C12 cells treated with 1 µM S1P for 24 h. Interestingly, CB2 protein level was decreased ($p < 0.059$), while TRPV1 protein level was increased ($p < 0.05$ vs. control), in line with qRT-PCR results. LC/MS analysis was undertaken to further evaluate the possible influence of S1P on endogenous levels of AEA and 2-AG. In line with metabolic enzyme protein expression, no significant variations in the levels of these two eCBs were measured in cells treated with 1 M S1P for 24 h.

C2C12 cells express FAAH, the main hydrolytic enzyme of AEA, therefore, to avoid the interference caused by the enzyme activity on the degradation of AEA, a stable non-

hydrolizable analogue of AEA that is methanandamide (mAEA) was used. Since AEA was shown to play a key role in energy homeostasis (Catanzaro et al., 2009; Gasperi et al., 2007), the mitochondrial membrane potential (ΔYm) was evaluated in C2C12 cells treated with mAEA at different doses (2.5; 5.0; 10 µM) for 24 h, with different procedures. In collaboration with colleagues at the University of Teramo we demonstrated that low doses of mAEA (2.5 and 5 µM) significantly increased ΔYm values compared to controls ($p < 0.01$ and $p < 0.05$, respectively), meanwhile the highest dose (10 µM) induced the opposite effect ($p < 0.05$), which was reverted in the presence of I-RTX, the selective TRPV1 antagonist, but not affected by others eCB-receptors antagonists. Since the cytotoxicity assay results indicated a reduction in cell viability upon exposure to 10 µM mAEA for 24 h, we decided to carry on the investigation using 5 µM concentration of mAEA.

The Mito-Tracker Red CMX-Ros fluorescent dye, which stains mitochondria proportionally to their membrane potential, was used to further analyse the effect of mAEA on mitochondrial activity in C2C12 treated for 24h. Laser-scanning confocal microscopy allowed the detection of fluorescence intensity, which was normalized to the cell number in each field. As shown in figure 8, in 24 h serum starved C2C12 myoblasts ΔYm significantly increased by 77.7 ± 7.5% compared to growing myoblasts (**** $p < 0.0001$), and it was further increased by 33.5 ± 2.9% (*** $p < 0.001$) upon challenge with 5 µM mAEA.

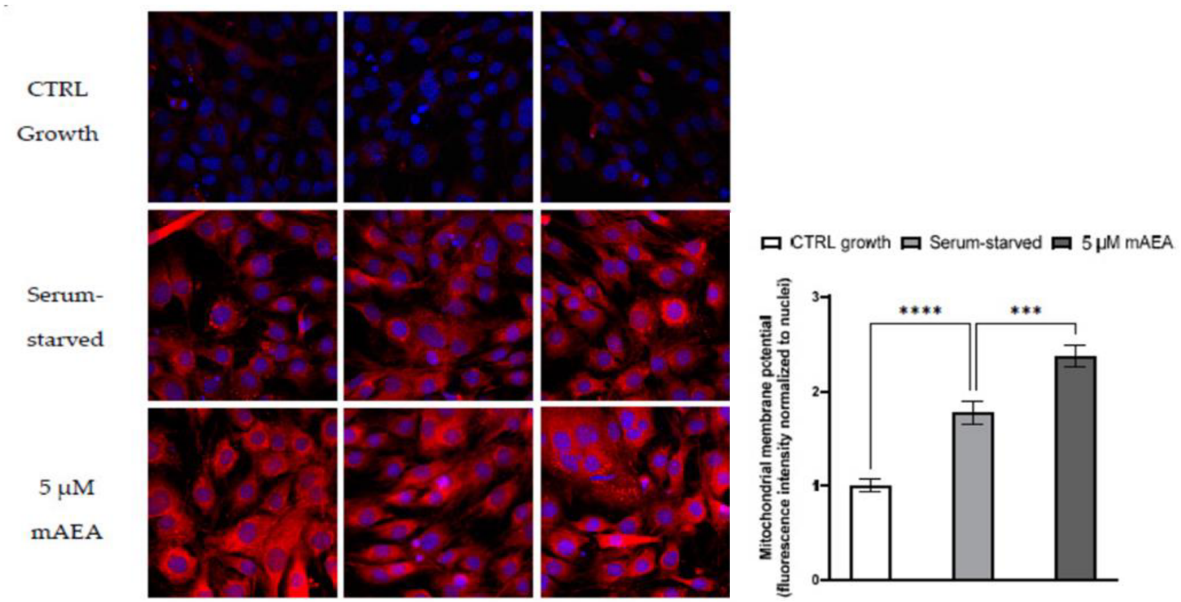

Figure 8. Effect of 5 µM mAEA on mitochondrial membrane potential. Confluent serum-starved C2C12 myoblasts were treated, or not, with 5 µM mAEA for 24 h and compared to growing (CTRL growth) myoblasts. Fluorescence intensity of Mito-Tracker Red CMX-Ros (Ex/Em: 579/599) was normalized to cell number and data are reported as mean ± SEM of six field per condition in each of the three independent experiments. Statistical analysis was performed by ONE-WAY ANOVA followed by Bonferroni post-hoc test [*** $p < 0.001$, **** $p < 0.0001$]. (Standoli et al., 2022)

The 5 µM mAEA challenge was carried out also in the presence of 1 µM S1P for 24 h with the intention of examining if S1P would affect mAEA activity on ΔYm. S1P completely reversed the mAEA-dependent increase in ΔYm under these circumstances (fig. 9).

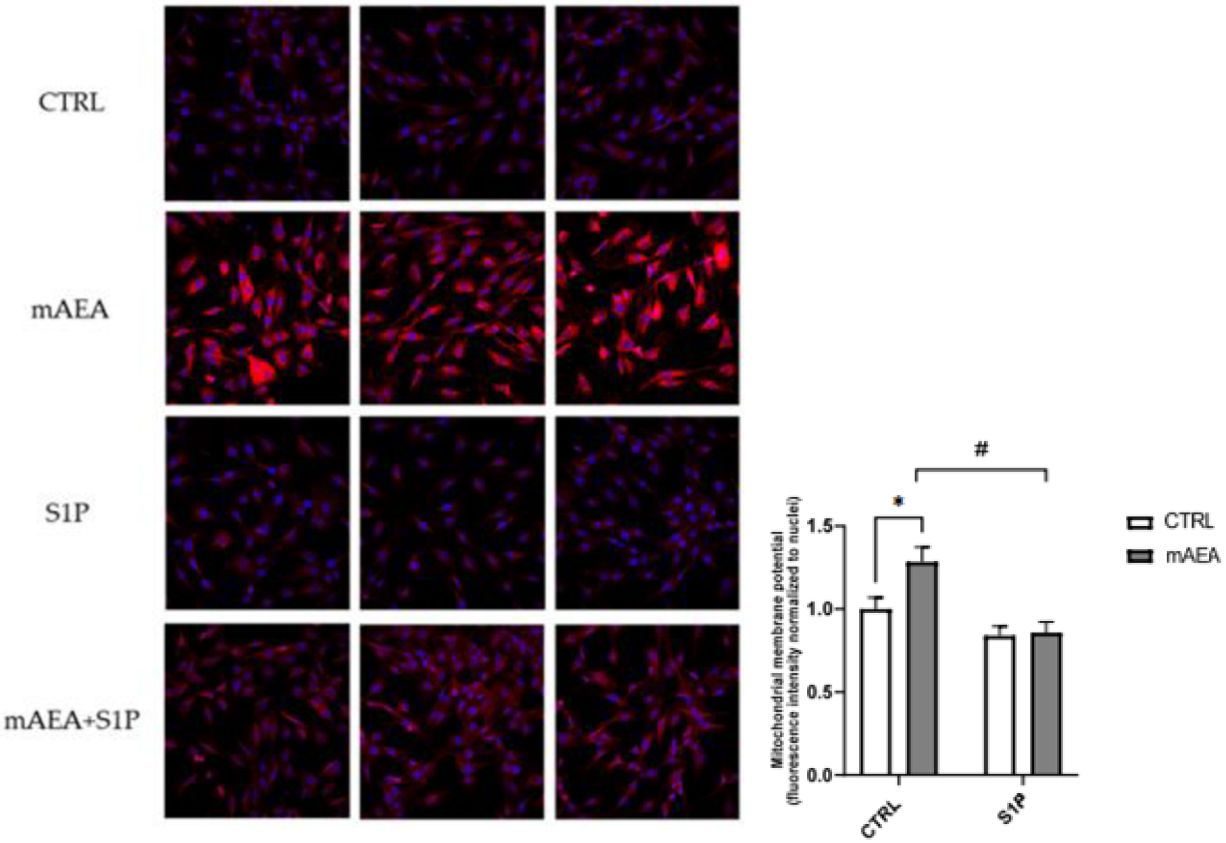

Figure 9. Effect of S1P on mAEA-induced mitochondrial membrane potential in C2C12 myoblasts. Confluent serum-starved cells were treated with 5 µM mAEA in the presence or absence of 1 µM S1P for 24 h. Fluorescence intensity of Mito-Tracker Red CMX-Ros (Ex/Em: 579/599) was normalized to cell number and data are reported as mean ± SEM of six field per condition in three independent experiments. Statistical analysis was performed by TWO-WAY ANOVA followed by Bonferroni post-hoc test [* $p < 0.05$ mAEA vs CTRL, # $p < 0.05$ S1P+mAEA vs mAEA]. (Standoli et al., 2022)

Furthermore, the role of eCB-binding receptors in the 5 µM mAEA-induced increase in ΔYm was investigated. TRPV1 inhibition by I-RTX suppressed the activity of 5 µM mAEA on ΔYm, although SR1 and SR2 were ineffective (fig.10).

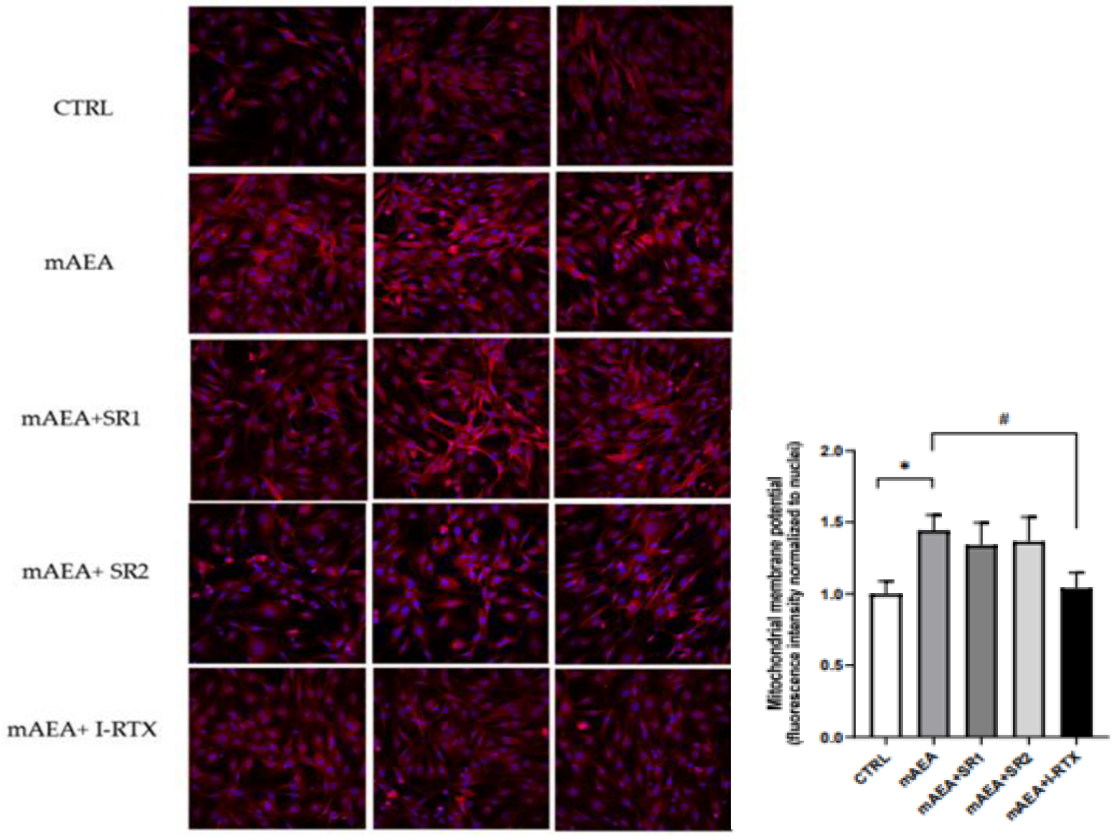

Figure 10. Role of eCB receptors on mitochondrial activity induced by 5 µM mAEA in C2C12 myoblast. Confluent serum-starved C2C12 myoblasts were treated with 5 µM mAEA for 24 h in the presence of eCB receptor antagonists (SR1, SR2 or I-RTX). The fluorescence intensity of Mito-Tracker Red CMX-Ros (Ex/Em: 579/599) was normalized to cell number, and data are reported as mean ± SEM of six field per condition in each of the three independent experiments. Statistical analysis was performed by ONE-WAY ANOVA [* $p < 0.05$] and TWO-WAY ANOVA [# $p < 0.05$] followed by Bonferroni post-hoc test. (Standoli et al., 2022)

The expression of PGC1α and respiratory chain complexes was assessed by Western blot analysis after 24 h of treatment to investigate the molecular mechanism involved in the effects of 5 µM mAEA on mitochondrial activity. As demonstrated in figure 11, the protein level of PGC1α was dramatically increased, whereas the protein content of the respiratory chain complexes was unaffected by the 5 µM mAEA challenge.

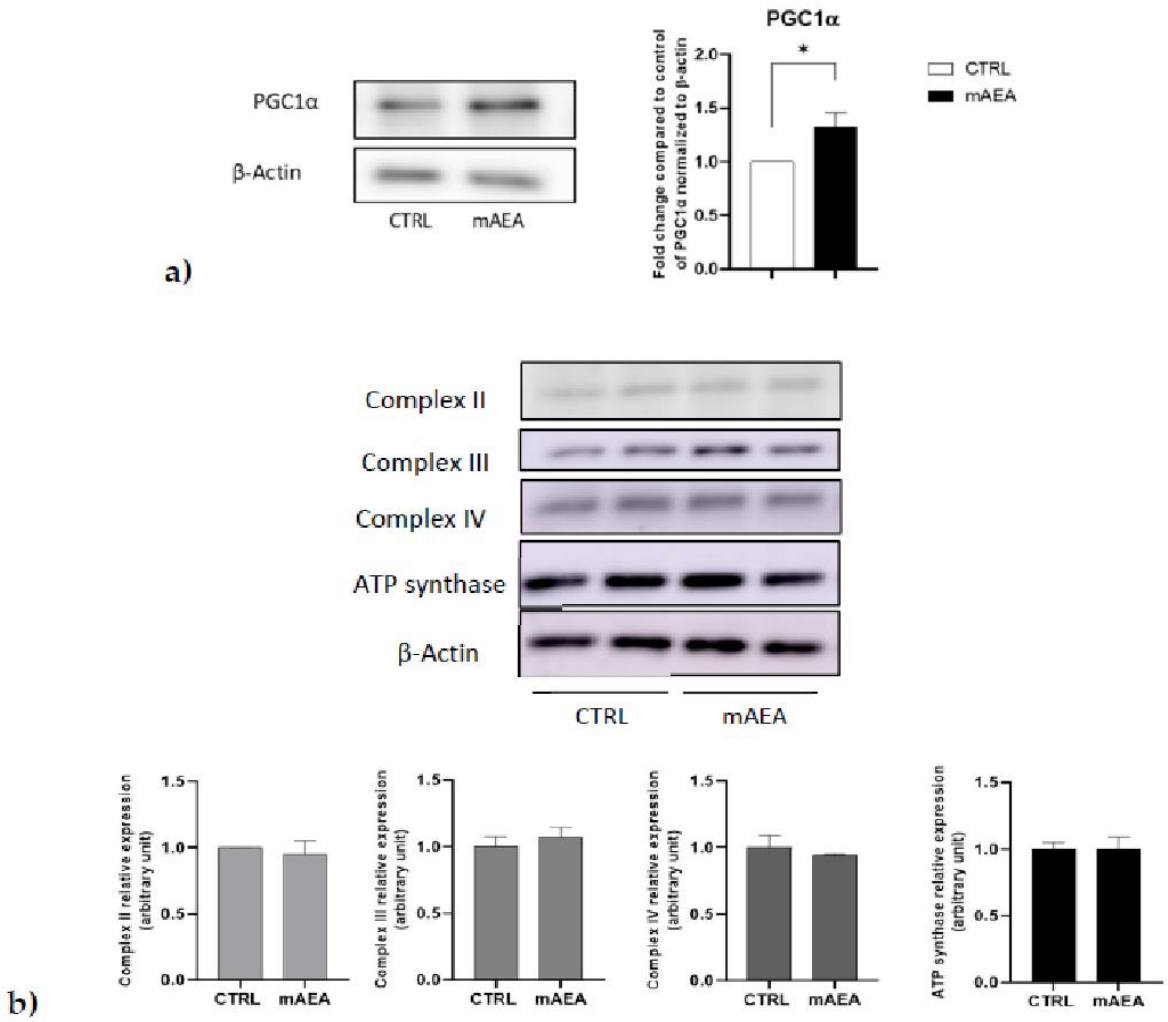

Figure 11. Effect of mAEA on PGC1α (a) and respiratory chain complexes' (b) expression. C2C12 myoblasts were treated with mAEA (5 µM) for 24 h. Samples were subjected to SDS-PAGE and Western blot analysis using anti-PGC1α, as well as OXPHOS WB Antibody Cocktail specific for respiratory chain complexes and anti-β-actin antibody as housekeeping. The data were reported after densitometric analysis of the bands as means ± SEM normalized to β-actin of three independent experiments performed in duplicate. The data were reported after densitometric analysis of the bands as means ± SEM normalized to β-actin of three independent experiments. Statistical analysis was performed by analysis of variance using Student t-test [* $p < 0.05$ vs. control cells (CTRL)]. (Standoli et al., 2022)

Moreover, high-resolution respirometry was used to test the ability of 5 µM mAEA to influence oxygen consumption. C2C12 myoblasts were treated with 5 µM mAEA for 24 hours before being collected and measured by the Oroboros-O2K system for basal oxygen consumption (ROUTINE), proton leak (LEAK), and maximal oxygen consumption (E). mAEA had no effect on any of these respiratory measures in C2C12 myoblasts at 5 µM (fig. 12).

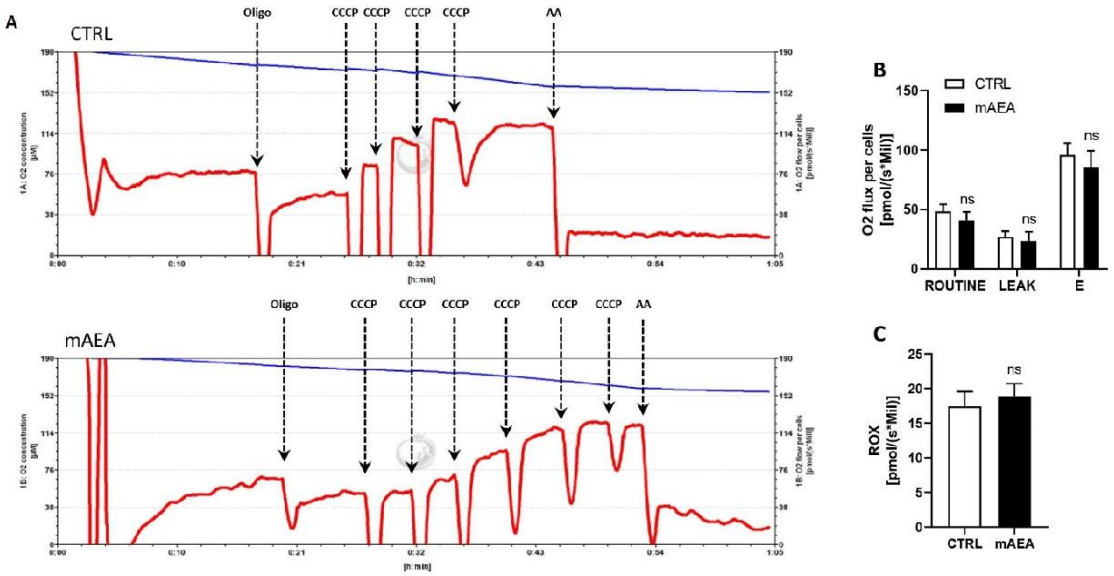

Figure 12. High-resolution respirometry of C2C12 myoblasts following mAEA treatment. C2C12 cells were treated or not with mAEA (5 µM) for 24 h. After detachment, myoblasts were subjected to high-resolution respirometry analysis by the Oroboros-O2K instrument. (A) Representative graphs of cell-respirometry analysis in the control (top) and treatment (bottom) conditions. The blue curve represents the oxygen concentration, whereas the red slope shows the oxygen consumption before and after the serial injections of oligomycin (Oligo), uncoupler CCCP and Antimycin (AA). (B) Bar chart graph of basal oxygen consumption (ROUTINE), proton leak (LEAK) and maximal oxygen consumption (E) values subtracted from residual oxygen consumption (ROX) in CTRL and mAEA treated cells. (C) ROX was also measured after AA administration. Data were reported as means ± SEM of the oxygen flux normalized on cell number of three independent experiments; ns= not significant. (Standoli et al., 2022)

To analyse the possible involvement of TRPV1 in S1P induced myogenic differentiation, C2C12 myoblasts treated with 1 µM S1P for 18h were subjected to real time PCR and expression levels of TRPV1 and Myogenin mRNA were quantified. This specific time interval has been chosen in order to evaluate Myogenin mRNA content, since Myogenin is an early myogenic marker, which protein increases during the first 24h of differentiation. Upon S1P stimulus both TRPV1 and Myogenin mRNA levels increased compared to untreated cells.

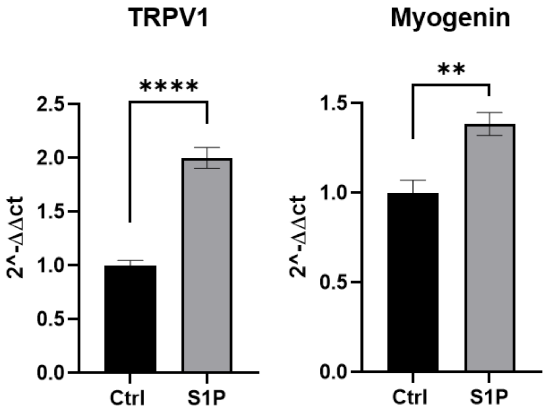

Figure 13. Effect of S1P on mRNA expression of TRPV1 and Myogenin. C2C12 cells were left untreated (in black) or were treated for 18 h with 1 µM S1P (in grey). The values are expressed as $2^{(-\Delta\Delta Ct)}$ and normalized to β-Actin. Data are presented as means ± SD. Statistical analysis was performed by Student's t-test [** $p < 0.01$ and **** $p < 0.0001$].

Since TRPV1 was found to be involved in mAEA-induced mitochondrial membrane potential, we proceeded with investigating the mRNA expression levels of TRPV1 during the differentiation process, quantified by real time PCR. 80% confluent C2C12 myoblast were shifted in serum-free media and collected at different time points, from 0 h to 4 days of differentiation. During myogenic differentiation TRPV1 mRNA levels increased up to~130 folds in 4 days differentiated myotubes compared control myoblasts (fig. 13). The increased expression of TRPV1 during the myogenic differentiation suggests a possible role of the channel in this process.

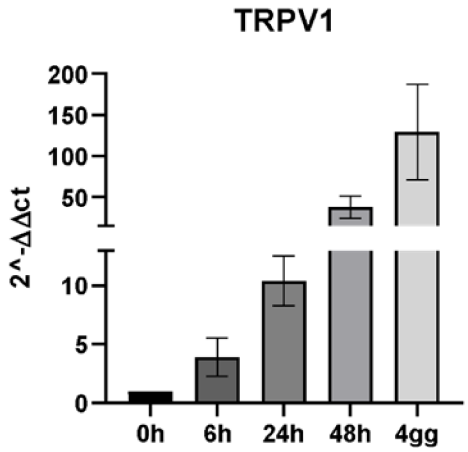

Figure 14. Expression levels of TRPV1 mRNA during myogenic differentiation. C2C12 at 80% confluence were shifted in serum-free media to induce myogenic differentiation, and collected after 0, 6, 24, 48 h and 4 days. The values are expressed as $2^{(-\Delta\Delta Ct)}$ and normalized to β-Actin. Data are presented as means ± SEM. Statistical analysis was performed by Brown-Forsythe ANOVA test [$p < 0.0001$].

In order to verify the effect of the endocannabinoid AEA on myogenic differentiation, C2C12 cells were seeded on microscopy slides and treated with different doses of mAEA, stable analogue of AEA, (0.1-1-5-10 µM) for 4 days. After being fixed and permeabilized, slides were incubated with a specific anti-MHC antibody (MHC is a late myogenic marker) and cell nuclei were stained with DAPI. The fusion index is a method for determining muscle cell myotubes formation and it was evaluated as the ratio between nuclei inside MHC-positive cells and total nuclei. As reported in figure 15 confocal images and the fusion index analysis showed a dose-dependent inhibitory effect of mAEA on myogenic differentiation, with 10 µM being the most effective dose. Indeed 10 µM mAEA was able to reduce the fusion index up to 50% compared to untreated cells.

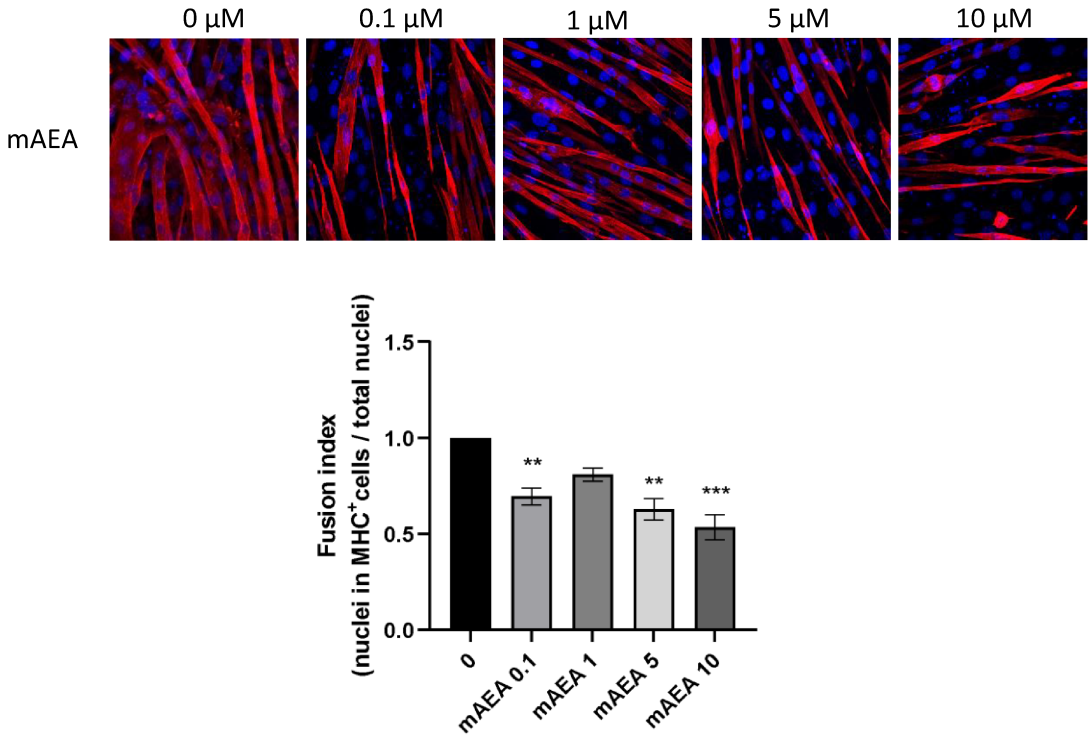

Figure 15. Dose-dependent effect of mAEA on myogenic differentiation. Confluent serum-starved C2C12 myoblasts were treated with 0, 0.1, 1.0, 5.0, 10 µM mAEA for 4 days. Slides, after being fixed and permeabilized, were incubated with a specific anti-MHC antibody (in red) and nuclei were stained using DAPI (in blue). The fusion index was evaluated as the ratio between nuclei inside MHC-positive cells and total nuclei. Data are reported as means ± SEM of at least six fields per condition in each of the three independent experiments. Statistical analysis was performed by ONE-WAY ANOVA followed by Bonferroni post-hoc test [** $p < 0.01$, *** $p < 0.001$].

Furthermore, the role of eCB-binding receptors in the negative effect of 10 µM mAEA on myogenic differentiation was investigated. Cells were treated with 0.1 µM eCBs receptor antagonists (SR1, SR2, I-RTX) 30 minutes before adding mAEA for 4 days. As it is shown in figure 16, mAEA treatment significantly decreased the fusion index, the effect being completely phenocopied by TRPV1 blockade after I-RTX treatment, while SR1 completely reverted and SR2 did not change the anti-myogenic action of mAEA.

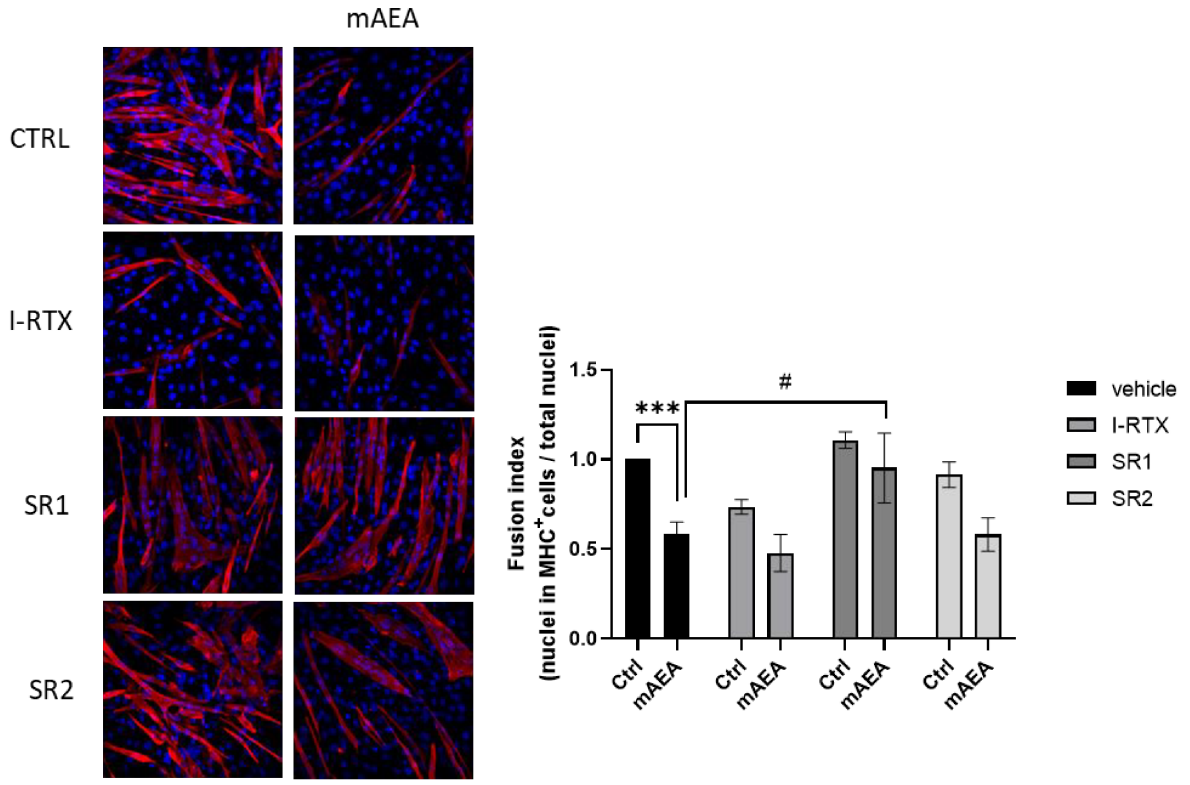

Figure 16. Role of eCB receptors on myogenic differentiation. Confluent serum-starved C2C12 myoblasts were treated with 10 µM mAEA for 4 days in the presence of 0.1 µM eCB receptor antagonists (SR1, SR2 or I-RTX). Slides, after being fixed and permeabilized, were incubated with a specific anti-MHC antibody (in red) and nuclei were stained using DAPI (in blue). Data are reported as means ± SEM of at least six fields per condition in each of the three independent experiments. Statistical analysis was performed by Student's t-test and TWO-WAY ANOVA followed by Bonferroni post-hoc test [# $p < 0.05$, *** $p < 0.001$].

Capsaicin, an active component of chili peppers, is a specific agonist of TRPV1. When capsaicin binds to and activates TRPV1 positive ions, such as sodium and calcium, flow through the channel into the cell and depolarize nociceptive neuros, leading to the sensation of burning and spiciness. Capsaicin has been shown to be a known promoter of myogenic differentiation (Kurosaka et al., 2016). To verify if myogenic differentiation induced by both molecules is a TRPV1-dependent process, serum-free C2C12 cells were treated with 0.1 µM I-RTX 30 minutes before being challenged with 1 µM S1P or CAP for 4 days. As expected, the fusion index value was significantly enhanced upon S1P and CAP treatments compared to control cells. The pro-differentiating effect of both agents was potently inhibited by the incubation of I-RTX, suggesting a role of TRPV1 in the promyogenic action induced by S1P and CAP (figure 17).

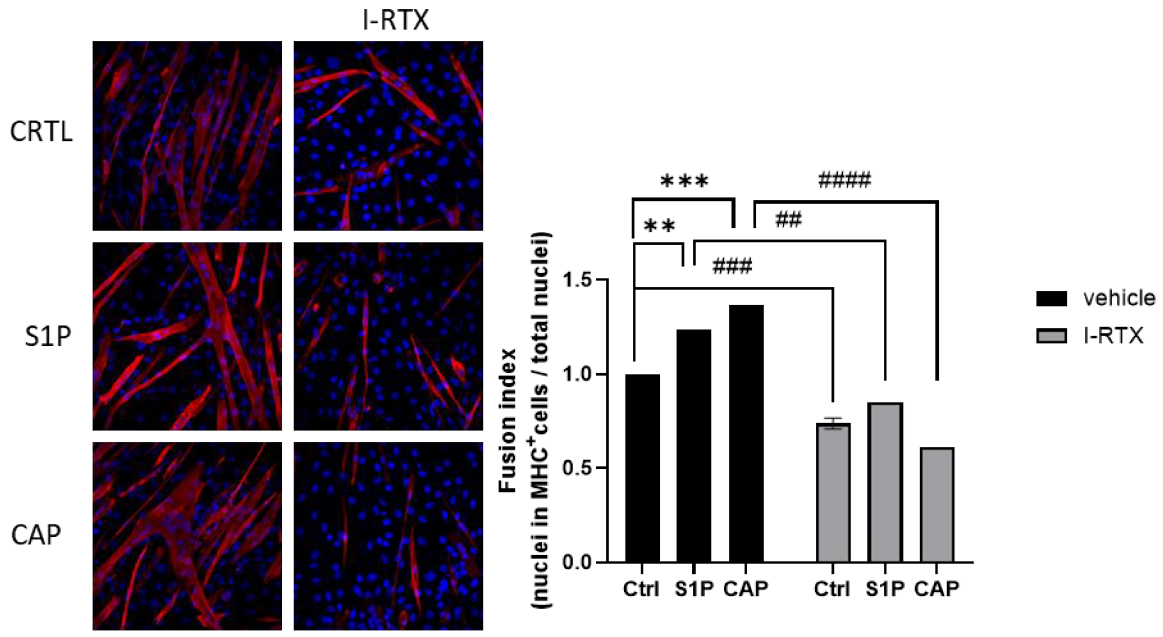

Figure 17. Role of TRPV1 in the differentiation effect induced by S1P and CAP. Confluent serum-starved C2C12 myoblasts were treated with 1 µM S1P or 1 µM CAP for 4 days in the presence of 0.1 µM I-RTX. Slides, after being fixed and permeabilized, were incubated with a specific anti-MHC antibody (in red) and nuclei were stained using DAPI (in blue). Data are reported as mean ± SEM of at least six fields per condition in each of the two independent experiments. Statistical analysis was performed by TWO-WAY ANOVA followed by Bonferroni post-hoc test [** $p < 0.01$, *** $p < 0.001$, **** $p < 0.0001$, ## $p < 0.01$, ### $p < 0.001$].

To specifically silence TRPV1 receptor expression, avoiding possible non-specific effects of I-RTX, RNA interference technique was used. TRPV1 downregulation was assessed with real time PCR, and the level of TRPV1 mRNA expression in silenced cells was approximatively 50% lower than the control (fig. 18A). Cells treated with siTRPV1 for 24h, were then challenged with 10 µM mAEA, 1 µM S1P or 1 µM CAP for 4 days. Data analysis showed a marked reduction of the fusion index upon mAEA treatment, on the contrary CAP enhanced this value. Moreover, the down-regulation of TRPV1 inhibited myoblast differentiation and reduced the pro-myogenic effect of S1P and CAP (fig. 18 B). Altogether these findings suggest the crucial role of TRPV1 in the myogenic differentiation process, and its essential role in the promotion of myoblasts differentiation induced by S1P and CAP.

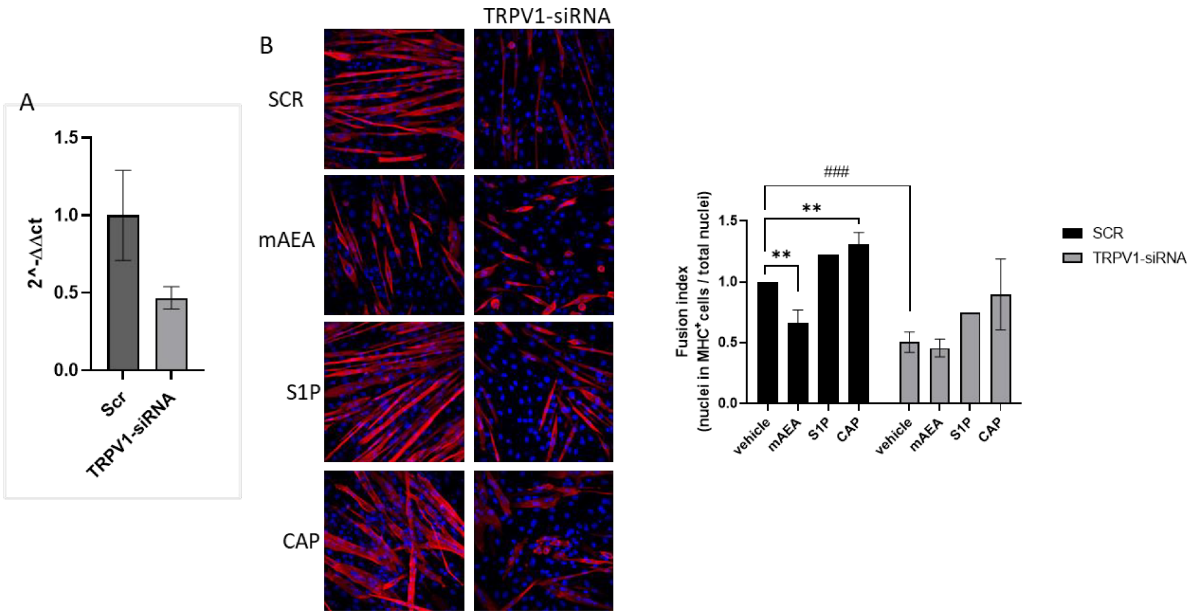

Figure 18. Down-regulation of TRPV1 using RNA interference inhibits myogenic differentiation.
A: C2C12 myoblasts were transfected with siRNA specific against TRPV1 (TRPV1-siRNA) or siRNA scramble used as control (SCR) following the procedure described in materials and methods section. After 24h transfection cells were collected and the downregulation of TRPV1 was assessed by real time PCR technique. The values are expressed as $2^{(-\Delta\Delta Ct)}$ and normalized to β-Actin. Data are reported as mean ± SD.
B: siRNA transfected C2C12 were treated with 10 µM mAEA, 1 µM S1P or 1 µM CAP for 4 days. Slides, after being fixed and permeabilized, were incubated with a specific anti-MHC antibody (in red) and nuclei were stained using DAPI (in blue). Data are reported as mean ± SEM of at least six fields per condition in each of the three independent experiments. Statistical analysis was performed by Student's t-test [** $p < 0.01$, ### $p < 0.001$].

To further confirm the results obtained in the immunofluorescence experiments conducted within 4 days of differentiation we performed Western Blott experiments investigating the protein levels of two myogenic markers, Myogenin and Caveolin 3, whose expression is upregulated within 24 and 48 h of differentiation, respectively. First, we evaluated both proteins content by Western Blot in C2C12 cells upon mAEA challenge. 80% confluent C2C12 myoblasts were serum-starved and treated with different doses of mAEA for 24 and 48 h. Cells were collected and lysates were processed as described in material and methods (chapter 2 of this section). Specifical antibodies against Myogenin and Caveolin 3 were used to detect the protein band. Data analysis showed a reduction of both protein content upon mAEA exposure and a statistically significant variation at the highest dose (10 µM mAEA, fig.19).

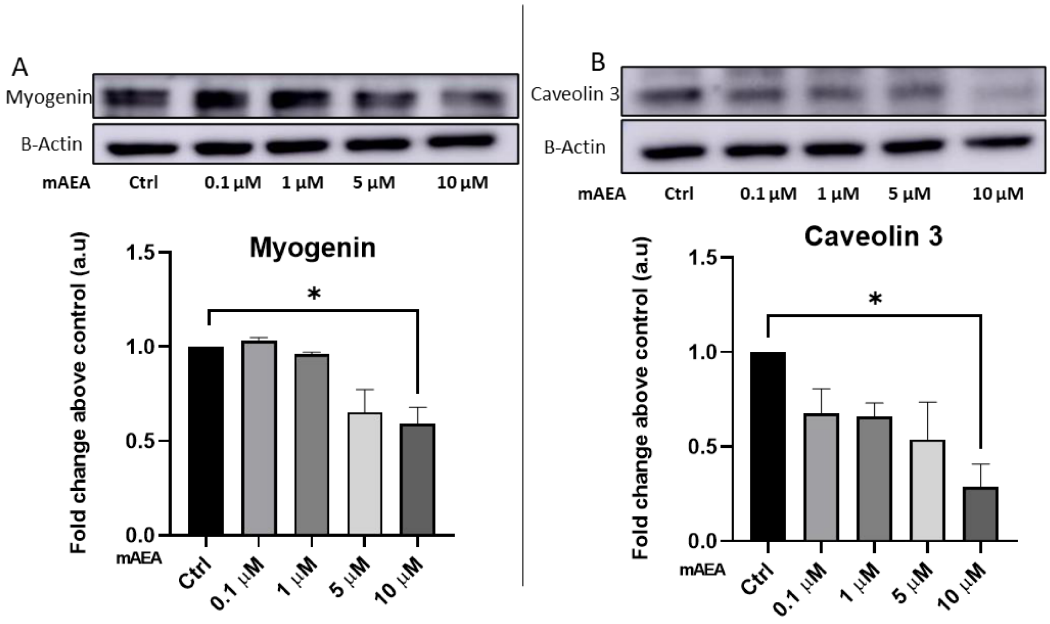

Figure 19. Myogenic markers reduction upon 24 and 48 h mAEA challenge. Confluent serum-starved C2C12 myoblasts were treated with 0, 0.1, 1.0, 5.0, 10 µM mAEA for 24 (A) and 48 (B) hours. Samples were subjected to Western blotting analysis using specific anti-Myogenin (A) and anti-Caveolin 3 antibodies (B). Densitometric analysis values are expressed as relative optical density and normalized to β-Actin. The values represent the means ± SEM of at least two independent experiments. Statistical analysis was performed by ONE-WAY ANOVA followed by Bonferroni post-hoc test [* $p < 0.05$].

To confirm the role of the endocannabinoid's receptors on the anti-myogenic action of mAEA we treated C2C12 serum-starved cells with eCBs receptor antagonists in the presence of 10 µM mAEA for 24 h. Twenty four hours of mAEA challenge inhibited Myogenin protein expression and the administration of TRPV1 receptor antagonist I-RTX further reduced the inhibitory effect of mAEA on myogenesis. SR1 effect was in line with the results of the immunofluorescence assay at 4 days of differentiation (fig. 16), even if in this case it wasn't statistically significant.

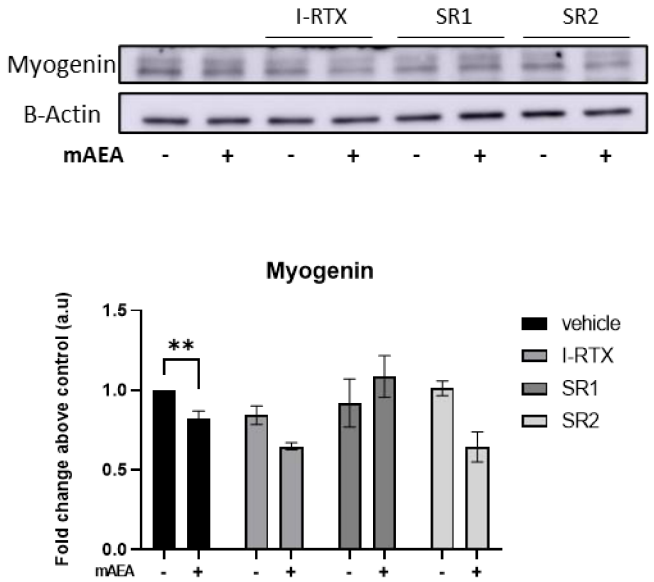

Figure 20. Role of eCB receptors on myogenic differentiation. Confluent serum-starved C2C12 myoblasts were treated with 10 µM mAEA for 24 h in the presence of 0.1 µM eCB receptor antagonists (SR1, SR2 or I-RTX). Samples were subjected to Western blotting analysis using a specific anti-Myogenin antibody. Densitometric analysis values are expressed as relative optical density and normalized to β-Actin. The values represent the means ± SEM of at least two independent experiments. Statistical analysis was performed by TWO-WAY ANOVA test followed by Bonferroni post hoc test. [** $p < 0.01$]. "+" with mAEA, "-" without mAEA.

To confirm the role of TRPV1 in myogenic differentiation C2C12 cells were transfected with siRNA specific against murine TRPV1 and treated with S1P, CAP or mAEA. The densitometric analysis performed after the Western Blot revealed a significant reduction in Myogenin protein content upon TRPV1 down-regulation, highlighting the role of the receptor cationic channel in the myogenic differentiation as previously reported in the immunofluorescence analyses.

Results were in line with previous data showing a negative myogenic effect of mAEA, as well as a promotion of Myogenin expression upon S1P and CAP challenge, whereas TRPV1 down-regulation was responsible for decreasing the CAP-induced promyogenic effect (fig. 21).

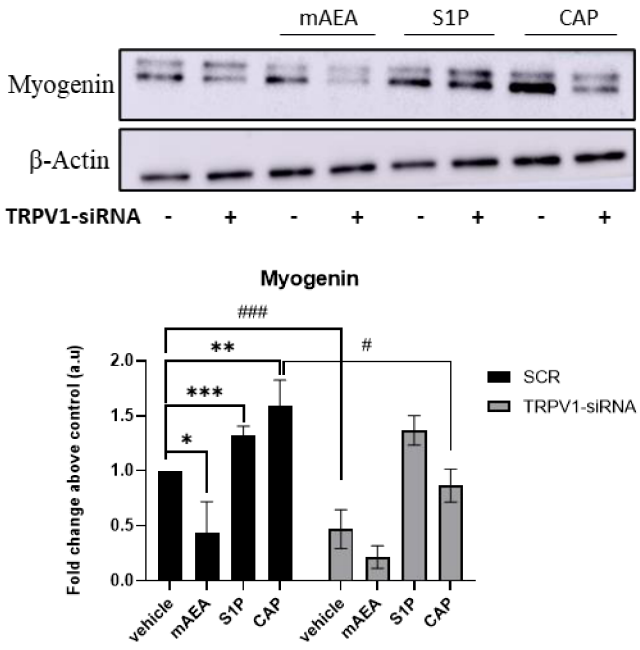

Figure 21. Role of TRPV1 receptor on myogenic differentiation. C2C12 myoblasts were transfected following the materials and methods procedure with siRNA specific against TRPV1 (siTRPV1) or siRNA scramble used as control. After 24h transfection cells were serum-starved and treated with 10 µM mAEA, 1 µM S1P or 1 µM CAP for 24 h. Samples were subjected to Western blotting analysis using a specific anti-Myogenin antibody. Densitometric analysis values are expressed as relative optical density and normalized to β-Actin. The values represent the mean ± SEM of at least one experiment. Statistical analysis was performed by TWO-WAY ANOVA test followed by Bonferroni post hoc test. [* $p < 0.05$, ** $p < 0.01$, *** $p < 0.001$, # $p < 0.05$, ### $p < 0.001$].

S1P is one of the bioactive molecules responsible for the release of Ca^{2+} in the cytoplasm, and therefore the regulation of a variety of cellular processes (Young & Nahorski, 2002). Since our study showed the upregulation of TRPV1 expression levels upon S1P treatment in C2C12 myoblasts and TRPV1 is a cation channel permeable to Ca^{2+}, we wondered if S1P signalling could be involved in the activation of this channel in C2C12 myoblast cell line. To monitor intracellular Ca^{2+} concentration upon S1P or Capsaicin stimulation, we used the Fura2 fluorescence dual-wavelength method. C2C12 cells were pre-treated with 1 µM S1P (fig 22 C and D), or left untreated (control cells, fig. 22 A and B), and after 24 h incubated with Fura2-AM as described in material and methods (chapter 2.11 of this section). Cells were then treated with different concentrations of Capsaicin (ranging from 0 to 300 µM) to induce the activation of TRPV1, before being stimulated with S1P (fig. 22 B and D). Capsaicin demonstrated a dose-dependent effect in increasing spikes of Ca^{2+}, whose concentrations were comparable between S1P pre-treated or not for 24 h. S1P challenge alone induced a

Ca^{2+} increase becoming smaller after the pre-treatment with increasing concentration of Capsaicin, suggesting a desensitisation effect induced by Capsaicin. No difference in Ca^{2+} concentration was found between S1P pre-treated cells for 24 h and control cells.

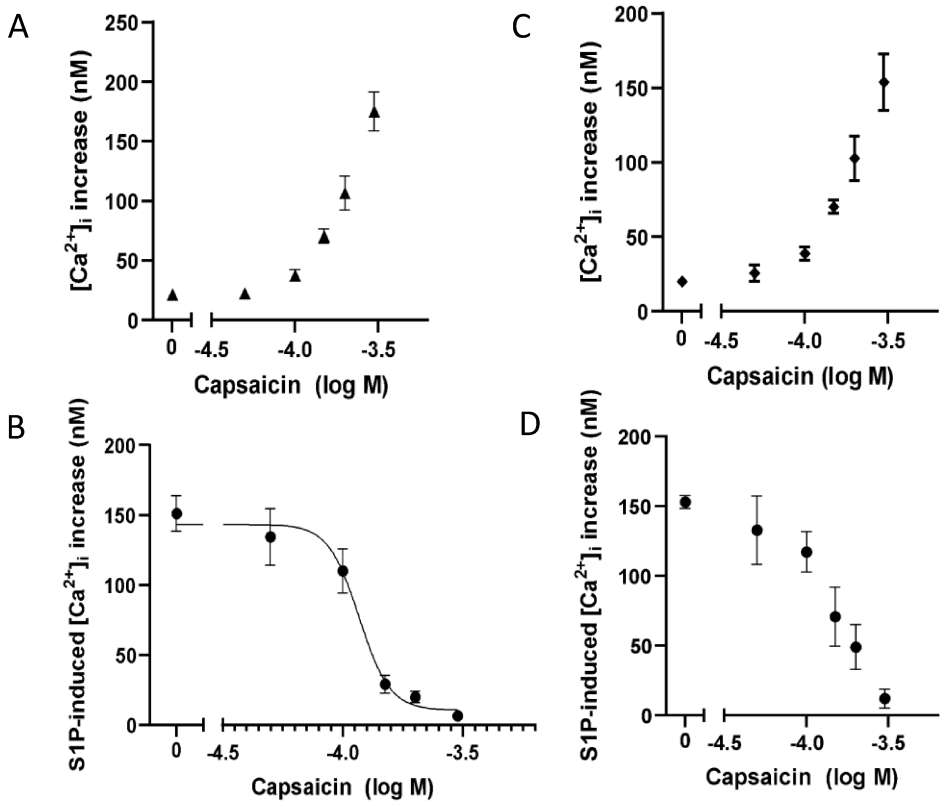

Figure 22. Calcium influx concentration measurements by the Fura2 fluorescence dual-wavelength method. 80% confluent C2C12 cells were pre-treated with 1 µM S1P (C and D) for 24 h or left untreated (A and B). The day after, cells were subjected to Ca^{2+} concentration measurements: in A and C cells were treated with 0, 50, 100, 150, 200, 300 µM Capsaicin; in B and D 1 µM S1P was added after Capsaicin treatment. X-axis represents Capsaicin concentration in logarithmic scale, Y-axis represents the intracellular calcium concentration induced by the presence of Capsaicin (A and C) or S1P (B and D). Data are reported as mean ± SEM of at least duplicate for each condition in four independent experiments.

Since S1P induced Ca^{2+} increase was altered in the presence of the TRPV1 agonist Capsaicin, we repeated the same measurements in the presence of I-RTX, TRPV1 antagonist, in order to verify the S1P-induced Ca^{2+} increase was due to the activation of TRPV1. C2C12 were treated with DMSO (as control) or 1 µM I-RTX for 10 minutes before being stimulated with 1 µM S1P. Although S1P-induced Ca^{2+} increase was reduced by the antagonism of TRPV1, no statistically significant difference was found compared to the control (fig. 23).

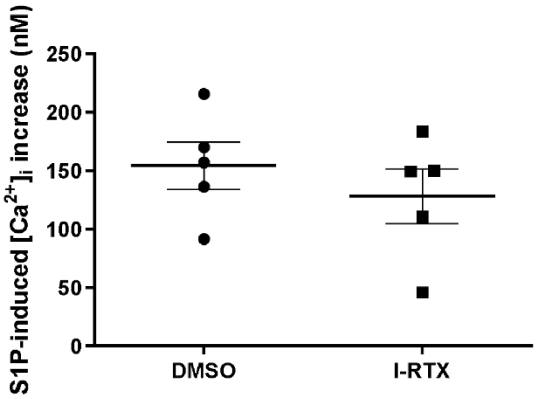

Figure 23. Role of TRPV1 in S1P-induced Ca^{2+} increase. C2C12 cells were pre-treated with DMSO or 1 µM I-RTX, as reported in (Luo et al., 2012), before being stimulated with 1 µM S1P. Ca^{2+} influx concentration measured by Fura2 fluorescence dual-wavelength method. Data are reported as mean ± SEM of at least four cuvettes per condition of five independent experiments.

Thapsigargin (TG) is a non-competitive inhibitor of the SERCA, which raises intracellular Ca^{2+} concentration by blocking the ability of the cell to pump the cation inside the ER. The increase of Ca^{2+} induced by TG in C2C12, was abolished in myoblasts pre-treated with high concentrations of Capsaicin (200-300 µM) as reported in figure 24, suggesting a depletion of the Ca^{2+} store, i.e. the ER.

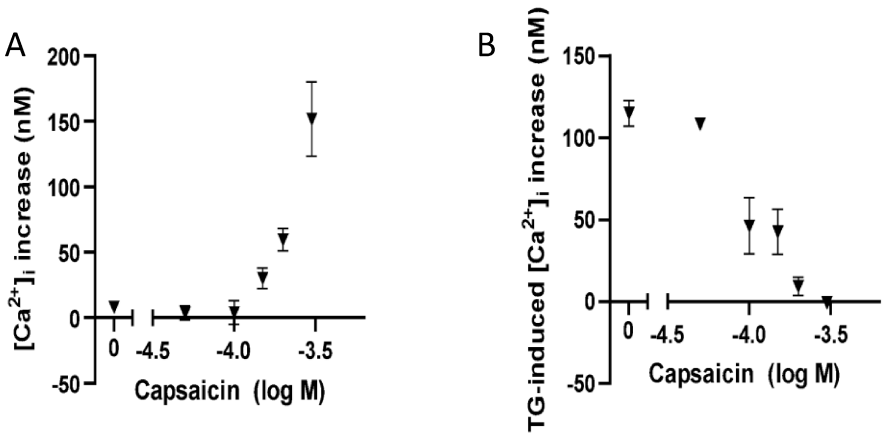

Figure 24. Depletion of Ca^{2+} store mediated by high doses of Capsaicin. C2C12 cells were pre-treated with different concentrations of Capsaicin (0, 50, 100, 150, 200, 300 µM) (A), before being stimulated with 1 µM TG (B). Data are reported as mean ± SEM of at least duplicate for each condition in four independent experiments.

To verify if the Capsaicin-induced Ca^{2+} spike was due to a release of Ca^{2+} from the intracellular stores or its influx from outside the cells, C2C12 were subjected to Fura2 fluorescence dual-wavelength method in two different conditions. Before the experiments cells were resuspended in HBSS containing (fig. 24 B) or not containing (fig. 24 A) Ca^{2+}. The addition of 300 µM Capsaicin resulted in a greater spike of Ca^{2+} in C2C12 resuspended in HBSS containing Ca^{2+} compared to C2C12 in Ca-free content. This result suggests that Capsaicin induces an influx of Ca^{2+} from outside the cells rather than from the ER in myoblasts. Since in C2C12 the TRPV1 channel was demonstrated to be expressed in the ER and not in the plasma membrane, a possible explanation to this phenomenon could be researched in the Ca^{2+}-induced Ca^{2+} increase. Capsaicin, acting on TRPV1, could induce a little release of Ca^{2+} from the ER (fig. 25 A), which induced a greater influx of Ca^{2+} from outer space.

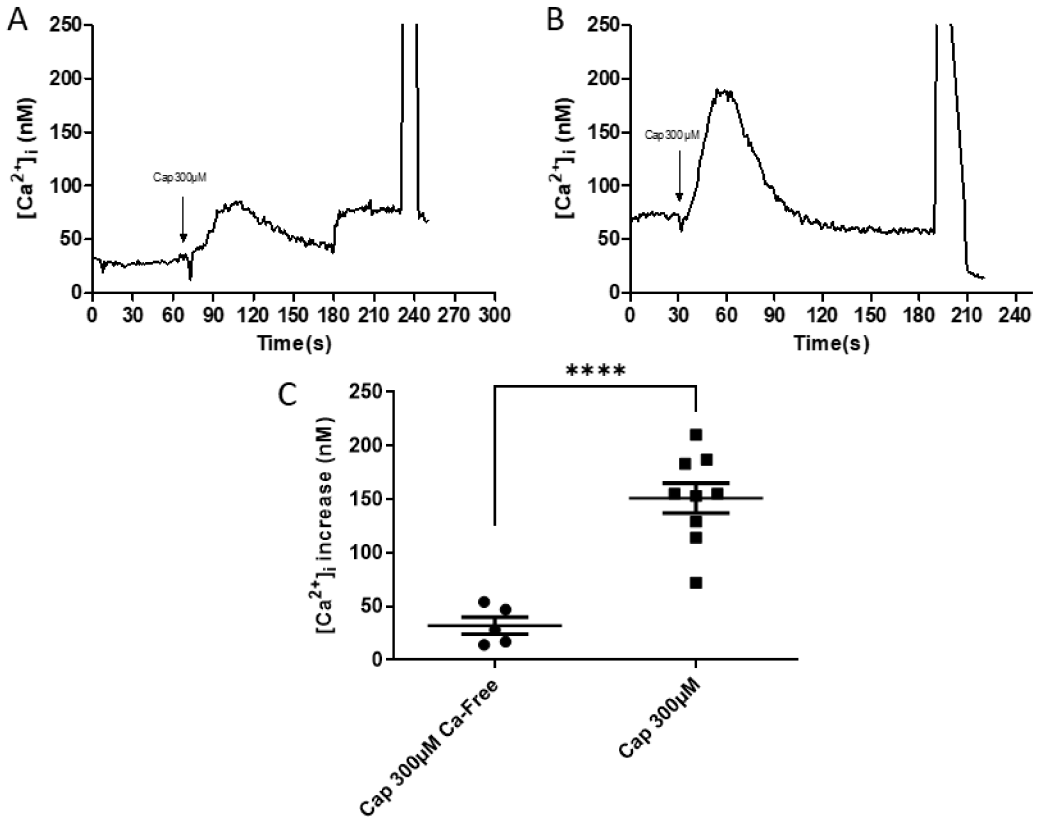

Figure 25. Capsaicin induced Ca^{2+} increase in different environmental contents. Ca^{2+} influx concentrations were measured by the Fura2 fluorescence dual-wavelength method in C2C12 cells suspended in HBSS containing (B) or not containing (A) Ca^{2+}. Addition of 300 µM Capsaicin resulted in a greater spike of Ca^{2+} in B compared to A. In C data are reported as mean ± SEM of at least four cuvettes per condition of one experiment.

With the aim to clarify which S1P receptors were involved in the S1P-induced Ca^{2+} increase, C2C12 myoblasts were pre-treated with different S1P receptors antagonists before the addition of 1 µM S1P. $S1P_2$ antagonism by 10 µM JTE-013 didn't show any effect (fig. 26 A) in myoblasts, therefore we challenge C2C12 myoblasts with VPC23019, dual $S1P_{1-3}$ antagonist. The pre-treatment with 10 µM VPC23019 for 80 seconds was shown to inhibit the S1P-induced Ca^{2+} increase (fig. 26 B). TY-52156 $S1P_3$ antagonist didn't mimic the effect of VPC23019, ruling out the possibility of $S1P_3$ to meditate S1P signalling in the induction of Ca^{2+} influx (fig. 26 C). However, the employment of the $S1P_1$ agonist SAR247799 (1 µM) didn't show the same effect of S1P in the induction of Ca^{2+} increase (data not shown).

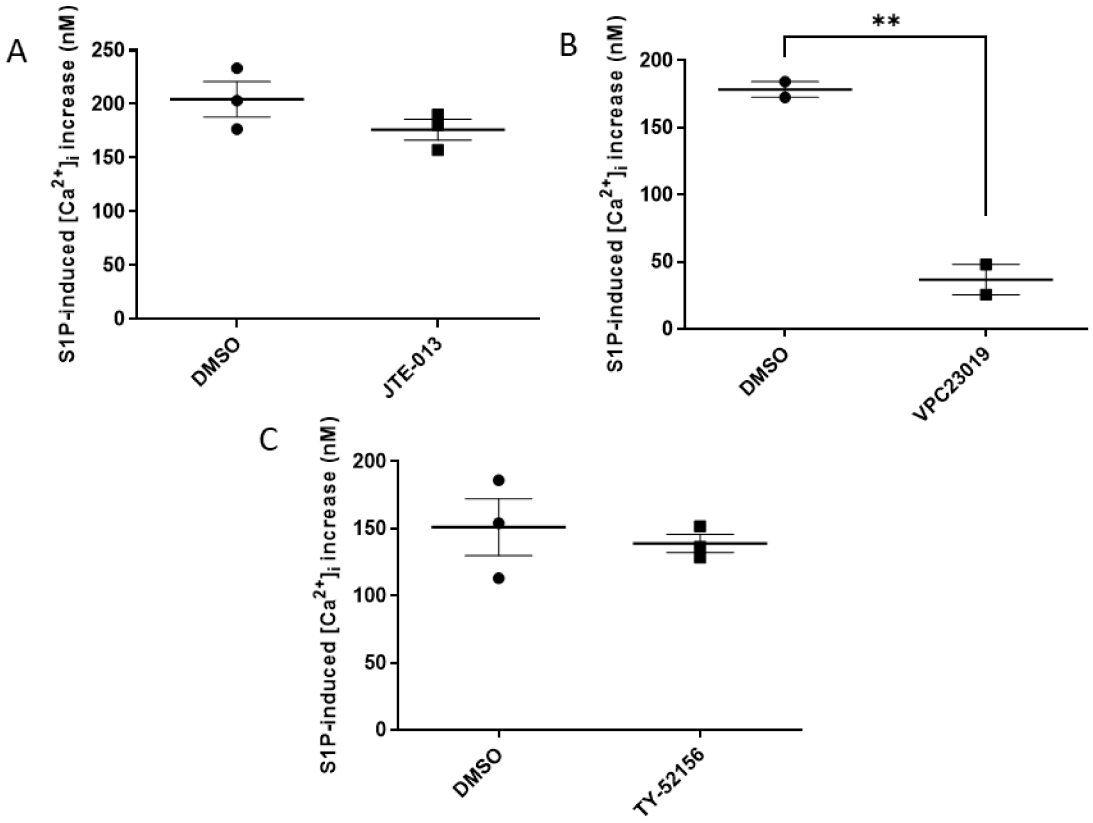

Figure 26. Role of S1P receptor in S1P-induced Ca^{2+} increase. C2C12 myoblasts were challenged with 1 µM S1P after being treated with 10 µM JTE-013 for 30 seconds (A), 10 µM VPC23019 for 80 seconds (B), or TY-52156 for 30 seconds (C). Data are reported as mean ± SEM of at least two independent experiments. Statistical analysis was performed by student t test [** $p < 0.01$].

4 Discussion

eCBs and S1P are bioactive lipids that play vital roles in the regulation of a variety of key biological processes. Intriguingly, these two lipid systems are made up of many enzymes that modulate their cellular tone, as well as unique receptor targets that convey their effects via a complicated network of signal transduction pathways that are only partially known. Both systems are active in skeletal muscle and exert their effect in the various aspects of skeletal muscle biology: from the promotion of cell muscle migration, proliferation and differentiation to the regulation of insulin responsiveness (Donati et al., 2013; Iannotti et al., 2014). In addition, the fact that both signalling systems are dysregulated in a prominent skeletal-muscle illness, Duchenne muscular dystrophy, emphasises the importance of the two families of lipid mediators in the control of skeletal-muscle cell biology. In this context, CB1 was found to be overexpressed in murine dystrophic muscles as well as in dystrophic patient muscle biopsies(Iannotti et al., 2018), whereas dystrophic murine muscles exhibited SPL upregulation and S1P deficiency. Moreover, pharmacological blockade of SPL in dystrophic murine muscles exerted beneficial effects mediated by increased S1P, which binds to and inhibits histone deacetylase (Nguyen-Tran et al., 2014).

For our study we employed the C2C12 myoblast cell line, which is a common and valuable model to investigate essential mechanisms in skeletal muscle biology, at the molecular level. To explore a possible functional interplay between S1P and eCBs systems in skeletal muscle, we started to investigate the role of S1P in the induction of gene expression of eCBs metabolic enzymes and the specific receptors. In collaboration with the university of Teramo, after S1P stimulus, the expression of eCBs receptors and metabolic enzymes was assessed at mRNA and protein level, and AEA and 2-AG content was quantified through Liquid chromatography-mass spectrometry analysis. Notably, S1P at 24 h was found responsible of the selective up-regulation of TRPV1 at both mRNA and protein levels. CB2 protein content, but not the mRNA, was reduced by S1P. Whereas mRNA levels of GPR55 receptor, as well as FAAH and DAGLβ enzymes were transiently increased by S1P at 24 h, and only GPR55 was found to be decreased at 48 h. Discrepancy between gene and protein expression in response to a cue is not novel to cell biology, since it has already been reported in other studies (Bari et al., 2005; Colombo et

al., 2009; Glanemann et al., 2003; Pasquariello, Oddi, et al., 2009). Although S1P altered the expression of some genes involved in the eCBs metabolic and signalling pathway, no changes in AEA and 2-AG endogenous contents were detected.

Emerging studies suggest that the ECS can influence mitochondrial integrity and function. Cannabinoid receptor ligands, for example, have been found to have negative effects on mitochondrial integrity, oxidative phosphorylation, and ATP generation in cells and/or isolated mitochondria (Lipina et al., 2014). In light of this, we wanted to examine if the stable anandamide analogue mAEA might affect mitochondrial membrane potential, a critical functional parameter of these organelles. Interestingly, our results demonstrate that mAEA at the lowest concentration of 5 µM significantly increased ΔYm, whereas the highest dose of 10 µM had the opposite effect. Furthermore, the alterations in ΔYm induced by mAEA were discovered to be mediated by TRPV1, as they were abolished in the presence of its specific antagonist I-RTX. Similarly, treatment of mitochondria isolated from mice liver with higher concentrations (up to 50 µM) of AEA reduced ΔYm to 70% of untreated controls while increasing membrane fluidity. These effects, however, didn't seem to be mediated by CB1, CB2, or TRPV1 (Catanzaro et al., 2009). In rat cortical neurons as well, AEA at 30 µM was able to diminish mitochondrial membrane potential, it promoted cytochrome c translocation, and activated Caspase 3, ultimately leading to cell death independent of its receptor targets (Movsesyan et al., 2004). Instead, AEA dose-dependently, and again in the micromolar range, caused mitochondria-dependent apoptosis in human neuroblastoma SH-SY5Y cells, which was mediated by CB1 (Pasquariello et al., 2009). Our experiments also showed a reduction in the ΔYm of C2C12 myoblasts challenged with 50 µM AEA for 24 h, although the molecular mechanism by which AEA exerted this effect wasn't examined (data not shown). The opposite functional changes induced by low and high doses of mAEA on the ΔYm could rely on the different activation of TRPV1. In the first case subtle increases in intracellular calcium positively affect mitochondrial membrane potential, whereas the mitochondrial calcium overload causes the dysregulation of mitochondrial membrane potential and the subsequent mitochondrial dysfunction. However, overall, it appears that AEA can impact mitochondrial activity through a variety of methods, depending on cell type and species.

S1P and its signalling pathway have a role in the control of mitochondrial homeostasis and regulation of mitochondrial dynamics (Fugio et al., 2020). Therefore, it doesn't surprise the

ability of S1P to counteract the AEA depolarizing effect, discovered in C2C12. Similarly, in cardiomyocytes, S1P stimulation preserved mitochondrial membrane potential under oxidative stress (Xiang et al., 2014). It is known that C2C12 cells express four of the S1P receptors, but in this study, we didn't investigate the S1P mechanism of action in the modulation of the sensibility of myoblasts to eCBs. Future research will be required to determine the precise function played by one or more receptor subtypes in the observed effects.

TRPV1 activation by capsaicin has been shown to increase free cytosolic calcium and improve energy metabolism by upregulating PGC1α in C2C12 myotubes and skeletal muscles (Luo et al., 2012). PGC1α is a transcription coactivator which stimulates mitochondrial biogenesis and promotes the remodelling of muscle tissue to a fiber-type composition that is metabolically more oxidative and less glycolytic in nature (Liang & Ward, 2006). In our research we found that a low dose of mAEA is responsible for the induction of PGC1α expression, without affecting oxygen consumption. Overall, these results reveal a new critical cross-talk between S1P and eCB systems in skeletal-muscle cells, identifying the Ca^{2+} channel TRPV1 as a pivotal target.

On this basis, we proceeded in investigating the effect of mAEA on myogenic differentiation, following the expression of myogenic markers by Realtime PCR, western blot and confocal immunofluorescence analysis and studied the involvement of TRPV1 in myogenesis using pharmacological approaches and RNA interference. We found a time-dependent increase in TRPV1 expression, at mRNA level, during myogenic differentiation, consistent with a study on primary myoblasts, which reported TRPV1 and MHC increase at both mRNA and protein level after 24 and 48 h differentiation (Kurosaka et al., 2016). We also demonstrated a dose-dependent anti-myogenic action of mAEA, through immunofluorescence technique, in C2C12 myoblasts treated with 0-0.1-1.0-5.0-10 μM mAEA for 4 days. Only the dose of 1 μM mAEA didn't give a statistically significant response. A similar effect was observed by Zhao and colleagues: the highest dose of mAEA (10 μM) decreased C2C12 differentiation, while 1 μM mAEA didn't alter this process (Zhao et al., 2010). To clarify which of the eCBs receptors mediated the mAEA negative effect upon myoblast differentiation, C2C12 were exposed to SR1, SR2, or I-RTX before mAEA challenge. For the mAEA stimulation we choose the highest and most effective dose of mAEA (10 μM). After 4 days of differentiation, we calculated the

fusion index, a valuable parameter to evaluate cell differentiation state. Interestingly I-RTX alone decreased the fusion index, suggesting a pro-myogenic action of TRPV1 on myoblast differentiation. Indeed, some studies showed a progression in the differentiation process upon TRPV1 activation: heat induces myogenic transcription factors increasing myotubes formation through TRPV1 (Obi et al., 2019); capsaicin, acting on TRPV1, increases protein and mRNA levels of myogenic markers in primary myoblasts, and the TRPV1 knockdown by siRNA reduces the numbers of nuclei per myotube (Kurosaka et al., 2016); cannabidiol promotes the differentiation of murine C2C12 myoblast into myotubes by increasing intracellular Ca^{2+} concentration mostly via TRPV1 activation (Iannotti et al., 2019). On the other hand, CB1 antagonism reverted the negative effect of mAEA on myogenic differentiation. In this context TRPV1 seems to be a pro-myogenic receptor, while CB1 an anti-myogenic one. When TRPV1 is blocked by its antagonist, mAEA can bind to CB1, exerting its negative effect, which fails in the presence of CB1 antagonist. The anti-myogenic action of CB1 has already been suggested: CB1-2-AG mediated activation inhibited myotube formation via K_v7 channel inhibition (Iannotti et al., 2014); CB1 antagonism blocked the anti-myogenic effect of mAEA (Zhao et al., 2010); moreover, CB1 antagonism enhanced the expression of myogenic markers (Myogenin and MHC) promoting differentiation in human satellite cells (Iannotti et al., 2018). In our study, CB2 antagonism alone didn't affect the differentiation process, since SR2 treatment was not able to revert mAEA effect on the fusion index. This data suggests that CB2 is not involved in the negative effect of mAEA on myoblast differentiation. On the contrary, it could have a role in the progression of the myotube formation since its agonism enhanced myogenic differentiation (M. Zhang et al., 2019).

It is known that capsaicin and S1P are enhancers of cellular differentiation together with the experimental evidence that S1P treatment can increase TRPV1 levels of expression both at RNA and protein levels. Therefore, we examined the role of TRPV1 in the differentiation process induced by S1P and capsaicin. The pro-differentiating effect of both agents on C2C12 myoblasts was reverted by the presence of I-RTX, highlighting the fundamental role of TRPV1 during the myogenic differentiation process.

To confirm pharmacological inhibition of the TRPV1 mediated by I-RTX in the immunofluorescent analyses, we perform RNA interference experiments to knock-down TRPV1 using a specific siRNA. The use of siRNA specifically designed against a targeted protein

is more efficient in the dissection of molecular mechanisms responsible for biological actions, avoiding side effects, rather than the use of pharmacological antagonists, which may have unspecific interactions with other proteins. Once demonstrated the specific down-regulation of TRPV1 induced by siRNA treatment for 24 h by real time PCR, we challenged silenced C2C12 cells with mAEA, S1P and capsaicin for 4 days. As expected, TRPV1 down-regulation had severe effects on myotubes formation, decreasing the fusion index up to 50% with respect to control condition. Moreover, TRPV1 silencing reduced the promyogenic effect of S1P and CAP.
Western blot technique was used to quantify the relative protein expression of Myogenin and Caveolin 3, two myogenic markers whose expression is induced during the first days of differentiation, respectively 24 and 48 h. C2C12 cells were shifted to starvation medium and subjected to the same stimuli employed in the immunofluorescence experiments, collecting the cells after 24 and 48 h treatment. Both Myogenin and Caveolin 3 protein content showed a reduction upon mAEA challenge, with 10 µM being the most effective dose. C2C12 cells were exposed for 24 h to eCBs receptor antagonists in the presence of mAEA, and the change in Myogenin protein expression after 24 h treatment was similar to the variation in the fusion index at 4 days differentiation, confirming the role of eCBs receptors during the differentiation process. Moreover, TRPV1 knockdown induced a huge reduction in Myogenin expression at 24 h differentiation, and reverted the pro-myogenic action of S1P and CAP, once again confirming the importance of TRPV1 channel in the correct progress of the myogenic differentiation.

Among sphingolipids S1P appears to be an evolutionary conserved Ca^{2+} signalling molecule. Extracellular S1P induces intracellular Ca^{2+} increases in many cell types (Meyer Zu Heringdorf, 2004) including C2C12 myoblasts (Meacci et al., 2002). Extracellular S1P mainly couples to the PLC pathway through $S1PR_{2-3}$. In HEK-239 cells, it has been reported that intracellular S1P causes Ca^{2+} mobilization from thapsigargin-sensitive stores, which is most likely independent of ryanodine receptors, as it was found in cells lacking these Ca^{2+} channels (Meyer Zu Heringdorf et al., 2003). Since our finding showed an increased expression of TRPV1 upon 24 h-challenge with S1P in C2C12, we investigated whether the S1P-induced Ca^{2+} increase was amplified by the 24 h S1P treatment. Unfortunately, neither capsaicin nor S1P stimulation provoked an amplified effect on increasing intracellular Ca^{2+} concentration in S1P treated cells compared to untreated cells. Moreover, capsaicin induced a dose dependent desensitization

effect, since incremented concentration of the molecule reduced the S1P Ca^{2+}-induced increase. In murine skeletal muscle adult fibers TRPV1 is located at the ER level (Lotteau et al., 2013). S1P is capable of promoting Ca^{2+} release from intracellular stores in C2C12, and since the TRPV1 agonist capsaicin blocked the S1P effect, we assumed that S1P could indirectly activate TRPV1 channel, modulating Ca^{2+} intracellular concentration. Indeed, an *in vitro* study demonstrated that TRPV1 is involved in S1P-induced Ca^{2+} responses in mice sensory neurons (Kittaka et al., 2020). Therefore, we investigated the role of TRPV1 in the S1P effect antagonising the receptor with I-RTX, which was applied to C2C12 myoblasts 10 minutes before the Ca^{2+} measurements. S1P was then applied to cells and the quantification of the intracellular Ca^{2+} concentration revealed no statistically significant differences with control cells. Moreover, the pretreatment with increasing concentration of capsaicin inhibited the thapsigargin-induced Ca^{2+} release from the ER, leading to the depletion of Ca^{2+} store. The depletion of intracellular Ca^{2+} store induced by high doses of capsaicin is a new discovered effect, which is not to be underestimated since high doses of capsaicin (200-300 μM) have been used in C2C12 cell line (Diao et al., 2021; Ferdowsi et al., 2021). This latter result, together with the inability of TRPV1 antagonism to prevent S1P-induced Ca^{2+} increase, led us hypothesised that the S1P effect blockade on Calcium increase by capsaicin at high doses was due to the depletion of the ER store rather than to the action of both molecules on TRPV1 as first hypothesised. High doses of capsaicin were actually capable of inducing a bigger spike of Ca^{2+} in cells suspended in HBSS containing Ca^{2+} rather than without Ca^{2+}, revealing that the Ca^{2+} mostly derived from the external milieu rather than from internal stores in myoblasts. This result has two possible explanations. In the first TRPV1 has been demonstrated to be expressed in the ER in skeletal muscle fibers and therefore in differentiated cells (Lotteau et al., 2013). In our experiments we used myoblasts (the undifferentiated form of mice skeletal muscle cells). It is then possible that, in our model, TRPV1 could localize also at the cell membrane and translocate to the ER during differentiation into myotubes. The second explanation could be researched in the Ca^{2+}-induced Ca^{2+} increase. Capsaicin, acting on TRPV1, could induce a little release of Ca^{2+} from the ER, which induced a greater influx of Ca^{2+} from outer space. This phenomenon hasn't been demonstrated before, nor in this study, and further researchers are necessary to give an accurate explanation to the ER depletion induced by high doses of capsaicin.

The involvement of S1P receptors in the S1P-induced Ca^{2+} increase was investigated with the pharmacological inhibition of the receptors before the S1P challenge. From our results $S1P_2$ doesn't seem involved, while $S1P_{1-3}$ antagonism with VPC23019 reverted the S1P-induced effect. The $S1P_3$ specific antagonist didn't mimic the effect of VPC23019, apparently ruling out the possibility of $S1P_3$ to mediate the S1P effect. Actually, the effect of VPC23019 reverting S1P-induced Ca2+ could imply a synergistic role of S1P1-3 in mediating the S1P effect. Indeed, the single antagonism of S1P3 receptor doesn't exert a significant effect, while the antagonism of both the receptor isoforms (S1P1-3) reverts the S1P-induced effect. These results are in contrast with another study where the down-regulation of $S1P_3$ and $S1P_2$ by cell transfection with antisense oligodeoxyribonucleotides significantly reduced S1P-mediated Ca^{2+} mobilization in C2C12 (Meacci et al., 2002). Moreover, the $S1P_1$ agonist SAR247799 induced a spike of Ca^{2+} although not as much as the greater Ca^{2+} spike induced by S1P.

The specific receptors involved in the S1P-induced Ca^{2+} increase in C2C12 myoblasts are still unknown and the molecular mechanism has to be solved. Maybe the use of specific siRNA against S1P receptors, eliminating the nonspecific effect of pharmacological inhibitors, could be helpful to clarify this issue.

The crosstalk between S1P and ECBs systems has been studied *in vitro* and need further confirmations *in vivo* experimental models. Nevertheless S1P-S1PR signalling axis has been already demonstrated to be involved in skeletal muscle cell biology also *in vivo* as reported in (Bondì et al., 2024; Germinario, Bondì, et al., 2024; Germinario, Peron, et al., 2024). Future perspectives will be to evaluate this lipid system interplay in the physiopathology of skeletal muscle and could lead to the discovery of new pharmacological approaches against skeletal muscle disorders.

Section 2

1 Introduction

1.1 Photodynamic therapy

Sunlight has been used for centuries by ancient civilizations in combination with different plants to treat a variety of skin diseases. This concept is the basis of the modern and non-invasive therapy called Photodynamic Therapy (PDT), which is used in non-oncological diseases and cancers of varying types and locations (Kwiatkowski et al., 2018). PDT involves the interaction between three ingredients: light, a photosensitive compound (the photosensitizer, PS), and oxygen. The importance of this last element was noted about 100 years ago by Hermann von Tappeiner, who coined the term “photodynamic action” to describe an oxygen-dependent reaction after photosensitization (Rkein & Ozog, 2014). Indeed, PDT is based on the local or systemic application of PS accumulating in the pathological tissue, where, after exposure to light containing its action spectrum, reactive oxygen species (ROS), specifically singlet oxygen radicals, are generated, enabling the selective destruction of abnormal cells. ROS cause cell apoptosis or necrosis by affecting all intracellular components, including DNA and proteins (Babilas et al., 2010). Until its activation by irradiation, the PS needs to be nontoxic to protect the tissue and the patient. That is why PDT is considered a well-tolerated therapy by patients: selective action, painless protocols, and simplicity of application. Moreover, PDT is used in the treatment of chronic inflammation and drug-resistant bacterial infections (Kharkwal et al., 2011; Sperandio et al., 2013).

The PS accumulates in higher concentration in cancer cells rather than in healthy ones. This specific biodistribution is due to the tendency of the PS to combine with low density lipoproteins(LDL), which can supply the area with the necessary cholesterol to create membranes during the amplified cell division. Indeed, it has been demonstrated that highly mitotic tissues present an increased expression of LDL receptors on the cell surface, and that cancer cells show an increased uptake of LDL lipoproteins. (Kwiatkowski et al., 2018). The

affinity of the PS for serum LPS plays a fundamental role in the delivery of the PS to the tumour tissue. Besides the local activity of PDT, a systemic anticancer response is known to be activated by this therapy. PDT indeed affects the vascular system of the tumour and stimulates the immune system. ROS-induced vascular endothelial cell damage leads to tumour vessel occlusion, tumour hypoxia, and, eventually, cell death. Concurrently, PDT's direct destruction of tumour tissue results in the activation of phospholipases and cyclooxygenases, causing a massive release of inflammatory mediators.

The ideal PS is characterized by a set of conditions: chemical purity, stability at room temperature, minimal cytotoxicity in the dark, solubility in the tissue, inexpensive and simple synthesis, and easy availability. To note, the PS should exert a photosensitive effect only in the presence of a specific wavelength: maximal light absorption should occur between 600 and 800 nm. Light absorption at wavelengths above 800 nm does not give enough energy to promote oxygen in its singlet state and the generation of other reactive oxygen species. Concurrently, it should display the minimum absorption in the 400-600 nm range. This eliminates the possibility of increased photosensitivity produced by sunshine.

In the 1900s, the first dyes applied to the treatment of skin pathology were eosin red and erythrosine, which, due to their severe side effects, were abandoned and substituted in the late 1970s by the hematoporphyrin derivative Photofrin® (porfimer sodium). The prolonged photosensitization and the insufficient penetration of Photofrin® by topical application were resolved by the introduction of the porphyrin precursor 5-aminolevulinic acid (ALA) by Kennedy and colleagues in 1990, a small and easily penetrating molecule. ALA hydrochloride (Levulans®) is approved for PDT of actinic keratoses in combination with blue light in the United States (Zeitouni et al., 2003). The methylaminolaevulinate (MAL) is lipophilic and may offer some benefits over ALA: greater penetration, more specificity for target cells, and a reduction in the time of application.

Decreasing the concentration while increasing the specific penetration of the PS in the altered tissue is critical to improve the PDT quality. Therefore, novel PS-caged nanoparticles for drug delivery are currently under investigation.

A variety of light sources are available for PDT: lasers, mercury and xenon lamps and LEDs. Non-laser sources are chosen over lasers for dermatological applications because of their vast illumination field, low cost, and simple construction (Chilakamarthi & Giribabu, 2017), while

lasers produce a high intensity coherent monochromatic light that, coupled to fibre optic devices, can reach inaccessible sites and therefore are more effective for tumours. The use of lasers facilitates the calculation of the dose of light, which, in combination with the exposure time and the light-fluence rate (total energy of exposed light across a sectional area), determines the success of PDT.

The PS within the cells is irradiated with its specific wavelength and, after the photon absorption, is converted from the singlet ground energy state into the excited singlet state and eventually reaches the more stable excited triplet state. The excited triplet state can undergo two pathways: it can directly transfer protons or an electron to the biomolecules of the cancerous tissue; or energy can be transferred to the oxygen molecule, generating excited oxygen species. Generally, this second mechanism of photodynamic reaction is the most important process involved in PDT, but both mechanisms can contribute to its efficiency depending on oxygen concentration, tissue dielectric constant and pH, and PS structure. Highly reactive oxygen species cause photodamage to cell organelles and molecules, leading to different types of death depending on the location of the PS. Mitochondrial damage causes apoptosis, cell membrane alterations can lead to necrosis, while lysosomes or ER damage causes autophagy. Apoptosis is the major type of cell death after PDT, which causes photodamage to Bcl-2 and other related antiapoptotic proteins, inducing mitochondrial disruption and cytochrome c release, resulting in the activation of the caspase cascade (Mroz et al., 2011). Interestingly, high light irradiation and/or high PS concentration tends to induce cell death by necrosis, while low concentrations of PDT induce a more apoptotic response.

In the last decades many studies regarding the use of metal complexes as PS agents arise. Specifically, from the middle of the 70s, Ruthenium (II) polypyridyl complexes captured the attention in PDT scientific application thanks to their interesting photophysical and photochemical characteristics and their stability. These compounds have the same antitumoral potential of cisplatin with less side effects and a higher penetration rate. Moreover, Ruthenium (II) polypyridyl complexes' photoactivation properties, their DNA binding ability and singlet oxygen sensitizing features, make them ideal candidates as photosensitizer agents. Their use in PDT is gaining popularity because of the promising results gained in the treatment of a wide range of malignancies, including lung, bladder, and skin tumours, as well as bacterial infections (Conti et al., 2022). Nonetheless, Ruthenium(II)

photosensitizers have been shown to bind to albumin and transferrin in serum, allowing for extremely effective receptor-mediated transport into cancer cells (Imberti et al., 2020; Kaspler et al., 2016).

PDT has a very simple procedure of administration and activation: first, patients receive the photosensitizer intravenously, by mouth, or spread on the skin. After 24–72 hours, the drug will be uptaken by cancer cells, then the tumour will be exposed to light spatially limited to the solid tumor lesion. PDT works as well as surgery or radiation therapy and presents some advantages: no long-term side effects, less invasive than surgery, often done as an outpatient procedure, precisely targeting the area of the tumour, being repeated many times at the same site if needed, no scarring after the site heals, and costs less than other cancer treatments. Indeed, PDT can only treat areas where light can reach, meaning it can't be used to treat large cancers or cancers that have grown deeply into the skin or other organs, nor it can be used to treat cancers that have spread into many places. However, the Food and Drug Administration (FDA) has approved PDT to treat several diseases such as: actinic keratosis, cutaneous T-cell lymphoma, Barrett esophagus, basal cell and squamous skin cancer, esophageal (throat) cancer, and non-small cell lung cancer.

PDT has been studied intensively as an innovative strategy of therapy for those tumours, such as ovarian cancer, that show an acquired resistance to classical platinum-based chemotherapy.

1.2 Ruthenium complexes

Ruthenium complexes are part of transition metal complexes, compounds containing a metal centre, one or more metal molecules (ruthenium in this case). Originally designed to mimic platinum drugs for targeting DNA, they show more advantages: potent efficacy, less drug resistance, and low toxicity. Meanwhile, these complexes have been shown to generate ROS and can be used in diagnosis as tracers and probes for subcellular localization.

Ruthenium complexes can be found in three different oxidation states: Ru(IV) the most unstable form, which is limiting its development (Duan et al., 2009); Ru(III) which has good thermodynamic and kinetic stability and can be employed as prodrugs under biological

conditions of hypoxia, acidic pH, and high glutathione levels, demonstrating anticancer activity by reducing to corresponding Ru(II) counterparts *in vivo* (Antonarakis & Emadi, 2010; Minchinton & Tannock, 2006); and Ru(II) having the greatest photophysical and chemical properties among ruthenium complexes, which can directly suppress tumour cells (Zeng et al., 2015). Moreover, the lower oxidation state of Ru(II) complexes provides them a higher thermodynamic and kinetic stability than Ru(III) and a better antitumoral activity in vivo (Lin et al., 2018). Ruthenium(II) compounds can be excited at a specific wavelength (452nm) and emit in the red and infrared (maximum peak at 620nm), the same therapeutic window characterising PDT's PSs. At last, thanks to their octahedral geometry, Ru(II) compounds are easily accessible to different three-dimensional structures. Ligand structure modifications and encapsulation of Ru(II) compounds into nanomaterial systems could be a simple strategy to improve their water solubility as well as their targeting capabilities and antitumoral activity. Ruthenium complexes show multiple mechanisms of antitumoral effect: they can directly interfere with DNA replication and transcription, accumulate in specific organelles, or change the permeability of the cell membrane, inducing the tumoral cell death by apoptosis. Specific Ru(II) complexes, which can emit in the red and infrared spectrums, produce a large amount of singlet oxygen, causing cytotoxicity and cell death.

Interestingly, heterocyclic ligands with antioxidant activity could represent excellent binders for Ruthenium, and their antioxidant properties could be enhanced by their coordination at the metal core (Gecibesler et al., 2020). Notably, some Ru(II) complexes have been studied for their capability to work as scavengers of ROS (Marmion et al., 2004; Sasahara et al., 2020) and therefore as new molecular agents in antioxidant therapies of neurodegenerative pathologies.

In conclusion, Ruthenium(II) complexes can make versatile organometallic compounds capable of exerting an extensive range of biological activities.

1.3 Ovarian Cancer

Ovarian cancer is the 11th most common type of cancer in women, the 5th leading cause of cancer-related death in women, and the most fatal gynaecological cancer (Stewart et al., 2019). Ovarian cancer can develop from the three types of tissue and cells forming the ovary: epithelial cells, stromal cells, and germ cells. From the ovary, the tumour first spreads locally, then invades the opposite ovary, the uterus, and eventually goes intraperitoneally. Distant metastases are rare but can be found in the liver, lungs, pleura, adrenal glands, and spleen (Roett & Evans, 2009). Diagnosis of ovarian cancer can be difficult because it lacks specific symptoms. The incidence of ovarian cancer increases with age (> 50 years), and the major risk factors are related to family history and genetic predisposition. Mutations in BRCA1 and BRCA2 (tumour suppressor genes) and the MMR gene *MLH1* can increase the risk of the tumour from 1.6% to 40%, 18% and 10% respectively (Stewart et al., 2019). Although less common, Lynch syndrome is also associated with ovarian cancer. Ovulation itself has been linked to a higher risk of developing ovarian cancer, which, therefore, decreases in women who use oral contraceptives, have fewer menstrual cycles, have multiple pregnancies, and have an early menopause.

Treatment commonly involves surgery preceded or followed by chemotherapy, depending on the characteristics of the tumoral mass. Ovarian cancer's chemotherapy typically consists of platinum-based drugs combined with non-platins. Cisplatin (*cis*-diamminedichloroplatinum (II)) and its analogues interact with DNA forming mono-adducts that evolve in DNA crosslinks, which, if not repaired, block the replicative machinery directing cells towards apoptosis (Damia & Broggini, 2019). Another mechanism by which Cisplatin activates DNA damage and cell death is the induction of oxidative stress. This drug is indeed able to activate, in ovarian cancer cells, NF-kB, a transcriptional factor of proinflammatory agents such as Tumour Necrosis Factor (TNFα), IL-1, IL-6, and IL-8. Not only Cisplatin leads to the production of mitochondrial ROS, but it also decreases the pool of antioxidants such as glutathione (GSH) (Mikuła et al., 2019). Unfortunately, these events are not confined to the tumour area, opening the possibility of multiple side effects, including nephrotoxicity, neurotoxicity, ototoxicity, and bone marrow suppression. Moreover, sooner or later, the platinum-based therapy stops working because of the patients' acquired resistance to chemotherapy, nearly

85% of the cases. Therefore, new strategies and new therapeutic agents for the treatment of ovarian cancer are needed, and the possibility of a resolution could be found in the study and application of Ruthenium complexes.

PDT has been suggested as a cancer cell sensitizer to platinum-based chemotherapy through mitochondrial targeting (Rickard et al., 2023). In ovarian cancer *in vivo* and *in vitro* models, PDT has been shown to cooperate with platinum-based chemotherapy (Cramer et al., 2020; del Carmen et al., 2005; Goff et al., 1996) and target platinum-resistant ovarian cancer cells (Nath et al., 2020). Besides, preclinical studies propose PDT as a feasible strategy for disseminating ovarian cancer treatment (Duska et al., 1999; Rizvi et al., 2010), however, these promising results are counterbalanced by the non-specific localization of the treatment and the cutaneous phototoxicity. Nanoparticles, as ideal carriers, could be used for enhancing the accumulation of the PS in the tumour, and currently nanoparticle-encapsulated porphyrin photosensitizers are studied as novel PDT drugs in ovarian cancer treatment (Liu et al., 2021). Given the acquired resistance to traditional platinum medications, PDT could become another weapon in the treatment of ovarian cancer, and understanding the necessity for novel and more capable photosensitive compounds, this study addresses Ruthenium complexes as potential new PS.

1.4 Non-Melanoma Skin Cancer

Non-melanoma skin cancer (NMSC) represents about 95% of all skin cancers and is the most common tumour among the Caucasian population, with an incidence rising 3-10% annually (Griffin & Lear, 2016). It arises from epidermal-derived cells and includes many cancerous types, mainly divided into cutaneous squamous cell carcinoma (SCC) and basal cell carcinoma (BCC). The risk of NMSC depends on biological and non-biological factors: sex (higher risk for men), immunosuppressive diseases such as AIDS, dysregulation of gene expression (PTCH1 gene alterations lead to uncontrollable skin cell mitosis and multiple BCC development), high-fat diet, and UVR exposure, which induces ROS production, alter biomolecule structures, and lead to the formation of DNA adducts resulting in DNA break. UVRs are absorbed by epidermal keratinocyte cells and promote the mutation of p53, which has a significant role in the

maintenance of genome stability and drives the activation of carcinogenesis processes. Several treatments against skin cancer exist, however, they are not fully satisfactory, and the overall survival rate of cancer patients remains low. Clinically, chemotherapy is the most frequent approach, but chemotherapy drugs are toxic, and their systemic application is limited by their poor solubility and bioavailability, unsuitable pharmacokinetics, and non-selective distribution, resulting in undesirable side effects (Khan et al., 2022). Topical application is a valid alternative pathway, it is non-invasive, it can prolong the period of drug maintenance within the therapeutic window, avoiding its degradation in the gastrointestinal tract, and the easy application improves the patient's compliance to the therapy. However, topical application of drugs is not obstacles-free. Indeed, the upper layer of the skin (stratum corneum) represents the main barrier resisting the entry of anticancer compounds. In addition, several skin cancers are characterized by a higher presence of keratin, lipids, and the formation of keratotic papules and erythematous plaques in malignant cells, providing an additional noteworthy barrier to the passive transport of the drug to the target site (Khan et al., 2022). Because of their ability to improve the penetration of bioactive chemicals into the tumour cells, micro/nanoparticle-based systems have been intensively investigated for topical therapy of skin malignancies. These new technologies applied in PDT, which is by itself a non-invasive selective therapy and doesn't induce drug resistance, could be the turning point for the treatment of skin cancer diseases. PDT standardised protocols have already demonstrated their high efficacy in non-hyperkeratotic actinic keratoses, Bowen's disease, and BCC with better cosmetic effects over conventional procedures (Morton et al., 2013).

1.5 Ruthenium complexes in neurological diseases

The chemical integrity of the brain is completely dependent on the normal and proper functioning of the central nervous system (CNS). It is generally known that the brain consumes a huge quantity of oxygen and has a high lipid content, making it vulnerable to oxidative stress. A high intake of oxygen results in an excess of ROS generation. Neuronal membranes have been shown to have a high content of polyunsaturated fatty acids, which are extremely reactive to ROS (Singh et al., 2019). Low levels of ROS are required for normal cellular

signalling, and an exogenously or endogenously induced and regulated increase in ROS amount is promptly rebalanced. When the adaptive systems are compromised or the ROS production increases excessively over time, it creates a state of oxidative stress where ROS induce damage to cellular macromolecules such as DNA, lipids, and proteins, ultimately leading to necrosis and apoptotic cell death. The oxidative stress is one of the risk factors for the development and progression of chronic neurological diseases such as Parkinson's disease (PD), Alzheimer's disease (AD), Huntington's disease (HD), and amyotrophic lateral sclerosis (ALS).

Under normal conditions, an average of 1%-2% of the molecular O_2 absorbed by animal cells is transformed into ROS via electron loss from the mitochondrial transport chain. When the mitochondrial respiratory chain is disrupted by chemical components (respiratory inhibitors) or mutations in mitochondrial genes that encode respiratory enzymes, ROS generation and accumulation increase. The most important ROS are superoxide anion (O_2^-), hydroxyl radical ($^{\cdot}OH$), hydrogen peroxide (H_2O_2), singlet oxygen ($^1O_2$). ROS subtract an electron (oxidate) to the nearest molecule, which becomes itself a reactive species spreading the oxidation to other molecules. Antioxidants are stable compounds that can stop this propagational chain by donating an electron to the oxidant molecule, preventing damage from oxidative stress. Antioxidants are classified based on their mechanism of action. For example, there are enzymes that can catalyse the breakdown of O_2^- (Superoxide dismutases, SODs) and H_2O_2 (Catalases), or molecules that donate hydrogen to peroxide radicals.

Therapeutic approaches aimed at reducing oxidative stress could be a valid option to slow down the clinical evolution of associated pathologies such as neurological diseases. In addition to their prospective use as anticancer medicines, ruthenium complexes have demonstrated encouraging results as neuroprotective drugs in the field of neurology (Campelo et al., 2012). In the brain of chronic induced-cerebral hypoperfusion Swiss mice, Ruthenium red (RR) treatment was shown to lower thiobarbituric acid levels, increase glutathione levels, and restore superoxide dismutase levels and activity of its reduced isoform. RR also reduced acetylcholinesterase activity, perhaps saving cholinergic activity (Singh & Sharma, 2016). The antioxidant properties of Ruthenium compounds are added to their ability to be used as diagnostic tools for neurodegenerative diseases, based on their capability of forming aggregates with b-amyloid peptides generated in the early stages of as Parkinson's and

Alzheimer's diseases (Cali et al., 2021). Despite accumulating evidence, additional research is needed to dissect the protective mechanisms of ruthenium-based drugs on neurologic disorders. Therefore, this work presents two new antioxidant Ru(II) complexes and aims to evaluate their protective effect on cell damage induced by pro-oxidant species and the involved molecular mechanisms.

2 Materials and methods

2.1 A2780 cell culture

Human A2780 ovarian cancer cell culture was obtained from the European Collection of Authenticated Cell Cultures (ECACC 93112519, Wiltshire, England). A2780 were maintained in RPMI-1640 medium containing 10% FBS, 100 U/mL penicillin/streptomycin, 2 mM L-glutamine, at 37°C in 5% CO_2 atmosphere. RPMI was purchased from Sigma-Aldrich (St. Louis, MO, USA). A2780 cells were shifted to RPMI without serum supplemented with 1 mg/mL BSA and treated with each Ru(II) complex (0.1, 1 and 10 µM) for 24 h. After incubation, cells were photoactivated with a 30Wthree-arm LED light lamp (430–470 nm emission, 30 W) for 20 min at the distance of 5 cm from the cell culture plate and then kept under dark in the incubator at 37°C, 5% CO_2. Cells were washed twice with PBS and then collected after photoactivation at different times depending on the experiment conditions.

2.2 A-431 cell culture

Human A-431 squamous carcinoma cell line was purchased by ATCC® (CRL-1555™ Manassas, VA, USA). A-431 were grown in DMEM supplemented with 10% FBS, 100 U/mL penicillin/streptomycin, and 2 mM L-glutamine. The cell line was maintained in a 5% CO_2 atmosphere at 37°C. Cells were treated with ruthenium complexes (Ru1, Ru2, Ru2-cubo) solubilized in DMSO and diluted in complete medium (0.025-25 µM). Final concentration of DMSO was kept below 0.6% to avoid unspecific toxicity from the solvent. After incubation, cells were photoactivated with a 30Wthree-arm LED light lamp (430–470 nm emission, 30 W) for 30 min at the distance of 5 cm from the cell culture plate, or incubated in the dark for the same time, and then processed following each experiment condition.

2.3 SH-SY5Y cell culture

Human SH-SY5Y neuroblastoma cell line was maintained in 1:1 DMEM:F12 HAM nutrient mixture (Sigma-Aldrich, St. Louis, MO, USA), supplemented with 10% FBS, 100 U/mL penicillin/streptomycin, and 2 mM L-glutamine, at 37°C in 5% CO2 atmosphere. SH-SY5Y cells are commonly used in neurosciences as an in vitro model to study molecular mechanisms of neurodegenerative diseases such as Alzheimer e Parkinson. They can be used as undifferentiated cells, or they can be easily induced to express a neuron like phenotype. The differentiation process was induced at 70% of confluency, shifting the cells to 1% FBS media and adding 10µM retinoic acid (RA). Cells were maintained in the differentiation media for 7 days, which was changed every two days.

2.4 MTT Assay

The MTT (3-(4,5-dimethylthiazol-2-yl)-2,5-diphenyltetrazolium bromide) assay is a standard colorimetric test for assessing cell viability. Cells were plated in 96-multiwell at least 5 wells per condition. After the treatment cells were washed twice with PBS, 200 µL MTT 1X solution were added to each well and cells were then incubated at 37°C in the dark. Depending on the cell line, the MTT 1X solution was prepared by diluting 1:10 the stock solution in RPMI DMEM or DMEM/F12 without phenol red, which can interfere with the incorporation of the dye. Living cells can uptake the yellow dye, by endocytosis, and the NAD(P)H-dependent cellular oxidoreductase enzyme reduces the tetrazolium dye MTT to its insoluble formazan, which has a purple colour. After the incubation time, MTT was removed, and cells were lysate with DMSO 100% (150 µL /well). This leads to the solubilisation of the formazan crystals and the colour intensity of each well was quantified by a spectrophotometer at 595 nm. The degree of cell viability is dependent on the degree of the formazan production and directly proportional to the intensity of the purple colour.

2.5 Caspase-3 Activity Assay

A2780 or SH-SY5Y cells were seeded in 6-well plates and after 24 h were subjected to different treatments depending on the experimental conditions. After the treatments, cells were washed twice with PBS and collected in a buffer containing Tris-HCl 20 mM pH 7.4, NaCl 250 mM, EDTA 2 mM, Triton X-100 0.1%, DTT 1mM, Na3VO4, PMSF 0.5 mM and protease inhibitor cocktail (Sigma-Aldrich, USA). Samples were left in ice for 30 minutes before being lysed by two sonication cycles of 20 seconds and centrifugated at 16.000xg, 5 minutes 4°C. Protein lysates (30 µg) were resuspended in a buffer containing Hepes-KOH 50 mM pH 7, glycerol 10%, EDTA 2 mM, 3-[(3- cholomidopropyl)-dimethylammonio]-1-propanesulfunate 0.1% plus DDT 10 µM and Ac-DEVD-AFC 50 µM substrate (Cayman Chemical Company, MI, USA). Caspase-3 activity depends on Asp216 cleavage and the tetrapeptide was used to quantify it. The reaction was monitored quantitatively by measuring shift in fluorescence upon cleavage. Ac-DEVD-CHO (200 nM) specific inhibitor of caspase-3 (Cayman Chemical Company, MI, USA) was used as a negative control, incubated with all cell lysates 15 minutes before adding the substrate. After 2 hours incubation at 37°C in the dark, samples were measured at 505 nm wavelength with 400 nm excited wavelength by fluorescence spectrometer (Cary Eclipse Fluorescence Spectrometer, Bio-Rad, CA, USA).

2.6 Laser-Scanning Confocal Microscopy

A2780, A-431 or SH-SY5Y cells were seeded into microscope slides and after 24 h were subjected to different treatments depending on the experimental conditions. Mito-Tracker Red CMXRos (#M7512; Ex/Em: 579/599 nm) and CM-H_2DCFDA (#C6827; Ex/Em:492–495/517–527 nm) probes (Invitrogen, Thermo Fisher Scientific INC,Waltham, MA, USA) were used to detect the mitochondrial membrane potential and ROS production, respectively. After diffusing through the cell membrane, DCFH-DA probe is hydrolysed by esterase in DCFH and oxidised by radical species forming DCF, a fluorescent compound which indicates the presence of cytosolic ROS. The two probes were diluted in RPMI or DMEM medium without phenol red or PBS, incubated for 30 min at 37°C in dark and then fixed in 2% paraformaldehyde, as

suggested by the manufacturer's instruction, and slides were processed as described in 2.9 of section 1.
Ru(II) complexes excitation was performed using a 405 nm laser diode, acquiring emission in the range of 600/620 nm.

2.7 Western blot analysis

A2780 or SH-SY5Y lysates were quantified for total protein content by the Bradford Protein assay, resuspended in Leammli's sodium dodecyl sulphate (SDS) sample buffer, and subjected to SDS-PAGE and transferred to PVDF membranes, as previously described in 2.4, 2.5 and 2.6 of section 1. Anti-caspase 3 and anti-PARP antibodies were purchased from Cell Signaling Technology (Danvers, MA, USA).

2.8 Real-Time PCR

SH-SY5Y cells were plated in 6-well plates (500.000 cells/well), the day after cells were shifted to 1% FBS media and treated with 10 µM of the antioxidant S1 for 18 h. Subsequently, 100 µM H_2O_2 or 3 ng/ml LPS were added for 3 and 24 h. Cells were then processed as described in 2.7 of section 1. TaqMan probes specific for inflammatory cytokines (IL-1β, IL-6, TNFα and COX2) were purchased from Thermo Fisher Scientific INC (MA, USA).

2.9 ICP-AES Measurements

In order to study the internalization of Ru(II) complexes in A2780, A-431 or SH-SY5Y cells the ICP-AES technique was performed. It is an analytical technique used to determine the concentration of a variety of inorganic metallic and non-metallic substances. Cells were seeded into p100 petri dishes and after reaching the desired confluence were treated with different Ru(II) complexes and incubated at 37°C in dark depending on the experimental conditions. Then, cells were washed twice in cold PBS, collected in ice by scraping the surface

of the plate with 1 ml of PBS into 15 ml tubes, and centrifuged at 1000xg for 5 minutes. Pellets were maintained at -80°C until the ICP analysis was performed. Ru content in the samples was determined using an axial Varian 720-ES Inductively Coupled Plasma Atomic Emission Spectrometer (ICP-AES).
Measurements were performed in triplicate.

2.10 Fluorescence-activated cell sorting (FACS)

FACS is a specialised type of flow cytometry, and it is based on the principle that cells can be labelled with a fluorescent dye. As cells pass through the laser beam the flow cytometer can measure the fluorescence intensity of a single cell. In our study we labelled SH-SY5Y cells with the specific probes in order to quantify the cytosolic or mitochondrial ROS production of cells upon H_2O_2 exposure in the presence/absence of S1. SH-SY5Y were pre-treated with S1 for 18 h before being exposed to 100-250 µM H_2O_2 for 2 h. Cells were detached with Trypsin 1X and incubated with 1 µM DCFH-DA for 15 minutes in suspension in dark in order to identify cytosolic ROS or labelled in adhesion with 2,5 µM MitoSOX Red mitochondrial superoxide indicator for 10 minutes in order to quantify mitochondrial ROS production. Fluorescent intensity of labelled cells was quantified with the cytofluorimeter BD FACSCanto II.

2.11 Statistical analysis

In order to obtain a statistical analysis of the experimental results, Student's *t*-test and one-way or two-way analysis of variance (ANOVA), followed by Bonferroni post-hoc analysis, were performed. A level of $p<0.05$ was considered statistically significant.
Densitometry analysis of Western Blot images was carried out with imageJ software and for all the graphical images, GraphPad Prism v8.4.3 (GraphPad Software, La Jolla, CA, USA) was used.

3 Results and discussion

3.1 Ru(II) Complexes in PDT of Epithelial Ovarian Cancer Cells

Ovarian cancer is an aggressive and late diagnosed gynaecologic cancer, and the major cause of tumour-associated death in women. The “golden standard” approach relies on platinum- and taxane-based chemotherapies, which soon become useless due to the development of therapeutic resistance. The employment of Ruthenium(II) polypyridyl complexes (RPCs) in PDT has been extensively studied for becoming an alternative therapeutic strategy to overcome drug resistance.

The collaboration with the Department of Chemistry “Ugo Schiff” give us the possibility to study the *in vitro* effect of some Ru(II) complexes as potential agents in the PDT: $Ru1^{2+}$, $Ru2^{2+}$, $[CuRu1]^{4+}$ and $[Cu_2Ru2]^{6+}$. On the one hand our colleagues at the department of Chemistry synthesised the molecules and investigated their acid-base properties and redox state, on the other hand we evaluated the *in vitro* anticancer efficacy of Ru(II) complexes and the production of ROS on A2780 human ovarian cancer cells as well as the molecular mechanism underlying their effect. This chapter reports data from a published article entitled “Highly Charged Ru(II) Polypyridyl Complexes as Photosensitizer Agents in Photodynamic Therapy of Epithelial Ovarian Cancer Cells”. The candidate of this thesis is a co-author of the above-mentioned article (see appendix).

The human ovarian cancer cell line A2780 was established from ovarian endometroid adenocarcinoma tissue of an untreated patient, and it is widely used as a model to evaluate the anti-cancer potency and drug delivery of various drugs on ovarian cancer. With the purpose to set the proper time of incubation before photoactivation, the kinetics of internalization of RPCs and their intracellular distribution was checked in A2780. The localized distribution of $Ru1^{2+}$ and $Ru2^{2+}$ was barely detectable after 15 minutes incubation, while it increased at 6 h, reaching a plateau at 24 h incubation. $[CuRu1]^{4+}$ and $[Cu_2Ru2]^{6+}$ showed a less intense fluorescence emission and a kinetic profile similar to the ones of $Ru1^{2+}$ and $Ru2^{2+}$. The fluorometric analysis as well, used to evaluate the kinetics of internalization of Ru (II)

compounds, showed a fluorescent signal at 600 nm wavelength that increased from 6 to 18 h and reached a plateau at 24 h incubation (fig. 1). If administered at the same concentration, $Ru1^{2+}$ and $Ru2^{2+}$ have a comparable emission. Since $Ru2^{2+}$ had a higher fluorescence intensity compared to $Ru1^{2+}$, it seems to be more efficiently internalised by cells. The uptake of Ru(II) complexes was also evaluated by measuring the content of ruthenium in cell lysates with ICP analysis after 24 h incubation with 10 µM of each compound. Indeed Cu(II)-free and Cu(II)-containing complexes have different emissive properties. $Ru2^{2+}$ showed the highest internalization capacity, followed by $Ru1^{2+}$, while $[CuRu1]^{4+}$ and $[Cu_2Ru2]^{6+}$ levels were comparable. Moreover, in C2C12 myoblasts RPCs were undetectable after 24 h incubation, demonstrating that ovarian cancer cells, but not the non-cancerous cell line, efficiently internalized the complexes (data not shown, see Conti et al., 2022, figure S10, Supplementary Materials).

Based on these results, we chose to set the time of incubation with Ru(II) complexes before photoactivation at 24 h.

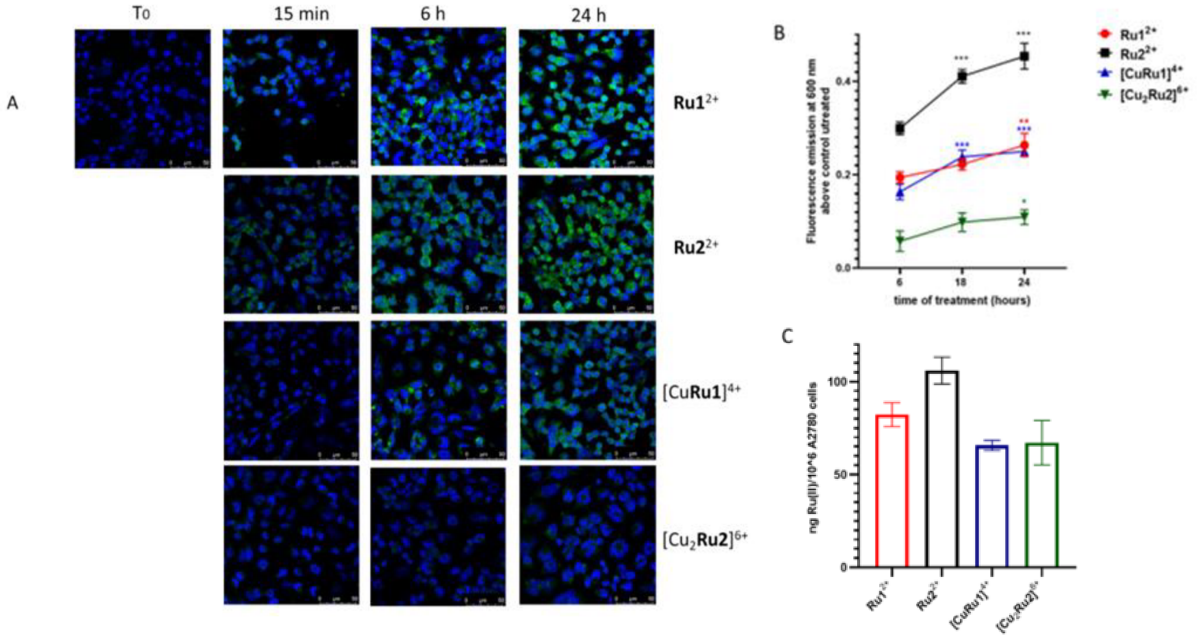

Figure 1. Internalization of Ru(II) complexes in A2780 cells. (A) Laser-scanning confocal microscopy was performed in A2780 cells incubated with each Ru(II) complex (10 µM) for the indicated time. DAPI (λexc = 405 nm, λem = 461 nm) was used to stain nuclei (blue spots), while the fluorescence emission in green represents that of Ru(II) complexes (λexc = 405 nm, λem = 600–640 nm). (B) Fluorometric analysis was performed in A2780 incubated with Ru(II) complexes (10 µM each) for 6–18–24 h. Data are reported as mean ± SD of fluorescence emission at 600 nm after subtraction of the background (untreated A2780 cells). The internalization of Ru(II) complexes was statistically significant according

to ONE-WAY ANOVA followed by Bonferroni post hoc test [* $p < 0.05$, ** $p < 0.01$, *** $p < 0.001$]. (C) Amount of internalized ruthenium after 24 h of incubation of 10^6 A2780 cells with each Ru(II) compound (10 µM). Data represent the mean ± SD of three independent experiments. The ruthenium content in the control sample, namely cells not treated with Ru(II) complexes, was not detectable.

The dose-dependent effect of $Ru1^{2+}$, $Ru2^{2+}$, $[CuRu1]^{4+}$ and $[Cu_2Ru2]^{6+}$ on dark cytotoxicity and photoactivity was evaluated through MTT assays in A2780 cells incubated for 24 h with different concentrations of RPCs and exposed or not to photoirradiation 24 h before being analysed. In the photoirradiation experiments, cells were irradiated with a light-emitting laser diode (LED, λmax = 434 nm, 30 W) for 20 minutes at a distance of 5 cm from the bottom of the plates. As reported in figure 2, under dark conditions all the compounds showed low cytotoxicity, above all Cu-containing compounds, that could be associated with their lower capacity to be internalized. Cell viability decreased up to 35% only in 10 µM $Ru1^{2+}$ and $Ru2^{2+}$ treated cells. On the contrary, after photoactivation $Ru1^{2+}$ and $Ru2^{2+}$ strongly decreased cell viability starting from 100 nM, while Cu-containing compounds were less effective and showed significant effects at higher concentrations (from 1 µM). Interestingly, the effect of $[Cu_2Ru2]^{6+}$ was considerably less pronounced compared to the one of $[CuRu1]^{4+}$. This would imply that differences in the chemical structures and chemical-physical properties may play a role in the biological response of this class of compounds, in addition to the similar cellular internalisation and modes of activation of the latter two Ru(II) complexes. Since PDT photosensitizers could exert cytotoxic effects on normal cells close to the tumour tissue we performed MTT assays in non-cancer cells, C2C12 myoblasts, under the same photoactivation conditions. Ru(II) complexes show negligible cytotoxicity and a minor photoactivity in myoblasts compared to A2780 cells, in agreement with the negligible internalization capacity of the PSs in this non-cancer cell model (data not shown, see Conti et al., 2022, Figure S13 Supplementary Materials).

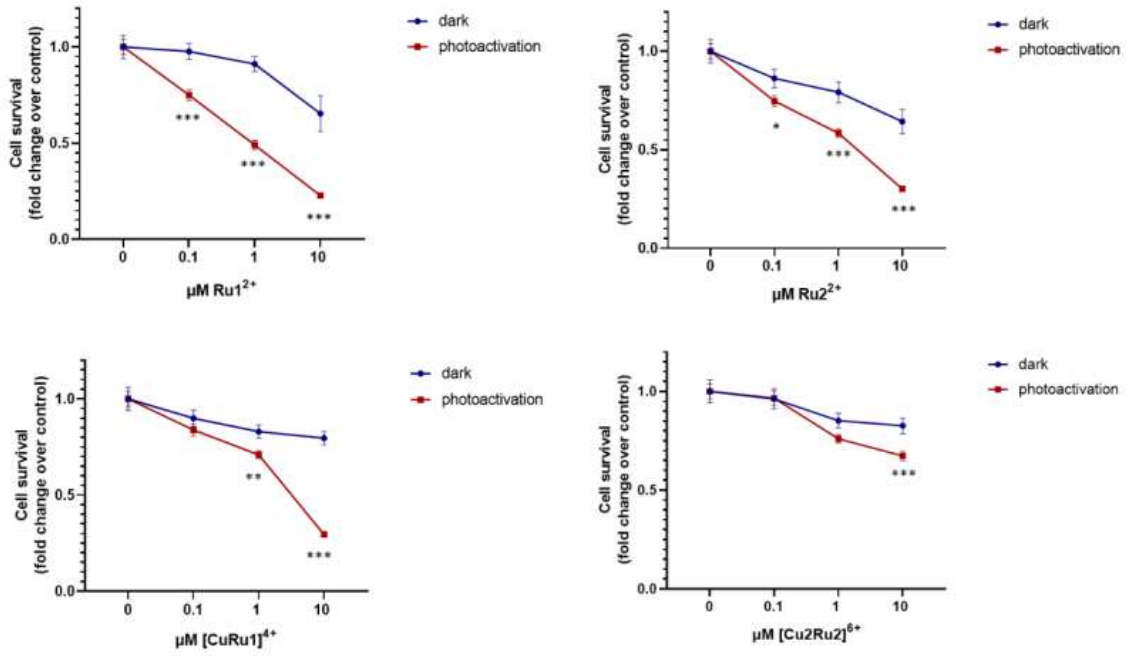

Figure 2. Dose-dependent effect of Ru(II) complexes on cell survival of ovarian cancer cells after photosensitization. A2780 were incubated for 24 h in the presence of Ru(II) complexes, $Ru1^{2+}$, $Ru2^{2+}$, $[CuRu1]^{4+}$ and $[Cu_2Ru2]^{6+}$ at the following concentrations (0, 0.1 μM, 1 μM, 10 μM) in serum-deprived culture media (RPMI with BSA 0.1%). Cells were photoactivated for 20 min, as described in the Materials and Methods section. MTT reduction tests were performed in triplicate, representative of three independent experiments with similar results. Data reported are mean ± SD, fold change of absorbance at 570 nm over untreated control. The effect of photoactivation of Ru(II) complexes on the inhibition of cell survival was statistically significant according to TWO-WAY ANOVA followed by Bonferroni post hoc test [* $p < 0.05$, ** $p < 0.01$, *** $p < 0.001$].

The involvement of apoptosis as a possible mechanism responsible for the selective anti-survival effect of RPCs was evaluated by different approaches. As shown in figure 3, the treatment with each compound under dark condition didn't stimulate caspase 3 activity, while the photoactivation significantly promoted the protease activity of the pro-apoptotic enzyme. Moreover, the proteolytic cleavage of caspase 3, that accompanies its activation, was evaluated by Western blot technique. Notably, the cleavage, and therefore the activation, of caspase 3 occurred only after the irradiation of cells treated with the Ru(II) complexes, suggesting the involvement of caspase 3 in the anti-survival effect induced by photoactivation of Ru(II) complexes in A2780 cells.

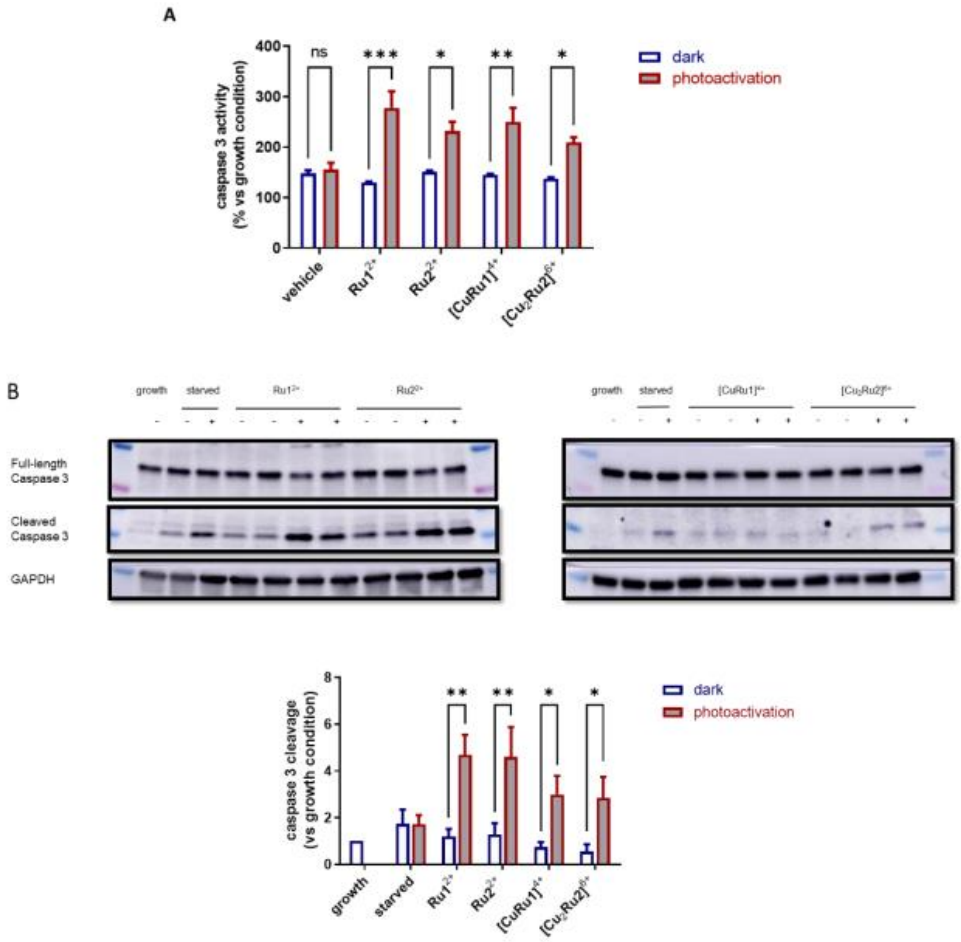

Figure 3. Effect of Ru(II) complexes on caspase 3 activation in ovarian cancer cells after photosensitization. A2780 cells were treated with 10 µM of each Ru(II) complex for 24 h. Cells were photoactivated (red) or not (blue), collected after 24 h of light irradiation, homogenized, and total protein concentration was analysed in each lysate. (A) Caspase 3 activity assay was performed in 30 µg of total cell lysates by using a specific fluorogenic substrate Ac-DEVD-ACF (ex/em: 400/505 nm). Data are reported as mean ± SD of fluorescence compared to control cells under growth condition (10% FBS RPMI), set as 100. The effect of photoactivation was statistically significant for each Ru(II) complex tested according to TWO-WAY ANOVA analysis followed by Bonferroni post hoc test [* $p < 0.05$, ** $p < 0.01$, *** $p < 0.001$]. (B) Western blot analysis was performed in 30 µg total cell lysates using specific anti-caspase 3 antibodies. Densitometric analysis of cleaved caspase 3 was performed in three independent experiments performed in duplicate. Data are the mean ± SD and are reported as cleaved caspase 3 levels normalized to GAPDH, fold change over FBS control (growth), set as 1. Results are statistically significant according to TWO-WAY ANOVA followed by Bonferroni post hoc test [* $p < 0.05$, ** $p < 0.01$, not significant (ns)].

The programmed cell death and its involvement in the photoactivity of Ru(II) complexes was confirmed by measuring the cleavage of poly ADP-ribose polymerase (PARP), one of the major hallmarks of apoptosis. Under normal circumstances PARP is able to detect single strand DNA breaks and activates DNA damage repair responses. The specific inactivation of PARP by

proteolytic cleavage induced by caspase cascade pathway emerged only after the photoactivation of each Ru(II) complexes, with a higher extent for $Ru1^{2+}$.

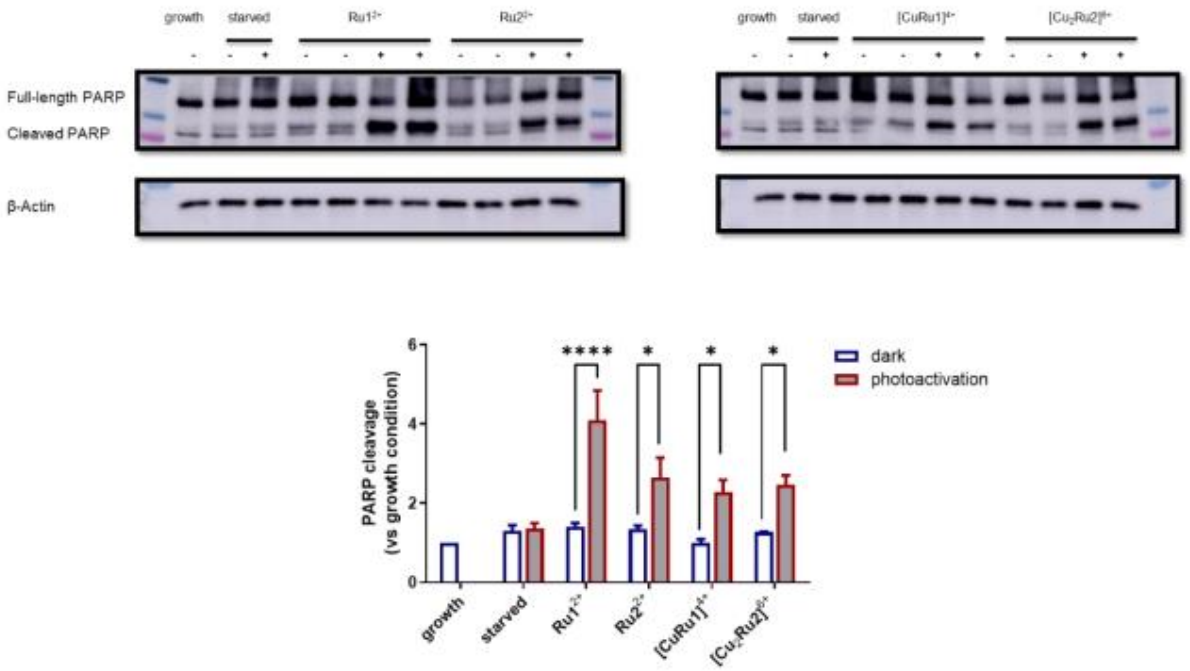

Figure 4. Effect of Ru(II) complexes on PARP cleavage in ovarian cancer cells after photosensitization. A2780 cells were treated for 24 h with each Ru(II) complex before being photoactivated and collected after 24 h of light irradiation. Western blot analysis was performed in 30 µg total cell lysates using specific anti-PARP (46D11) antibody. Densitometric analysis of cleaved form of PARP was performed in three independent experiments conducted in duplicate. Data are the mean ± SEM and are reported as cleaved protein levels normalized to β-actin, fold change over FBS control. Results are statistically significant according to TWO-WAY ANOVA followed by Bonferroni post hoc test [* $p < 0.05$, **** $p < 0.0001$].

In mammalian cells, mitochondria are essential for the intrinsic pathway of apoptosis, and in some cellular systems, loss of mitochondrial membrane potential (ΔYm) is seen as an early sign of the apoptotic process. Therefore, ΔYm was analysed after Ru(II) complexes administration in A2780 cells using a cationic fluorescent probe, which accumulates in the negatively charged mitochondrial matrix, by laser-scanning confocal microscopy imaging. Under dark conditions the ΔYm was not affected by the presence of the photosensitizers, as reported in figure 5. After photoirradiation $Ru1^{2+}$ and $Ru2^{2+}$ caused a dramatic loss of ΔYm in almost all the cells that acquired a morphological feature of pyknotic nuclei, representing an initial phase of chromatin condensation prior to DNA fragmentation. $[CuRu1]^{4+}$ and $[Cu2Ru2]^{6+}$ didn't affect the ΔYm nor the cell morphology. Given the cationic nature of Ru(II) complexes,

to assess the possible localization of RPCs into mitochondria after photoirradiation, we performed a colocalization test employing a mitochondria-specific probe. The random distribution of Ru(II) complexes compared to mitochondria (data not shown, see Conti et al., 2022, figure S9 Supplementary Materials) showed by the confocal microscopy images ruled out the possibility that mitochondrial depolarization induced by photoactivation depended on Ru(II) complexes' localization in these organelles. Finally, in order to clarify if the Ru(II) complexes were internalized through endosomes vesicles reaching the ER, we performed animmunofluorescence analysis using the anti-Rab5 antibody, marker of early endosomes. Results didn't show a colocalization of Rab5 withthe Ru(II) complexes, rulling out the possible involvement of a Rab5 dependent-pathway in the internalization pathway of Ru(II) complexes. (data not shown, see Conti et al., 2022, figure S11 Supplementary Materials) .

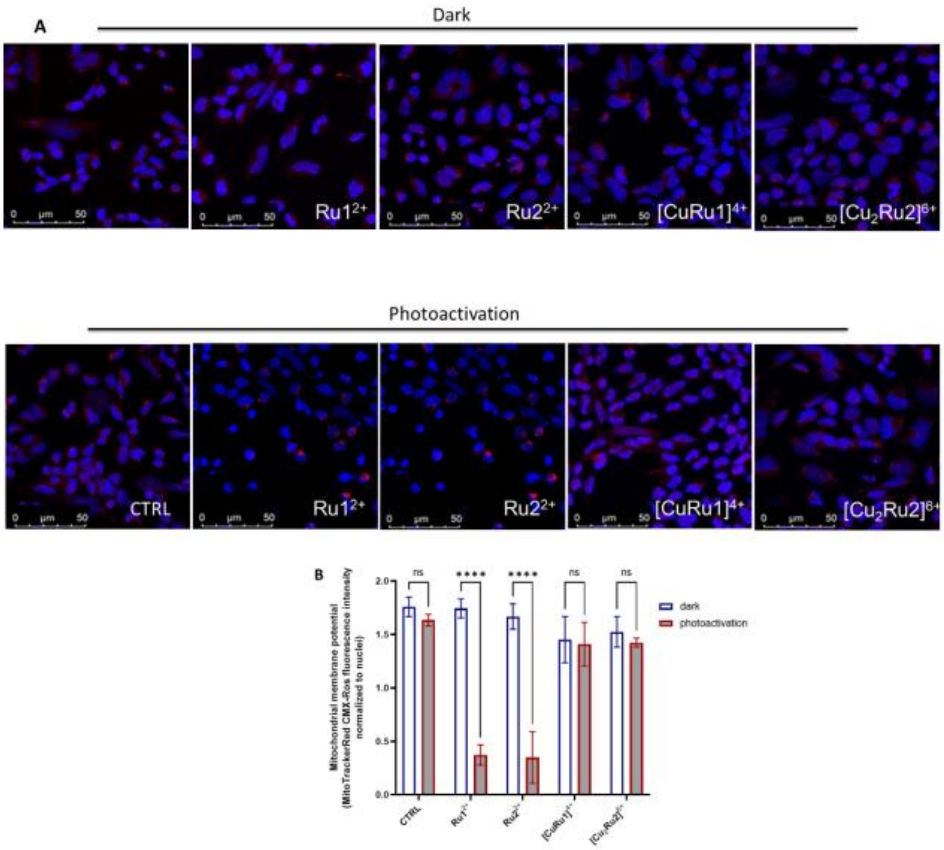

Figure 5. Effect of Ru(II) complexes on mitochondrial membrane potential after photoactivation. Mitochondrial membrane potential of A2780 cells was detected using cationic fluorescent dye Mito-Tracker Red CMXRos, which proportionally accumulates in the negatively charged mitochondrial matrix. (A) A2780 cells were plated in microscope slides and challenged or not (CTRL) with 10 µM of each Ru(II)-complex. After 24 h of incubation, A2780 were subjected to photoactivation or not (dark) for 20 min, 2 h before being labeled with Mitotraker Red CMXRos and fixed in paraformaldehyde, as described in the Materials and Methods section. Confocal analysis was performed using 63X oil immersion objective. Images were representative of six fields of each condition in three independent

experiments with analogous results. (B) Data are reported as mean ± SD of Mito-Tracker Red CMXRos fluorescence intensity normalized to the number of nuclei in six fields for each condition in three independent experiments by using Leica Application Software. Results are statistically significant according to two-way ANOVA followed by Bonferroni post hoc test [**** $p < 0.0001$, not significant (ns)].

With the purpose of dissecting the possible involvement of ROS production in the biological effect induced by $Ru1^{2+}$ and $Ru2^{2+}$ photosensitizers, confocal analysis was performed in A2780 cells employing the CM-H_2DCFDA probe to detect cytosolic ROS after Ru(II) complexes administration upon photoactivation compared to the dark conditions. Under dark conditions cytosolic ROS were almost completely undetectable, whereas, after 2 h photoactivation cytosolic ROS were detected in both $Ru1^{2+}$ and $Ru2^{2+}$ treaded cells (fig. 6). ROS could therefore play a role in the proapoptotic induction exerted by $Ru1^{2+}$ and $Ru2^{2+}$ photosensitizers.

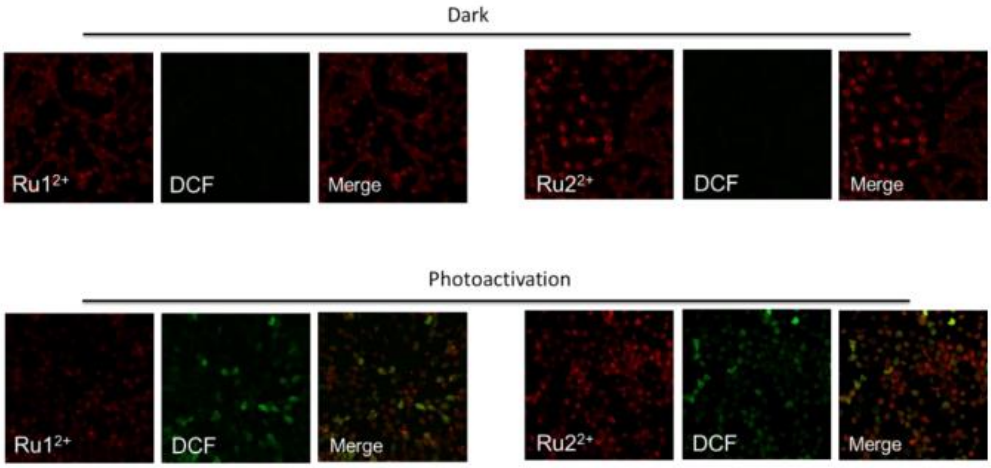

Figure 6. Effect of Ru(II) complexes, $Ru1^{2+}$ and $Ru2^{2+}$, on ROS production after photoactivation. ROS production in A2780 cells was detected using CM-H_2DCFDA. A2780 cells were plated on microscope slides and challenged with 10 µM of each Ru complex. After 24 h of incubation, A2780 were exposed to photoactivation or not (dark) for 20 min, 2 h before being labeled with CM-H_2DCFDA (DCF) and fixed in paraformaldehyde, as described in the Materials and Methods section. Confocal analysis was performed using 63X oil immersion objective. The fluorescence of Ru(II) complexes is shown in red (λexc/λem: 405/600–640 nm) and DCF in green (λexc/λem: ~492–495/517–527 nm). Images were representative of six fields of each condition in three independent experiments with analogous results.

Platinum-based anti-cancer drugs have severe side effects and, in some cases, such as in ovarian cancer, patients acquire a resistance to the platinum based therapy which leads to a poor prognosis. Therefore, efforts are needed in this research field to develop other potential anti-cancer drugs. Ru(II) polypyridyl complexes have shown remarkable anti-tumour activity

coupled with advantages over platinum drugs, such as higher potency, lower toxicity, minor drug resistance, and they are expected to become a new generation of clinical metal anti-cancer drugs.

In collaboration with the Department of Chemistry "Ugo Schiff", we investigated the biological potential of some RPCs, new possible photosensitizers for PDT application, in an *in vitro* model of ovarian cancer. The Ru(II) compounds examined in this study were reported to have low cytotoxicity in non-cancer and cancer cells under dark conditions, which changed into a strict dose-dependent and strong anti-tumour effect after photoactivation. $Ru1^{2+}$ and $Ru2^{2+}$ showed a substantial increase in activity upon light activation, which is consistent with the strong singlet oxygen sensitising capabilities of these molecules. Among the mixed heteronuclear complex, $[CuRu1]^{4+}$ displayed the sharpest photoactivity, showing that, in addition to singlet oxygen sensitization, heteronuclear compounds must have access to additional oxidative pathways in order to have photoinduced efficacy comparable to that of copper-free complexes. Indeed, in a cell free *in vitro* system $[CuRu]^{4+}$ shows the highest activity, while in a cell system it shows the lowest photoactivity, probably due to the lowest capability to be internalized by the cells. Moreover, $Ru1^{2+}$ and $Ru2^{2+}$ above all, showed better internalization capacity by A2780 compared to non-cancer cells. This efficient cellular uptake could be the result of a specific portion of the Ru(II) compounds which could offer better chemical-physical features for cellular internalization, compared to similar compounds. Although the mechanism of internalization of RPCs wasn't investigated in detail, it seems to be independent of the Rab5-associated early endosome pathway. However, the hydrophilic nature of RPCs and their observed localized cellular distribution suggest the occurrence of alternative endocytotic pathway rather than a passive transport. The cell death mediated by the apoptotic process is quite advantageous for the organism since it prevents the release of intracellular content and the subsequent activation of the inflammatory response. The photoactivation of the Ru(II) complexes led to a potent activation of caspase 3 and to the cleavage of both caspase 3 and PARP, pointing out a crucial role for apoptosis in the anti-tumoral effect of the photosensitisers. Moreover, we demonstrated that $Ru1^{2+}$ and Ru^{2+}, but not $[CuRu1]^{4+}$ nor $[Cu_2Ru]^{6+}$, caused a dramatic loss of ΔYm after photoactivation, concomitant

to a ROS cytosolic production as soon as 2 h after irradiation, representing an upstream event that trigger the apoptotic process. Indeed, one of the functions of mitochondria during apoptosis is the release of pro-apoptotic proteins in the cytosol, and disruption of mitocondrial membrane integrity, that is associated with a collapse of ΔYm, can represent an early event of the apoptotic process. As previously mentioned, it has been reported that Ru(II)complexes can directly interfere with DNA replication and transcription. However, in this work, we didn't detect the Ru(II) complexes within the nucleus but rather localized into segregated areas of the cytosol, suggesting that the programmed cell death is likely independent of their interaction with DNA.

In conclusion this work demonstrates that all the four Ru(II) complexes are internalized selectively into the ovarian cancer cell line A2780, have a low cytotoxicity under dark conditions, and display specific photoactivation-induced programmed cell death. Apoptosis was found to be the main mechanism of cell death, and in $Ru1^{2+}$ and $Ru2^{2+}$ treated cells it was associated with mitochondrial ΔYm loss and ROS production.

3.2 Cubosome encapsulated Ru(II) Complexes in PTD of Non-Melanoma Skin Cancer

RPCs have been largely employed in the research of suitable PSs in PDT and, over the past few years, much interest has been devoted to the use of the π-expansive benzo[i]dipyrido[3,2-a:2′,3′ c]phenazine (dppn) ligand in the rational design of RPCs. Although this peculiar ligand can improve the photobiological activity of the resulting compounds, Ru(II) compounds featuring two ddpn ligands have been only sparingly explored. Additionally, these systems' typical hydrophobic nature may restrict their anticancer action, resulting in poor absorption and poor therapeutic results. In order to overcome these limitations, nanocarriers have been extensively researched as a developmental strategy to raise the water solubility of insoluble drug candidates, avoid drug degradation, and improve their distribution. Among the innovative exploited nano-systems, there are cubosomes: bicontinuous cubic liquid crystalline nanoparticles with a three-dimensional arrangement of the lipid bilayer forming a honeycomb-like inner structure. Cubosomes are characterized by an inner portion completely filled with the lipid matrix, providing a greater hydrophobic volume and thus a higher loading efficiency than single-bilayer liposomes. Recent studies have proven their useful biomedical applications for diagnostic purposes, anticancer activity, and PDT.

In this contest, thanks to a new collaboration with the Department of Chemistry “Ugo Schiff”, we explored the potential as PSs of two Ru(II) compounds featuring two dppn ligands simultaneously coordinated to the Ru(II) centers; $[Ru\ (dppn)_2(dmbpy)]^{2+}$ (Ru1) and $[Ru(dppn)_2(dcbpy^{2-})]$ (Ru2) (dmbpy = 4,4′-dimethyl-2,2′-bipyridine, dcbpy2− = 2,2′-bipyridine-4,4′-dicarboxylate). To further ascertain their potential as PSs, Ru1 and Ru2 were also encapsulated in monoolein-based cubosomes stabilized with Pluronic F108. Our colleagues of the chemistry department synthesised and characterized the molecules, investigated the singlet oxygen sensitizing properties of Ru(II)-complexes and their DNA interaction. On the other hand, we took care to test their *in vitro* phototoxicity and biocompatibility on non-melanoma skin cancer cells, a model tumour selected for the feasibility of its treatment by photodynamic therapy. Data are reported in a published article entitled “Ruthenium(II) polypyridyl complexes with π-expansive ligands: synthesis and Cubosome encapsulation for

photodynamic therapy of non-melanoma skin cancer", of which the candidate of this thesis is a co-author (see appendix).

.

3.3 Antioxidant effect new Ruthenium Complexes in human neuroblasts (Manuscript in preparation)

Two new potential antioxidant Ruthenium(II) complexes were synthetised by colleagues of the Chemistry Department "Ugo Schiff": S1 ([Ru(2,6-bis(4-metil-2-benzossazoil)(2,3-diamminonaftalene)Cl]PF_6) and its analogue S2 ([Ru(2,2',6',2''-terpiridina 2,3-diamminonaftalene)Cl]PF_6). The specific aim of our research group in this study was to evaluate their protective effect on the induced cellular damage in a neuroblastoma cell line. As pro-oxidant/pro-apoptotic species able to increase oxidative stress in cells we used H_2O_2, promoter of cellular oxidative damage in several experimental models of neurodegenerative processes (de Oliveira et al., 2017), as well as Cisplatin (CDDP), a chemotherapeutic drug that induces neurotoxicity, and Lipopolysaccharides (LPS), a component of the outer membrane of Gram-negative bacteria. In both glial cells and neurons LPS leads to the production of inflammatory cytokines like TNFα, IL-1β and IL-6 (Pandur et al., 2019).

S1 and S2 are two non-photoactive complexes, whose antioxidant activity was first evaluated by chemical assays showing S1 to have a higher antioxidant efficiency than S2. The antioxidant activity of the complexes was then evaluated in cells.

SH-SY5H neuroblast cell viability was analysed by MTT assay upon H_2O_2, CDDP and LPS treatment for 24 h (fig. 7). H_2O_2 challenge reduced cell viability at high concentrations (100-250 µM), CDDP showed a dose-dependent cytotoxic effect, which was completely lethal at high doses, while LPS didn't significantly alter cell survival. Therefore, for the following experiments we decided to continue with 100 µM H_2O_2, and the lower concentrations for CDDP treatments.

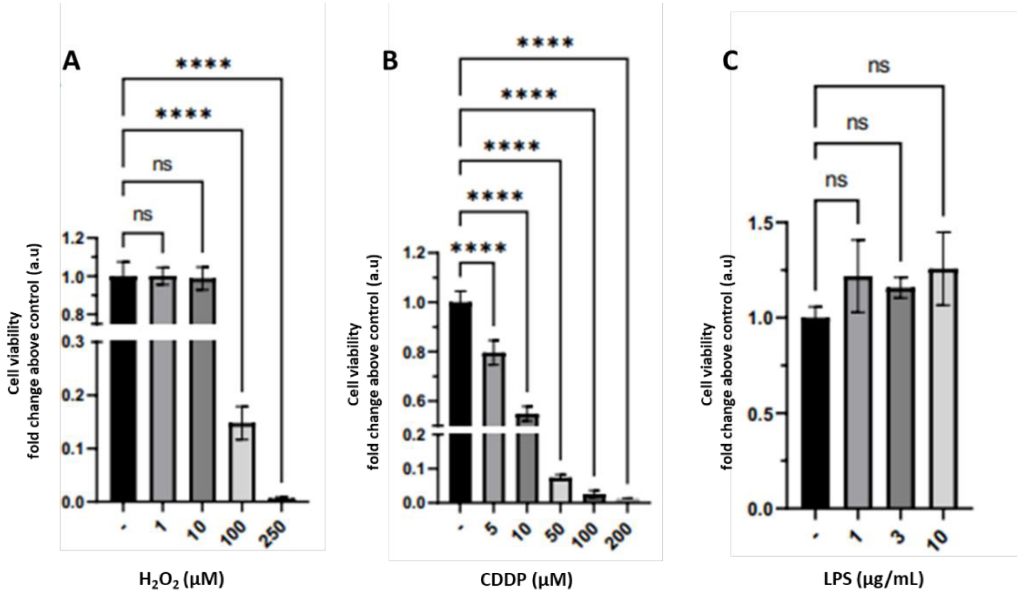

Figure 7. Analysis of cell viability with MTT assay. SH-SY5Y were seeded into 96-well plate and treated with H_2O_2 (1-10-100-250 µM) in A, CDDP (5-10-50-100-200 µM) in B and LPS (1-3-10 µg/ml) in C for 24 h. Experiments were performed in octuplicate, and data represent the mean ± SD of at least two independent experiments. Statistical analysis was performed by one-way ANOVA followed by Bonferroni post hoc test [**** $p < 0.0001$, not significant (ns)].

In order to investigate S1 uptake by SH-SY5Y an ICP-MS analysis was performed upon SH-SY5H cells treated with 1 or 10 µM S1 for 6 and 24 h (fig. 8). S1 uptake was visible at 6 h treatment at both concentrations and it became higher at 10 µM concentration after 24 h. For this reason, we decided to treat cells with 10 µM S1 for 18 h, followed by a 6 h challenge with pro-oxidant species, reaching 24 h of total treatment.

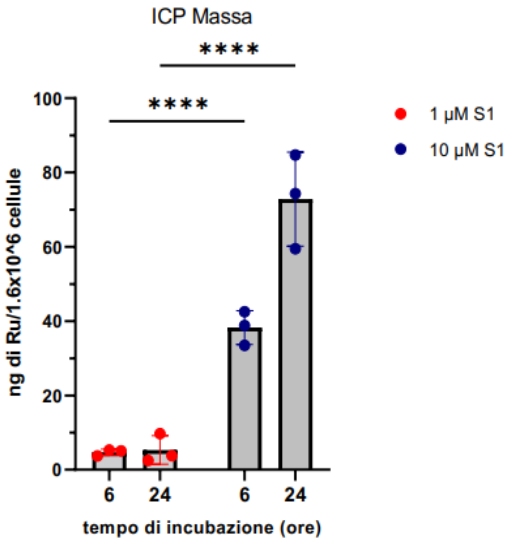

Figure 8. S1 internalization in SH-SY5Y. SH-SY5Y (1.600.000 cellule/p60), were treated with 1-10 µM S1 for 6 and 24 h and analysed by ICP-MS to evaluate the concentration of Ru(II) internalised by cells. Data are reported as the mean ± SEM of three samples for each condition. Statistical analysis was performed by two-way ANOVA followed by Bonferroni post-hoc test [**** $p < 0.0001$].

Once verified the internalization of S1 inside SH-SY5Y cells, we confirmed its negligible cytotoxicity with MTT assay as it is shown in figure 9, and we further tested its efficiency in preventing H_2O_2 and CDDP-induced cell death. Results indicated that incubation with 10 µM S1 for 18 h significantly reverted H_2O_2 negative effect on cell viability, while it didn't show any effect on CDDP-induced cell death. CDDP was therefore excluded in the following experiments.

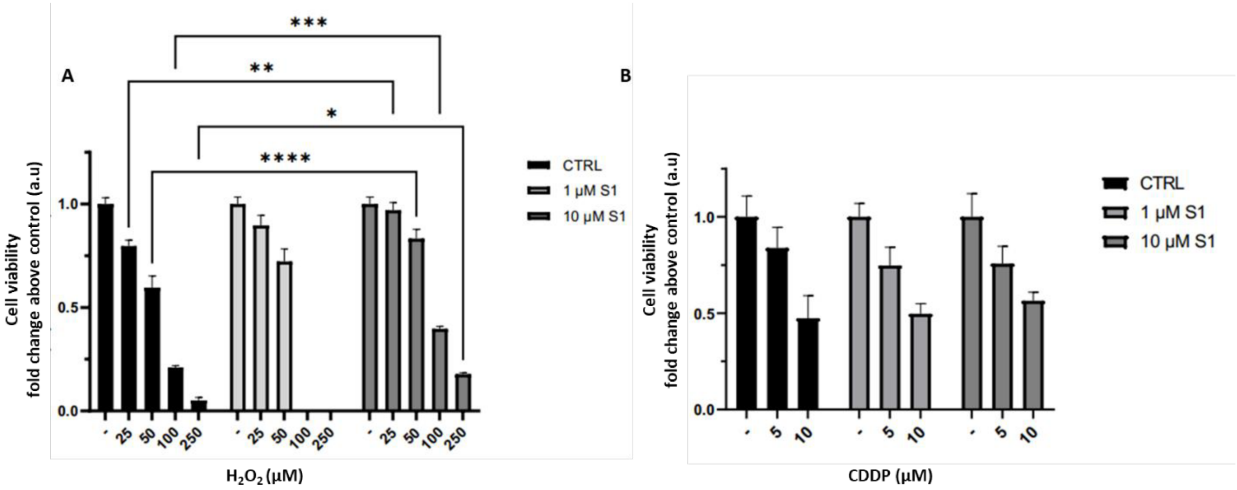

Figure 9. S1 effect on cell viability. SH-SY5Y were seeded into 96-well plate and pre-treated with 1 µM or 10 µM S1 for 18 h, before adding H_2O_2 (25-50-100-250 µM, in A) or (CDDP 5-10 µM, in B) for 24 h. Experiments were performed in octuplicate, and data represent the mean ± SEM of at least three independent experiments. Statistical analysis was performed by two-way ANOVA followed by Bonferroni post hoc test [* $p < 0.05$, ** $p < 0.01$, *** $p < 0.001$, **** $p < 0.0001$].

On this basis, we tested S1 neuroprotective effect on H_2O_2 cytotoxicity in differentiated SH-SY5Y. Cells were differentiated for 7 days in 10 µM RA before being pre-treatment with S1 for 18 h and challenged with H_2O_2. As reported in figure 10, both differentiated and undifferentiated cells show a reduction in cell viability with increasing concentrations of H_2O_2, with the differentiated cells being the most sensitive to the pro-oxidant hydrogen peroxide since they showed an enhanced cell death even at lower concentrations. Moreover, to verify the antioxidant effect of S2 compared to S1 in SH-SY5Y cells, the MTT analysis was performed in the presence of 10 µM S2. As expected, S2 could not prevent H_2O_2 cytotoxicity. On the contrary S1 was confirmed to be a more efficient antioxidant, therefore we focused on investigating the molecular mechanism responsible for S1-induced cells survival effect.

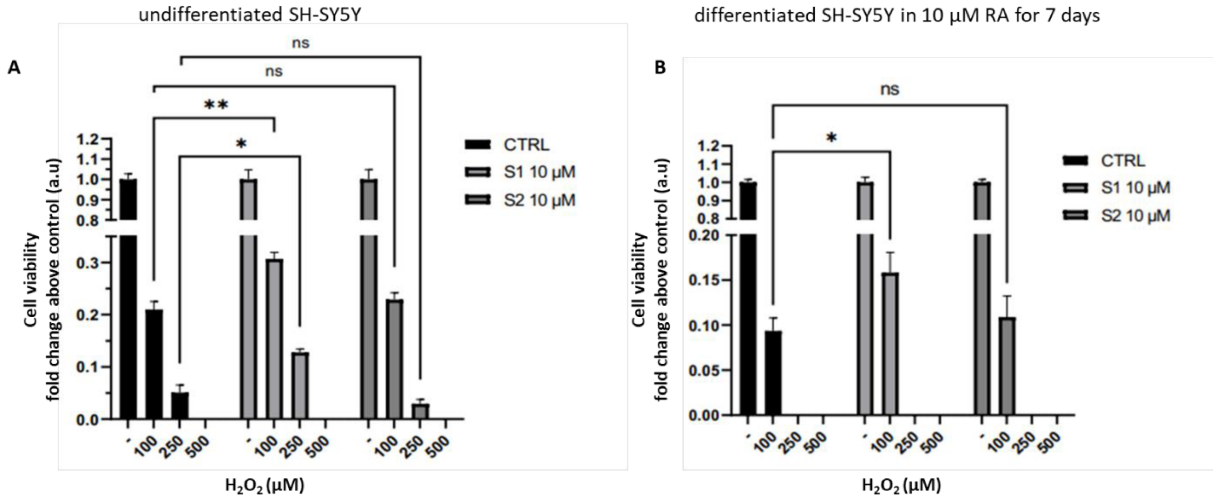

Figure 10. S1 and S2 effect on cell viability in SH-SY5Y under different differentiation conditions. SH-SY5Y were seeded into 96-well plates and pre-treated with 1 µM or 10 µM S1 or S2 for 18 h, before adding H2O2 (100-250-500 µM) for 24 h. MTT assay was performed in undifferentiated cells (A) and in differentiated cells (B) cells. SH-SY5Y cells were differentiated by administration of 10 µM RA dissolved in 1% FBS media for 7 days. Data represent the mean ± SEM of at least three independent experiments. Statistical analysis was performed by two-way ANOVA followed by Bonferroni post hoc test [* $p < 0.05$, ** $p < 0.01$, not significant (ns)].

It's worthy to note that concentrations of H_2O_2 lower than 500 µM induce an apoptotic response, while higher concentrations lead to a necrosis cell death (Ahmad et al., 2003). Indeed, as shown in figure 11, 100 µM H_2O_2 treatment for 6 h resulted in the cleavage of caspase 3 and PARP and therefore the activation of the apoptotic response, while S1 pre-treatment wasn't able to prevent H_2O_2 apoptotic-induction.

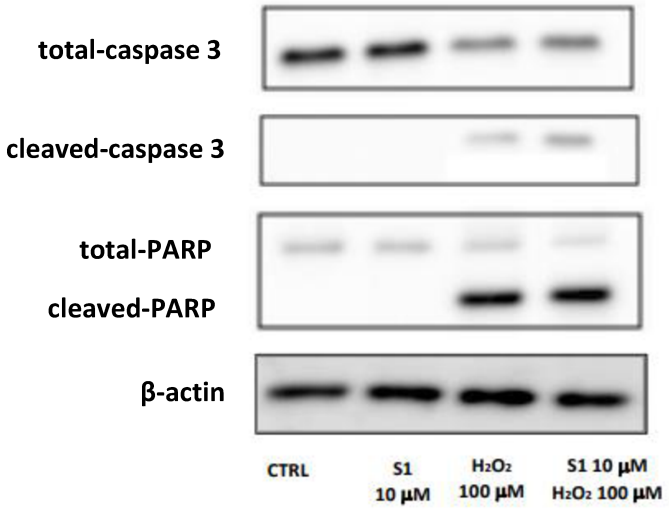

Figure 11. S1 effect on H2O2-induced cell death. SH-SY5Y were pre-treated with 10 µM S1 for 18 h, before being challenged with 100 µM H_2O_2 for 6 h. Lysates were subjected to Western blotting analysis using specific anti-caspase 3 or anti-PARP. β-Actin was used as housekeeping gene.

Morever, we performed a fluorometric assay, in order to detect the activity of caspase 3. Samples were incubated with a specific caspase 3 substrate, which emits fluorescence once it is cleaved by the enzyme. Thus, the fluorescence intensity is an indirect measure of the enzyme activity. Results confirmed the Western blot data: 100 µM H_2O_2 lead to the activation of caspase 3-mediated apoptotic cell death, which is not significantly reverted by 18 h S1 pre-treatment (fig. 12).

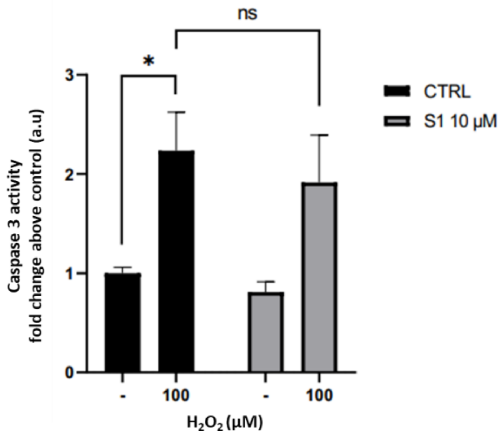

Figure 12. Caspase 3 activity assay. SH-SY5Y were pre-treated with 10 µM S1 for 18 h, before being challenged with 100 µM H_2O_2 for 6 h. Protein lysates (20 µg) were incubated with 50 µM Ac-DEVD-AFC (caspase 3 substrate) for 2h at 37°C. Data represent the mean ± SEM of at least three independent experiments. Statistical analysis was performed by two-way ANOVA followed by Bonferroni post hoc test [* $p < 0.05$, not significant (ns)].

To test the S1 antioxidant activity upon H_2O_2-mediated ROS generation we used the probe DCFH-DA in confocal microscope imaging to reveal the cytosolic ROS production. SH-SY5Y challenged with 100 µM H_2O_2 for 6 h showed an enhancement in ROS levels, while S1 pre-treatment for 18 h was efficient in preventing the H_2O_2-induced ROS increase (fig. 13).

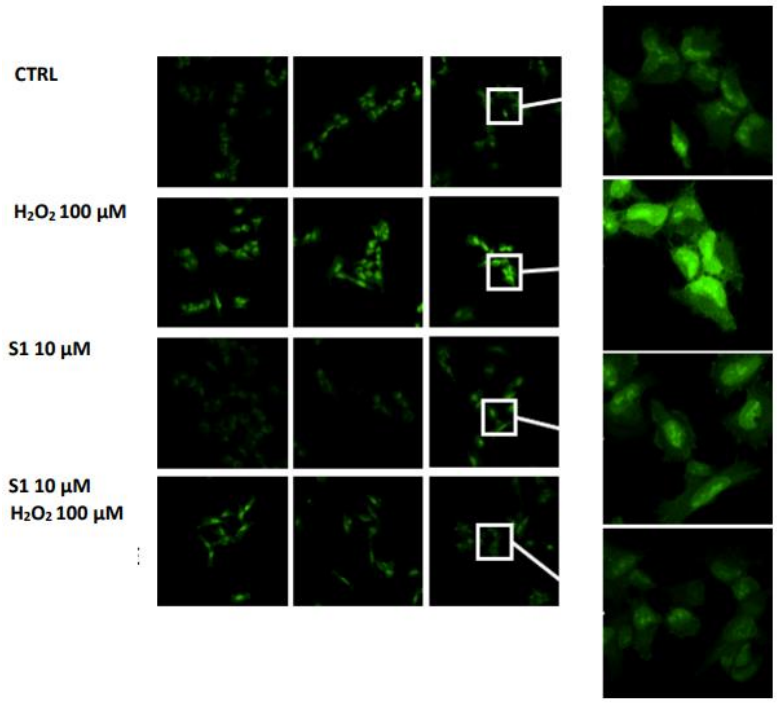

Figure 13. S1 antioxidant activity on H2O2-mediated ROS production. SH-SY5Y were seeded on microscope slides and pre-treated with 10 µM S1 for 18 h, before being challenged with 100 µM H_2O_2 for 6 h. Then slides were labelled with CM-H2DCFDA (DCF) and fixed in paraformaldehyde, as described in the Materials and Methods section. Confocal analysis was performed using 63X oil immersion objective.

We further quantified ROS production induced by H_2O_2 by Fluorescence Activated Cell Sorting (FACS) using DCFH-DA to detect cytosolic ROS. Flow cytometry data confirmed the confocal images: S1 pre-treatment was able to attenuate the production of ROS mediated by H_2O_2 at both concentrations of the pro-oxidant stimulus (100 and 250 µM, fig. 14).

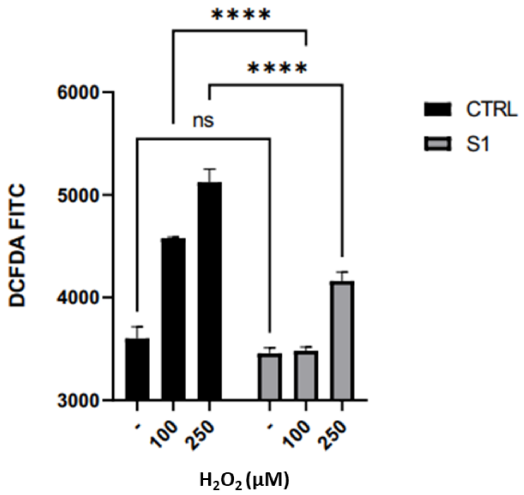

Figure 14. S1 antioxidant activity in flow cytometry. SH-SY5Y were pre-treated with 10 µM S1 for 18 h, before being challenged with 100 or 250 µM H_2O_2 for 2 h. Cells were incubated with 1 µM CM-H2DCFDA (DCF) for 15 minutes in dark. Data represent the mean ± SEM of at least two independent experiments. Statistical analysis was performed by two-way ANOVA followed by Bonferroni post hoc test [**** $p < 0.0001$, not significant (ns)].

Altogether these results indicate the capability of S1 to prevent the formation of ROS induced by H_2O_2, confirming the preliminary chemical experiments in a biological model of neuroblasts cell line.

Mitochondrial dysfunction has been associated with several neurological diseases. Compounds that may be used to prevent or cure these disorders are gaining interest among the scientific community (de Oliveira et al., 2017). Therefore, we determined the H_2O_2-induced alterations on the mitochondria using the probe Mito-Tracker Red CMXRos. As we can see in figure 15, H_2O_2 challenge for 6 h induced a fragmentation of cells mitochondria, while S1 pre- treatment had a protective effect, preventing the mitochondrial fission. These results reported in figure 15 suggest that S1 attenuates H_2O_2-induced mitochondrial damage, which can play an important role in the protection of SH-SY5Y from the cytotoxic effect of H_2O_2.

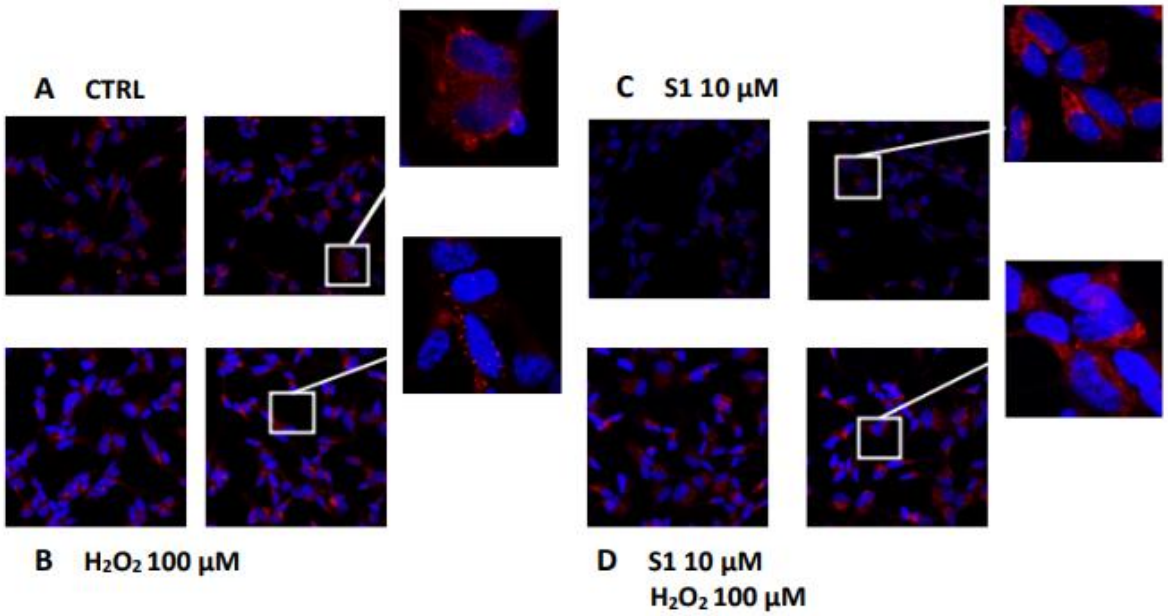

Figure 15. S1 effect on mitochondrial function. SH-SY5Y cells were seeded on microscope slides and pre-treated with 10 µM S1 for 18 h (C and D), before being challenged with 100 µM H_2O_2 for 6 h (B and D). Then slides were labelled with Mito-Tracker Red CMXRos 100 nM per 30min and fixed in paraformaldehyde, as described in the Materials and Methods section. Confocal analysis was performed using 63X oil immersion objective.

Mitochondrial ROS production was also quantified by FACS upon H_2O_2 exposure using a mitochondrial superoxide indicator. H_2O_2 induced mitochondrial ROS production, which was not attenuated in the presence of S1 (data not shown). S1 antioxidant activity is therefore efficient in reducing cytosolic but not mitochondrial ROS.

Recent studies suggest inflammation as a crucial role in the progression of neurodegeneration (Kwon & Koh, 2020; W. Zhang et al., 2023). Activated microglia as well as other cells residing in the tissue can express pro-inflammatory cytokines, which have negative effects during neurodegenerative diseases. Therefore, we evaluated the expression of inflammatory markers upon H_2O_2 or LPS challenge at RNA levels to reveal a possible anti-inflammatory effect of S1 (fig. 16). Specifically, we analysed the gene expression of TNFα, COX2, IL-1β and IL-6 upon H_2O_2 or LPS challenge for 3 or 24 h in the presence or absence of S1. Our data showed an enhanced expression of COX2 upon LPS treatment for 3 h, which was reduced by the pre-treatment with S1, in a not statistically significant manner. IL-1 β expression was also

enhanced by both H2O2 and LPS challenge at 24 h and reduced by S1 pre-treatment, even if the reduction was not statistically significant.

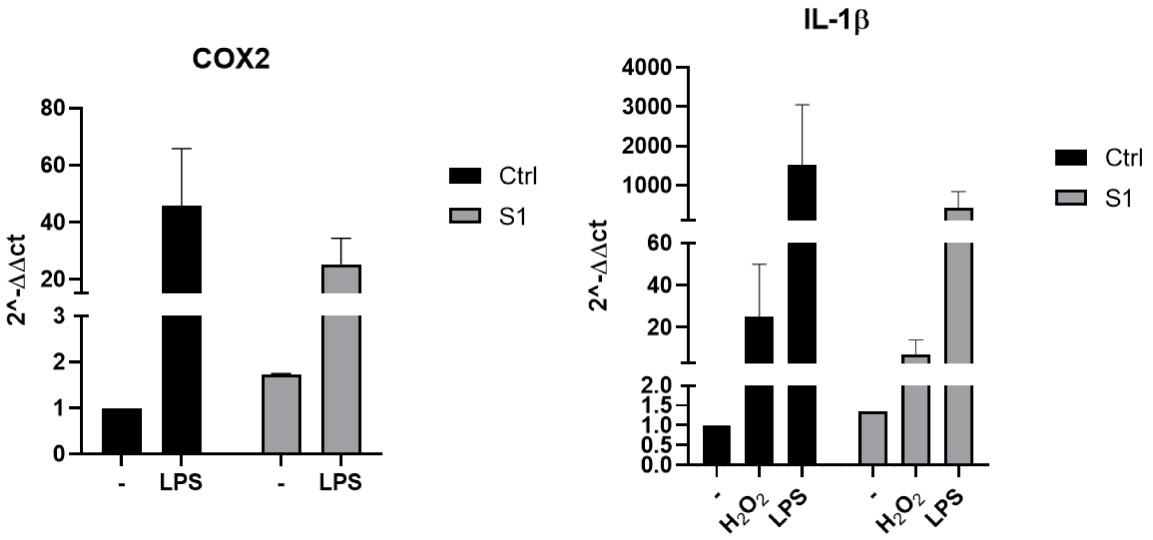

Figure 16. Anti-inflammatory activity of S1 in undifferentiated SH-SY5Y. SH-SY5Y were pre-treated with 10 µM S1 for 18 h, before being challenged with 100 µM H_2O_2 or 3 µg/ml LPS for 3 and 24 h. The RNA expression levels of COX2 at 3 h treatments and IL-1β at 24 h treatments were assessed with real time PCR technique. The values are expressed as $2^{(-\Delta\Delta Ct)}$ and normalized to β-Actin. Data are reported as mean ± SEM of at least two independent experiments.

We analysed the gene expression of the inflammatory markers also in differentiated SH-SY5Y cells upon H_2O_2 for 3 or 24 h in the presence or absence of S1. Our preliminary data showed an enhanced expression of COX2 and TNFα upon H_2O_2 treatment for 3 h, which was reduced by the 18 h pre-treatment with S1. IL-1 β expression was also enhanced by H_2O_2 challenge at 24 h and significantly reduced by S1 pre-treatment (fig. 17).

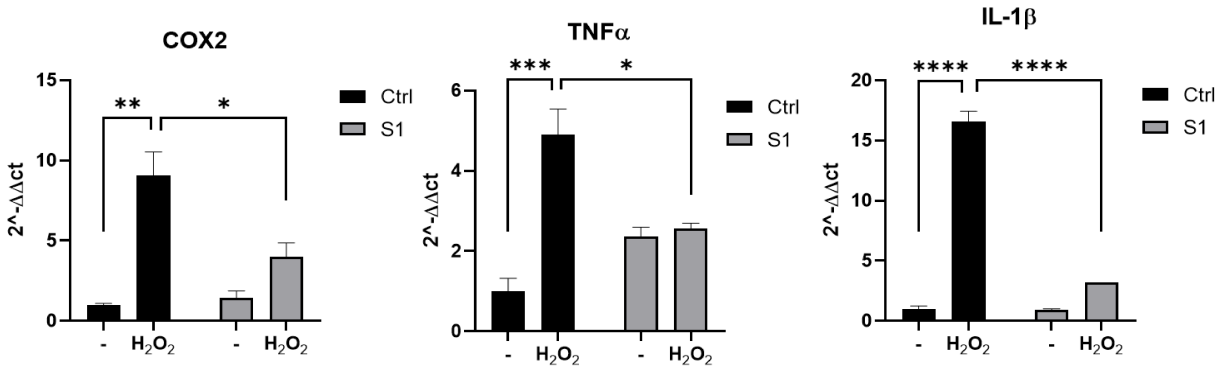

Figure 17. Anti-inflammatory activity of S1 in differentiated SH-SY5Y. SH-SY5Y cells were differentiated using 10 µM RA dissolved in 1% FBS media for 7 days. Differentiated cells were pre-treated with 10 µM S1 for 18 h, before being challenged with 100 µM H_2O_2 for 3 or 24 h. The RNA expression levels of COX2 at 3 h treatments, TNFα at 3 h treatments and IL-1β at 24 h treatments were assessed with real time PCR technique. The values are expressed as $2^{(-\Delta\Delta Ct)}$ and normalized to β-Actin. Data are reported as mean ± SEM of at least one experiment. Statistical analysis was performed by two-way ANOVA followed by Bonferroni post hoc test [* $p < 0.05$, ** $p < 0.01$, *** $p < 0.001$ **** $p < 0.0001$].

Differently from the two topics discussed in chapters 3.1 and 3.2 of this section, where Ru(II) complexes were tested as possible new photosensitisers in PDT of ovarian cancer and non-melanoma skin cancer, capable of producing ROS, in latter study we tested the biological effect of two other innovative Ru(II) complexes, with different chemical structures, that acts as antioxidant compounds. Indeed, the Ru(II) complexes here analysed work as scavengers of ROS and could be possibly used as antioxidant agents in the treatment of neurodegenerative diseases. The characteristics and the antioxidant activity of the new Ru(II) complexes S1 and S2 were analysed by chemical assay and then applied in cell biology. In particular, S1 neuroprotective effect was evaluated in the neuroblastoma cell line SH-SY5Y upon pro-apoptotic/pro-oxidant molecules challenge. These cells were found able to internalise S1 at 18 h treatment. H_2O_2 challenge caused a reduction in cell viability, the activation of the apoptotic cell death, mitochondrial disfunctions, enhanced cytosolic and mitochondrial ROS production and increased expression of inflammatory markers. S1 18 h pre-treatment reduced H_2O_2-induced cytotoxicity, along with cytosolic ROS production and mitochondrial fission. Its cytosolic antioxidant activity wasn't found efficient to reduce mitochondrial ROS nor the apoptotic response induced by H_2O_2. Moreover, S1 wasn't able to revert the CDDP cytotoxicity. This latter result could be explained by the fact that CDDP can bind directly to DNA leading to a ROS-independent damage, and therefore the antioxidant activity of S1 is ineffective. Regarding S1 anti-inflammatory activity, 18 h S1 pre-treatment was able to reduce

some of the investigated inflammatory markers upon LPS or H_2O_2 challenge in differentiated neuroblasts.

In conclusion, these original results show that antioxidant Ru(II) complex, S1, or parent Ruthenium complexes could be potentially useful as new pharmacological tools in neurodegenerative diseases associated with a high oxidative stress.

References

Ahern, G. P., Brooks, I. M., Miyares, R. L., & Wang, X. Bin. (2005). Extracellular cations sensitize and gate capsaicin receptor TRPV1 modulating pain signaling. *Journal of Neuroscience*, *25*(21), 5109–5116. https://doi.org/10.1523/JNEUROSCI.0237-05.2005

Ahmad, K. A., Clement, M.-V., & Pervaiz, S. (2003). Pro-oxidant activity of low doses of Resveratrol inhibits Hydrogen Peroxide induced apoptosis. *Annals of the New York Academy of Sciences*, 365–373.

Antonarakis, E. S., & Emadi, A. (2010). *Ruthenium-based chemotherapeutics: are they ready for prime time? 66*(1), 1–9. https://doi.org/10.1007/s00280-010-1293-1.Ruthenium-based

Atwood, B. K., & MacKie, K. (2010). CB 2: A cannabinoid receptor with an identity crisis. In *British Journal of Pharmacology* (Vol. 160, Issue 3, pp. 467–479). https://doi.org/10.1111/j.1476-5381.2010.00729.x

Babilas, P., Schreml, S., Landthaler, M., & Szeimies, R. M. (2010). Photodynamic therapy in dermatology: State-of-the-art. *Photodermatology Photoimmunology and Photomedicine*, *26*(3), 118–132. https://doi.org/10.1111/j.1600-0781.2010.00507.x

Baggelaar, M. P., Maccarrone, M., & van der Stelt, M. (2018). 2-Arachidonoylglycerol: A signaling lipid with manifold actions in the brain. In *Progress in Lipid Research* (Vol. 71, pp. 1–17). Elsevier Ltd. https://doi.org/10.1016/j.plipres.2018.05.002

Bari, M., Paradisi, A., Pasquariello, N., & Maccarrone, M. (2005). Cholesterol-dependent modulation of type 1 cannabinoid receptors in nerve cells. *Journal of Neuroscience Research*, *81*(2), 275–283. https://doi.org/10.1002/jnr.20546

Beltramo, M., Stella, N., Calignano, A., Lin, S. Y., Makriyannis, A., & Piomelli, D. (1997). Functional Role of High-Affinity Anandamide Transport, as Revealed by Selective Inhibition. *Science*, *277*, 1094–1097. www.sciencemag.org

Benítez-Angeles, M., Morales-Lázaro, S. L., Juárez-González, E., & Rosenbaum, T. (2020). TRPV1: Structure, endogenous agonists, and mechanisms. *International Journal of Molecular Sciences*, *21*(10). https://doi.org/10.3390/ijms21103421

Bentzinger, C. F., Wang, Y. X., Dumont, N. A., & Rudnicki, M. A. (2013). Cellular dynamics in

the muscle satellite cell niche. *EMBO Reports*, *14*(12), 1062–1072. https://doi.org/10.1038/embor.2013.182

Bernacchioni, C., Cencetti, F., Blescia, S., Donati, C., & Bruni, P. (2012). Sphingosine kinase/sphingosine 1-phosphate axis: a new player for insulin-like growth factor-1-induced myoblast differentiation. *Skeletal Muscle*, *2*(1), 1. https://doi.org/10.1186/2044-5040-2-15

Bernacchioni, C., Ghini, V., Squecco, R., Idrizaj, E., Garella, R., Puliti, E., Cencetti, F., Bruni, P., & Donati, C. (2021). Role of sphingosine 1-phosphate signalling axis in muscle atrophy induced by tnfα in c2c12 myotubes. *International Journal of Molecular Sciences*, *22*(3), 1–19. https://doi.org/10.3390/ijms22031280

Bernacchionp, C., Cencettp, F., Kwon2, M. J., Gwak2, H. S., Jeong2, S. K., Brunp, P., & Donatii, C. (2011). THE SPHINGOSINE KINASE ACTIVATOR K6PC-5 STIMULATES C2C12 MYOBLAST DIFFERENTIATION 55. In *INTERNATIONAL JOURNAL OF IMMUNOPATHOLOGY AND PHARMACOLOGY* (Vol. 24, Issue 1).

Berridge, M. J., Lipp, P., & Bootman, M. D. (2000). THE VERSATILITY AND UNIVERSALITY OF CALCIUM SIGNALING. *MOLECULAR CELL BIOLOGY*, *1*.

Bevan, S., Quallo, T., & Andersson, D. A. (2014). TRPV1. *Handbook of Experimental Pharmacology*, *222*, 207–245. https://doi.org/10.1007/978-3-642-54215-2_9

Bhattacharya, D., & Scimè, A. (2020). Mitochondrial Function in Muscle Stem Cell Fates. *Frontiers in Cell and Developmental Biology*, *8*(June), 1–15. https://doi.org/10.3389/fcell.2020.00480

Biga, M. L., Dawson, S., Harwell, A., Hopkins, R., Kaufmann, J., Mike, L., Matern, P., Morrison-Graham, K., Quick, D., & Ruyeon, J. (2017). Anatomy & Physiology. In *Anatomy & Physiology*. https://doi.org/10.5399/osu/1116

Birnbaumer, L., Yidirim, E., & Abramowitz, J. (2003). A comparison of the genes coding for canonical TRP channels and their M, V and P relatives. *Cell Calcium*, *33*(5–6), 419–432. https://doi.org/10.1016/S0143-4160(03)00068-X

Bisogno, T., Howell, F., Williams, G., Minassi, A., Cascio, M. G., Ligresti, A., Matias, I., Schiano-Moriello, A., Paul, P., Williams, E. J., Gangadbaran, U., Hobbs, C., Di Marzo, V., & Doherty, P. (2003). Cloning of the first sn1-DAG lipases points to the spatial and temporal regulation of endocannabinoid signaling in the brain. *Journal of Cell Biology*,

163(3), 463–468. https://doi.org/10.1083/jcb.200305129

Bisogno, T., Maccarrone, M., De Petrocellis, L., Jarrahian, A., Finazzi-Agro Á, A., Hillard, C., & Marzo, V. Di. (2001). The uptake by cells of 2-arachidonoylglycerol, an endogenous agonist of cannabinoid receptors. *Eur. J. Biochem.*, *268*, 1982–1989.

Blankman, J. L., Simon, G. M., & Cravatt, B. F. (2007). A Comprehensive Profile of Brain Enzymes that Hydrolyze the Endocannabinoid 2-Arachidonoylglycerol. *Chemistry and Biology*, *14*(12), 1347–1356. https://doi.org/10.1016/j.chembiol.2007.11.006

Blau, H. M., Chiu, C.-P., & Webster, C. (1983). Cytoplasmic Activation of Human Nuclear Genes in Stable Heterocaryons. *Cell*, *32*, 1171–1180.

Blázquez, C., Sánchez, C., Daza, A., Galve-Roperh, I., & Guzmán, M. (1999). The stimulation of ketogenesis by cannabinoids in cultured astrocytes defines carnitine palmitoyltransferase I as a new ceramide-activated enzyme. *Journal of Neurochemistry*, *72*(4), 1759–1768. https://doi.org/10.1046/j.1471-4159.1999.721759.x

Bojesen, I. N., & Hansen, H. S. (2003). Binding of anandamide to bovine serum albumin. *Journal of Lipid Research*, *44*(9), 1790–1794. https://doi.org/10.1194/jlr.M300170-JLR200

Bondì, M., Germinario, E., Pirazzini, M., Zanetti, G., Cencetti, F., Donati, C., Gorza, L., Betto, R., Bruni, P., & Danieli-betto, D. (2024). *Ablation of S1P 3 receptor protects mouse soleus from age-related drop in muscle mass , force , and regenerative capacity*. 67, 54–67. https://doi.org/10.1152/ajpcell.00027.2017

Bouaboula, M., Hilairet, S., Marchand, J., Fajas, L., Le Fur, G., & Casellas, P. (2005). Anandamide induced PPARγ transcriptional activation and 3T3-L1 preadipocyte differentiation. *European Journal of Pharmacology*, *517*(3), 174–181. https://doi.org/10.1016/j.ejphar.2005.05.032

Brailoiu, G. C., Oprea, T. I., Zhao, P., Abood, M. E., & Brailoiu, E. (2011). Intracellular cannabinoid type 1 (CB1) receptors are activated by anandamide. *Journal of Biological Chemistry*, *286*(33), 29166–29174. https://doi.org/10.1074/jbc.M110.217463

Bravo, G. Á., Cedeño, R. R., Casadevall, M. P., & Ramió-Torrentà, L. (2022). Sphingosine-1-Phosphate (S1P) and S1P Signaling Pathway Modulators, from Current Insights to Future Perspectives. In *Cells* (Vol. 11, Issue 13). MDPI. https://doi.org/10.3390/cells11132058

Burattini, S., Ferri, R., Battistelli, M., Curci, R., Luchetti, F., & Falcieri, E. (2004). C2C12 murine

myoblasts as a model of skeletal muscle development: Morpho-functional characterization. *European Journal of Histochemistry*, *48*(3), 223–233. https://doi.org/10.4081/891

Cali, M. P., Pereira, L. M. B., Teodoro, M. D., Sellani, T. A., Rodrigues, E. G., & Carlos, R. M. (2021). Comparison of Aβ (1–40, 1–28, 11–22, and 29–40) aggregation processes and inhibition of toxic species generated in early stages of aggregation by a water-soluble ruthenium complex. *Journal of Inorganic Biochemistry*, *215*(March), 111314. https://doi.org/10.1016/j.jinorgbio.2020.111314

Calise, S., Blescia, S., Cencetti, F., Bernacchioni, C., Donati, C., & Bruni, P. (2012). Sphingosine 1-phosphate stimulates proliferation and migration of satellite cells. Role of S1P receptors. *Biochimica et Biophysica Acta - Molecular Cell Research*, *1823*(2), 439–450. https://doi.org/10.1016/j.bbamcr.2011.11.016

Campelo, M. W. S., Oriá, R. B., Lopes De França, L. G., De Castro Brito, G. A., Dos Santos, A. A., De Vasconcelos, R. C., Da Silva, F. O. N., Nobrega, B. N., Bento-Silva, M. T., & De Vasconcelos, P. R. L. (2012). Preconditioning with a novel metallopharmaceutical NO donor in anesthetized rats subjected to brain ischemia/reperfusion. *Neurochemical Research*, *37*(4), 749–758. https://doi.org/10.1007/s11064-011-0669-x

Camprubí-Robles, M., Planells-Cases, R., & Ferrer-Montiel, A. (2009). Differential contribution of SNARE-dependent exocytosis to inflammatory potentiation of TRPV1 in nociceptors. *FASEB Journal*, *23*(11), 3722–3733. https://doi.org/10.1096/fj.09-134346

Cartier, A., & Hla, T. (2019). Sphingosine 1-phosphate: Lipid signaling in pathology and therapy. In *Science* (Vol. 366, Issue 6463). American Association for the Advancement of Science. https://doi.org/10.1126/science.aar5551

Catanzaro, G., Rapino, C., Oddi, S., & Maccarrone, M. (2009). Anandamide increases swelling and reduces calcium sensitivity of mitochondria. *Biochemical and Biophysical Research Communications*, *388*(2), 439–442. https://doi.org/10.1016/j.bbrc.2009.08.037

Caterina, M. J., Schumacher, M. A., Tominaga, M., Rosen, T. A., Levine, J. D., & Julius, D. (1997). *The capsaicin receptor: a heat-activated ion channel in the pain pathway*.

Cencetti, F., Bernacchioni, C., Nincheri, P., Donati, C., & Bruni, P. (2010). Transforming Growth Factor-□1 Induces Transdifferentiation of Myoblasts into Myofibroblasts via Up-Regulation of Sphingosine Kinase-1/S1P3 Axis. *Molecular Biology of the Cell*, *21*, 1111–

1124.

Chicca, A., Marazzi, J., Nicolussi, S., & Gertsch, J. (2012). Evidence for bidirectional endocannabinoid transport across cell membranes. *Journal of Biological Chemistry*, *287*(41), 34660–34682. https://doi.org/10.1074/jbc.M112.373241

Chilakamarthi, U., & Giribabu, L. (2017). Photodynamic Therapy: Past, Present and Future. *Chemical Record*, *17*(8), 775–802. https://doi.org/10.1002/tcr.201600121

Colombo, G., Rusconi, F., Rubino, T., Cattaneo, A., Martegani, E., Parolaro, D., Bachi, A., & Zippel, R. (2009). Transcriptomic and proteomic analyses of mouse cerebellum reveals alterations in RasGRF1 expression following in vivo chronic treatment with delta 9-tetrahydrocannabinol. *Journal of Molecular Neuroscience*, *37*(2), 111–122. https://doi.org/10.1007/s12031-008-9114-2

Conti, L., Giacomazzo, G. E., Valtancoli, B., Perfetti, M., Privitera, A., Giorgi, C., Sfragano, P. S., Palchetti, I., Pecchioli, S., Bruni, P., & Cencetti, F. (2022). Highly Charged Ru(II) Polypyridyl Complexes as Photosensitizer Agents in Photodynamic Therapy of Epithelial Ovarian Cancer Cells. *International Journal of Molecular Sciences*, *23*(21). https://doi.org/10.3390/ijms232113302

Cordeiro, A. V., Silva, V. R. R., Pauli, J. R., da Silva, A. S. R., Cintra, D. E., Moura, L. P., & Ropelle, E. R. (2019). The role of sphingosine-1-phosphate in skeletal muscle: Physiology, mechanisms, and clinical perspectives. *Journal of Cellular Physiology*, *234*(7), 10047–10059. https://doi.org/10.1002/jcp.27870

Coussin, F., Scott, R. H., Wise, A., & Nixon, G. F. (2002). Comparison of sphingosine 1-phosphate-induced intracellular signaling pathways in vascular smooth muscles. *Circulation Research*, *91*(2), 151–157. https://doi.org/10.1161/01.RES.0000028150.51130.36

Cramer, G., Lewis, R., Gymarty, A., Hagan, S., Mickler, M., Evans, S., Punekar, S. R., Shuman, L., Simone, C. B., Hahn, S. M., Busch, T. M., Fraker, D., & Cengel, K. A. (2020). Preclinical Evaluation of Cetuximab and Benzoporphyrin Derivative-Mediated Intraperitoneal Photodynamic Therapy in a Canine Model. *Photochemistry and Photobiology*, *96*(3), 684–691. https://doi.org/10.1111/php.13247

Cravatt, B. F., Demarest, K., Patricelli, M. P., Bracey, M. H., Giang, D. K., Martin, B. R., & Lichtman, A. H. (2001). Supersensitivity to anandamide and enhanced endogenous

cannabinoid signaling in mice lacking fatty acid amide hydrolase. *PNAS*, *98*(16), 9371–9376. www.pnas.orgcgidoi10.1073pnas.161191698

Cravatt, B. F., Giang, D. K., Mayfield, S. P., Boger, D. L., Lerner, R. A., & Gilula, N. B. (1996). Molecular characterization of an enzyme that degrades neuromodulatory fatty-acid amides. *Nature*, *384*, 83–87.

Cravatt, B. F., Saghatelian, A., Hawkins, E. G., Clement, A. B., Bracey, M. H., & Lichtman, A. H. (2004). Functional disassociation of the central and peripheral fatty acid amide signaling systems. *PNAS*, *101*(29), 10821–10826. www.pnas.orgcgidoi10.1073pnas.0401292101

Curci, R., Battistelli, M., Burattini, S., D'Emilio, A., Ferri, P., Lattanzi, D., Ciuffoli, S., Ambrogini, P., Cuppini, R., & Falcieri, E. (2008). Surface and inner cell behaviour along skeletal muscle cell in vitro differentiation. *Micron*, *39*(7), 843–851. https://doi.org/10.1016/j.micron.2007.12.007

Dalle, S., & Koppo, K. (2021). Cannabinoid receptor 1 expression is higher in muscle of old vs. young males, and increases upon resistance exercise in older adults. *Scientific Reports*, *11*(1). https://doi.org/10.1038/s41598-021-97859-3

Dalle, S., Schouten, M., Meeus, G., Slagmolen, L., & Koppo, K. (2022). Molecular networks underlying cannabinoid signaling in skeletal muscle plasticity. In *Journal of Cellular Physiology* (Vol. 237, Issue 9, pp. 3517–3540). John Wiley and Sons Inc. https://doi.org/10.1002/jcp.30837

Damia, G., & Broggini, M. (2019). *Platinum Resistance in Ovarian Cancer : Role of DNA Repair*. 1–15. https://doi.org/10.3390/cancers11010119

de Oliveira, M. R., Fürstenau, C. R., de Souza, I. C. C., & da Costa Ferreira, G. (2017). Tanshinone I Attenuates the Effects of a Challenge with H2O2 on the Functions of Tricarboxylic Acid Cycle and Respiratory Chain in SH-SY5Y Cells. *Molecular Neurobiology*, *54*(10), 7858–7868. https://doi.org/10.1007/s12035-016-0267-7

De Petrocellis, L., & Di Marzo, V. (2009). Role of endocannabinoids and endovanilloids in Ca2+ signalling. *Cell Calcium*, *45*(6), 611–624. https://doi.org/10.1016/j.ceca.2009.03.003

del Carmen, M. G., Rizvi, I., Chang, Y., Moor, A. C. E., Oliva, E., Sherwood, M., Pogue, B., & Hasan, T. (2005). Synergism of epidermal growth factor receptor-targeted immunotherapy with photodynamic treatment of ovarian cancer in vivo. *Journal of the*

National Cancer Institute, *97*(20), 1516–1524. https://doi.org/10.1093/jnci/dji314

Demuth, D. G., & Molleman, A. (2006). Cannabinoid signalling. In *Life Sciences* (Vol. 78, Issue 6, pp. 549–563). Elsevier Inc. https://doi.org/10.1016/j.lfs.2005.05.055

Desvergne, B., Wahli, W., & Wahli, W. (1999). Peroxisome Proliferator-Activated Receptors: Nuclear Control of Metabolism*. *Endocrine Reviews*, *20*(5), 649–688. https://academic.oup.com/edrv/article/20/5/649/2530847

Dhopeshwarkar, A., & Mackie, K. (2014). CB2cannabinoid receptors as a therapeutic target-what does the future hold? *Molecular Pharmacology*, *86*(4), 430–437. https://doi.org/10.1124/mol.114.094649

Di Marzo, V, & De Petrocellis, L. (2010). Endocannabinoids as Regulators of Transient Receptor Potential (TRP) Channels: a Further Opportunity to Develop New Endocannabinoid-Based Therapeutic Drugs. In *Current Medicinal Chemistry* (Vol. 17).

Di Marzo, Vincenzo, Fontana, A., Cadas, H., Schinelli, S., Cimino, G., Schwartz, J.-C., & Plomelli, D. (1994). Formation and Inactivation of endogenous cannabinoid anandamide in central neurons. *Nature*, *372*(6507), 686–691.

Diao, Z., Matsui, T., & Funaba, M. (2021). Stimulation of myogenesis by ascorbic acid and capsaicin. *Biochemical and Biophysical Research Communications*, *568*, 83–88. https://doi.org/10.1016/j.bbrc.2021.06.067

Docherty, R., Yeats, J., Bevan HWGM Boddeke, S., Docherty -JC Yeats Bevan, R. S., & Boddeke, H. (1996). Inhibition of calcineurin inhibits the desensitization of capsaicin-evoked currents in cultured dorsal root ganglion neurones from adult rats. In *Pflfigers Arch Eur J Physiol* (Vol. 431). Springer-Verlag.

Donati, C., Cencetti, F., & Bruni, P. (2013). Sphingosine 1-phosphate axis: A new leader actor in skeletal muscle biology. *Frontiers in Physiology*, *4 NOV*(November), 1–10. https://doi.org/10.3389/fphys.2013.00338

Donati, C., Meacci, E., Nuti, F., Becciolini, L., Farnararo, M., & Bruni, P. (2005a). Sphingosine 1-phosphate regulates myogenic differentiation: a major role for S1P 2 receptor . *The FASEB Journal*, *19*(3), 1–22. https://doi.org/10.1096/fj.04-1780fje

Donati, C., Meacci, E., Nuti, F., Becciolini, L., Farnararo, M., & Bruni, P. (2005b). Sphingosine 1-phosphate regulates myogenic differentiation: a major role for S1P 2 receptor . *The FASEB Journal*, *19*(3), 1–22. https://doi.org/10.1096/fj.04-1780fje

Donati, C., Nincheri, P., Cencetti, F., Rapizzi, E., Farnararo, M., & Bruni, P. (2007). Tumor necrosis factor-α exerts pro-myogenic action in C2C12 myoblasts via sphingosine kinase/S1P2 signaling. *FEBS Letters*, *581*(23), 4384–4388. https://doi.org/10.1016/j.febslet.2007.08.007

Duan, L., Fischer, A., Xu, Y., & Sun, L. (2009). *Isolated Seven-Coordinate Ru (IV) Dimer Complex with [HOHOH] - Bridging Ligand as an Intermediate for Catalytic Water Oxidation*. *Iv*, 10397–10399.

Duska, L. R., Hamblin, M. R., Miller, J. L., & Hasan, T. (1999). Combination photoimmunotherapy and cisplatin: Effects on human ovarian cancer ex vivo. *Journal of the National Cancer Institute*, *91*(18), 1557–1563. https://doi.org/10.1093/jnci/91.18.1557

El Mechoulam, R. :, Ben-Shabat, S., Hanus, L., Ligumsky, M., Kaminski, N. E., Schatz, A. R., Gopher, A., Almog, S., Martin, B. R., Compton, D. R., Pertwee, R. G., Griffin, G., Bayewitch, M., Barg, J., & Vogel, Z. (1995). IDENTIFICATION OF AN ENDOGENOUS 2-MONOGLYCERIDE, PRESENT IN CANINE GUT, THAT BINDS TO CANNABINOID RECEPTORS. *Biochemical Pharmacology*, *50*(1), 83–90.

Fasia, L., Karava, V., & Siafaka-Kapadai, A. (2003). Uptake and metabolism of [3H]anandamide by rabbit platelets: Lack of transporter? *European Journal of Biochemistry*, *270*(17), 3498–3506. https://doi.org/10.1046/j.1432-1033.2003.03724.x

Felder, C. C., Joyce, K. E., Briley, E. M., Mansouri, J., Mackie, K., Blond, O., Lai, Y., Ma, A. L., & Mitchell, R. L. (1995). Comparison of the Pharmacology and Signal Transduction of the Human Cannabinoid CB1 and CB2 Receptors. In *MOLECULAR PHARMACOLOGY* (Vol. 48).

Ferdowsi, P. V., Ahuja, K. D. K., Beckett, J. M., & Myers, S. (2021). TRPV1 activation by capsaicin mediates glucose oxidation and ATP production independent of insulin signalling in mouse skeletal muscle cells. *Cells*, *10*(6). https://doi.org/10.3390/cells10061560

Fezza, F., Bari, M., Florio, R., Talamonti, E., Feole, M., & Maccarrone, M. (2014). Endocannabinoids, related compounds and their metabolic routes. In *Molecules* (Vol. 19, Issue 11, pp. 17078–17106). MDPI AG. https://doi.org/10.3390/molecules191117078

Frontera, W. R., & Ochala, J. (2015). Skeletal Muscle: A Brief Review of Structure and

Function. *Behavior Genetics*, *45*(2), 183–195. https://doi.org/10.1007/s00223-014-9915-y

Fry, C. S., Lee, J. D., Mula, J., Kirby, T. J., Jackson, J. R., Liu, F., Yang, L., Mendias, C. L., Dupont-Versteegden, E. E., McCarthy, J. J., & Peterson, C. A. (2015). Inducible depletion of satellite cells in adult, sedentary mice impairs muscle regenerative capacity without affecting sarcopenia. *Nature Medicine*, *21*(1), 76–80. https://doi.org/10.1038/nm.3710

Fu, J., Bottegoni, G., Sasso, O., Bertorelli, R., Rocchia, W., Masetti, M., Guijarro, A., Lodola, A., Armirotti, A., Garau, G., Bandiera, T., Reggiani, A., Mor, M., Cavalli, A., & Piomelli, D. (2012). A catalytically silent FAAH-1 variant drives anandamide transport in neurons. *Nature Neuroscience*, *15*(1), 64–69. https://doi.org/10.1038/nn.2986

Fugio, L. B., Coeli-Lacchini, F. B., & Leopoldino, A. M. (2020). Sphingolipids and Mitochondrial Dynamic. *Cells*, *9*(3). https://doi.org/10.3390/cells9030581

Galbiati, F., Volonté, D., Engelman, J. A., Scherer, P. E., & Lisanti, M. P. (1999). Targeted Down-regulation of Caveolin-3 Is Sufficient to Inhibit Myotube Formation in Differentiating C2C12 Myoblasts. *The Journal of Biological Chemistry*, *274*(42), 30315–30321. http://www.jbc.org

Galve-Rophert, I., Sánchez, C., Cortés, M. L., Gomez del Pulgar, T., Izquierdo, M., & Guzman, M. (2000). *Anti-tumoral action*. *2*, 313–319. https://www-nature-com.e.bibl.liu.se/articles/nm0300_313.pdf

Gasperi, V., Dainese, E., Oddi, S., Sabatucci, A., & Maccarrone, M. (2013). GPR55 and its Interaction with Membrane Lipids: Comparison with Other Endocannabinoid-Binding Receptors. In *Current Medicinal Chemistry* (Vol. 20).

Gasperi, V., Fezza, F., Pasquariello, N., Bari, M., Oddi, S., Finazzi Agrò, A., & Maccarrone, M. (2007). Endocannabinoids in adipocytes during differentiation and their role in glucose uptake. *Cellular and Molecular Life Sciences*, *64*(2), 219–229. https://doi.org/10.1007/s00018-006-6445-4

Gecibesler, Ý. H., Dayan, O., & Demirtas, Ý. (2020). *ANTIOXIDANT ACTIVITY OF RUTHENIUM (II) COMPLEXES CONTAINING TRIDENTATE TRIAMINES AND THEIR CAPABILITY TO INHIBIT XANTHINE OXIDASE*. *53*(10), 914–920. https://doi.org/10.1007/s11094-020-02099-w

Geddo, F., Antoniotti, S., Querio, G., Salaroglio, I. C., Costamagna, C., Riganti, C., & Gallo, M.

P. (2021). Plant-derived trans-β-caryophyllene boosts glucose metabolism and atp synthesis in skeletal muscle cells through cannabinoid type 2 receptor stimulation. *Nutrients*, *13*(3), 1–14. https://doi.org/10.3390/nu13030916

Gehrmann, M., Liebisch, G., Schmitz, G., Anderson, R., Steinem, C., De Maio, A., Pockley, G., & Multhoff, G. (2008). Tumor-specific Hsp70 plasma membrane localization is enabled by the glycosphingolipid Gb3. *PLoS ONE*, *3*(4). https://doi.org/10.1371/journal.pone.0001925

Germinario, E., Bondì, M., Cencetti, F., Donati, C., Nocella, M., Colombini, X. B., Betto, R., Bruni, P., Bagni, M. A., & Danieli-betto, D. (2024). *S1P 3 receptor influences key physiological properties of fast-twitch extensor digitorum longus muscle*. 4(58), 1288–1300. https://doi.org/10.1152/japplphysiol.00345.2015

Germinario, E., Peron, S., Toniolo, L., Betto, R., Cencetti, F., Donati, C., Bruni, P., Danieli-betto, D., Bruni, P., & Sp, D. D. (2024). *S1P 2 receptor promotes mouse skeletal muscle regeneration.* 3, 707–713. https://doi.org/10.1152/japplphysiol.00300.2012

Ghosh, T. K., Bian, J., & Gill, D. L. (1994). Sphingosine 1-phosphate generated in the endoplasmic reticulum membrane activates release of stored calcium. *Journal of Biological Chemistry*, *269*(36), 22628–22635. https://doi.org/10.1016/s0021-9258(17)31692-7

Giacomazzo, G. E., Schlich, M., Casula, L., Galantini, L., Del Giudice, A., Pietraperzia, G., Sinico, C., Cencetti, F., Pecchioli, S., Valtancoli, B., Conti, L., Murgia, S., & Giorgi, C. (2023). Ruthenium(ii) polypyridyl complexes with π-expansive ligands: synthesis and cubosome encapsulation for photodynamic therapy of non-melanoma skin cancer. *Inorganic Chemistry Frontiers*, *10*(10), 3025–3036. https://doi.org/10.1039/d2qi02678c

Giuffrida, A., Rodríguez De Fonseca, F., & Piomelli, D. (2000). Quantification of bioactive acylethanolamides in rat plasma by electrospray mass spectrometry. *Analytical Biochemistry*, *280*(1), 87–93. https://doi.org/10.1006/abio.2000.4509

Glanemann, C., Loos, A., Gorret, N., Willis, L. B., O'Brien, X. M., Lessard, P. A., & Sinskey, A. J. (2003). Disparity between changes in mRNA abundance and enzyme activity in Corynebacterium glutamicum: Implications for DNA microarray analysis. *Applied Microbiology and Biotechnology*, *61*(1), 61–68. https://doi.org/10.1007/s00253-002-1191-5

Glaser, S. T., Abumrad, N. A., Fatade, F., Kaczocha, M., Studholme, K. M., & Deutsch, D. G. (2003). *Evidence against the presence of an anandamide transporter* (Vol. 100, Issue 7). PNAS. www.pnas.orgcgidoi10.1073pnas.0730816100

Goff, B. A., Blake, J., Bamberg, M. P., & Hasan, T. (1996). Treatment of ovarian cancer with photodynamic therapy and immunoconjugates in a murine ovarian cancer model. *British Journal of Cancer*, *74*(8), 1194–1198. https://doi.org/10.1038/bjc.1996.516

Gonsiorek, W., Lunn, C., Fan, X., Narula, S., Lundell, D., & Hipkin, R. W. (2000). *Endocannabinoid 2-Arachidonyl Glycerol Is a Full Agonist through Human Type 2 Cannabinoid Receptor: Antagonism by Anandamide*. http://www.molpharm.org

González-Mariscal, I., Krzysik-Walker, S. M., Doyle, M. E., Liu, Q. R., Cimbro, R., Santa-Cruz Calvo, S., Ghosh, S., Cieala, A., Moaddel, R., Carlson, O. D., Witek, R. P., O'Connell, J. F., & Egan, J. M. (2016). Human CB1 Receptor Isoforms, present in Hepatocytes and β-cells, are Involved in Regulating Metabolism. *Scientific Reports*, *6*. https://doi.org/10.1038/srep33302

González-Mariscal, I., Montoro, R. A., O'Connel, J. F., Kim, Y., Gonzalez-Freire, M., Liu, Q. R., Alfaras, I., Carlson, O. D., Lehrmann, E., Zhang, Y., Becker, K. G., Hardivillé, S., Ghosh, P., & Egan, J. M. (2019). Muscle cannabinoid 1 receptor regulates Il-6 and myostatin expression, governing physical performance and whole-body metabolism. *FASEB Journal*, *33*(5), 5850–5863. https://doi.org/10.1096/fj.201801145R

Griffin, L. L., & Lear, J. T. (2016). Photodynamic therapy and non-melanoma skin cancer. *Cancers*, *8*(10). https://doi.org/10.3390/cancers8100098

Hait, N. C., Allegood, J., Maceyka, M., Strub, G. M., Harikumar, K. B., Singh, S. K., Luo, C., Marmorstein, R., Kordula, T., Milstien, S., & Spiegel, S. (2009). Regulation of histone acetylation in the nucleus by sphingosine-1-phosphate. *Science*, *325*(5945), 1254–1257. https://doi.org/10.1126/science.1176709

Hannun, Y. A., & Obeid, L. M. (2008). Principles of bioactive lipid signalling: Lessons from sphingolipids. In *Nature Reviews Molecular Cell Biology* (Vol. 9, Issue 2, pp. 139–150). https://doi.org/10.1038/nrm2329

Hebert-Chatelain, E., Reguero, L., Puente, N., Lutz, B., Chaouloff, F., Rossignol, R., Piazza, P. V., Benard, G., Grandes, P., & Marsicano, G. (2014). Cannabinoid control of brain bioenergetics: Exploring the subcellular localization of the CB1 receptor. *Molecular*

Metabolism, *3*(4), 495–504. https://doi.org/10.1016/j.molmet.2014.03.007

Hemmings, D. G., Xu, Y., & Davidge, S. T. (2004). Sphingosine 1-phosphate-induced vasoconstriction is elevated in mesenteric resistance arteries from aged female rats. *British Journal of Pharmacology*, *143*(2), 276–284. https://doi.org/10.1038/sj.bjp.0705752

Hermann, A., Kaczocha, M., & Deutsch, D. G. (2006). 2-Arachidonoylglycerol (2-AG) Membrane Transport: History and Outlook. *The AAPS Journal*, *8*(2), 409–412. http://www.aapsj.org

Herzberg, N. H., Zwart, R., Wolterman, R. A., Ruiter, J. P. N., Wanders, R. J. A., Bolhuis, P. A., & van den Bogert, C. (1993). Differentiation and proliferation of respiration-deficient human myoblasts. *BBA - Molecular Basis of Disease*, *1181*(1), 63–67. https://doi.org/10.1016/0925-4439(93)90091-E

Howlett, A C, Barth, F., Bonner, T. I., Cabral, G., Casellas, P., Devane, W. A., Felder, C. C., Herkenham, M., Mackie, K., Martin, B. R., Mechoulam, R., & Pertwee, R. G. (2002). International Union of Pharmacology. XXVII. Classification of Cannabinoid Receptors. *Pharmacological Reviews*, *54*(2), 161–202. http://pharmrev.aspetjournals.org

Howlett, Allyn C, Blume, L. C., & Dalton, G. D. (2010). CB 1 Cannabinoid Receptors and their Associated Proteins. In *Curr Med Chem* (Vol. 17, Issue 14).

Hughes, S. M., Chi, M. M. Y., Lowry, O. H., & Gundersen, K. (1999). Myogenin induces a shift of enzyme activity from glycolytic to oxidative metabolism in muscles of transgenic mice. *Journal of Cell Biology*, *145*(3), 633–642. https://doi.org/10.1083/jcb.145.3.633

Iannotti, F. A., Barrese, V., Formisano, L., Miceli, F., & Taglialatela, M. (2013). Specification of skeletal muscle differentiation by repressor element-1 silencing transcription factor (REST)-regulated Kv7.4 potassium channels. *Molecular Biology of the Cell*, *24*(3), 274–284. https://doi.org/10.1091/mbc.E11-12-1044

Iannotti, F. A., Pagano, E., Guardiola, O., Adinolfi, S., Saccone, V., Consalvi, S., Piscitelli, F., Gazzerro, E., Busetto, G., Carrella, D., Capasso, R., Puri, P. L., Minchiotti, G., & Di Marzo, V. (2018). Genetic and pharmacological regulation of the endocannabinoid CB1 receptor in Duchenne muscular dystrophy. *Nature Communications*, *9*(1). https://doi.org/10.1038/s41467-018-06267-1

Iannotti, F. A., Pagano, E., Moriello, A. S., Alvino, F. G., Sorrentino, N. C., D'Orsi, L., Gazzerro,

E., Capasso, R., De Leonibus, E., De Petrocellis, L., & Di Marzo, V. (2019). Effects of non-euphoric plant cannabinoids on muscle quality and performance of dystrophic mdx mice. *British Journal of Pharmacology*, *176*(10), 1568–1584. https://doi.org/10.1111/bph.14460

Iannotti, F. A., Silvestri, C., Mazzarella, E., Martella, A., Calvigioni, D., Piscitelli, F., Ambrosino, P., Petrosino, S., Czifra, G., Bíŕo, T., Harkany, T., Taglialatela, M., & Di Marzo, V. (2014). The endocannabinoid 2-AG controls skeletal muscle cell differentiation via CB1 receptor-dependent inhibition of Kv7 channels. *Proceedings of the National Academy of Sciences of the United States of America*, *111*(24). https://doi.org/10.1073/pnas.1406728111

Imberti, C., Zhang, P., Huang, H., & Sadler, P. J. (2020). New Designs for Phototherapeutic Transition Metal Complexes. *Angewandte Chemie - International Edition*, *59*(1), 61–73. https://doi.org/10.1002/anie.201905171

Iredale, P. A., & Dickenson, J. M. (n.d.). *Measurement of Intracellular Free Calcium Ion Concentration in Cell Populations Using Fura*.

Jiang, P., Wang, L., Zhang, M., Zhang, M., Wang, C., Zhao, R., & Guan, D. (2020). Cannabinoid type 2 receptor manipulates skeletal muscle regeneration partly by regulating macrophage M1/M2 polarization in IR injury in mice. *Life Sciences*, *256*. https://doi.org/10.1016/j.lfs.2020.117989

Jiwlawat, N., Lynch, E., Jeffrey, J., Van Dyke, J. M., & Suzuki, M. (2018). Current progress and challenges for skeletal muscle differentiation from human pluripotent stem cells using transgene-free approaches. In *Stem Cells International* (Vol. 2018). Hindawi Limited. https://doi.org/10.1155/2018/6241681

Kaczocha, M., Glaser, S. T., & Deutsch, D. G. (2009). Identification of intracellular carriers for the endocannabinoid anandamide. *Proceedings of the National Academy of Sciences of the United States of America*, *106*(15), 6375–6380. www.pnas.org/cgi/content/full/

Kaczocha, M., & Haj-Dahmane, S. (2021). Mechanisms of endocannabinoid transport in the brain. In *British Journal of Pharmacology*. John Wiley and Sons Inc. https://doi.org/10.1111/bph.15469

Kaspler, P., Lazic, S., Forward, S., Arenas, Y., Mandel, A., & Lilge, L. (2016). A ruthenium(II) based photosensitizer and transferrin complexes enhance photo-physical properties,

cell uptake, and photodynamic therapy safety and efficacy. *Photochemical and Photobiological Sciences*, *15*(4), 481–495. https://doi.org/10.1039/c5pp00450k

Khan, N. H., Mir, M., Qian, L., Baloch, M., Ali Khan, M. F., Rehman, A. ur, Ngowi, E. E., Wu, D. D., & Ji, X. Y. (2022). Skin cancer biology and barriers to treatment: Recent applications of polymeric micro/nanostructures. *Journal of Advanced Research*, *36*, 223–247. https://doi.org/10.1016/j.jare.2021.06.014

Kharkwal, G. B., Sharma, S. K., Huang, Y. Y., Dai, T., & Hamblin, M. R. (2011). Photodynamic therapy for infections: Clinical applications. *Lasers in Surgery and Medicine*, *43*(7), 755–767. https://doi.org/10.1002/lsm.21080

Kittaka, H., DeBrecht, J., & Mishra, S. K. (2020). Differential contribution of sensory transient receptor potential channels in response to the bioactive lipid sphingosine-1-phosphate. *Molecular Pain*, *16*. https://doi.org/10.1177/1744806920903515

Kurosaka, M., Ogura, Y., Funabashi, T., & Akema, T. (2016). Involvement of Transient Receptor Potential Cation Channel Vanilloid 1 (TRPV1) in Myoblast Fusion. *Journal of Cellular Physiology*, *231*(10), 2275–2285. https://doi.org/10.1002/jcp.25345

Kwiatkowski, S., Knap, B., Przystupski, D., Saczko, J., Kędzierska, E., Knap-Czop, K., Kotlińska, J., Michel, O., Kotowski, K., & Kulbacka, J. (2018). Photodynamic therapy – mechanisms, photosensitizers and combinations. *Biomedicine and Pharmacotherapy*, *106*(July), 1098–1107. https://doi.org/10.1016/j.biopha.2018.07.049

Kwon, H. S., & Koh, S. H. (2020). Neuroinflammation in neurodegenerative disorders: the roles of microglia and astrocytes. *Translational Neurodegeneration*, *9*(1), 1–12. https://doi.org/10.1186/s40035-020-00221-2

Le Stunff, H., Giussani, P., Maceyka, M., Lépine, S., Milstien, S., & Spiegel, S. (2007). Recycling of sphingosine is regulated by the concerted actions of sphingosine-1-phosphate phosphohydrolase 1 and sphingosine kinase 2. *Journal of Biological Chemistry*, *282*(47), 34372–34380. https://doi.org/10.1074/jbc.M703329200

Leung, D., Saghatelian, A., Simon, G. M., & Cravatt, B. F. (2006). Inactivation of N-Acyl Phosphatidylethanolamine Phospholipase D Reveals Multiple Mechanisms for the Biosynthesis of Endocannabinoids † NIH Public Access. *Biochemistry*, *45*(15), 4720–4726. http://pubs.acs.org.

Liang, H., & Ward, W. F. (2006). PGC-1α: A key regulator of energy metabolism. *American*

Journal of Physiology - Advances in Physiology Education, *30*(4), 145–151. https://doi.org/10.1152/advan.00052.2006

Liedhegner, E. S., Vogt, C. D., Sem, D. S., Cunningham, C. W., & Hillard, C. J. (2014). Sterol Carrier Protein-2: Binding Protein for Endocannabinoids. *Molecular Neurobiology*, *50*(1), 149–158. https://doi.org/10.1007/s12035-014-8651-7

Lin, K., Zhao, Z., Bo, H., Hao, X., Wang, J., & Wang, J. (2018). *Applications of Ruthenium Complex in Tumor Diagnosis and Therapy*. *9*(November), 1–10. https://doi.org/10.3389/fphar.2018.01323

Lipina, C., Irving, A. J., & Hundal, H. S. (2014). Mitochondria: A possible nexus for the regulation of energy homeostasis by the endocannabinoid system? *American Journal of Physiology - Endocrinology and Metabolism*, *307*(1). https://doi.org/10.1152/ajpendo.00100.2014

Lipina, C., Walsh, S. K., Mitchell, S. E., Speakman, J. R., Wainwright, C. L., & Hundal, H. S. (2019). GPR55 deficiency is associated with increased adiposity and impaired insulin signaling in peripheral metabolic tissues. *FASEB Journal*, *33*(1), 1299–1312. https://doi.org/10.1096/fj.201800171R

Liu, J., Wang, L., Harvey-White, J., Huang, B. X., Kim, H.-Y., Luquet, S., Palmiter, R. D., Krystal, G., Rai, R., Mahadevan, A., Razdan, R. K., & Kunos, G. (2008). Multiple Pathways Involved in the Biosynthesis of Anandamide. *Neuropharmacology*, *54*(1), 1–7.

Liu, Q. R., Pan, C. H., Hishimoto, A., Li, C. Y., Xi, Z. X., Llorente-Berzal, A., Viveros, M. P., Ishiguro, H., Arinami, T., Onaivi, E. S., & Uhl, G. R. (2009). Species differences in cannabinoid receptor 2 (CNR2 gene): Identification of novel human and rodent CB2 isoforms, differential tissue expression and regulation by cannabinoid receptor ligands. *Genes, Brain and Behavior*, *8*(5), 519–530. https://doi.org/10.1111/j.1601-183X.2009.00498.x

Liu, R., Gao, Y., Liu, N., & Suo, Y. (2021). Nanoparticles loading porphyrin sensitizers in improvement of photodynamic therapy for ovarian cancer. *Photodiagnosis and Photodynamic Therapy*, *33*, 102156. https://doi.org/10.1016/j.pdpdt.2020.102156

Liu, Y. L., Connoley, I. P., Wilson, C. A., & Stock, M. J. (2005). Effects of the cannabinoid CB1 receptor antagonist SR141716 on oxygen consumption and soleus muscle glucose uptake in Lepob/Lep ob mice. *International Journal of Obesity*, *29*(2), 183–187.

https://doi.org/10.1038/sj.ijo.0802847

Livak, K. J., & Schmittgen, T. D. (2001). Analysis of relative gene expression data using real-time quantitative PCR and the 2-ΔΔCT method. *Methods*, *25*(4), 402–408. https://doi.org/10.1006/meth.2001.1262

Loh, K. C., Leong, W. I., Carlson, M. E., Oskouian, B., Kumar, A., Fyrst, H., Zhang, M., Proia, R. L., Hoffman, E. P., & Saba, J. D. (2012). Sphingosine-1-phosphate enhances satellite cell activation in dystrophic muscles through a S1PR2/STAT3 signaling pathway. *PLoS ONE*, *7*(5). https://doi.org/10.1371/journal.pone.0037218

Lotteau, S., Ducreux, S., Romestaing, C., Legrand, C., & Van Coppenolle, F. (2013). Characterization of Functional TRPV1 Channels in the Sarcoplasmic Reticulum of Mouse Skeletal Muscle. *PLoS ONE*, *8*(3). https://doi.org/10.1371/journal.pone.0058673

Lowe, H., Toyang, N., Steele, B., Bryant, J., & Ngwa, W. (2021). The endocannabinoid system: A potential target for the treatment of various diseases. In *International Journal of Molecular Sciences* (Vol. 22, Issue 17). MDPI. https://doi.org/10.3390/ijms22179472

Luo, Z., Ma, L., Zhao, Z., He, H., Yang, D., Feng, X., Ma, S., Chen, X., Zhu, T., Cao, T., Liu, D., Nilius, B., Huang, Y., Yan, Z., & Zhu, Z. (2012). TRPV1 activation improves exercise endurance and energy metabolism through PGC-1α upregulation in mice. *Cell Research*, *22*(3), 551–564. https://doi.org/10.1038/cr.2011.205

Maccarrone, M. (2017). Metabolism of the endocannabinoid anandamide: Open questions after 25 years. *Frontiers in Molecular Neuroscience*, *10*. https://doi.org/10.3389/fnmol.2017.00166

Maccarrone, M. (2021). Chapter 1: Quest for Magic Bullets to Solve the Endocannabinoid Puzzle. In *RSC Drug Discovery Series* (Vols. 2021-January, Issue 76, pp. 1–9). Royal Society of Chemistry. https://doi.org/10.1039/9781839160752-00001

Maccarrone, M., Dainese, E., & Oddi, S. (2010). Intracellular trafficking of anandamide: new concepts for signaling. *Trends in Biochemical Sciences*, *35*(11), 601–608. https://doi.org/10.1016/j.tibs.2010.05.008

Maceyka, M., Harikumar, K. B., Milstien, S., & Spiegel, S. (2012). Sphingosine-1-phosphate signaling and its role in disease. In *Trends in Cell Biology* (Vol. 22, Issue 1, pp. 50–60). https://doi.org/10.1016/j.tcb.2011.09.003

Mackie, K. (2005). Distribution of Cannabinoid Receptors in the Central and Peripheral

Nervous System. In *HEP* (Vol. 168). Springer-Verlag.

Mair, K. M., Robinson, E., Kane, K. A., Pyne, S., Brett, R. R., Pyne, N. J., & Kennedy, S. (2010). Interaction between anandamide and sphingosine-1-phosphate in mediating vasorelaxation in rat coronary artery. *British Journal of Pharmacology*, *161*(1), 176–192. https://doi.org/10.1111/j.1476-5381.2010.00878.x

Mandard, S., Müller, M., & Kersten, S. (2004). Peroxisome proliferator-activated receptor α target genes. In *Cellular and Molecular Life Sciences* (Vol. 61, Issue 4, pp. 393–416). https://doi.org/10.1007/s00018-003-3216-3

Martin, S., & Parton, R. G. (2006). Late endosome. *Nature Reviews, Molecular Cell Biology*, *7*, 373–378. www.nature.com/reviews/molcellbio

Matsuda, L. A., Lolait, S. J., Brownstein, M. J., Young, A. C., & Bonner, T. I. (1990). *Structure of a cannabinoid receptor and functional expression of the cloned eDNA*.

Mccarthy, J. J., Mula, J., Miyazaki, M., Erfani, R., Garrison, K., Farooqui, A. B., Srikuea, R., Lawson, B. A., Grimes, B., Keller, C., Van Zant, G., Campbell, K. S., Esser, K. A., Dupont-Versteegden, E. E., & Peterson, C. A. (2011). Effective fiber hypertrophy in satellite cell-depleted skeletal muscle. *Development and Stem Cells*, *138*(17), 3657–3666. https://doi.org/10.1242/dev.068858

McCudden, C. R., Hains, M. D., Kimple, R. J., Siderovski, D. P., & Willard, F. S. (2005). G-protein signaling: Back to the future. In *Cellular and Molecular Life Sciences* (Vol. 62, Issue 5, pp. 551–577). https://doi.org/10.1007/s00018-004-4462-3

McFarland, M. J., & Barker, E. L. (2004). Anandamide transport. In *Pharmacology and Therapeutics* (Vol. 104, Issue 2, pp. 117–135). https://doi.org/10.1016/j.pharmthera.2004.07.008

Meacci, E., Cencetti, F., Donati, C., Nuti, F., Farnararo, M., Kohno, T., Igarashi, Y., & Bruni, P. (2003). Down-regulation of EDG5/S1P2 during myogenic differentiation results in the specific uncoupling of sphingosine 1-phosphate signalling to phospholipase D. *Biochimica et Biophysica Acta - Molecular and Cell Biology of Lipids*, *1633*(3), 133–142. https://doi.org/10.1016/S1388-1981(03)00106-9

Meacci, E., Cencetti, F., Formigli, L., Squecco, R., Donati, C., Tiribilli, B., Quercioli, F., Zecchi Orlandini, S., Francini, F., & Bruni, P. (2002). Sphingosine 1-phosphate evokes calcium signals in C 2 C 12 myoblasts via Edg3 and Edg5 receptors. In *Biochem. J* (Vol. 362).

Meacci, E., Nuti, F., Donati, C., Cencetti, F., Farnararo, M., & Bruni, P. (2008). Sphingosine kinase activity is required for myogenic differentiation of C2C12 myoblasts. *Journal of Cellular Physiology*, *214*(1), 210–220. https://doi.org/10.1002/jcp.21187

Meyer Zu Heringdorf, D. (2004). Lysophospholipid receptor-dependent and -independent calcium signaling. *Journal of Cellular Biochemistry*, *92*(5), 937–948. https://doi.org/10.1002/jcb.20107

Meyer Zu Heringdorf, D., Liliom, K., Schaefer, M., Danneberg, K., Jaggar, J. H., Tigyi, G., & Jakobs, K. H. (2003). Photolysis of intracellular caged sphingosine-1-phosphate causes Ca 2+ mobilization independently of G-protein-coupled receptors. *FEBS Letters*, *554*(3), 443–449. https://doi.org/10.1016/S0014-5793(03)01219-5

Michalik, L., Auwerx, J., Berger, J. P., Chatterjee, V. K., Glass, C. K., Gonzalez, F. J., Grimaldi, P. A., Kadowaki, T., Lazar, M. A., O'Rahilly, S., Palmer, C. N. A., Plutzky, J., Reddy, J. K., Spiegelman, B. M., Staels, B., & Wahli, W. (2006). International union of pharmacology. LXI. Peroxisome proliferator-activated receptors. In *Pharmacological Reviews* (Vol. 58, Issue 4, pp. 726–741). https://doi.org/10.1124/pr.58.4.5

Mikuła, J., Anna, P., Martyna, W., Paweł, P., Beata, U., & Krasińska, B. (2019). Comprehensive review on how platinum - and taxane - based chemotherapy of ovarian cancer affects biology of normal cells. *Cellular and Molecular Life Sciences*, *76*(4), 681–697. https://doi.org/10.1007/s00018-018-2954-1

Minchinton, A. I., & Tannock, I. F. (2006). *Drug penetration in solid tumours*. *6*(August), 583–592. https://doi.org/10.1038/nrc1893

Mohapatra, D. P., & Nau, C. (2005). Regulation of Ca2+-dependent desensitization in the vanilloid receptor TRPV1 by calcineurin and cAMP-dependent protein kinase. *Journal of Biological Chemistry*, *280*(14), 13424–13432. https://doi.org/10.1074/jbc.M410917200

Morciano, G., Marchi, S., Morganti, C., Sbano, L., Bittremieux, M., Kerkhofs, M., Corricelli, M., Danese, A., Karkucinska-Wieckowska, A., Wieckowski, M. R., Bultynck, G., Giorgi, C., & Pinton, P. (2018). Role of Mitochondria-Associated ER Membranes in Calcium Regulation in Cancer-Specific Settings. *Neoplasia (United States)*, *20*(5), 510–523. https://doi.org/10.1016/j.neo.2018.03.005

Moriello, A. S., & De Petrocellis, L. (2016). Assay of TRPV1 receptor signaling. In *Methods in Molecular Biology* (Vol. 1412, pp. 65–76). Humana Press Inc.

https://doi.org/10.1007/978-1-4939-3539-0_7

Morton, C. A., Szeimies, R. M., Sidoroff, A., & Braathen, L. R. (2013). European guidelines for topical photodynamic therapy part 1: Treatment delivery and current indications - Actinic keratoses, Bowen's disease, basal cell carcinoma. *Journal of the European Academy of Dermatology and Venereology*, *27*(5), 536–544. https://doi.org/10.1111/jdv.12031

Mosqueira, M., Brinkmeier, H., & Jaimovich, E. (2021). Editorial: Calcium Homeostasis in Skeletal Muscle Function, Plasticity, and Disease. *Frontiers in Physiology*, *12*(March), 10–12. https://doi.org/10.3389/fphys.2021.671292

Movsesyan, V. A., Stoica, B. A., Yakovlev, A. G., & Knoblach, S. M. (2004). *Anandamide-induced cell death in primary neuronal cultures : role of calpain and caspase pathways*. 1121–1132. https://doi.org/10.1038/sj.cdd.4401442

Mroz, P., Yaroslavsky, A., Kharkwal, G. B., & Hamblin, M. R. (2011). Cell death pathways in photodynamic therapy of cancer. *Cancers*, *3*(2), 2516–2539. https://doi.org/10.3390/cancers3022516

Munro, S., Thomas, K. L., & Abu·Shaar, M. (1993). Molecular characterization of a peripheral receptor for cannabinoids. *Nature*, *365*, 61–65.

Nakane, S., Oka, S., Arai, S., Waku, K., Ishima, Y., Tokumura, A., & Sugiura, T. (2002). 2-Arachidonoyl-sn-glycero-3-phosphate, an arachidonic acid-containing lysophosphatidic acid: occurrence and rapid enzymatic conversion to 2-arachidonoyl-sn-glycerol, a cannabinoid receptor ligand, in rat brain. *Academic Press*, 51–58. www.academicpress.com

Nakano, D., & Machida, S. (2022). Mitochondrial fusion- and fission-related protein expression in the regulation of skeletal muscle mass. *Physiological Reports*, *10*(8), 1–8. https://doi.org/10.14814/phy2.15281

Nath, S., Pigula, M., Khan, A. P., Hanna, W., Ruhi, M. K., Dehkordy, F. M., Pushpavanam, K., Rege, K., Moore, K., Tsujita, Y., Conrad, C., Inci, F., Del Carmen, M. G., Franco, W., Celli, J. P., Demirci, U., Hasan, T., Huang, H. C., & Rizvi, I. (2020). Flow-induced shear stress confers resistance to carboplatin in an adherent three-dimensional model for ovarian cancer: A role for EGFR-targeted photoimmunotherapy informed by physical stress. *Journal of Clinical Medicine*, *9*(4). https://doi.org/10.3390/jcm9040924

Nguyen-Tran, D. H., Hait, N. C., Sperber, H., Qi, J., Fischer, K., Ieronimakis, N., Pantoja, M., Hays, A., Allegood, J., Reyes, M., Spiegel, S., & Ruohola-Baker, H. (2014). Molecular mechanism of sphingosine-1-phosphate action in Duchenne muscular dystrophy. *DMM Disease Models and Mechanisms*, *7*(1), 41–54. https://doi.org/10.1242/dmm.013631

Nilius, B., Owsianik, G., & Voets, T. (2008). Transient receptor potential channels meet phosphoinositides. *EMBO Journal*, *27*(21), 2809–2816. https://doi.org/10.1038/emboj.2008.217

Niphakis, M. J., Lum, K. M., Cognetta, A. B., Correia, B. E., Ichu, T. A., Olucha, J., Brown, S. J., Kundu, S., Piscitelli, F., Rosen, H., & Cravatt, B. F. (2015). A Global Map of Lipid-Binding Proteins and Their Ligandability in Cells. *Cell*, *161*(7), 1668–1680. https://doi.org/10.1016/j.cell.2015.05.045

Obi, S., Nakajima, T., Hasegawa, T., Nakamura, F., Sakuma, M., Toyoda, S., Tei, C., & Inoue, T. (2019). Heat induces myogenic transcription factors of myoblast cells via transient receptor potential vanilloid 1 (Trpv1). *FEBS Open Bio*, *9*(1), 101–113. https://doi.org/10.1002/2211-5463.12550

Oddi, S., Fezza, F., Pasquariello, N., D'Agostino, A., Catanzaro, G., De Simone, C., Rapino, C., Finazzi-Agrò, A., & Maccarrone, M. (2009). Molecular Identification of Albumin and Hsp70 as Cytosolic Anandamide-Binding Proteins. *Chemistry and Biology*, *16*(6), 624–632. https://doi.org/10.1016/j.chembiol.2009.05.004

Oddi, S., Fezza, F., Pasquariello, N., De Simone, C., Rapino, C., Dainese, E., Finazzi-Agrò, A., & Maccarrone, M. (2008). Evidence for the intracellular accumulation of anandamide in adiposomes. *Cellular and Molecular Life Sciences*, *65*(5), 840–850. https://doi.org/10.1007/s00018-008-7494-7

Okamoto, Y., Morishita, J., Tsuboi, K., Tonai, T., & Ueda, N. (2004). Molecular Characterization of a Phospholipase D Generating Anandamide and Its Congeners. *Journal of Biological Chemistry*, *279*(7), 5298–5305. https://doi.org/10.1074/jbc.M306642200

Owada, Y., Yoshimoto, T., & Kondo, H. (1996). Spatio-temporally differential expression of genes for three members of fatty acid binding proteins in developing and mature rat brains. In *Journal of Chemical Neuroanatomy* (Vol. 12).

Pandur, E., Varga, E., Tamási, K., Pap, R., Nagy, J., & Sipos, K. (2019). Effect of inflammatory

mediators lipopolysaccharide and lipoteichoic acid on iron metabolism of differentiated SH-SY5Y cells alters in the presence of BV-2 microglia. *International Journal of Molecular Sciences*, *20*(1). https://doi.org/10.3390/ijms20010017

Pasquariello, N., Catanzaro, G., Marzano, V., Amadio, D., Barcaroli, D., Oddi, S., Federici, G., Urbani, A., & Agro, A. F. (2009). *Characterization of the Endocannabinoid System in Human Neuronal Cells and Proteomic Analysis of*. *284*(43), 29413–29426. https://doi.org/10.1074/jbc.M109.044412

Pasquariello, N., Oddi, S., Malaponti, M., & Maccarrone, M. (2009). Chapter 17 Regulation of Gene Transcription and Keratinocyte Differentiation by Anandamide. In *Vitamins and Hormones* (1st ed., Vol. 81, Issue C). Elsevier Inc. https://doi.org/10.1016/S0083-6729(09)81017-0

Paugh, S. W., Cassidy, M. P., He, H., Milstien, S., Sim-Selley, L. J., Spiegel, S., & Selley, D. E. (2006). Sphingosine and its analog, the immunosuppressant 2-amino-2-(2-[4-octylphenyl]ethyl)-1,3-propanediol, interact with the CB1 cannabinoid receptor. *Molecular Pharmacology*, *70*(1), 41–50. https://doi.org/10.1124/mol.105.020552

Pertwee, R. G, Howlett, A. C., Abood, M. E., Alexander, S. P. H., Di Marzo, V., Elphick, M. R., Greasley, P. J., Hansen, H. S., Kunos, G., Mackie, K., Mechoulam, R., & Ross, R. A. (2010). International Union of Basic and Clinical Pharmacology. LXXIX. Cannabinoid receptors and their ligands: Beyond CB1 and CB2. *Pharmacological Reviews*, *62*(4), 588–631. https://doi.org/10.1124/pr.110.003004

Pertwee, Roger G. (1997). *Pharmacology of Cannabinoid CB1 and CB2 Receptors* (Vol. 74, Issue 2).

Pesta, D., & Gnaiger, E. (2012). High-resolution respirometry: OXPHOS protocols for human cells and permeabilized fibers from small biopsies of human muscle. *Methods in Molecular Biology*, *810*, 25–58. https://doi.org/10.1007/978-1-61779-382-0_3

Pitson, M. S. ., Moretti, P. A. B. ., Zebol, J. R. ., Lynn, H. E. ., Xia, P. ., Vadas, M. A. ., & Wattenberg, B. W. (2003). Activation of sphingosine kinase 1 by ERK1/2-mediated phosphorylation. *The EMBO Journal*, *22*(20), 5491–5500.

Pucci, M., Pasquariello, N., Battista, N., Di Tommaso, M., Rapino, C., Fezza, F., Zuccolo, M., Jourdain, R., Agrò, A. F., Breton, L., & Maccarrone, M. (2012). Endocannabinoids stimulate human melanogenesis via type-1 cannabinoid receptor. *Journal of Biological*

Chemistry, 287(19), 15466–15478. https://doi.org/10.1074/jbc.M111.314880

Pulli, I., Asghar, M. Y., Kemppainen, K., & Törnquist, K. (2018). Sphingolipid-mediated calcium signaling and its pathological effects. *Biochimica et Biophysica Acta - Molecular Cell Research*, *1865*(11), 1668–1677. https://doi.org/10.1016/j.bbamcr.2018.04.012

Rahman F, A., & Quadrilatero, J. (2023). Emerging role of mitophagy in myoblast differentiation and skeletal muscle remodeling. *Seminars in Cell and Developmental Biology*, *143*(November 2021), 54–65. https://doi.org/10.1016/j.semcdb.2021.11.026

Rapizzi, E., Donati, C., Cencetti, F., Nincheri, P., & Bruni, P. (2008). Sphingosine 1-phosphate differentially regulates proliferation of C2C12 reserve cells and myoblasts. *Molecular and Cellular Biochemistry*, *314*(1–2), 193–199. https://doi.org/10.1007/s11010-008-9780-y

Rapizzi, E., Donati, C., Cencetti, F., Pinton, P., Rizzuto, R., & Bruni, P. (2007). Sphingosine 1-phosphate receptors modulate intracellular Ca2+ homeostasis. *Biochemical and Biophysical Research Communications*, *353*(2), 268–274. https://doi.org/10.1016/j.bbrc.2006.12.010

Reddy, P. V, Natarajan, V., Schmid, P. C., & Schmid, H. H. O. (1983). N-ACYLATION OF DOG HEART ETHANOLAMINE PHOSPHOLIPIDS BY TRANSACYLASE ACTIVITY. In *Biochimica et Biophysics Acta* (Vol. 750).

Rhee, M. H., Bayewitch, M., Avidor-Reiss, T., Levy, R., & Vogel, Z. (1998). Cannabinoid receptor activation differentially regulates the various adenylyl cyclase isozymes. *Journal of Neurochemistry*, *71*(4), 1525–1534. https://doi.org/10.1046/j.1471-4159.1998.71041525.x

Rickard, B. P., Overchuk, M., Obaid, G., Ruhi, M. K., Demirci, U., Fenton, S. E., Santos, J. H., Kessel, D., & Rizvi, I. (2023). Photochemical Targeting of Mitochondria to Overcome Chemoresistance in Ovarian Cancer†. *Photochemistry and Photobiology*, *99*(2), 448–468. https://doi.org/10.1111/php.13723

Rizvi, I., Celli, P. J., Evans, L. C., Abu-Yousif, A., Muzikansky, A., Pogue, W. B., Finkelstein, D., & Hasan, T. (2010). Synergistic Enhancement of Carboplatin Efficacy with Photodynamic Therapy in a Three-dimensional Model for Micrometastatic Ovarian Cancer. *Cancer Res.*, *70*(22), 9319–9328. https://doi.org/10.1158/0008-5472.CAN-10-1783.Synergistic

Rkein, A. M., & Ozog, D. M. (2014). Photodynamic therapy. *Dermatologic Clinics*, *32*(3), 415–

425. https://doi.org/10.1016/j.det.2014.03.009

Rochard, P., Rodier, A., Casas, F., Cassar-Malek, I., Marchal-Victorion, S., Daury, L., Wrutniak, C., & Cabello, G. (2000). Mitochondrial activity is involved in the regulation of myoblast differentiation through myogenin expression and activity of myogenic factors. *Journal of Biological Chemistry*, *275*(4), 2733–2744. https://doi.org/10.1074/jbc.275.4.2733

Rockwell, C. E., Snider, N. T., Thompson, J. T., Vanden Heuvel, J. P., & Kaminski, N. E. (2006). Interleukin-2 suppression by 2-arachidonyl glycerol is mediated through peroxisome proliferator-activated receptor γ independently of cannabinoid receptors 1 and 2. *Molecular Pharmacology*, *70*(1), 101–111. https://doi.org/10.1124/mol.105.019117

Roett, M. A., & Evans, P. (2009). Ovarian cancer: An overview. *American Academy of Family Physicians*, *80*(6), 609–616.

Rosen, H., Gonzalez-Cabrera, P. J., Sanna, M. G., & Brown, S. (2009). Sphingosine 1-phosphate receptor signaling. In *Annual Review of Biochemistry* (Vol. 78, pp. 743–768). https://doi.org/10.1146/annurev.biochem.78.072407.103733

Roviezzo, F., Bucci, M., Delisle, C., Brancaleone, V., Lorenzo, A. Di, Mayo, I. P., Fiorucci, S., Fontana, A., Gratton, J., & Cirino, G. (2006). Expression of Concern: Essential requirement for sphingosine kinase activity in eNOS-dependent NO release and vasorelaxation. *The FASEB Journal*, *20*(2), 340–342. https://doi.org/10.1096/fj.05-4647fje

Ruiz de Azua, I., & Lutz, B. (2019). Multiple endocannabinoid-mediated mechanisms in the regulation of energy homeostasis in brain and peripheral tissues. In *Cellular and Molecular Life Sciences* (Vol. 76, Issue 7, pp. 1341–1363). Birkhauser Verlag AG. https://doi.org/10.1007/s00018-018-2994-6

Ryberg, E., Vu, H. K., Larsson, N., Groblewski, T., Hjorth, S., Elebring, T., Sjögren, S., & Greasley, P. J. (2005). Identification and characterisation of a novel splice variant of the human CB1 receptor. *FEBS Letters*, *579*(1), 259–264. https://doi.org/10.1016/j.febslet.2004.11.085

Salazar, H., Jara-Oseguera, A., Hernández-García, E., Llorente, I., Arias-Olguín, I. I., Soriano-García, M., Islas, L. D., & Rosenbaum, T. (2009). Structural determinants of gating in the TRPV1 channel. *Nature Structural and Molecular Biology*, *16*(7), 704–710. https://doi.org/10.1038/nsmb.1633

Sanchez, T., & Hla, T. (2004). Structural and functional characteristics of S1P receptors. *Journal of Cellular Biochemistry*, *92*(5), 913–922. https://doi.org/10.1002/jcb.20127

Sanson, B., Wang, T., Sun, J., Wang, L., Kaczocha, M., Ojima, I., Deutsch, D., & Li, H. (2014). Crystallographic study of FABP5 as an intracellular endocannabinoid transporter. *Acta Crystallographica Section D: Biological Crystallography*, *70*(2), 290–298. https://doi.org/10.1107/S1399004713026795

Savinainen, J. R., Jaè, T., Laine, K., & Laitinen, J. T. (2001). Despite substantial degradation, 2-arachidonoylglycerol is a potent full ecacy agonist mediating CB 1 receptor-dependent G-protein activation in rat cerebellar membranes. In *British Journal of Pharmacology* (Vol. 134). www.nature.com/bjp

Sawzdargo, M., Nguyen, T., Lee, D. K., Lynch, K. R., Cheng, R., Heng, H. H. Q., George, S. R., & O'dowd, B. F. (1999). Identification and cloning of three novel human G protein-coupled receptor genes GPR52, CGPR53 and GPR55: GPR55 is extensively expressed in human brain 1. *Molecular Brain Research*, *64*, 193–198.

Sergi, M., Montesano, C., Napoletano, S., Pizzoni, D., Manetti, C., Colistro, F., Curini, R., & Compagnone, D. (2012). Analysis of bile acids profile in human serum by ultrafiltration clean-up and LC-MS/MS. *Chromatographia*, 75(9–10), 479–489. https://doi.org/10.1007/s10337-012-2218-4

Shen, T., Liu, Y., Randall, W. R., & Schneider, M. F. (2006). Parallel mechanisms for resting nucleo-cytoplasmic shuttling and activity dependent translocation provide dual control of transcriptional regulators HDAC and NFAT in skeletal muscle fiber type plasticity. *Journal of Muscle Research and Cell Motility*, *27*(5–7), 405–411. https://doi.org/10.1007/s10974-006-9080-7

Schmidt, M., Schüler, S. C., Hüttner, S. S., von Eyss, B., & von Maltzahn, J. (2019). Adult stem cells at work: regenerating skeletal muscle. *Cellular and Molecular Life Sciences*, *76*(13), 2559–2570. https://doi.org/10.1007/s00018-019-03093-6

Shire, D., Carillon, C., Kaghad, M., Calandra, B., Rinaldi-Carmona, M., Le Fur, G., Caput, D., & Ferrara, P. (1995). An Amino-terminal Variant of the Central Cannabinoid ReceptorResulting from Alternative Splicing. *The Journal of Biological Chemistry*, *270*(8), 3726–3731.

Siehler, S., & Manning, D. R. (2002). Pathways of transduction engaged by sphingosine 1-

phosphate through G protein-coupled receptors. *Biochemica et Biophysica Acta*, 94–99. www.bba-direct.com

Simon, G. M., & Cravatt, B. F. (2006). Endocannabinoid biosynthesis proceeding through glycerophospho-N-acyl ethanolamine and a role for α/β-hydrolase 4 in this pathway. *Journal of Biological Chemistry*, *281*(36), 26465–26472. https://doi.org/10.1074/jbc.M604660200

Singh, A., Kukreti, R., Saso, L., & Kukreti, S. (2019). Oxidative stress: A key modulator in neurodegenerative diseases. *Molecules*, *24*(8), 1–20. https://doi.org/10.3390/molecules24081583

Singh, K., & Dilworth, F. J. (2013). Differential modulation of cell cycle progression distinguishes members of the myogenic regulatory factor family of transcription factors. *FEBS Journal*, *280*(17), 3991–4003. https://doi.org/10.1111/febs.12188

Singh, P., & Sharma, B. (2016). Reversal in Cognition Impairments, Cholinergic Dysfunction, and Cerebral Oxidative Stress Through the Modulation of Ryanodine Receptors (RyRs) and Cysteinyl Leukotriene-1 (CysLT1) Receptors. *Current Neurovascular Research*, *13*(1), 10–21. https://doi.org/10.2174/1567202612666151026105610

Soleimani, V. D., Punch, V. G., Kawabe, Y. ichi, Jones, A. E., Palidwor, G. A., Porter, C. J., Cross, J. W., Carvajal, J. J., Kockx, C. E. M., van IJcken, W. F. J., Perkins, T. J., Rigby, P. W. J., Grosveld, F., & Rudnicki, M. A. (2012). Transcriptional Dominance of Pax7 in Adult Myogenesis Is Due to High-Affinity Recognition of Homeodomain Motifs. *Developmental Cell*, *22*(6), 1208–1220. https://doi.org/10.1016/j.devcel.2012.03.014

Sperandio, F. F., Huang, Y.-Y., & Hamblin, M. R. (2013). Antimicrobial Photodynamic Therapy to Kill Gram-negative Bacteria. *Recent Pat Antiinfect Drug Discov*, *8*(2), 108–120.

Spiegel, S., & Milstien, S. (2003). Sphingosine-1-phosphate: An enigmatic signalling lipid. In *Nature Reviews Molecular Cell Biology* (Vol. 4, Issue 5, pp. 397–407). https://doi.org/10.1038/nrm1103

Standoli, S., Pecchioli, S., Tortolani, D., Di Meo, C., Fanti, F., Sergi, M., Bacci, M., Seidita, I., Bernacchioni, C., Donati, C., Bruni, P., Maccarrone, M., Rapino, C., & Cencetti, F. (2022). The TRPV1 Receptor Is Up-Regulated by Sphingosine 1-Phosphate and Is Implicated in the Anandamide-Dependent Regulation of Mitochondrial Activity in C2C12 Myoblasts. *International Journal of Molecular Sciences*, *23*(19), 11103.

https://doi.org/10.3390/ijms231911103

Stella, N., Schweitzer, P., & Piomelli, D. (1997). A second endogenous. *Nature*, *388*, 773–777.

Stewart, C., Ralyea, C., & Lockwood, S. (2019). Ovarian Cancer: An Integrated Review. *Seminars in Oncology Nursing*, *35*(2), 151–156. https://doi.org/10.1016/j.soncn.2019.02.001

Strub, G. M., Paillard, M., Liang, J., Gomez, L., Allegood, J. C., Hait, N. C., Maceyka, M., Price, M. M., Chen, Q., Simpson, D. C., Kordula, T., Milstien, S., Lesnefsky, E. J., & Spiegel, S. (2011). Sphingosine-1-phosphate produced by sphingosine kinase 2 in mitochondria interacts with prohibitin 2 to regulate complex IV assembly and respiration. *The FASEB Journal*, *25*(2), 600–612. https://doi.org/10.1096/fj.10-167502

Taylor, V. A., Stone, H. K., Schuh, M. P., Zhao, X., Setchell, K. D., & Erkan, E. (2019). Disarranged Sphingolipid Metabolism From Sphingosine-1-Phosphate Lyase Deficiency Leads to Congenital Nephrotic Syndrome. *Kidney International Reports*, *4*(12), 1763–1769. https://doi.org/10.1016/j.ekir.2019.07.018

Tedesco, L., Valerio, A., Dossena, M., Cardile, A., Ragni, M., Pagano, C., Pagotto, U., Carruba, M. O., Vettor, R., & Nisoli, E. (2010). Cannabinoid receptor stimulation impairs mitochondrial biogenesis in mouse white adipose tissue, muscle, and liver: The role of eNOS, p38 MAPK, and AMPK pathways. *Diabetes*, *59*(11), 2826–2836. https://doi.org/10.2337/db09-1881

Toman, R. E., & Spiegel, S. (2002). Lysophospholipid receptors in the nervous system. *Neurochemical Research*, *27*(7–8), 619–627. https://doi.org/10.1023/A:1020219915922

Tominaga, M., & Tominaga, T. (2005). Structure and function of TRPV1. In *Pflugers Archiv European Journal of Physiology* (Vol. 451, Issue 1, pp. 143–150). Springer Verlag. https://doi.org/10.1007/s00424-005-1457-8

Tóth, A., Blumberg, P. M., & Boczán, J. (2009). Chapter 15 Anandamide and the Vanilloid Receptor (TRPV1). *Vitamins and Hormones*, *81*(C), 389–419. https://doi.org/10.1016/S0083-6729(09)81015-7

Turu, G., & Hunyady, L. (2010). Signal transduction of the CB1 cannabinoid receptor. In *Journal of Molecular Endocrinology* (Vol. 44, Issue 2, pp. 75–85). https://doi.org/10.1677/JME-08-0190

Ueda, H., Kobayashi, T., Kishimoto, M., Tsutsumi, T., & Okuyama, H. (1993). A Possible

Pathway of Phosphoinositide Metabolism Through EDTA-Insensitive Phospholipase A, Followed by Lysophosphoinositide-Specific Phospholipase C in Rat Brain. *Journal of Neurochemistry*.

Vlachová, V., Teisinger, J., Sušánková, K., Lyfenko, A., Ettrich, R., Vyklicky´1, L., & Vyklicky´1, V. (2003). *Functional Role of C-Terminal Cytoplasmic Tail of Rat Vanilloid Receptor 1*. http://www.rcsb.org/pdb/

Wagatsuma, A. (2013). A role for mitochondria as a potential regulator of myogenesis. *Basic Biology and Current Understanding of Skeletal Muscle*, *2013*, 251–287.

Wong, C. Y., Al-Salami, H., & Dass, C. R. (2020). C2C12 cell model: its role in understanding of insulin resistance at the molecular level and pharmaceutical development at the preclinical stage. *Journal of Pharmacy and Pharmacology*, *72*(12), 1667–1693. https://doi.org/10.1111/jphp.13359

Xiang, S. Y., Ouyang, K., Yung, B. S., Miyamoto, S., Smrcka, A. V., Chen, J., & Brown, J. H. (2014). PLCε, PKD1, and SSH1L Transduce RhoA Signaling to Protect Mitochondria from Oxidative Stress in the Heart. *NIH Public Acces*, *6*(306), 17. https://doi.org/10.1126/scisignal.2004405.PLC

Yaffe D., & Saxel O. (1977). Serial passaging and differentiation of myogenic cells isolated from dystrophic mouse muscle. *Nature*, *270*.

Ye, F., & Hoppel, C. L. (2013). Measuring oxidative phosphorylation in human skin fibroblasts. *Analytical Biochemistry*, *437*(1), 52–58. https://doi.org/10.1016/j.ab.2013.02.010

Yoshida N., Yoshida S., Koishi K., Masuda K., & Nabeshima Y. (1998). Cell heterogeneity upon myogenic differentiation: down-regulation of MyoD and Myf-5 generates 'reserve cells.' *Journal of Cell Science*, *111*, 769–779.

Young, K. W., & Nahorski, S. R. (2002). Sphingosine 1-phosphate: a Ca 2+ release mediator in the balance. *Cell Calcium*, *32*, 335–341. https://doi.org/10.1016/S0143-4160(02)00183-5

Zeitouni, N. C., Oseroff, A. R., & Shieh, S. (2003). Photodynamic therapy for nonmelanoma skin cancers: Current review and update. *Molecular Immunology*, *39*(17–18), 1133–1136. https://doi.org/10.1016/S0161-5890(03)00083-X

Zeng, L., Chen, Y., Huang, H., Wang, J., Zhao, D., & Ji, L. (2015). *Cyclometalated Ruthenium (II) Anthraquinone Complexes Exhibit Strong Anticancer Activity in Hypoxic Tumor Cells*. *Ii*,

15308–15319. https://doi.org/10.1002/chem.201502154

Zhang, H. Y., Bi, G. H., Li, X., Li, J., Qu, H., Zhang, S. J., Li, C. Y., Onaivi, E. S., Gardner, E. L., Xi, Z. X., & Liu, Q. R. (2015). Species differences in cannabinoid receptor 2 and receptor responses to cocaine self-administration in mice and rats. *Neuropsychopharmacology*, *40*(4), 1037–1051. https://doi.org/10.1038/npp.2014.297

Zhang, M., Zhang, M., Wang, L., Yu, T., Jiang, S., Jiang, P., Sun, Y., Pi, J., Zhao, R., & Guan, D. (2019). Activation of cannabinoid type 2 receptor protects skeletal muscle from ischemia-reperfusion injury partly via Nrf2 signaling. *Life Sciences*, *230*(77), 55–67. https://doi.org/10.1016/j.lfs.2019.05.056

Zhang, S. S., Zhou, S., Crowley-Mchattan, Z. J., Wang, R. Y., & Li, J. P. (2021). A review of the role of endo/sarcoplasmic reticulum-mitochondria ca2+ transport in diseases and skeletal muscle function. *International Journal of Environmental Research and Public Health*, 18(8). https://doi.org/10.3390/ijerph18083874

Zhang, W., Xiao, D., Mao, Q., & Xia, H. (2023). Role of neuroinflammation in neurodegeneration development. *Signal Transduction and Targeted Therapy*, *8*(1), 267. https://doi.org/10.1038/s41392-023-01486-5

Zhang, X., Huang, J., & McNaughton, P. A. (2005). NGF rapidly increases membrane expression of TRPV1 heat-gated ion channels. *EMBO Journal*, *24*(24), 4211–4223. https://doi.org/10.1038/sj.emboj.7600893

Zhao, D., Pond, A., Watkins, B., Gerrard, D., Wen, Y., Kuang, S., & Hannon, K. (2010). Peripheral endocannabinoids regulate skeletal muscle development and maintenance. *European Journal of Translational Myology*, *20*(4), 167. https://doi.org/10.4081/ejtm.2010.1814

Zhu, L. N., Ren, Y., Chen, J. Q., & Wang, Y. Z. (2013). Effects of myogenin on muscle fiber types and key metabolic enzymes in gene transfer mice and C2C12 myoblasts. *Gene*, *532*(2), 246–252. https://doi.org/10.1016/j.gene.2013.09.028

Zou, S., & Kumar, U. (2018). Cannabinoid receptors and the endocannabinoid system: Signaling and function in the central nervous system. In *International Journal of Molecular Sciences* (Vol. 19, Issue 3). MDPI AG. https://doi.org/10.3390/ijms19030833

Zygmunt, P. M., Ermund, A., Movahed, P., Andersson, D. A., Simonsen, C., Jönsson, B. A. G., Blomgren, A., Birnir, B., Bevan, S., Eschalier, A., Mallet, C., Gomis, A., & Högestätt, E. D.

(2013). Monoacylglycerols activate TRPV1 - A link between phospholipase C and TRPV1. *PLoS ONE*, *8*(12). https://doi.org/10.1371/journal.pone.0081618

Appendix

International Journal of
Molecular Sciences

MDPI

Article

The TRPV1 Receptor Is Up-Regulated by Sphingosine 1-Phosphate and Is Implicated in the Anandamide-Dependent Regulation of Mitochondrial Activity in C2C12 Myoblasts

Sara Standoli [1,†], Sara Pecchioli [2,†], Daniel Tortolani [3], Camilla Di Meo [1], Federico Fanti [1], Manuel Sergi [1], Marina Bacci [2], Isabelle Seidita [2], Caterina Bernacchioni [2], Chiara Donati [2], Paola Bruni [2,*], Mauro Maccarrone [3,4,*], Cinzia Rapino [5,‡] and Francesca Cencetti [2,‡]

1 Faculty of Bioscience and Technology for Food Agriculture and Environment, University of Teramo, 64100 Teramo, Italy
2 Department of Experimental and Clinical Biomedical Sciences Mario Serio, University of Florence, 50121 Firenze, Italy
3 European Centre for Brain Research (CERC)/Santa Lucia Foundation IRCCS, 00143 Rome, Italy
4 Department of Biotechnological and Applied Clinical Sciences, University of L'Aquila, 67100 L'Aquila, Italy
5 Faculty of Veterinary Medicine, University of Teramo, 64100 Teramo, Italy
* Correspondence: paola.bruni@unifi.it (P.B.); mauro.maccarrone@univaq.it (M.M.)
† These authors contributed equally to this work.
‡ These authors contributed equally to this work.

Citation: Standoli, S.; Pecchioli, S.; Tortolani, D.; Di Meo, C.; Fanti, F.; Sergi, M.; Bacci, M.; Seidita, I.; Bernacchioni, C.; Donati, C.; et al. The TRPV1 Receptor Is Up-Regulated by Sphingosine 1-Phosphate and Is Implicated in the Anandamide-Dependent Regulation of Mitochondrial Activity in C2C12 Myoblasts. *Int. J. Mol. Sci.* **2022**, *23*, 11103. https://doi.org/10.3390/ijms231911103

Academic Editors: Katharina Kubatzky and Elisabeth Seebach

Received: 25 July 2022
Accepted: 16 September 2022
Published: 21 September 2022

Publisher's Note: MDPI stays neutral with regard to jurisdictional claims in published maps and institutional affiliations.

Abstract: The sphingosine 1-phosphate (S1P) and endocannabinoid (ECS) systems comprehend bioactive lipids widely involved in the regulation of similar biological processes. Interactions between S1P and ECS have not been so far investigated in skeletal muscle, where both systems are active. Here, we used murine C2C12 myoblasts to investigate the effects of S1P on ECS elements by qRT-PCR, Western blotting and UHPLC-MS. In addition, the modulation of the mitochondrial membrane potential (ΔΨm), by JC-1 and Mitotracker Red CMX-Ros fluorescent dyes, as well as levels of protein controlling mitochondrial function, along with the oxygen consumption were assessed, by Western blotting and respirometry, respectively, after cell treatment with methanandamide (mAEA) and in the presence of S1P or antagonists to endocannabinoid-binding receptors. S1P induced a significant increase in TRPV1 expression both at mRNA and protein level, while it reduced the protein content of CB2. A dose-dependent effect of mAEA on ΔΨm, mediated by TRPV1, was evidenced; in particular, low doses were responsible for increased ΔΨm, whereas a high dose negatively modulated ΔΨm and cell survival. Moreover, mAEA-induced hyperpolarization was counteracted by S1P. These findings open new dimension to S1P and endocannabinoids cross-talk in skeletal muscle, identifying TRPV1 as a pivotal target.

Keywords: transient receptor potential vanilloid type 1; methanandamide; sphingosine 1-phosphate; mitochondrial membrane potential; C2C12 myoblasts

1. Introduction

Sphingosine-1-phosphate (S1P) is a lysosphingolipid that derives from the hydrolysis of ceramide and the subsequent phosphorylation of sphingosine, catalyzed, respectively, by multiple ceramidases and sphingosine kinase 1 (SphK1) and 2 (SphK2) [1,2].

Once generated, S1P can be degraded by S1P lyase (SPL) [3,4], or alternatively recycled into ceramide through S1P phosphatases (SPP) and ceramide synthases. In addition, S1P can be released outside the cell via unspecific transporters, such as ATP-binding cassette transporters and the specific Spinster homolog 2 [5], and MFSD2B [6] carriers. All these metabolic pathways are necessary to maintain the sphingolipid biostat, crucial for a wide range of physiological processes, including determination of cell fate [7]. Once exported outside the cell, S1P can bind to five different G-protein coupled receptors, called

S1P1-5 [8]. These S1P receptor subtypes are coupled to multiple G proteins and are differently expressed in the various cell types; thus, they can activate distinct signaling pathways, which, in turn, drive specific biological processes [9]. Consequently, S1P receptors impact on biological processes such as angiogenesis, immune response, tumorigenesis, embryonic development and skeletal muscle properties [8,10].

Of note, most of the biological processes under S1P control are also regulated by the endocannabinoid system (ECS) [11,12], which comprises the bioactive lipids family of endocannabinoids (eCBs) and a complex array of their receptor targets and metabolic enzymes necessary for their biosynthesis and degradation [13,14]. The first eCBs that were discovered, and that remain the most widely studied to date, are N-arachidonoyl ethanolamine (AEA) and 2-arachidonoyl glycerol (2-AG) [15].

AEA is the ethanolamide of arachidonic acid, produced mainly through the catalytic activity of N-acylphosphatidylethanolamine-specific phospholipase D (NAPE-PLD), and degraded principally by fatty acid amide hydrolase (FAAH) [16]. 2-AG is often the most abundant eCB in human cells, tissues and fluids, and is produced by diacylglycerol-lipases α and β (DAGL α and β), to be then hydrolyzed principally by monoacylglycerol lipase (MAGL) [13,17]. Both AEA and 2-AG bind primarily to G protein-coupled type 1 and 2 cannabinoid receptors (CB_1 and CB_2), which are expressed throughout the human body [18]. It is now apparent that eCBs can also bind to non-CB_1/non-CB_2 receptors, such as the orphan G-protein-coupled receptor GPR55 [19–21], and the transient receptor potential vanilloid 1 (TRPV1) channel [22]. Each receptor triggers a distinct signal transduction cascade, as detailed elsewhere [12,18,20–23].

Interestingly, S1P and eCB signaling pathways could interact with each other [24]. Not only S1P receptors and CB_1/CB_2 share 20% sequence identity [25], but also the activation of CB_1 regulates sphingolipid metabolism with ceramide accumulation [26]. For instance, (i) both AEA and S1P act synergistically to regulate rat coronary artery reactivity [27], (ii) AEA treatment increases the phosphorylation of SphK1, and (iii) AEA-mediated vasorelaxation is attenuated by inhibition of SphK1 and SphK2; notably, the latter effect of AEA engages S1P3 [27]. More recently, it has been demonstrated that AEA can modulate SphK1 to increase the generation of S1P, thus mediating changes in blood pressure through S1P1 [24]. Of interest, the non-selective S1P receptor modulator FTY720 (2-amino-2-(2-[4-octylphenyl]ethyl)-1,3-propanediol), as well as endogenous sphingosine, have been shown to dose-dependently inhibit in vitro binding of selective CB_1 antagonists and agonists to ectopically expressed mouse CB_1 in CHO-K1 cells [28]. Yet, clear evidence of a possible cross-talk between S1P and eCB systems remains elusive. Here, we sought to fill this knowl- edge gap by interrogating the effect of S1P on eCB signaling in murine C2C12 myoblasts that express both systems [29–31]. In this context, it should be recalled that metabolism and signaling of S1P were found to be involved in skeletal-muscle biology [31–34], and that metabolism and signaling of eCBs have been shown to control skeletal muscle cell differentiation [35] along with myometrium contractility [36]. Thus, here we ascertained the possible modulation of the main ECS elements at gene and protein expression levels, along with the content of AEA and 2-AG in C2C12 myoblasts challenged with S1P. Moreover, due to the effect of AEA on energy homeostasis [37–39], mitochondrial membrane potential (ΔΨm) was measured in C2C12 cells treated with the non-hydrolyzable AEA analogue methanandamide (mAEA) [40], in the presence of S1P, as well as of agonists and antagonists to eCB-binding receptors.

We provide unprecedented evidence that S1P selectively increases TRPV1 expression in skeletal muscle C2C12 cells, and that TRPV1 transmits a dual action of mAEA depending on its concentration: at high dose (10 μM) mAEA decreases cell survival and inhibits mitochondrial activity, whereas at low doses (<5 μM) it increases mitochondrial membrane potential and induces the expression of peroxisome proliferator-activated receptor gamma coactivator 1-α (PGC1α), a transcriptional coactivator of genes implicated in the regulation of mitochondrial biogenesis and function [41]. Overall, this study discloses a new modula-

tory role of S1P in skeletal-muscle cells, which engages a distinct ECS element and supports the concept that different bioactive lipids can indeed cross-talk with each other.

2. Results

2.1. Effect of S1P on the Expression of ECS Elements

The mRNA expression of eCB-binding receptors (CB_1, CB_2, GPR55, TRPV1) and AEA and 2-AG metabolic enzymes (NAPE-PLD, FAAH, DAGLα, DAGLβ, and MAGL) was evaluated by qRT-PCR in C2C12 cells treated for 24 and 48 h with S1P at 1 μM, a dose that was shown to be effective to induce myogenic differentiation [32]. Upon exposure to S1P for 24 h, CB_1 and CB_2 mRNA expression showed a trend towards increase, yet not statistically significant, whereas GPR55 and TRPV1 mRNA levels were significantly enhanced ($p < 0.01$ vs. control) (Figure 1a). FAAH, DAGLα and DAGLβ were also significantly increased ($p < 0.01$ vs. control, for FAAH and DAGLβ; $p < 0.05$ vs. control, for DAGLα), unlike NAPE-PLD and MAGL that remained unaffected (Figure 1b).

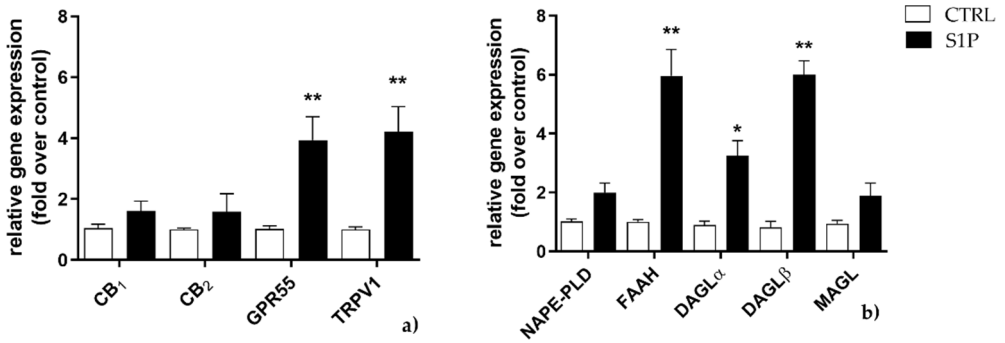

Figure 1. Effect of S1P on mRNA expression of endocannabinoid (eCB)-binding receptors (**a**) and metabolic enzymes (**b**) at 24 h. C2C12 cells were left untreated (in white) or were treated for 24 h with 1 μM of S1P (in black). The values are expressed as $2^{(-\Delta\Delta Ct)}$ and normalized to β-Actin and GAPDH. Data are presented as means ± SEM ($n = 5$). Statistical analysis was performed by TWO-WAY ANOVA test followed by Bonferroni post hoc test. [* $p < 0.05$, ** $p < 0.01$ vs. control cells (CTRL)].

Such an increase in selected elements of the ECS returned to control levels when S1P exposure was prolonged for additional 24 h (Figure 2a,b), with the exception of GPR55 gene expression, which was significantly reduced ($p < 0.01$ vs. control) (Figure 2a).

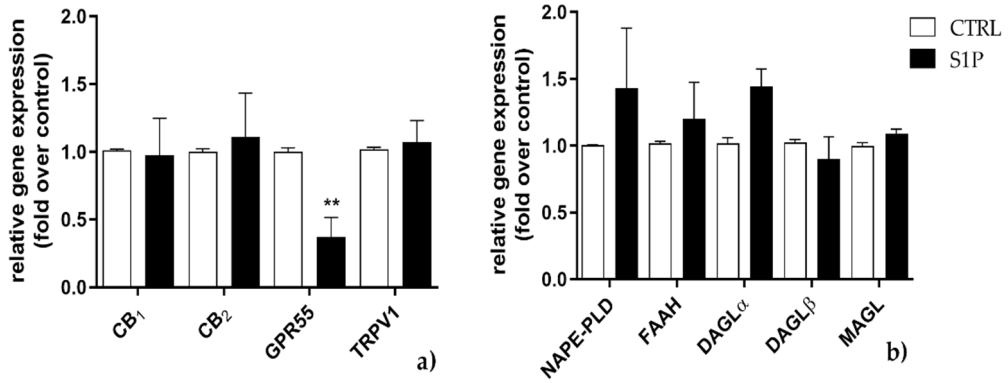

Figure 2. Effect of S1P on mRNA expression of endocannabinoid (eCB)-binding receptors (**a**) and metabolic enzymes (**b**) at 48 h. C2C12 cells were left untreated (in white) or were treated for 48 h with 1 μM of S1P (in black). The values are expressed as $2^{(-\Delta\Delta Ct)}$ and normalized to β-Actin and GAPDH. Data are presented as means ± SEM ($n = 5$). Statistical analysis was performed by TWO-WAY ANOVA test followed by Bonferroni post hoc test. [** $p < 0.01$ vs. control cells (CTRL)].

Then, the protein expression of eCB-binding receptors, AEA and 2-AG metabolic enzymes was evaluated by Western blot in C2C12 cells treated with 1 μM S1P for 24 h. In treated cells CB_2 protein level was significantly decreased ($p < 0.059$) compared to controls (Figure 3a), whereas TRPV1 protein level was significantly increased ($p < 0.05$ vs. control), in keeping with qRT-PCR data (Figure 1a). Remarkably, protein expression of any other ECS element was unaffected (Figure 3b–g), while CB_1 and DAGLα were below the detection limit.

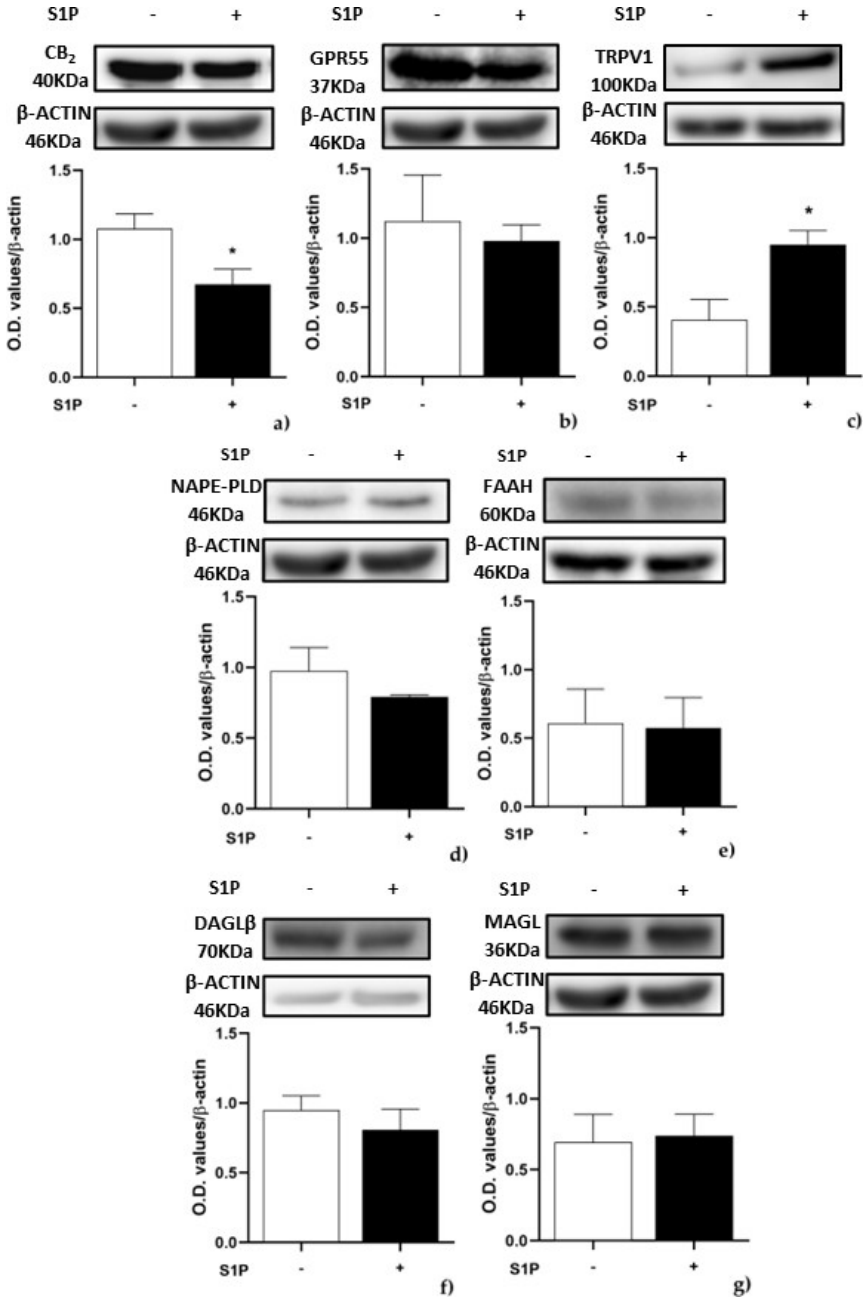

Figure 3. Effect of S1P on protein expression of endocannabinoid (eCB)-binding receptors and metabolic enzymes: C2C12 cells were left untreated (in white) or were treated for 24 h with 1 μM S1P (in black). Samples were subjected to Western blotting analysis using specific antibodies against the following proteins: (**a**) CB_2; (**b**) GPR55; (**c**) TRPV1; (**d**) NAPE-PLD; (**e**) FAAH; (**f**) DAGLβ; (**g**) MAGL. Densitometric analysis values are expressed as relative optical density and normalized to β-Actin. The values represent the mean ± SEM of three independent experiments ($n = 3$). Statistical analysis was performed by ONE-WAY ANOVA test followed by Bonferroni post hoc test. [* $p < 0.05$ vs. control cells (CTRL)]. "+" with S1P, "−" without S1P.

To further investigate the possible effect of S1P on the endogenous levels of AEA and 2-AG, LC/MS analysis was performed. In keeping with protein expression of metabolic enzymes, no significant differences in the levels of these two eCBs were observed in cells treated with 1 μM S1P for 24 h (Figure 4).

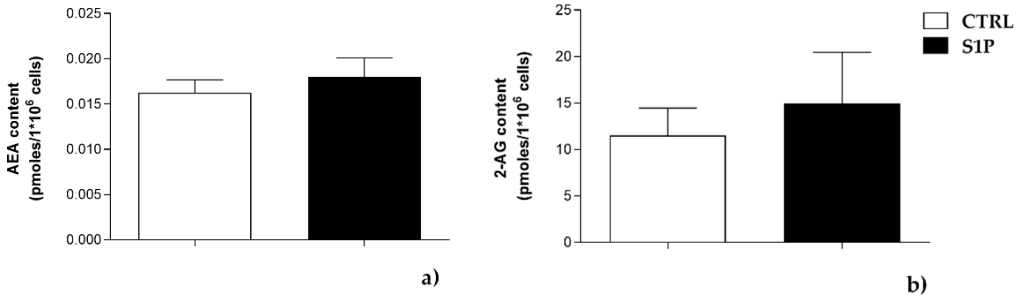

Figure 4. Effect of 1μM S1P on endogenous levels of AEA (**a**) and 2-AG (**b**), measured by using liquid chromatographic–mass spectrometry (LC-MS) analysis. The values represent the means ± SEM of three independent experiments (n = 3). Statistical analysis was performed by ONE-WAY ANOVA test, followed by Bonferroni post hoc test.

2.2. *Effect of Methanandamide on Mitochondrial Membrane potential*

As shown by gene and protein expression data, C2C12 cells did express FAAH, the main hydrolytic enzyme of AEA (Figures 1–3). Therefore, to rule out any interference of this enzyme activity, for subsequent cell treatments the non-hydrolysable, stable analogue of AEA methanandamide (mAEA) [40] was used. In particular, the mitochondrial membrane potential (ΔΨm) was evaluated in C2C12 cells treated with mAEA at different doses (2.5–5.0–10 μM) for 24 h, because of the key role of AEA on energy homeostasis [42,43]. ΔΨm values were measured with JC-1, a fluorescent dye that forms aggregates in the mitochondria with a red emission (~590 nm) but reverts to monomers with a green emission (~526 nm) when the mitochondrial membrane starts to depolarize [44]. Treatment for 24 h at lower doses of mAEA (2.5 μM and 5.0 μM) significantly ($p < 0.01$ and $p < 0.05$, respectively) increased ΔΨm values compared to controls (Figure 5). Yet, at the highest dose of 10 μM mAEA significantly ($p < 0.05$) decreased the ratio of aggregated to monomeric form of JC-1, by 48 ± 5.9%, compared to untreated controls (Figure 5).

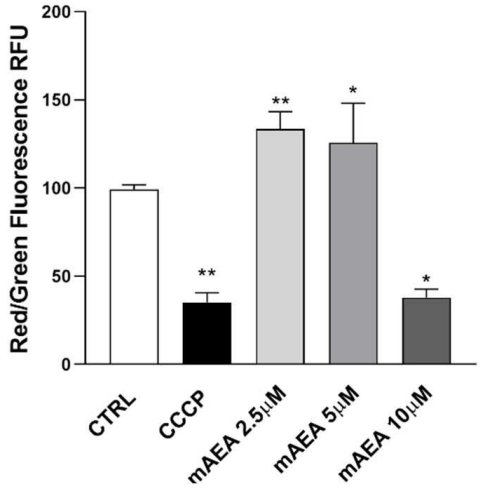

Figure 5. The polarization state of mitochondrial membrane was assessed after the cells were exposed to mAEA, at different doses (2.5, 5.0 and 10 μM) for 24 h, or to the oxidative phosphorylation inhibitor CCCP (50 μM) used as a positive control for (ΔΨm) decrease. Values are expressed as ratio of red (~590 nm)/ green (~529 nm) fluorescent intensity. Ratio are presented as mean ± SEM of three independent experiments (n = 3). [* $p < 0.05$, ** $p < 0.01$ vs. control cells (CTRL)].

The depolarization induced by 10 μM mAEA was further investigated in the presence of S1P, and interestingly mAEA failed to affect ΔΨm when cells were incubated in the presence of S1P, and vice versa S1P was unable to alter ΔΨm in the absence of mAEA (Figure 6). Taken together, these data suggested a possible crosstalk between the two lipid signaling systems. Moreover, to interrogate whether the mAEA depolarizing effect was mediated by eCB-binding receptors, the analysis was performed also in the presence of their selective antagonists: 0.1 μM SR1 for CB_1 [45], 0.1 μM SR2 for CB_2 [45], 0.1 μM ML193 for GPR55 [46], and 0.1 μM I-RTX for TRPV1 [47,48]. None of the antagonists affected ΔΨm when applied alone, yet pre-treatment with the specific antagonists of eCB-binding receptors prevented the depolarizing activity of 10 μM mAEA, whereas in the presence of I-RTX, selective TRPV1 antagonist, mAEA increased ΔΨm (#### $p < 0.0001$ vs mAEA alone) (Figure 6).

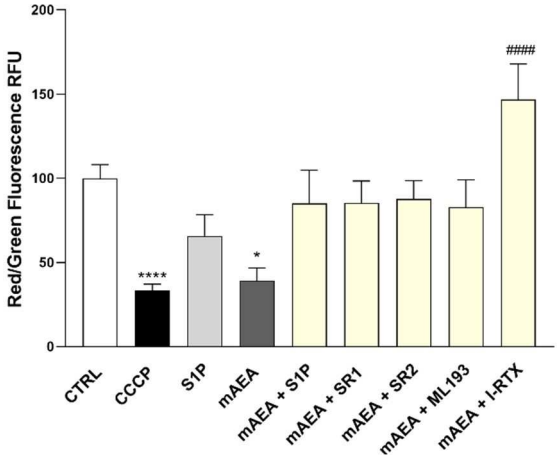

Figure 6. The polarization state of the mitochondrial membrane was assessed after the cells were exposed to mAEA (10 μM), and mAEA + S1P (1 μM) and in the presence of selective antagonists to eCB-binding receptors (SR1, SR2, ML193 and I-RTX) for 24 h. Values are expressed as ratio of red (~590 nm)/green (~529 nm) fluorescent intensity. Ratio are presented as mean ± SEM of three independent experiments ($n = 3$). Statistical analysis was performed by ONE-WAY ANOVA followed by Bonferroni post-hoc test [* $p < 0.05$, **** $p < 0.0001$ vs. control cells (CTRL); #### $p < 0.0001$ vs. mAEA].

Since 10 μM mAEA markedly depolarized the mitochondrial membrane, we checked whether it could impair C2C12 cell viability. When added for 24 h, mAEA showed a dose-dependent cytotoxicity, and at 10 μM, it significantly reduced cell viability by 30 ± 3.0% (Figure 7).

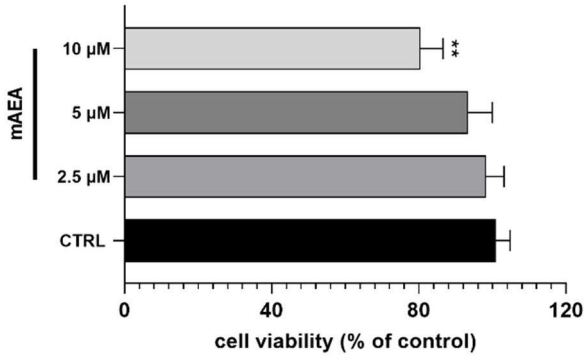

Figure 7. Assessment of cell viability using MTT assay on C2C12 myoblasts treated with mAEA at different doses (2.5, 5.0 and 10 μM) for 24 h. Values are expressed as % of control cells and presented as mean ± SEM of three independent experiment ($n = 3$). Statistical analysis was performed by ONE-WAY ANOVA followed by Bonferroni post-hoc test [** $p < 0.01$ vs. control cells (CTRL)].

In order to further analyze the effect of different concentrations of mAEA on mitochondrial activity, ΔΨm was measured in growing and serum-starved C2C12 myoblasts upon treatment for 24 h with mAEA at 5 μM, the dose immediately below the toxic one. For these assays, the Mitotracker Red CMX-Ros fluorescent dye was used, which stains mitochondria proportionally to their membrane potential. Laser-scanning confocal microscopy allowed the detection of fluorescence intensity, which was normalized to the cell number in each field. As shown in Figure 8, in 24 h serum starved C2C12 myoblasts ΔΨm significantly increased by 77.7 ± 7.5% compared to growing myoblasts (**** $p < 0.0001$), and it was further increased by 33.5 ± 2.9% (*** $p < 0.001$) upon challenge with 5 μM mAEA.

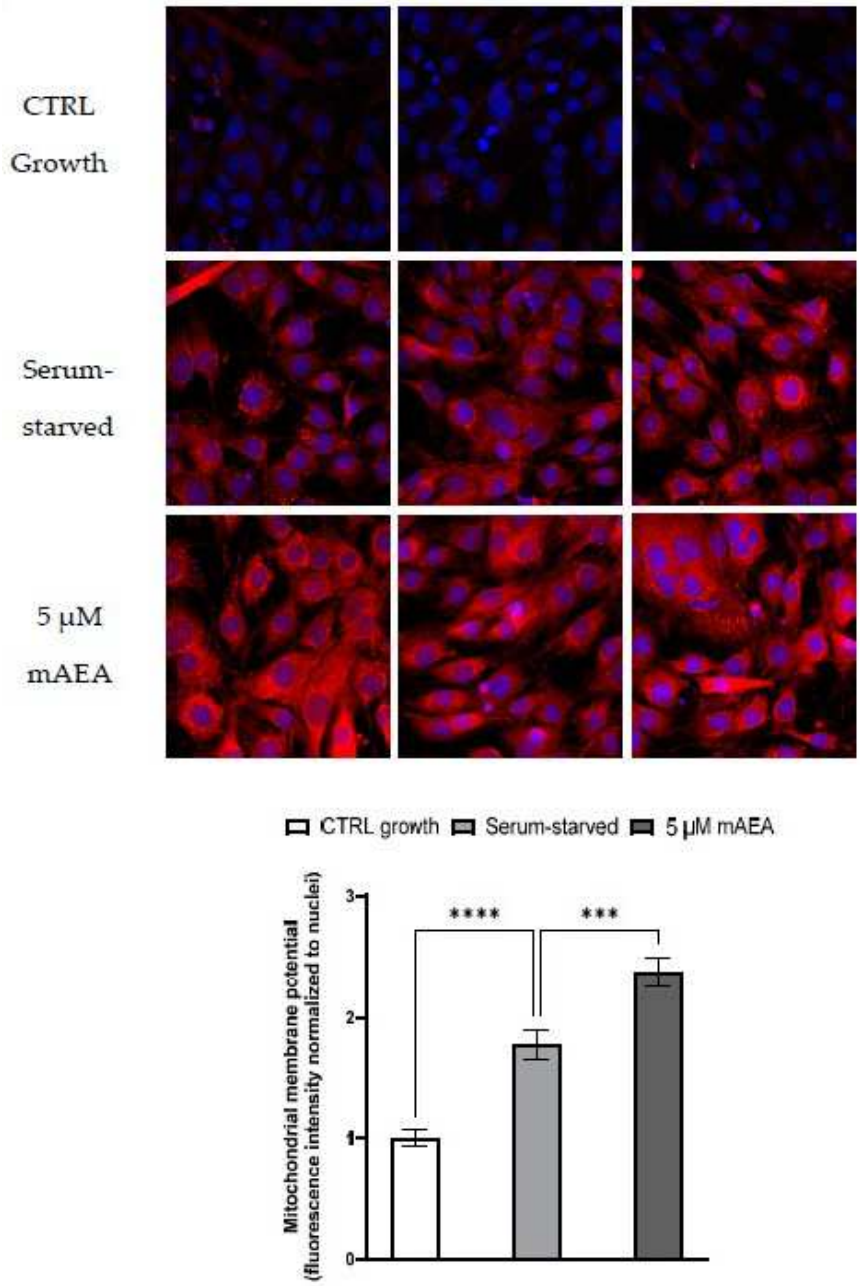

Figure 8. Effect of 5 μM mAEA on mitochondrial membrane potential. Confluent serum-starved C2C12 myoblasts were treated, or not, with 5 μM mAEA for 24 h and compared to growing (CTRL growth) myoblasts. Fluorescence intensity of Mitotracker Red CMX-Ros (Ex/Em: 579/599) was normalized to cell number and data are reported as mean ± SEM of six field per condition in each of the three independent experiments. Statistical analysis was performed by ONE-WAY ANOVA followed by Bonferroni post-hoc test [*** $p < 0.001$, **** $p < 0.0001$].

With the aim of interrogating whether S1P might affect mAEA activity on ΔΨm, the 5 μM mAEA challenge was performed also in the presence of 1 μM S1P for 24 h. Under these conditions, the mAEA-dependent increase in ΔΨm was fully reverted by S1P (Figure 9).

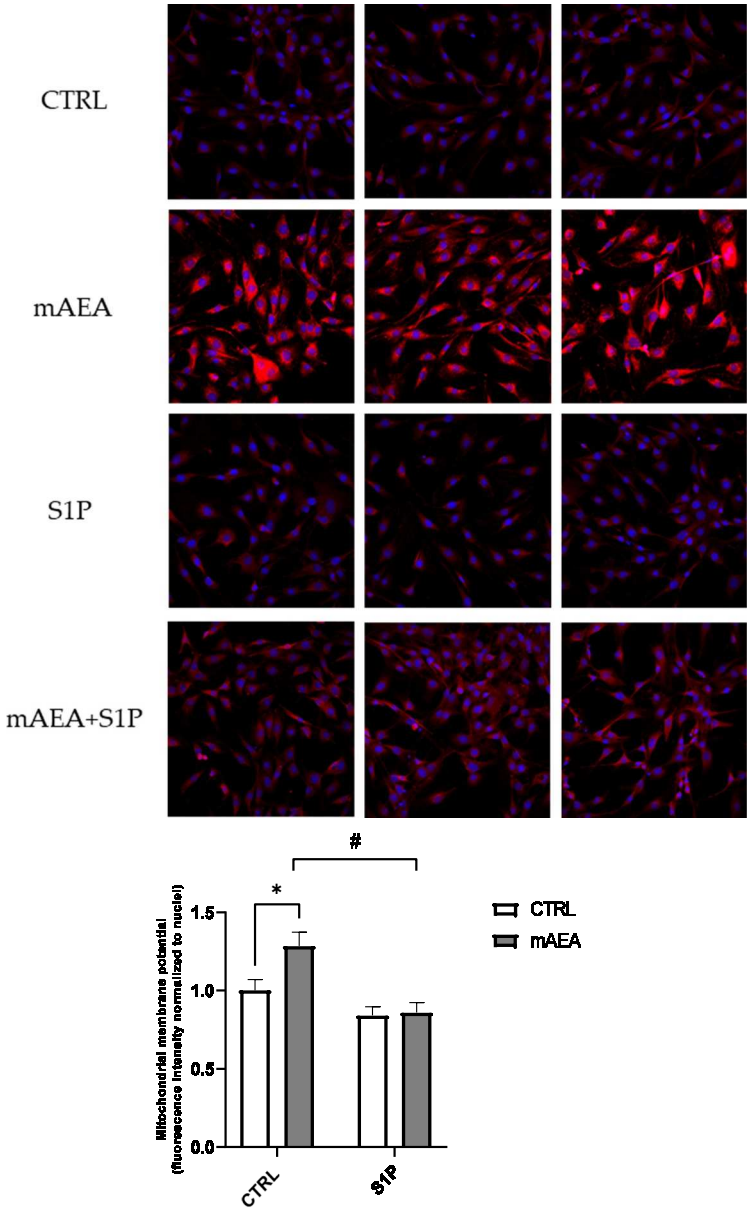

Figure 9. Effect of S1P on mAEA-induced mitochondrial membrane potential in C2C12 myoblasts. Confluent serum-starved cells were treated with 5 μM mAEA in the presence or absence of 1 μM S1P for 24 h. Fluorescence intensity of Mitotracker Red CMX-Ros (Ex/Em: 579/599) was normalized to cell number and data are reported as mean ± SEM of six field per condition in three independent experiments. Statistical analysis was performed by TWO-WAY ANOVA followed by Bonferroni post-hoc test [* $p < 0.05$ mAEA vs CTRL, # $p < 0.05$ S1P+mAEA vs mAEA].

Moreover, based on the protein expression data, the role of eCB-binding receptors in 5 μM mAEA-induced increase in ΔΨm was studied. The specific blockade of TRPV1 by I-RTX abrogated the activity of 5 μM mAEA on ΔΨm, whereas SR1 and SR2 were ineffective (Figure 10).

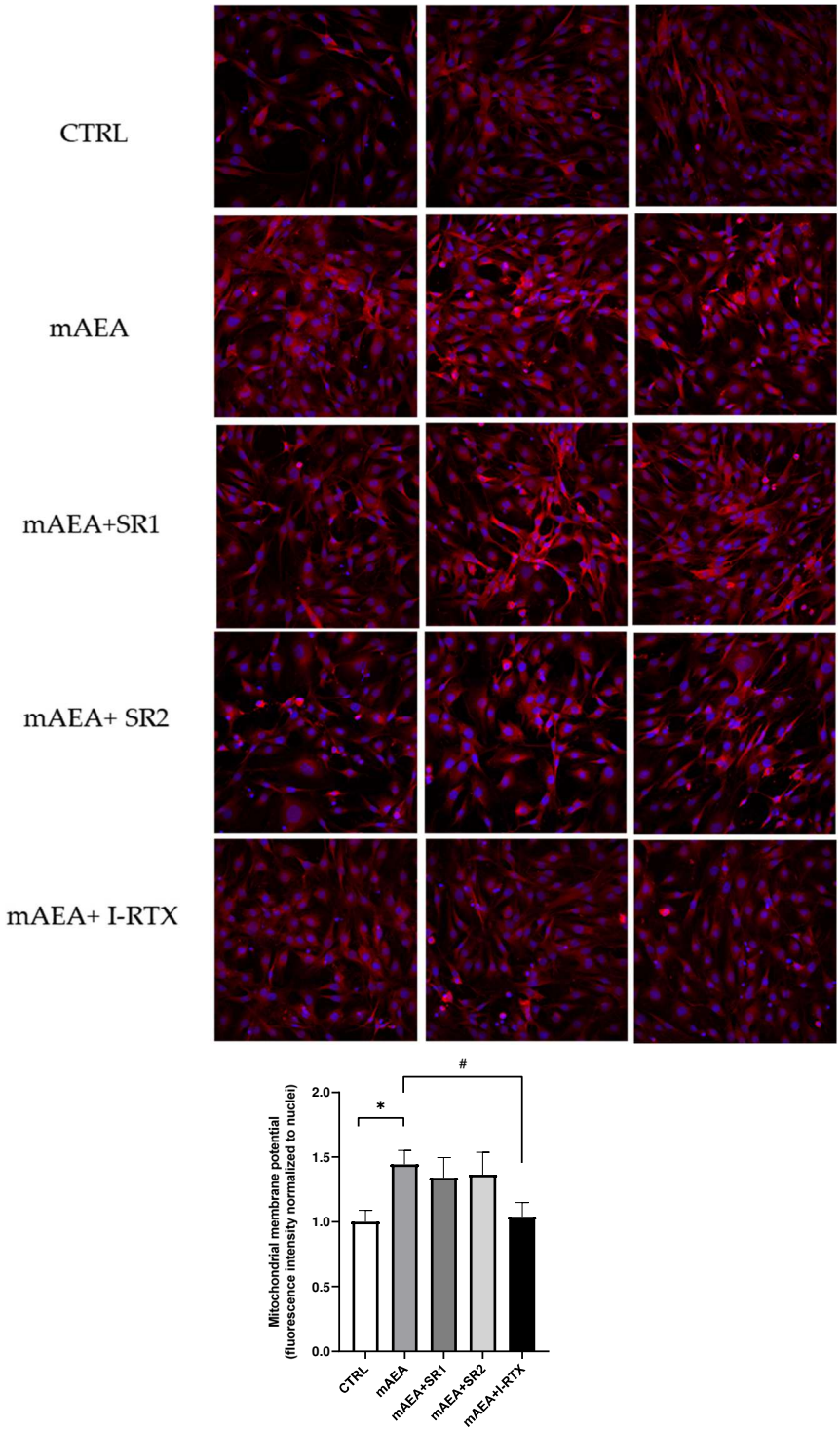

Figure 10. Role of eCB receptors on mitochondrial activity induced by 5 μM mAEA in C2C12 myoblasts. Confluent serum-starved C2C12 myoblasts were treated with 5 μM mAEA for 24 h in the presence of eCB receptor antagonists (SR1, SR2 or I-RTX). The fluorescence intensity of Mitotracker Red CMX-Ros (Ex/Em: 579/599) was normalized to cell number, and data are reported as mean ± SEM of six field per condition in each of the three independent experiments. Statistical analysis was performed by ONE-WAY ANOVA [* $p < 0.05$] and TWO-WAY ANOVA [# $p < 0.05$] followed by Bonferroni post-hoc test.

2.3. Effect of Methanandamide on PGC1α, Respiratory Chain Complex Expression and Oxygen Consumption

With the goal to analyze the molecular mechanism involved in the effects of 5 μM mAEA on mitochondrial function, the expression of PGC1α and respiratory chain complexes was measured by Western blot analysis upon treatment for 24 h. As shown in Figure 11, the protein content of PGC1α was significantly enhanced, whereas that of the respiratory chain complexes were not affected by 5 μM mAEA challenge.

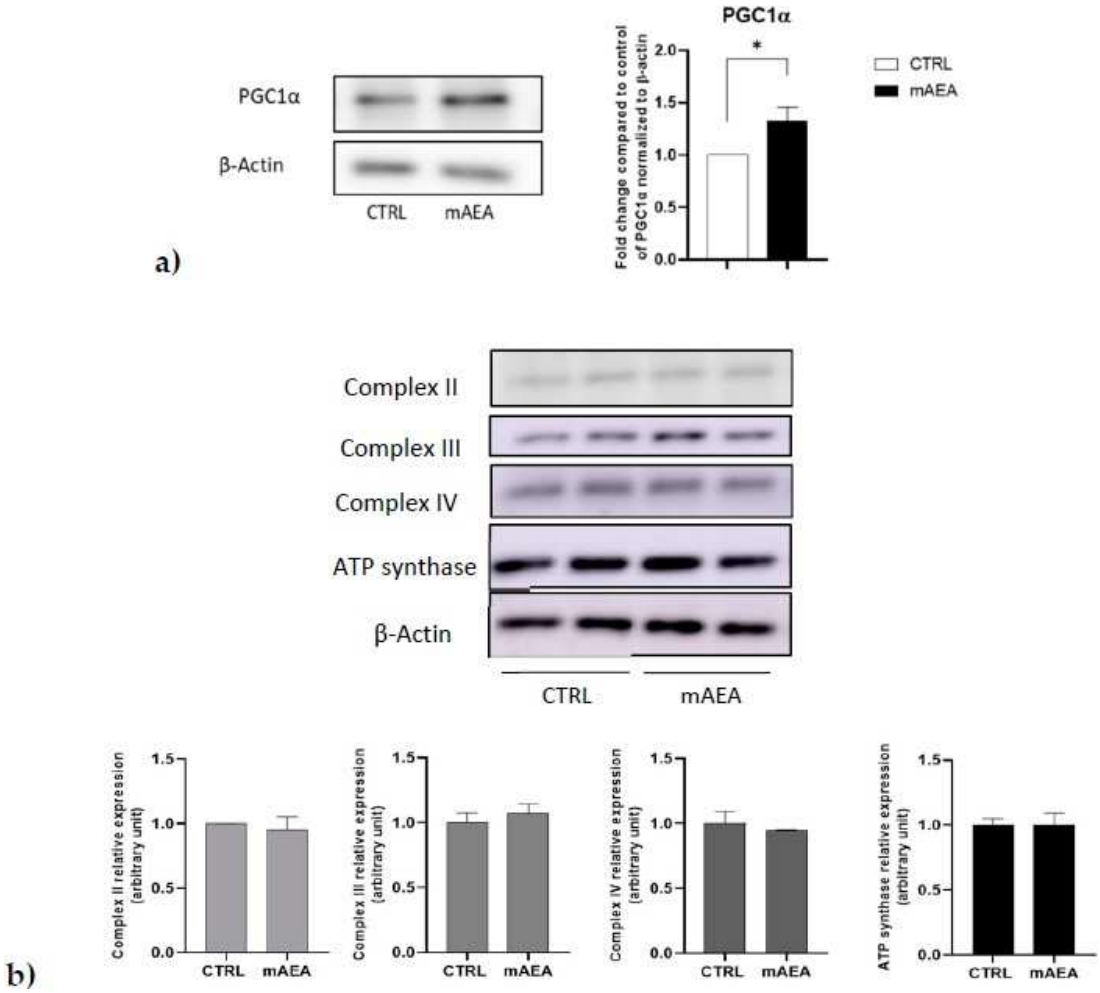

Figure 11. Effect of mAEA on PGC1α (**a**) and respiratory chain complexes' (**b**) expression. C2C12 myoblasts were treated with mAEA (5 μM) for 24 h. Samples were subjected to SDS-PAGE and Western blot analysis using anti-PGC1α, as well as OXPHOS WB Antibody Cocktail specific for respiratory chain complexes and anti-β-actin antibody as housekeeping. The data were reported after densitometric analysis of the bands as means ± SEM normalized to β-actin of three independent experiments performed in duplicate. The data were reported after densitometric analysis of the bands as means ± SEM normalized to β-actin of three independent experiments. Statistical analysis was performed by analysis of variance using Student *t*-test [* $p < 0.05$ vs. control cells (CTRL)].

Moreover, the ability of 5 μM mAEA to affect oxygen consumption was examined by high-resolution respirometry. To this end, C2C12 myoblasts were treated with 5 μM mAEA for 24 h, then were collected and subjected to basal oxygen consumption (ROUTINE), proton leak (LEAK) and maximal oxygen consumption (E) measurement by the Oroboros-O2K system. At 5 μM, mAEA was unable to affect any of these respiratory parameters in C2C12 myoblasts (Figure 12).

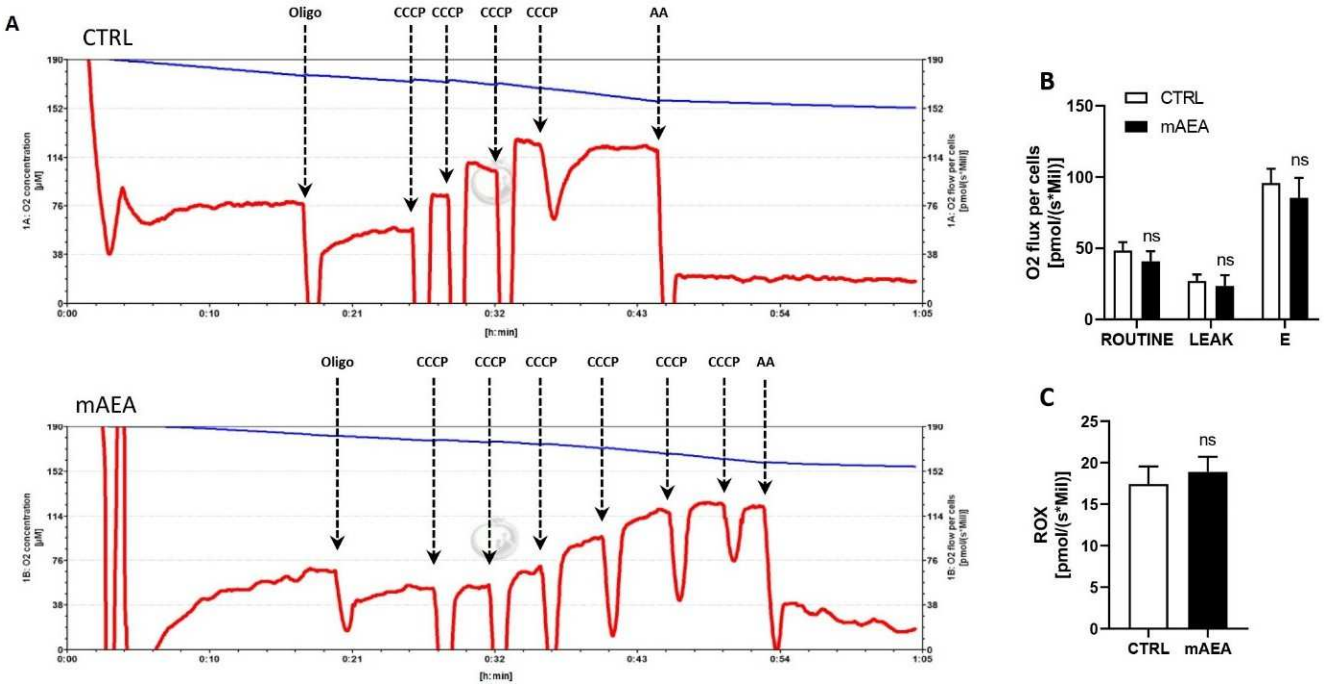

Figure 12. High-resolution respirometry of C2C12 myoblasts following mAEA treatment. C2C12 cells were treated or not with mAEA (5 μM) for 24 h. After detachment, myoblasts were subjected to high-resolution respirometry analysis by the Oroboros-O2K instrument. (**A**) Representative graphs of cell-respirometry analysis in the control (top) and treatment (bottom) conditions. The blue curve represents the oxygen concentration, whereas the red slope shows the oxygen consumption before and after the serial injections of oligomycin (Oligo), uncoupler CCCP and Antimycin (AA). (**B**) Bar chart graph of basal oxygen consumption (ROUTINE), proton leak (LEAK) and maximal oxygen consumption (E) values subtracted from residual oxygen consumption (ROX) in CTRL and mAEA treated cells. (**C**) ROX was also measured after AA administration. Data were reported as means ± SEM of the oxygen flux normalized on cell number of three independent experiments; ns= not significant.

3. Discussion

eCBs and S1P are bioactive lipids, which are critically important for the regulation of a plethora of key biological processes [8,13]. Intriguingly, these two lipid systems are composed by multiple enzymes that regulate their cellular tone, and specific receptor targets that transmit their effects, via a complex array of signal transduction pathways that remain only partly understood [8,13].

Here, unprecedented evidence is provided for a modulatory role of S1P on selected elements of ECS in cultured murine skeletal-muscle C2C12 cells, which are are widely used as a valuable model for interrogating, at the molecular level, key processes in skeletal muscle.

Importantly, S1P and eCB systems regulate fundamental biological events in skeletal muscle cell biology [10,35]. Indeed, S1P is known to activate muscle resident stem cells, favoring tissue repair by promoting also their proliferation and differentiation [49–51]. Moreover, it regulates tissue mechanical properties and responsiveness to insulin [10,52]. Myogenesis is also modulated by ECS, since CB_1 expression has been reported to be up-regulated during myoblast differentiation and 2-AG was found to act via CB_1 as endogenous repressor of myoblast differentiation, while mAEA treatment inhibited myogenesis [29,35]. The key role of the two families of lipid mediators in the control of skeletal-muscle cell biology is further underscored by the evidence that both signaling systems are dysregulated in a major skeletal-muscle disease, namely Duchenne muscular dystrophy [53,54]. In this context, CB_1 was found to be overexpressed in murine dystrophic muscles, as well as in

muscle biopsies of dystrophic patients [53], while muscles of dystrophic mice exhibited S1P lyase (SPL) upregulation and S1P deficiency, and accordingly pharmacological blockade of SPL in dystrophic mouse muscles exerted beneficial effects mediated by enhanced S1P, which in turn binds to and inhibits histone deacetylase [54].

In the present study, the possible functional interplay between the S1P and eCB systems has been explored in murine myoblasts by examining, as a first approach whether S1P treatment can modify receptor-mediated responsiveness to eCBs or the endogenous metabolism of these lipids. To this end, the expression of individual receptors and eCB-metabolic enzymes upon S1P challenge has been investigated both at mRNA and protein levels, and AEA and 2-AG cell content has been quantified. Notably, S1P at 24 h was found responsible of the selective up-regulation of TRPV1. Conversely, the protein content of CB_2 was reduced by S1P, even though this variation was not mirrored by mRNA levels. In addition, mRNA levels of GPR55 receptor, as well as FAAH and DAGLβ enzymes in S1P-treated myoblasts were transiently increased by S1P at 24 h, and only GPR55 was found to be decreased at 48 h. It seems noteworthy that the present gene expression data on DAGL isozymes are consistent with the notion that non-neuronal cells (such as myoblasts) predominantly express DAGLβ, whereas DAGLα is more abundant within the brain [55]. In this context, it should also be noted that discrepancies between mRNA and protein expression of a specific target in treated cells are not quite unprecedented. Indeed, similar disparities between changes in mRNA abundance and protein content have been already reported [56], also within the ECS, by others [57] and by us [58,59]. Interestingly, an interaction between GPR55 and S1P5 receptor has already been demonstrated in a colon cancer cell line [60]. In particular, S1P5 strongly and specifically interacts with GPR55, and the activation of each receptor led to increased cell proliferation, ERK phosphorylation and cancer-associated gene expression. Conversely, co-activation of both receptors inhibited the above mentioned events, supporting the occurrence of a functional crosstalk [60]. In the herein-investigated model of murine myoblasts, S1P significantly rearranges cell sensitivity to eCBs without changing their endogenous content, suggesting a potential impact on the signal transduction driven by these lipid mediators.

Although important molecular effects of eCBs in skeletal muscle have been identified [53], so far it is not known if they engage the regulation of mitochondrial activity, which is essential for skeletal muscle metabolism and proper tissue plasticity. It should be recalled that AEA is known to play a key role in energy homeostasis [37–39], and indeed it can affect the shape and function of isolated mitochondria [42]. In line with this, some reports have even suggested a mitochondrial localization of CB_1, supporting the view that AEA-dependent effects on energy production are triggered by these particular CB_1 receptors [61,62]. Against this background, here we sought to ascertain whether the stable anandamide analogue mAEA could affect mitochondrial membrane potential, a key functional parameter of these organelles. Interestingly, our findings show that mAEA at the lowest concentration of 5 μM markedly enhanced ΔΨm, whereas the highest dose of 10 μM exerted an opposite effect. Moreover, in both cases the changes of ΔΨm elicited by mAEA were found to be mediated by TRPV1, since they were abrogated in the presence of its selective antagonist I-RTX. Likewise, treatment of mitochondria isolated from mice liver with higher concentrations (up to 50 μM) of AEA significantly decreased ΔΨm, down to ~70% of untreated controls, and they also increased membrane fluidity [42]. However, these effects were independent of CB_1, CB_2 or TRPV1 [42]. Similarly, in rat cortical neurons AEA, at the dose of 30 μM, was able to reduce mitochondrial membrane potential, induce the translocation of cytochrome c and activate caspase-3, overall leading to cell death independently of its receptor targets [63]. Instead, in human neuroblastoma SH-SY5Y cells, AEA dose-dependently, and again in the micromolar range, induced a mitochondria-dependent apoptosis, which in these cells was mediated by CB_1 [38]. Overall, there seem to be different mechanisms by which AEA can affect mitochondrial function, possibly also in relation to cell type and species-specificity.

Moreover, the ability of S1P to counteract the depolarizing effect of mAEA in C2C12 cells appears to be noteworthy. Yet, S1P alone did not affect the mitochondrial membrane potential, which is in agreement with its ability to act as pro-survival factor and to control mitophagy and mitochondria dynamics [64–66]. Altogether, these results add a new dimension to the signaling pathways triggered by S1P and eCBs, and identify the Ca^{2+} channel TRPV1 as a pivotal target crucially involved in their crosstalk. The latter observation is quite remarkable, because so far most of the effects of eCBs in murine myoblasts have been ascribed to CB_1/CB_2 receptors with one exception describing TRPV1 as responsible for Ca^{2+} increase and subsequent promyogenic effect induced by cannabidiol [67]. The molecular mechanism by which S1P modulates responsiveness of myoblasts to eCBs has not been here investigated, paying special attention to the biochemical effects transmitted by S1P via eCB system, rather than its mechanistic action. C2C12 myoblasts are known to express four out of five S1P receptor subtypes, namely S1P1, S1P2, S1P3 and S1P4 [68], hence future studies will be necessarily addressed to dissect the exact role exerted by one or more receptor subtypes in the observed effects, even if it is conceivable to hypothesize that S1P2 is implicated. Indeed, this receptor subtype, although less represented than other isoforms, at least at mRNA level, [68], is regarded as the dominant receptor subtype in this cell type, being capable of transmitting key biological effects such as cell differentiation, inhibition of cell motility and cell proliferation [32,69].

Another relevant issue is the possibility that, instead of a cross-talk, mAEA and S1P may interact directly with TRPV1. Indeed, recent evidence supports the direct activation of TRPV1 by S1P in the context of pain and itch [70]. However, the hypothetic agonism of S1P at TRPV1 could not account for the observed up-regulation of TRPV1 at protein and mRNA level elicited by S1P at 24 h. Unfortunately, the analysis of the elevation of intracellular Ca^{2+} in transfected cells does not appear a suitable read-out to clarify this issue, because extracellular S1P itself, acting via its specific receptors, may potently induce such an elevation in many cell types, C2C12 myoblasts included [71]. More sophisticated approaches, such as silencing S1P receptor subtypes in C2C12 myoblasts, would be more informative, and should be the subject of independent investigations.

It is tempting to speculate that the herein-observed up-regulation of TRPV1 induced by S1P can counteract the increase in mitochondrial membrane potential induced by low mAEA, causing calcium overload that impairs mitochondrial function, thus mimicking the effect elicited by high dose of mAEA. In this context, it is well known that the large calcium gradient maintained across the mitochondrial inner membrane represents a critical signaling potential for this cation [72]. It is noteworthy that TRPV1 activation by capsaicin has been proven to increase free cytosolic calcium and improve energy metabolism by upregulating PGC1α in C2C12 myotubes, as well as in skeletal muscles [73]. Furthermore, it has been demonstrated that TRPV1 ligands decrease mitochondrial membrane potential and oxygen consumption in isolated mitochondria from rat cardiomyocytes [74]. Notably, in the present study, we found that low doses of mAEA are responsible for the increase in mitochondrial membrane potential and induction of PGC1α expression, without affecting oxygen consumption, whereas the highest dose of mAEA turns the TRPV1 action to negatively modulate mitochondrial membrane polarization and cell survival. The opposite functional changes mediated by TRPV1 may rely on concentration-dependent responses that via subtle increases in intracellular calcium positively affect mitochondrial membrane potential, whereas through mitochondrial calcium overload cause dysregulation of mitochondrial membrane potential and subsequent mitochondrial dysfunction. On a final note, markedly different consequences of low or high doses of AEA are not unprecedented. Indeed, in primary human melanocytes low (<1 μM) AEA leads to melanogenesis, whereas high (>5 μM) AEA causes development of melanoma tumors [75].

Overall, this study reveals a new critical cross-talk between S1P and eCB systems in skeletal-muscle cells, identifying the Ca^{2+} channel TRPV1 as a pivotal target and thus opening the avenue to new molecular approaches to control skeletal-muscle disorders characterized by calcium dyshomeostasis.

4. Materials and Methods

4.1. Materials and Reagents

Dulbecco's modified Eagle's medium, foetal calf serum and penicillin/streptomycin were from Corning (Corning, NY, USA). Bovine serum albumin (BSA) was purchased from Sigma-Aldrich (St. Louis, MO, USA). Sphingosine-1-phosphate (S1P, cod.62570) and methanandamide (N-(2-hydroxy-1R-methylethyl)-5Z,8Z,11Z,14Z-eicosatetraenamide, cod.157182-49-5) were from Cayman Chemicals (Ann Arbor, MI, USA); N-arachidonoyl-ethanolamine (anandamide (AEA), cod. A0580) and 2-arachidonoil-glycerol (2-AG, cod. A8973) were from Sigma-Aldrich (St. Louis, MO, USA). AEA-d8 and 2-AG-d8 were purchased from Cayman Chemicals (Ann Arbor, MI, USA) and were used as internal standards. The selective antagonists of CB_1 SR141716A (SR1, cod. SML0800), of CB_2 SR144528 (SR2, cod. SML1899) and of GPR55 ML193 trifluoroacetate (ML193, cod. SML1340) were from Sigma-Aldrich (St. Louis, MO, USA). The TRPV1 selective antagonist 5′-iodoresiniferatoxin (I-RTX, cod. 1362) was from TOCRIS (Bristol, UK). For molecular biology studies RevertAid H Minus First Strand cDNA Synthesis Kit, from Thermo Scientific (Waltham, MA, USA), and SensiFASTTM SYBR Lo-ROX kit, from Bioline (London, UK) were used.

4.2. Cell Culture and Treatment

Murine C2C12 myoblasts cell line (ATCC® CRL-1772™) was grown in Dulbecco's modified Eagle's medium supplemented with 10% foetal bovine serum, 100 U/mL penicillin/streptomycin and 2 mM L-glutamine at 37 °C in a humidified 5% CO_2 atmosphere [68]. When 90% confluent, myogenic differentiation was reached by substituting the proliferation medium with DMEM supplemented with 1 mg/mL BSA [68]. Then, cells were treated with 1 µM S1P [32] and/or with different concentrations (2.5, 5.0 and 10 µM) of mAEA for 24 or 48 h.

4.3. Quantitative Real Time-Reverse Transcriptase-Polymerase Chain Reaction (qRT-PCR) Analyses

For the quantification of gene-expression levels of receptors and metabolizing enzymes of eCBs, mRNA was extracted from control and S1P-treated C2C12 cells by using TRIzol, according to the manufacturer's instructions (Life Technologies, Grand Island, NY, USA), and was quantified by using Thermo Scientific NanoDrop 2000 c UV-Vis spectrophotometer at 260 nm (Waltham, MA, USA). Subsequently, 1 µg of total mRNA was retrotranscribed in cDNA by using the RevertAid H Minus First Strand cDNA Synthesis Kit (Life Technologies, Grand Island, NY, USA). SensiFASTTM SYBR Lo-ROX kit was used to assess the relative abundance of CB_1, CB_2, GPR55, TRPV1, FAAH, DAGLα, DAGLβ, NAPE-PLD and MAGL on a 7500 Fast Real-time PCR System (Life Technologies, Grand Island, NY, USA), as described previously [31,76]. Primer sequences are reported in Table 1. The relative expression of different amplicons was calculated by the ΔΔCt method and converted to relative expression ratio $2^{(-\Delta\Delta Ct)}$ for statistical analysis [77]. All data were normalized to the endogenous reference genes GAPDH and β-Actin.

4.4. Western Blotting

Control and S1P- or mAEA-treated cells were lysed in RIPA buffer in the presence of a protease inhibitors cocktail (Sigma-Aldrich, St. Louis, MO). Then, they were sonicated three times and centrifuged at 9500 g for 15 min at 4 °C; supernatants were collected and protein content was determined by the Bio-Rad Protein assay (Bio-Rad Laboratories, Hemel Hempstead, UK). Cell lysates were mixed with Laemli sample buffer (heated for 10 min at 60 °C) so that an equal amount of protein per lane (20–70 µg) were subjected to a 10% sodium dodecyl sulfate–polyacrylamide gel electrophoresis (SDS-PAGE). Gels were then electroblotted onto polyvinylidene difluoride (PVDF) membrane (Amersham Hybond, GE Healthcare Life Science, Piscataway, NJ, USA). Subsequently, PVDF membranes were blocked with 5% milk, incubated overnight with the primary antibodies in cold room and then with the appropriate horseradish peroxidase-conjugated secondary antibody (cod.31461, Thermo Fisher Scientific, Waltham, MA, USA) for 1 h at room temperature.

Primary antibodies specific for the following proteins were used: β-actin (cod.4970, Cell Signaling, Danvers, MA, USA), CB_1 C-Terminal (cod. 10006590, Cayman Chemical, Ann Arbor, MI, USA), CB_2 (cod.101550, Cayman Chemical), GPR55 (cod. 10224, Cayman Chemical), TRPV1 (cod. TA336871, OriGene, Rockville, MD, USA), FAAH (cod.101600, Cayman chemical), DAGLα (cod.PA5-23765, Invitrogen, Waltham, MA, USA), DAGLβ (cod.12574, Cell Signaling), MAGL (cod.10212, Cayman Chemical), NAPE-PLD (cod.10305, Cayman Chemical) and PGC1α (cod. SAB1411922, Sigma-Aldrich, St. Louis, MO, USA).

Table 1. List of the primers used to assess the relative abundance of eCB-binding receptors and metabolic enzymes.

	Forward Primer (5′->3′)	Reverse Primer (5′->3′)
β-ACTIN	TGTTACCAACTGGGACGA	GTCTCAAACATGATCTGGGTC
GAPDH	AACGGGAAGCTCACTGGCAT	GCTTCACCACCTTCTTGATG
CB_1	CCAAGAAAAGATGACGGCAG	AGGATGACACATAGCACCAG
CB_2	TCGCTTACATCCTTCAGACAG	TCTTCCCTCCCAACTCCTTC
GPR55	ATTCGATTCCGTGGATAAGC	ATGCTGATGAAGTAGAGGC
TRPV1	TGAACTGGACTACCTGGAAC	TCCTTGAAGACCTCAGCATC
NAPE-PLD	AAGTGTGTCTTCTAGGTTCTCC	TTGTCAAGTTCCTCTTTGGAACC
FAAH	AGATTGAGATGTATCGCCAG	CTTCAGAATGTTGTCCCAC
DAGLα	AATGGCTATCATCTGGCTGAGC	TTCCGAGGGTGACATTCTTAGC
DAGLβ	TGTCAGCATGAGAGGAACCAT	CGCCAGGCGGATATAGAGC
MAGL	TTGTAGATACTGGAAGCCC	ATGGTGTCCACGTGTTGCAGC

Total OXPHOS WB Antibody Cocktail (Abcam) was used to analyze complex II, III, IV and ATP synthase.

Detection was performed by Clarity Western ECL substrate (Bio-Rad, Hercules, CA, USA) as developed by Azure Biosystems c400 (Sierra Ct, Dublin, CA, USA). Immunoreactive band intensities was quantified by densitometric analysis through the ImageJ software (NIH, Bethesda, MD, USA), as reported [45].

4.5. LC/MS Analysis

The lipid fractions from control and S1P-treated C2C12 cells were extracted with chloroform/methanol (2:1 *v*/*v*) in the presence of internal standards (1 ng mL^{-1} AEA-d8, 200 ng mL^{-1} 2-AG-d8). Then, a clean-up step was performed as previously reported [78]. Briefly, the organic phase was dried and then subjected to micro-solid phase extraction (μSPE) for a rapid clean-up, by using OMIX C18 tips from Agilent Technologies (Santa Clara, CA, USA). All analyses were performed on a Nexera LC 20 AD XR UHPLC system (Shimadzu Scientific Instruments, Columbia, MD, USA) with NUCLEODUR® C18 Isis column from Macherey-Nagel GmbH and Co. (Neumann, Germany), coupled with a 4500 Qtrap mass spectrometer from Sciex (Concord, ON, Canada) equipped with a Turbo V electrospray ionization (ESI) source, operating in positive mode. The levels of AEA and 2-AG were then calculated on the basis of their area ratios with the internal deuterated standard signal areas, and their amounts in pmoles were normalized to the number of cells, as reported [75].

4.6. Mitochondrial Membrane Potential Assays

Mitochondrial membrane potential (ΔΨm) status of C2C12 cells, untreated or treated with mAEA at different concentrations (2.5 μM, 5.0 μM and 10 μM) for 24 h, was assessed with the lipophilic cation JC-1 [48]. Briefly, cells were plated onto a 96 well/plate at a density of 15 × 10^4. Specific and selective eCB-binding receptor antagonists SR1 (CB_1), SR2 (CB_2), ML193 (GPR55) and 5′-IRTX (TRPV1) were administered to cells at a concentration of 0.1 μM [46–48,79–82], 15 min before the incubation with mAEA, alone or in combination with 1 μM S1P for 24 h. As positive control, the potent mitochondrial uncoupler carbonyl cyanide m-chlorophenyl hydrazone (CCCP) was used at 50 μM. Then, cells were washed with PBS and stained with 2 μM JC-1 dye for 15 min, and then were analyzed by Enspire

multimode plate reader (Perkin Elmer, MA, USA). Fluorescence intensities were calculated as red (590 nm) on green (526 nm) ratios, and were expressed as percentage (%) of controls as described [83].

The ΔΨm of C2C12 myoblasts was also assessed by Mito Tracker Red CMXRos (#M7512) probe (Thermo Fisher Scientific INC, MA, USA) and Laser scanning confocal microscopy after the treatment with mAEA (5 μM), in the presence of selective eCB-binding receptor antagonists, and/or 1 μM S1P for 24 h. Briefly, cells were seeded on microscope slides and grown for 24 h before being shifted in serum-free 0.1% BSA-containing medium in the presence or absence of mAEA. Specific and selective eCB-binding receptor antagonists were used as above described. The probe was diluted in DMEM medium without phenol red at a concentration of 50 nM, incubated for 30 min at 37 °C and 5% CO_2 in the dark, and then slides were fixed in 2% paraformaldehyde. Subsequently, cells were washed twice and incubated with a permeabilization and quenching solution (0.1% Triton X-100 and ethanolamine (1:165) in PBS). A DAPI solution (#MBD0015, Sigma-Aldrich, MA, USA) was used to detect nuclei. Slides were mounted by using Fluoromount Aqueous Mounting Medium (Sigma-Aldrich, MA, USA), and images were obtained in a Leica SP8 laser scanning confocal microscope (Leica Microsystems GmbH, Wetzlar, Germany) using a 40× oil immersion objective.

4.7. MTT Assay

Cells were seeded into 96-well plates, at density of 1.5 × 104 per well, and incubated overnight. The day after, cells were incubated with different concentrations of mAEA (2.5–5.0–10 μM) for 24 h. Cell viability was assessed by the mitochondrial-dependent reduction of 3-[4,5-dimethylthiazol-2-yl]-2,5-diphenyl tetrazolium bromide (MTT; Sigma, St. Louis, MO, USA) to purple formazan. After 3 h, the MTT solution was discarded and 100 μL of DMSO were added to dissolve the formazan crystals. Cells were analyzed by Enspire multimode plate reader (Perkin Elmer, MA, USA). The cell viability was calculated by subtracting the 630 nm OD background from the 570 nm OD total signal of cell-free blank of each sample, and was expressed as percentage of controls set to 100%.

4.8. Intact Myoblast Respiration Using High-Resolution Respirometry

Oxygen consumption was analyzed in 2 mL glass chambers at 37 °C using the Oroboros oxygraph-2K high-resolution respirometer (Oroboros Instruments, Innsbruck, Austria) and substrate, uncoupler, inhibitor, titration (SUIT) protocols, as reported [84]. The oxygen flux normalized on the cell number is calculated as the negative time derivative of the oxygen concentration, measured in sealed chambers, and normalized on the instrumental background (measured in a dedicated experiment before assaying the cells). C2C12 myoblasts treated with 5 μM mAEA or vehicle (ethanol) for 24 h were subjected to respirometry analysis. After instrumental air calibration, 300.000 cells resuspended in DMEM with 1 mg/mL BSA were introduced into the chambers and the basal respiratory activity was measured as routine respiration (R). The LEAK state (L) represents the non-phosphorylating state of uncoupled respiration due to proton leak, proton and electron slip, and cation cycling [85] after the inhibition of ATP synthase by oligomycin administration (5 nM). The capability of the electron transfer system (ETS) was measured by uncoupler titrations using the uncoupler CCCP (1.5 μM/titration steps) as the readout of the maximal capacity of oxygen utilization (E). The residual oxygen consumption (ROX) that remains after the inhibition of ETS was determined by antimycin A (2.5 μM) injection. Data acquisition and analysis were performed using DatLab software (version 7.4, Oroboros Instrument, Innsbruck, Austria), and the oxygen fluxes recorded in the individual titration steps were corrected for ROX.

4.9. Statistical Analysis

Data were analysed by the GraphPad Prism 9.3.1 (471) program (GraphPad Software, La Jolla, CA, USA), and were reported as means ± S.E.M of 3 to 5 independent experiments.

The statistical analysis was performed through the Student's *t*-test and one-way or two-way analysis of variance (ANOVA), followed by Bonferroni post-hoc analysis. A level of $p < 0.05$ was considered statistically significant.

Author Contributions: Conceptualization, C.R., F.C., M.M. and P.B.; methodology, S.S., S.P., D.T., F.F., M.B., I.S., C.B. and C.D.; validation, S.S. and S.P.; formal analysis, S.S. and S.P.; investigation, S.S., S.P., D.T., C.D.M., F.F., M.S., M.B., I.S., C.B. and C.D.; resources, S.S. and S.P.; data curation, S.S. and S.P.; writing—original draft preparation, S.S. and S.P.; writing—review and editing, C.R., F.C., M.M. and P.B.; visualization, S.S. and S.P.; supervision, M.M. and P.B.; project administration, M.M.; funding acquisition, M.M., C.R., F.C., P.B., C.D. and C.B. All authors have read and agreed to the published version of the manuscript.

Funding: This research was supported by the Italian Ministry for Instruction, University and Research (MIUR) under the National Operative Program (PON): Programma Operativo Nazionale Ricerca e Innovazione 2014-2020 (CCI 2014IT16M2OP005), Fondo Sociale Europeo (FSE), Azione I.1 "Dottorati Innovativi con caratterizzazione Industriale, by the Fondo di Finanziamento di Ricerca FARDIB, University of Teramo, and under competitive PRIN2017 grant (no. 2017BTHJ4R_001) to M.M. The work was supported by University of Florence (Fondi Ateneo to P.B., C.B., C.D. and F.C.). M.B. is a Fondazione Pezcoller/SIC De Gasperi Ronc fellow.

Institutional Review Board Statement: Not applicable.

Informed Consent Statement: Not applicable.

Data Availability Statement: All experimental data are presented in the article.

Acknowledgments: We thank Andrea Morandi (University of Florence) for the fruitful discussion and for providing feedback on the respirometry data analysis.

Conflicts of Interest: The authors declare no conflict of interest.

References

1. Hannun, Y.A.; Obeid, L.M. Principles of bioactive lipid signalling: Lessons from sphingolipids. *Nat. Rev. Mol. Cell Biol.* **2008**, *9*, 139–150. [CrossRef] [PubMed]
2. Bryan, L.; Kordula, T.; Spiegel, S.; Milstien, S. Regulation and functions of sphingosine kinases in the brain. *Biochim. Biophys. Acta Mol. Cell Biol. Lipids* **2008**, *1781*, 459–466. [CrossRef] [PubMed]
3. Spiegel, S.; Milstien, S. Sphingosine-1-phosphate: An enigmatic signalling lipid. *Nat. Rev. Mol. Cell Biol.* **2003**, *4*, 397–407. [CrossRef] [PubMed]
4. Peest, U.; Sensken, S.C.; Andréani, P.; Hänel, P.; van Veldhoven, P.P.; Gräler, M.H. S1P-lyase independent clearance of extracellular sphingosine 1-phosphate after dephosphorylation and cellular uptake. *J. Cell Biochem.* **2008**, *104*, 756–772. [CrossRef] [PubMed]
5. Takabe, K.; Paugh, S.W.; Milstien, S.; Spiegel, S. Inside-out signaling of sphingosine-1-phosphate: Therapeutic targets. *Pharmacol. Rev.* **2008**, *60*, 181–195. [CrossRef]
6. Kobayashi, N.; Kawasaki-Nishi, S.; Otsuka, M.; Hisano, Y.; Yamaguchi, A.; Nishi, T. MFSD2B is a sphingosine 1-phosphate transporter in erythroid cells. *Sci. Rep.* **2018**, *8*, 4969. [CrossRef]
7. Cuvillier, O.; Pirianov, G.; Kleuser, B.; Vanek, P.G.; Cosot, O.A.; Gutkind, J.S.; Spiegel, S. Suppression of ceramide-mediated programmed cell death by sphingosine-1-phosphate. *Nature* **1996**, *381*, 800–803. [CrossRef]
8. Rosen, H.; Goetzl, E.J. Sphingosine 1-phosphate and its receptors: An autocrine and paracrine network. *Nat. Rev. Immunol.* **2005**, *5*, 560–570. [CrossRef]
9. Cartier, A.; Hla, T. Sphingosine 1-phosphate: Lipid signaling in pathology and therapy. *Science* **2019**, *366*, eaar5551. [CrossRef]
10. Donati, C.; Cencetti, F.; Bruni, P. Sphingosine 1-phosphate axis: A new leader actor in skeletal muscle biology. *Front. Physiol.* **2013**, *4*, 338. [CrossRef]
11. Friedman, D.; French, J.A.; Maccarrone, M. Safety, efficacy, and mechanisms of action of cannabinoids in neurological disorders. *Lancet Neurol.* **2019**, *18*, 504–512. [CrossRef]
12. Maccarrone, M.; Guzmán, M.; Mackie, K.; Doherty, P.; Harkany, T. Programming of neural cells by (endo)cannabinoids: From physiological rules to emerging therapies. *Nat. Rev. Neurosci.* **2014**, *15*, 786–801. [CrossRef] [PubMed]
13. Maccarrone, M.; Rapino, C.; Francavilla, F.; Barbonetti, A. Cannabinoid signalling and effects of cannabis on the male reproductive system. *Nat. Rev. Urol.* **2020**, *18*, 19–32. [CrossRef] [PubMed]
14. Cristino, L.; Bisogno, T.; di Marzo, V. Cannabinoids and the expanded endocannabinoid system in neurological disorders. *Nat Rev. Neurol.* **2020**, *16*, 9–29. [CrossRef]
15. Luchicchi, A.; Pistis, M. Anandamide and 2-arachidonoylglycerol: Pharmacological properties, functional features, and emerging specificities of the two major endocannabinoids. *Mol. Neurobiol.* **2012**, *46*, 374–392. [CrossRef]

16. Maccarrone, M.; Dainese, E.; Oddi, S. Intracellular trafficking of anandamide: New concepts for signaling. *Trends Biochem. Sci.* **2010**, *35*, 601–608. [CrossRef]
17. Murataeva, N.; Straiker, A.; MacKie, K. Parsing the players: 2-arachidonoylglycerol synthesis and degradation in the CNS. *Br. J. Pharmacol.* **2014**, *171*, 1379–1391. [CrossRef]
18. Lu, H.C.; MacKie, K. An introduction to the endogenous cannabinoid system. *Biol. Psychiatry* **2016**, *79*, 516–525. [CrossRef]
19. Ryberg, E.; Larsson, N.; Sjögren, S.; Hjorth, S.; Hermansson, N.O.; Leonova, J.; Elebring, T.; Nilsson, K.; Drmota, T.; Greasley, P.J. The orphan receptor gpr55 is a novel cannabinoid receptor. *Br. J. Pharmacol.* **2007**, *152*, 1092–1101. [CrossRef]
20. Gasperi, V.; Dainese, E.; Oddi, S.; Sabatucci, A.; Maccarrone, M. GPR55 and its interaction with membrane lipids: Comparison with other endocannabinoid-binding receptors. *Curr. Med. Chem.* **2012**, *20*, 64–78. [CrossRef]
21. Ross, R.A. The enigmatic pharmacology of GPR55. *Trends Pharmacol. Sci.* **2009**, *30*, 156–163. [CrossRef] [PubMed]
22. Rosenbaum, T.; Sydney, A.S. TRPV1 receptors and signal transduction. In *TRP Ion Channel Function in Sensory Transduction and Cellular Signaling Cascades*; CRC Press: Boca Raton, FL, USA, 2007. [CrossRef]
23. Howlett, A.C.; Shim, J. *Cannabinoid Receptors and Signal Transduction*; Landes Bioscience: Austin, TX, USA, 2011.
24. Greig, F.H.; Nather, K.; Ballantyne, M.D.; Kazi, Z.H.; Alganga, H.; Ewart, M.A.; Zaborska, K.E.; Fertig, B.; Pyne, N.J.; Pyne, S.; et al. Requirement for sphingosine kinase 1 in mediating phase 1 of the hypotensive response to anandamide in the anaesthetised mouse. *Eur. J. Pharmacol.* **2019**, *842*, 1–9. [CrossRef] [PubMed]
25. Sanchez, T.; Hla, T. Structural and functional characteristics of S1P receptors. *J. Cell Biochem.* **2004**, *92*, 913–922. [CrossRef] [PubMed]
26. Galve-Roperh, I.; Sánchez, C.; Cortés, M.L.; del Pulgar, T.G.; Izquierdo, M.; Guzmán, M. Anti-tumoral action of cannabinoids: Involvement of sustained ceramide accumulation and extracellular signal-regulated kinase activation. *Nat. Med.* **2000**, *6*, 313–319. [CrossRef]
27. Mair, K.M.; Robinson, E.; Kane, K.A.; Pyne, S.; Brett, R.R.; Pyne, N.J.; Kennedy, S. Interaction between anandamide and sphingosine-1-phosphate in mediating vasorelaxation in rat coronary artery. *Br. J. Pharmacol.* **2010**, *161*, 176–192. [CrossRef]
28. Paugh, S.W.; Cassidy, M.P.; He, H.; Milstien, S.; Sim-Selley, L.J.; Spiegel, S.; Selley, D.E. Sphingosine and its analog, the immunosuppressant 2-amino-2-(2-[4-octylphenyl] ethyl)-1,3-propanediol, interact with the CB_1 cannabinoid receptor. *Mol. Pharmacol.* **2006**, *70*, 41–50. [CrossRef]
29. Zhao, D.; Pond, A.; Watkins, B.; Gerrard, D.; Wen, Y.; Kuang, S.; Hannon, K. Peripheral endocannabinoids regulate skeletal muscle development and maintenance. *Eur. J. Transl. Myol.* **2010**, *20*, 167–180. [CrossRef]
30. Kim, J.; Carlson, M.E.; Watkins, B.A. Docosahexaenoyl ethanolamide improves glucose uptake and alters endocannabinoid system gene expression in proliferating and differentiating C2C12 myoblasts. *Front. Physiol.* **2014**, *5*, 100. [CrossRef]
31. Bernacchioni, C.; Ghini, V.; Squecco, R.; Idrizaj, E.; Garella, R.; Puliti, E.; Cencetti, F.; Bruni, P.; Donati, C. Role of sphingosine 1-phosphate signalling axis in muscle atrophy induced by Tnfα in C2c12 myotubes. *Int. J. Mol. Sci.* **2021**, *22*, 1280. [CrossRef]
32. Donati, C.; Meacci, E.; Nuti, F.; Becciolini, L.; Farnararo, M.; Bruni, P. Sphingosine 1-phosphate regulates myogenic differentiation: A major role for $S1P_2$ receptor. *FASEB J.* **2005**, *19*, 1–22. [CrossRef]
33. Cencetti, F.; Bernacchioni, C.; Nincheri, P.; Donati, C.; Bruni, P. Transforming growth factor-1 induces transdifferentiation of myoblasts into myofibroblasts via up-regulation of sphingosine kinase-1/S1P 3 axis. *Mol. Biol. Cell* **2010**, *21*, 1111–1124. [CrossRef]
34. Bernacchioni, C.; Cencetti, F.; Blescia, S.; Donati, C.; Bruni, P. Sphingosine kinase/sphingosine 1-phosphate axis: A new player for insulin-like growth factor-1-induced myoblast differentiation. *Skelet. Muscle* **2012**, *2*, 15. [CrossRef]
35. Iannotti, F.A.; Silvestri, C.; Mazzarella, E.; Martella, A.; Calvigioni, D.; Piscitelli, F.; Ambrosino, P.; Petrosino, S.; Czifra, G.; Bír´o, T.; et al. The endocannabinoid 2-AG controls skeletal muscle cell differentiation via CB_1 receptor-dependent inhibition of K_V7 channels. *Proc. Natl. Acad. Sci. USA* **2014**, *111*, E2472–E2481. [CrossRef] [PubMed]
36. Pagano, E.; Orlando, P.; Finizio, S.; Rossi, A.; Buono, L.; Iannotti, F.A.; Piscitelli, F.; Izzo, A.A.; di Marzo, V.; Borrelli, F. Role of the endocannabinoid system in the control of mouse myometrium contractility during the menstrual cycle. *Biochem. Pharmacol.* **2017**, *124*, 83–93. [CrossRef] [PubMed]
37. Kunos, G.; Osei-Hyiaman, D.; Liu, J.; Godlewski, G.; Bátkai, S. Endocannabinoids and the control of energy homeostasis. *J. Biol. Chem.* **2008**, *283*, 33021–33025. [CrossRef] [PubMed]
38. Pasquariello, N.; Catanzaro, G.; Marzano, V.; Amadio, D.; Barcaroli, D.; Oddi, S.; Federici, G.; Urbani, A.; Agrò, A.F.; Maccarrone, M. Characterization of the endocannabinoid system in human neuronal cells and proteomic analysis of anandamide-induced apoptosis. *J. Biol. Chem.* **2009**, *284*, 29413–29426. [CrossRef]
39. Silvestri, C.; di Marzo, V. The Endocannabinoid system in energy homeostasis and the etiopathology of metabolic disorders. *Cell Metab.* **2013**, *17*, 475–490. [CrossRef]
40. Abadji, V.; Lin, S.; Taha, G.; Griffin, G.; Stevenson, L.A.; Pertwee, R.G.; Makriyannis, A. (R)-methanandamide: A chiral novel anandamide possessing higher potency and metabolic stability. *J. Med. Chem.* **1994**, *37*, 1889–1893. [CrossRef]
41. Huang, T.Y.; Zheng, D.; Houmard, J.A.; Brault, J.J.; Hickner, R.C.; Cortright, R.N. Overexpression of PGC-1α increases peroxisomal activity and mitochondrial fatty acid oxidation in human primary myotubes. *Am. J. Physiol. Endocrinol. Metab.* **2017**, *312*, E253–E263. [CrossRef]
42. Catanzaro, G.; Rapino, C.; Oddi, S.; Maccarrone, M. Anandamide increases swelling and reduces calcium sensitivity of mitochondria. *Biochem. Biophys. Res. Commun.* **2009**, *388*, 439–442. [CrossRef]

43. Gasperi, V.; Fezza, F.; Pasquariello, N.; Bari, M.; Oddi, S.; Finazzi Agrò, A.; Maccarrone, M. Endocannabinoids in adipocytes during differentiation and their role in glucose uptake. *Cell. Mol. Life Sci.* **2007**, *64*, 219–229. [CrossRef] [PubMed]
44. Sivandzade, F.; Bhalerao, A.; Cucullo, L. Analysis of the mitochondrial membrane potential using the cationic JC-1 dye as a sensitive fluorescent probe. *Bio-Protocol* **2019**, *9*, e3128. [CrossRef] [PubMed]
45. Pertwee, R.G. Receptors and channels targeted by synthetic cannabinoid receptor agonists and antagonists. *Curr. Med. Chem.* **2010**, *17*, 1360–1381. [CrossRef]
46. Kotsikorou, E.; Sharir, H.; Shore, D.M.; Hurst, D.P.; Lynch, D.L.; Madrigal, K.E.; Heynen-Genel, S.; Milan, L.B.; Chung, T.D.Y.; Seltzman, H.H.; et al. Identification of the GPR55 antagonist binding site using a novel set of high-potency GPR55 selective ligands. *Biochemistry* **2013**, *52*, 9456–9469. [CrossRef] [PubMed]
47. van der Stelt, M.; Trevisani, M.; Vellani, V.; de Petrocellis, L.; Moriello, A.S.; Campi, B.; McNaughton, P.; Geppetti, P.; di Marzo, V. Anandamide acts as an intracellular messenger amplifying Ca2+ influx via TRPV1 channels. *EMBO J.* **2005**, *24*, 3026–3037. [CrossRef]
48. Rigoni, M.; Trevisani, M.; Gazzieri, D.; Nadaletto, R.; Tognetto, M.; Creminon, C.; Davis, J.B.; Campi, B.; Amadesi, S.; Geppetti, P.; et al. Neurogenic responses mediated by vanilloid receptor-1 (TRPV1) are blocked by the high affnity antagonist, iodo-resiniferatoxin. *Br. J. Pharmacol.* **2003**, *138*, 977–985. [CrossRef]
49. Calise, S.; Blescia, S.; Cencetti, F.; Bernacchioni, C.; Donati, C.; Bruni, P. Sphingosine 1-phosphate stimulates proliferation and migration of satellite cells. role of s1p receptors. *Biochim. Biophys. Acta Mol. Cell Res.* **2012**, *1823*, 439–450. [CrossRef]
50. Loh, K.C.; Leong, W.I.; Carlson, M.E.; Oskouian, B.; Kumar, A.; Fyrst, H.; Zhang, M.; Proia, R.L.; Hoffman, E.P.; Saba, J.D. Sphingosine-1-phosphate enhances satellite cell activation in dystrophic muscles through a S1PR2/STAT3 signaling pathway. *PLoS ONE* **2012**, *7*, e37218. [CrossRef]
51. Nagata, Y.; Partridge, T.A.; Matsuda, R.; Zammit, P.S. Entry of muscle satellite cells into the cell cycle requires sphingolipid signaling. *J. Cell Biol.* **2006**, *174*, 245–253. [CrossRef]
52. Rapizzi, E.; Taddei, M.L.; Fiaschi, T.; Donati, C.; Bruni, P.; Chiarugi, P. Sphingosine 1-phosphate increases glucose uptake through trans-activation of insulin receptor. *Cell. Mol. Life Sci.* **2009**, *66*, 3207–3218. [CrossRef]
53. Iannotti, F.A.; Pagano, E.; Guardiola, O.; Adinolfi, S.; Saccone, V.; Consalvi, S.; Piscitelli, F.; Gazzerro, E.; Busetto, G.; Carrella, D.; et al. Genetic and pharmacological regulation of the endocannabinoid CB_1 receptor in duchenne muscular dystrophy. *Nat. Commun.* **2018**, *9*, 3950. [CrossRef]
54. Nguyen-Tran, D.H.; Hait, N.C.; Sperber, H.; Qi, J.; Fischer, K.; Ieronimakis, N.; Pantoja, M.; Hays, A.; Allegood, J.; Reyes, M.; et al. Molecular mechanism of sphingosine-1-phosphate action in duchenne muscular dystrophy. *DMM Dis. Models Mech.* **2014**, *7*, 41–54. [CrossRef] [PubMed]
55. Bisogno, T.; Howell, F.; Williams, G.; Minassi, A.; Cascio, M.G.; Ligresti, A.; Matias, I.; Schiano-Moriello, A.; Paul, P.; Williams, E.J.; et al. Cloning of the first Sn1-DAG lipases points to the spatial and temporal regulation of endocannabinoid signaling in the brain. *J. Cell Biol.* **2003**, *163*, 463–468. [CrossRef] [PubMed]
56. Glanemann, C.; Loos, A.; Gorret, N.; Willis, L.B.; O'brien, X.M.; Lessard, P.A.; Sinskey, A.J. Disparity between changes in MRNA abundance and enzyme activity in corynebacterium glutamicum: Implications for dna microarray analysis. *Appl. Microbiol. Biotechnol.* **2003**, *61*, 61–68. [CrossRef] [PubMed]
57. Colombo, G.; Rusconi, F.; Rubino, T.; Cattaneo, A.; Martegani, E.; Parolaro, D.; Bachi, A.; Zippel, R.; Rubino, T.; Parolaro, D.; et al. Transcriptomic and proteomic analyses of mouse cerebellum reveals alterations in RasGRF1 expression following in vivo chronic treatment with delta 9-tetrahydrocannabinol. *J. Mol. Neurosci.* **2009**, *37*, 111–122. [CrossRef]
58. Bari, M.; Paradisi, A.; Pasquariello, N.; Maccarrone, M. Cholesterol-dependent modulation of type 1 cannabinoid receptors in nerve cells. *J. Neurosci. Res.* **2005**, *81*, 275–283. [CrossRef]
59. Pasquariello, N.; Oddi, S.; Malaponti, M.; Maccarrone, M. Chapter 17 regulation of gene transcription and keratinocyte differentiation by anandamide. *Vitam. Horm.* **2009**, *81*, 441–467. [CrossRef]
60. Hong, H.; Yoon, B.; Ghil, S. Interactions between lysophosphatidylinositol receptor GPR55 and sphingosine-1-phosphate receptor S1P5 in live cells. *Biochem. Biophys. Res. Commun.* **2021**, *570*, 53–59. [CrossRef]
61. Bénard, G.; Massa, F.; Puente, N.; Lourenço, J.; Bellocchio, L.; Soria-Gómez, E.; Matias, I.; Delamarre, A.; Metna-Laurent, M.; Cannich, A.; et al. Mitochondrial CB_1 receptors regulate neuronal energy metabolism. *Nat. Neurosci.* **2012**, *15*, 558–564. [CrossRef]
62. Melser, S.; Zottola, A.C.P.; Serrat, R.; Puente, N.; Grandes, P.; Marsicano, G.; Hebert-Chatelain, E. Functional analysis of mitochondrial CB_1 cannabinoid receptors (MtCB1) in the brain. *Methods Enzymol.* **2017**, *593*, 143–174. [CrossRef]
63. Movsesyan, V.A.; Stoica, B.A.; Yakovlev, A.G.; Knoblach, S.M.; Lea, P.M.; Cernak, I.; Vink, R.; Faden, A.I. Anandamide-induced cell death in primary neuronal cultures: Role of calpain and caspase pathways. *Cell Death Differ.* **2004**, *11*, 1121–1132. [CrossRef] [PubMed]
64. Bartke, N.; Hannun, Y.A. Bioactive sphingolipids: Metabolism and function. *J. Lipid Res.* **2009**, *50*, S91–S96. [CrossRef] [PubMed]
65. Hait, N.C.; Oskeritzian, C.A.; Paugh, S.W.; Milstien, S.; Spiegel, S. Sphingosine kinases, sphingosine 1-phosphate, apoptosis and diseases. *Biochim. Biophys. Acta Biomembr.* **2006**, *1758*, 2016–2026. [CrossRef] [PubMed]
66. Fugio, L.B.; Coeli-Lacchini, F.B.; Leopoldino, A.M. Sphingolipids and mitochondrial dynamic. *Cells* **2020**, *9*, 581. [CrossRef]
67. di Marzo, V.; Iannotti, F.A.; Pagano, E.; Schiano Moriello, A.; Grazia Alvino, F.; Sorrentino, N.C.; Gazzerro, E.; Capasso, R.; de Leonibus, E.; de Petrocellis, L.; et al. Effects of non-euphoric plant cannabinoids on muscle quality and performance of dystrophic mdx mice. *Cannabinoid Res. Br. J. Pharmacol. Br. J. Pharmacol.* **2019**, *176*, 1568–1584. [CrossRef]

68. Rapizzi, E.; Donati, C.; Cencetti, F.; Nincheri, P.; Bruni, P. Sphingosine 1-phosphate differentially regulates proliferation of C2C12 reserve cells and myoblasts. *Mol. Cell Biochem.* **2008**, *314*, 193–199. [CrossRef]
69. Becciolini, L.; Meacci, E.; Donati, C.; Cencetti, F.; Rapizzi, E.; Bruni, P. Sphingosine 1-phosphate inhibits cell migration in C2C12 myoblasts. *Biochim. Biophys. Acta Mol. Cell Biol. Lipids* **2006**, *1761*, 43–51. [CrossRef]
70. Kittaka, H.; DeBrecht, J.; Mishra, S.K. Differential contribution of sensory transient receptor potential channels in response to the bioactive lipid sphingosine-1-phosphate. *Mol. Pain* **2020**, *16*, 1744806920903515. [CrossRef]
71. Meacci, E.; Cencetti, F.; Formigli, L.; Squecco, R.; Donati, C.; Tiribilli, B.; Quercioli, F.; Zecchi Orlandini, S.; Francini, F.; Bruni, P. Sphingosine 1-phosphate evokes calcium signals in C2C12 myoblasts via Edg3 and Edg5 receptors. *Biochem. J.* **2002**, *362*, 349–357. [CrossRef]
72. Duchen, M.R. Mitochondria and calcium: From cell signalling to cell death. *J. Physiol.* **2000**, *529*, 57–68. [CrossRef]
73. Luo, Z.; Ma, L.; Zhao, Z.; He, H.; Yang, D.; Feng, X.; Ma, S.; Chen, X.; Zhu, T.; Cao, T.; et al. TRPV1 activation improves exercise endurance and energy metabolism through PGC-1α upregulation in mice. *Cell Res.* **2012**, *22*, 551–564. [CrossRef] [PubMed]
74. Athanasiou, A.; Clarke, A.B.; Turner, A.E.; Kumaran, N.M.; Vakilpour, S.; Smith, P.A.; Bagiokou, D.; Bradshaw, T.D.; Westwell, A.D.; Fang, L.; et al. Cannabinoid receptor agonists are mitochondrial inhibitors: A unified hypothesis of how cannabinoids modulate mitochondrial function and induce cell death. *Biochem. Biophys. Res. Commun.* **2007**, *364*, 131–137. [CrossRef] [PubMed]
75. Pucci, M.; Pasquariello, N.; Battista, N.; di Tommaso, M.; Rapino, C.; Fezza, F.; Zuccolo, M.; Jourdain, R.; Agrò, A.F.; Breton, L.; et al. Endocannabinoids stimulate human melanogenesis via type-1 cannabinoid receptor. *J. Biol. Chem.* **2012**, *287*, 15466–15478. [CrossRef]
76. Bruno, G.; Cencetti, F.; Bernacchioni, C.; Donati, C.; Blankenbach, K.V.; Thomas, D.; Meyer zu Heringdorf, D.; Bruni, P. Bradykinin mediates myogenic differentiation in murine myoblasts through the involvement of SK1/Spns2/S1P 2 axis. *Cell Signal.* **2018**, *45*, 110–121. [CrossRef]
77. Livak, K.J.; Schmittgen, T.D. Analysis of relative gene expression data using real-time quantitative PCR and the $2^{-\Delta\Delta CT}$ method. *Methods* **2001**, *25*, 402–408. [CrossRef]
78. Sergi, M.; Montesano, C.; Napoletano, S.; Pizzoni, D.; Manetti, C.; Colistro, F.; Curini, R.; Compagnone, D. Analysis of bile acids profile in human serum by ultrafiltration clean-up and LC-MS/MS. *Chromatographia* **2012**, *75*, 479–489. [CrossRef]
79. Gervasi, M.G.; Osycka-Salut, C.; Caballero, J.; Vazquez-Levin, M.; Pereyra, E.; Billi, S.; Franchi, A.; Perez-Martinez, S. Anandamide capacitates bull spermatozoa through CB_1 and TRPV1 activation. *PLoS ONE* **2011**, *6*, e16993. [CrossRef] [PubMed]
80. Maccarone, R.; Rapino, C.; Zerti, D.; di Tommaso, M.; Battista, N.; di Marco, S.; Bisti, S.; Maccarrone, M. Modulation of type-1 and type-2 cannabinoid receptors by saffron in a rat model of retinal neurodegeneration. *PLoS ONE* **2016**, *11*, e0166827. [CrossRef]
81. Pertwee, R.G. Pharmacology of cannabinoid CB_1 and CB_2 receptors. *Pharmacol. Ther.* **1997**, *74*, 129–180. [CrossRef]
82. Heynen-Genel, S.; Dahl, R.; Shi, S.; Milan, L.; Hariharan, S.; Sergienko, E.; Hedrick, M.; Dad, S.; Stonich, D.; Su, Y.; et al. Probe report title: Screening for selective ligands for GPR55-agonists. In *Probe Reports from the NIH Molecular Libraries Program*; National Center for Biotechnology Information: Bethesda, MD, USA, 2011.
83. Liao, C.; Xu, D.; Liu, X.; Fang, Y.; Yi, J.; Li, X.; Guo, B. Iridium (III) complex-loaded liposomes as a drug delivery system for lung cancer through mitochondrial dysfunction. *Int. J. Nanomed.* **2018**, *13*, 4417–4431. [CrossRef]
84. Ye, F.; Hoppel, C.L. Measuring oxidative phosphorylation in human skin fibroblasts. *Anal. Biochem.* **2013**, *437*, 52–58. [CrossRef] [PubMed]
85. Pesta Dominik, G.E. High-resolution respirometry: OXPHOS protocols for human cells and permeabilized fibers from small biopsies of human muscle. *Methods Mol. Biol.* **2012**, *810*, 25–58. [CrossRef]

International Journal of
Molecular Sciences

MDPI

Article

Highly Charged Ru(II) Polypyridyl Complexes as Photosensitizer Agents in Photodynamic Therapy of Epithelial Ovarian Cancer Cells

Luca Conti [1], Gina Elena Giacomazzo [1], Barbara Valtancoli [1], Mauro Perfetti [1], Alberto Privitera [1], Claudia Giorgi [1,*], Patrick Severin Sfragano [1], Ilaria Palchetti [1], Sara Pecchioli [2], Paola Bruni [2] and Francesca Cencetti [2,*]

[1] Department of Chemistry "Ugo Schiff", University of Florence, 50019 Sesto Fiorentino, Italy
[2] Department of Experimental and Clinical Biomedical Sciences "Mario Serio", University of Florence, 50134 Florence, Italy
* Correspondence: claudia.giorgi@unifi.it (C.G.); francesca.cencetti@unifi.it (F.C.); Tel.: +39-0554573365 (C.G.); +39-0552751243 (F.C.)

Abstract: Ovarian cancer recurrence is frequent and associated with chemoresistance, leading to extremely poor prognosis. Herein, we explored the potential anti-cancer effect of a series of highly charged Ru(II)-polypyridyl complexes as photosensitizers in photodynamic therapy (PDT), which were able to efficiently sensitize the formation of singlet oxygen upon irradiation (**Ru1**$^{2+}$ and **Ru2**$^{2+}$) and to produce reactive oxygen species (ROS) in their corresponding dinuclear metal complexes with the Fenton active Cu(II) ion/s ([Cu**Ru1**]$^{4+}$ and [Cu_2**Ru2**]$^{6+}$). Their cytotoxic and anti-tumor effects were evaluated on human ovarian cancer A2780 cells both in the absence or presence of photoirradiation, respectively. All the compounds tested were well tolerated under dark conditions, whereas they switched to exert anti-tumor activity following photoirradiation. The specific effect was mediated by the onset of programed cell death, but only in the case of **Ru1**$^{2+}$ and **Ru2**$^{2+}$ was preceded by the loss of mitochondrial membrane potential soon after photoactivation and ROS production, thus supporting the occurrence of apoptosis via *type II* photochemical reactions. Thus, Ru(II)-polypyridyl-based photosensitizers represent challenging tools to be further investigated in the identification of new therapeutic approaches to overcome the innate chemoresistance to platinum derivatives of some ovarian epithelial cancers and to find innovative drugs for recurrent ovarian cancer.

Keywords: drug discovery; coordination complexes; phototoxicity; reactive oxygen species

Citation: Conti, L.; Giacomazzo, G.E.; Valtancoli, B.; Perfetti, M.; Privitera, A.; Giorgi, C.; Sfragano, P.S.; Palchetti, I.; Pecchioli, S.; Bruni, P.; et al. Highly Charged Ru(II) Polypyridyl Complexes as Photosensitizer Agents in Photodynamic Therapy of Epithelial Ovarian Cancer Cells. *Int. J. Mol. Sci.* **2022**, *23*, 13302. https://doi.org/10.3390/ijms232113302

Academic Editor: Young-Jin Kim

Received: 27 September 2022
Accepted: 27 October 2022
Published: 1 November 2022

1. Introduction

Ovarian cancer is one of the most common among gynecologic cancers and is the major cause of tumor-associated death in reproductive women [1,2]. Aggressive but asymptomatic progression frequently occurs followed by late diagnosis of advanced and metastatic stage in more than 70% of patients [3]. Surgery and chemotherapy are the major therapeutic choices, nevertheless with limited benefits, since the majority of ovarian cancer patients are initially sensitive to platinum- and taxane-based chemotherapies, which are the "golden standard" approach in ovarian cancer treatment, whereas almost half unfortunately suffer from recurrence, developing therapeutic resistance [4] in response to platinum-based chemotherapy. Therefore, innovative therapeutic strategies to overcome drug resistance are urgently needed.

Ruthenium polypyridyl complexes (RPCs) have been extensively studied and analyzed for their possibility of becoming alternative drugs in place of cisplatin [5–7]. Recently, their rich chemical–physical repertoire, which includes a wide range of photoluminescence characteristics, DNA binding abilities, tunable absorption properties and good singlet oxygen sensitizing features, made them ideal candidates as photosensitizer agents (PSs)

in the "so-called" photodynamic therapy (PDT). Their employment in this therapeutic approach continues to attract increasing attention due to the encouraging results obtained in the treatment of a wide variety of cancers, such as lung, bladder, skin tumors [8–11], and also bacterial infections [12–14].

In PDT, the PS is activated through irradiation with low-energy light to sensitize the generation of highly reactive species, namely reactive oxygen species (ROS), capable of ultimately leading to cytotoxic effects. This peculiar mechanism of action guarantees a complete spatial and temporal control over drug activation and thus offers the crucial advantage of potentially lowering the severe dose-limiting side effects normally occurring with standard therapeutics.

In general, ROS can be produced through distinct pathways. According to *Type I* reactions, the deactivation of the excited PS can occur via a direct electron or proton transfer to the surrounding biological substrates, leading to radical species that further interact with molecular oxygen to form ROS, such as superoxide, peroxides and hydroxyl radicals. *Type II* mechanisms are instead based on the direct interaction between the excited PS and ground-state molecular oxygen ($^3O_2$) to produce singlet oxygen ($^1O_2$), a highly cytotoxic species that is capable of rapidly reacting with biological targets (estimated half-life < 40 ns and radius of action of the order of 20 nm, in a biological environment) [15], leading to topical oxidative damages and, ultimately, to cellular death.

We have previously reported on the potential as PS agents of two highly charged Ru(II)-polypyridyl complexes $[Ru(phen)_2\mathbf{L'}]^{2+}$ (**Ru1**$^{2+}$) and $[Ru(phen)_2\mathbf{L''}]^{2+}$ (**Ru2**$^{2+}$), featuring the peculiar polyazamacrocyclic units **L′** and **L″** (**L′** = 4,4′-(2,5,8,11,14-pentaaza [15])-2,2′-bipyridilophane, **L″** = 4,4′-bis-[methylen-(1,4,7,10-tetraazacyclododecane)]-2,2′ bipyridine) and their corresponding copper(II) complexes [Cu**Ru1**]$^{4+}$ and [Cu_2**Ru2**]$^{6+}$ (see Scheme 1) [16,17]. Compared to the majority of RPCs used in PDT, the high number of easily protonable nitrogen groups gathered on the unique polyazamacrocyclic ligand of **Ru1**$^{2+}$, or on the two distinct cyclen (1,4,7,10-tetraazacyclododecane) moieties of **Ru2**$^{2+}$, confers to the resulting compounds the possibility to form highly charged species in aqueous media. This ensures excellent water solubility, a key requisite for biological application, but it also strengthens the capacity of ruthenium complexes to interact with possible biological targets, such as DNA. Importantly, the polyamine-based frameworks do not alter the good $^1O_2$ sensitizing properties of **Ru1**$^{2+}$ and **Ru2**$^{2+}$, making them appealing PSs for the generation of $^1O_2$ directly in aqueous matrices.

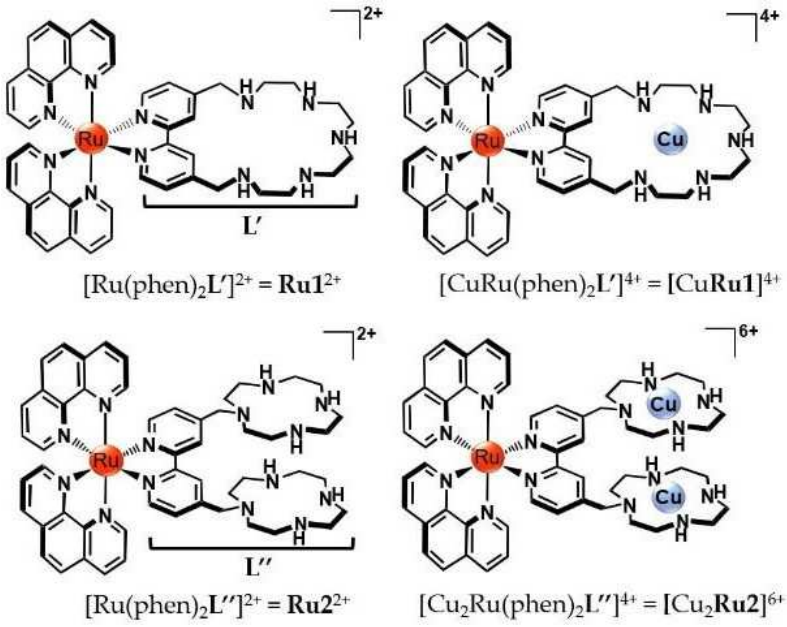

Scheme 1. Schematic representation of the ruthenium compounds studied in this work.

Furthermore, **L′** and **L″** allow stably binding up to two Fenton-active copper(II) ion/s, leading to the generation of mixed Ru(II)/Cu(II) complexed species, namely $[CuRu(phen)_2\mathbf{L'}]^{4+}$ ($[Cu\mathbf{Ru1}]^{4+}$) and $[Cu_2Ru(phen)_2\mathbf{L''}]^{6+}$ ($[Cu_2\mathbf{Ru2}]^{6+}$). These heteronuclear forms are able to generate other types of ROS, such as hydroxyl radicals, and thus may represent versatile tools in the research of alternative cytotoxic pathways to the singlet oxygen sensitization.

Prompted by the encouraging results previously displayed by $\mathbf{Ru1}^{2+}$ and $[Cu\mathbf{Ru1}]^{4+}$ in a human melanoma cell line [16], in this work, we explored the potential as photoresponsive anti-cancer compounds of all the $\mathbf{Ru1}^{2+}$, $[Cu\mathbf{Ru1}]^{4+}$, $\mathbf{Ru2}^{2+}$ and $[Cu_2\mathbf{Ru2}]^{6+}$ complexes in a unique and comparative study, where, in addition to the first comparison between the in-solution properties of these compounds, their in vitro anti-tumor efficacies were evaluated on A2780 human ovarian cancer cells. Moreover, a particular emphasis was placed on the study of the molecular mechanisms responsible for the observed anti-cancer effects by investigating the occurrence of apoptotic cell death, ROS production and mitochondrial function.

Our results show that ovarian cancer cells were capable of internalizing the ruthenium complexes at 6–24 h of incubation. Moreover, under dark conditions, these compounds exhibited extremely low cellular toxicity, which was particularly evident in non-cancer cells, whereas after photosensitization, they exerted a significant anti-tumor effect.

The results provided by this study can represent an important step forward in the research of alternative therapeutic approaches to platinum-based chemotherapy by employing ruthenium-based photoresponsive compounds.

2. Results

2.1. Protonation, Metal Binding of Ruthenium Compounds and Stability of the Mixed Ruthenium/Copper Complexed Species

The acid-base properties of $\mathbf{Ru1}^{2+}$ and $\mathbf{Ru2}^{2+}$ were investigated by means of potentiometric measurements in NMe_4Cl 0.1 M at 298 ± 0.1 K. The LogK values for the protonation constants and the corresponding distribution diagrams of the species present in solution are, respectively, reported in Table S1 and Figures S1 and S2 of SI. As shown, the presence of polyazamacrocycles **L′** and **L″** confers to the corresponding ruthenium compounds the ability to bind up to five ($[H_5\mathbf{Ru1}]^{7+}$) or six ($[H_6\mathbf{Ru2}]^{8+}$) protons in the overall range of pH investigated (between 2.5 and 10.5). Among the different protonated forms, the di- and tetra-protonated species $[H_2\mathbf{Ru1}]^{4+}$ and $[H_3\mathbf{Ru2}]^{5+}$ are the most abundant around neutral pH values (Figures S1 and S2, Supplementary Materials), including at the physiological pH value employed in biological experiments (vide infra). Nevertheless, for the sake of clarity, these species are simply referred to as $\mathbf{Ru1}^{2+}$ and $\mathbf{Ru2}^{2+}$ throughout the manuscript.

In addition to the ability to easily protonate in aqueous solution, the nitrogen donors gathered on the polyamine **L′** and **L″** frameworks can also act as suitable anchoring sites to host additional metal ions. Herein, we exploited this property to afford the formation of mixed heteronuclear Ru(II)/Cu(II) complexed species to evaluate whether the presence of Fenton-active Cu(II) center/s within the polyamine pockets of ruthenium compounds may have an influence on the biological potential of such hybrid, heteronuclear systems.

Analogously to the acid-base study, the formation of Ru(II)/Cu(II) complexes in solution was followed via potentiometric measurements; the LogK values for Cu(II) complexation by $\mathbf{Ru1}^{2+}$ and $\mathbf{Ru2}^{2+}$ and the corresponding distribution diagrams are, respectively, reported in Table 1 and Figures S3 and S4 of Supplementary Materials. As shown in Table 1, $\mathbf{Ru1}^{2+}$ and $\mathbf{Ru2}^{2+}$ form stable mono- and dinuclear complexes with Cu(II), with LogK values of 15.34 and 27.6 for the coordination of one ($\mathbf{Ru1}^{2+}$) and two ($\mathbf{Ru2}^{2+}$) Cu(II) ions. The coordination of copper is maintained in a wide range of pH, and, at the pH of the biological tests (7.4), these complexes are mainly present in their mononuclear $[Cu\mathbf{Ru}1]^{4+}$ and binuclear $[Cu_2\mathbf{Ru2}]^{6+}$ forms (Figures S3 and S4, Supplementary Materials).

Table 1. Stability constants of Cu(II), Zn(II), Ca(II) and Mg(II) complexes formed by $\mathbf{Ru1}^{2+}$ and $\mathbf{Ru2}^{2+}$ determined by means of potentiometric measurements in NMe_4Cl 0.1 M, at 298.1 ± 0.1 K.

Reaction	LogK	
	L = Ru1	**L = Ru2**
$\mathbf{L}^{2+} + Cu^{2+} = Cu\mathbf{L}^{4+}$	15.34 (6) [a]	16.72 (8)
$Cu\mathbf{L}^{4+} + H^{+} = CuH\mathbf{L}^{5+}$	5.60 (6)	7.58 (7)
$CuH\mathbf{L}^{5+} + H^{+} = CuH_2\mathbf{L}^{6+}$	3.91 (4)	5.89 (5)
$Cu\mathbf{L}^{4+} + OH^{-} = Cu\mathbf{L}(OH)^{3+}$	6.06 (4)	
$\mathbf{L}^{2+} + 2Cu^{2+} + OH^{-} = Cu_2\mathbf{L}(OH)^{5+}$	12.95 (5)	
$Cu\mathbf{L}^{4+} + Cu^{2+} = Cu_2\mathbf{L}^{6+}$		10.88 (7)
$Cu_2\mathbf{L}^{6+} + 2OH^{-} = Cu_2\mathbf{L}(OH)_2{}^{4+}$		9.48 (6)
$\mathbf{L}^{2+} + Zn^{2+} = Zn\mathbf{L}^{4+}$	8.90 (7)	14.91 (5)
$\mathbf{ZnL}^{4+} + H^{+} = ZnH\mathbf{L}^{5+}$	6.36 (7)	8.65 (4)
$ZnH\mathbf{L}^{5+} + H^{+} = ZnH_2\mathbf{L}^{6+}$	5.56 (6)	7.16 (5)
$ZnH_2\mathbf{L}^{6+} + H^{+} = ZnH_3\mathbf{L}^{7+}$	4.75 (8)	
$Zn\mathbf{L}^{4+} + 2OH^{-} = Zn\mathbf{L}(OH)_2{}^{2+}$	11.55 (4)	
$Zn\mathbf{L}^{4+} + Zn^{2+} = Zn_2\mathbf{L}^{6+}$		5.42 (7)
$Zn_2\mathbf{L}^{6+} + 3OH^{-} = Zn_2\mathbf{L}(OH)_3{}^{3+}$		15.48 (6)
$\mathbf{L}^{2+} + Ca^{2+} = Ca\mathbf{L}^{4+}$	2.62 (5)	2.55 (6)
$\mathbf{L}^{2+} + Mg^{2+} = Mg\mathbf{L}^{4+}$	2.23 (5)	2.06 (6)

[a] Values in parentheses are standard deviations in the standard deviations on the last significant figure.

Since different cations are naturally present in the biological environment, the metal-binding properties of ruthenium compounds toward other relevant metal ions were also considered. In particular, we focused on K^+, Na^+, Ca^{2+}, Mg^{2+} and Zn^{2+}, taken as the most abundant alkaline, alkaline-earth and transition cations in the cellular and extracellular matrices. As shown in Table 1, the most stable complexes among these cations were formed by Zn(II), with LogK values of 8.90 and 20.33, respectively, for the addition of one Zn(II) to $\mathbf{Ru1}^{2+}$ and two Zn(II) ions to $\mathbf{Ru2}^{2+}$. However, these values are considerably lower (up to ca. 1.7-fold) compared to Cu(II), thus highlighting the higher stability of the Ru(II)-Cu(II) complexed species compared to the ones formed by all the other cations tested. On the other hand, the affinity toward K^+ and Na^+ emerged to be too weak to permit an accurate determination of the relative LogK values via potentiometric analysis (LogK < 1.5).

The higher affinity of Ru(II) compounds for Cu(II) ion/s is further underlined by the selectivity diagrams reported in Figure S5 and determined as previously described [18]. As shown, the presence of Zn(II), Ca(II) and Mg(II), even in high concentrations, does not affect the formation of the Cu(II) complexes by both $\mathbf{Ru1}^{2+}$ and $\mathbf{Ru2}^{2+}$, and no Cu(II) release due to displacement by other metals takes place in the investigated range of pH. Metal decomplexation can only occur in low percentage (c.ca. 10%) at more acidic pH values, as expected, considering the protonation of polyamine residues of ruthenium compounds, which competes with metal binding in strong acidic conditions.

Therefore, taken together, these data underline the high stability of $[Cu\mathbf{Ru1}]^{4+}$ and $[Cu_2\mathbf{Ru2}]^{6+}$ in the adopted experimental conditions, suitable for the subsequent biological studies.

Lastly, it should also be mentioned that the coordination of Cu(II) markedly affects the fluorescence emission of the "metal-free" forms of ruthenium compounds. Indeed, $\mathbf{Ru1}^{2+}$ and $\mathbf{Ru2}^{2+}$ are highly luminescent and display an almost identical emission profile with a maximum centered at around 600 nm. Conversely, the presence of one ($[Cu\mathbf{Ru1}]^{4+}$) or two ($[Cu_2\mathbf{Ru2}]^{6+}$) Cu(II) ions within their polyamine pockets causes a tight decrease in the fluorescence emission (Figure S6, Supplementary Materials), an effect that can be naturally attributed to the paramagnetic nature of Cu(II) ion/s.

2.2. Reactive Oxygen Species (ROS) Production by Ruthenium Compounds

A key requisite for a candidate PS for PDT relies on its capacity to effectively produce ROS upon irradiation, such as the highly oxidant singlet oxygen $^1O_2$ species, which is produced according to *type-II*-based processes [19].

However, *type I* pathways can elicit severe damages as well [20]. Moreover, *type I* and *II* mechanisms can occur simultaneously, and recent studies underlined that radical species generated from *type I* processes can cooperate with $^1O_2$ to amplify the resulting PDT response, even under hypoxic conditions [21,22]. Therefore, the knowledge of the accessible pathways to PS agents is of paramount importance for their application in PDT.

As previously reported, $\mathbf{Ru1}^{2+}$ and $\mathbf{Ru2}^{2+}$ possess good singlet oxygen sensitizing properties, with comparable quantum yields (φ_Δ), respectively, of 0.29 ± 0.06 and 0.38 ± 0.08 (λ_{irr} = 400 nm, CH_3CN air-saturated solutions) [16,17]. On the contrary, the sensitization of $^1O_2$ becomes almost completely lost when Cu(II) is bound within the polyamine pockets of compounds. This effect can be easily rationalized with the fast deactivation of the excited states of $[Cu\mathbf{Ru1}]^{4+}$ and $[Cu_2\mathbf{Ru2}]^{6+}$ through internal conversion, which competes with the energy transfer to molecular oxygen.

For this reason, herein, we investigated the ability of $[Cu\mathbf{Ru1}]^{4+}$ and $[Cu_2\mathbf{Ru2}]^{6+}$ to elicit the formation of different typologies of ROS. This was performed through electron paramagnetic resonance (EPR), employing 5,5-dimethyl-1-pyrroline-N-oxide (DMPO) as the spin trap agent for free radicals (see Supplementary Materials for further details). Figure 1 reports a background experiment collected for a solution containing only H_2O_2 as co-reagent and DMPO, showing essentially no signal for ROS generation (blue trace in Figure 1). However, when $[Cu\mathbf{Ru1}]^{4+}$ or $[Cu_2\mathbf{Ru2}]^{6+}$ were added to the mixture, an EPR signal appeared (green and red traces for $[Cu_2\mathbf{Ru2}]^{6+}$ and $[Cu\mathbf{Ru1}]^{4+}$, respectively), clearly indicating ROS production by the mixed Ru(II)/Cu(II) complexes. The spectra recorded in the presence of $[Cu\mathbf{Ru1}]^{4+}$ and $[Cu_2\mathbf{Ru2}]^{6+}$ were strikingly similar, suggesting a comparable efficiency of the two systems in producing ROS.

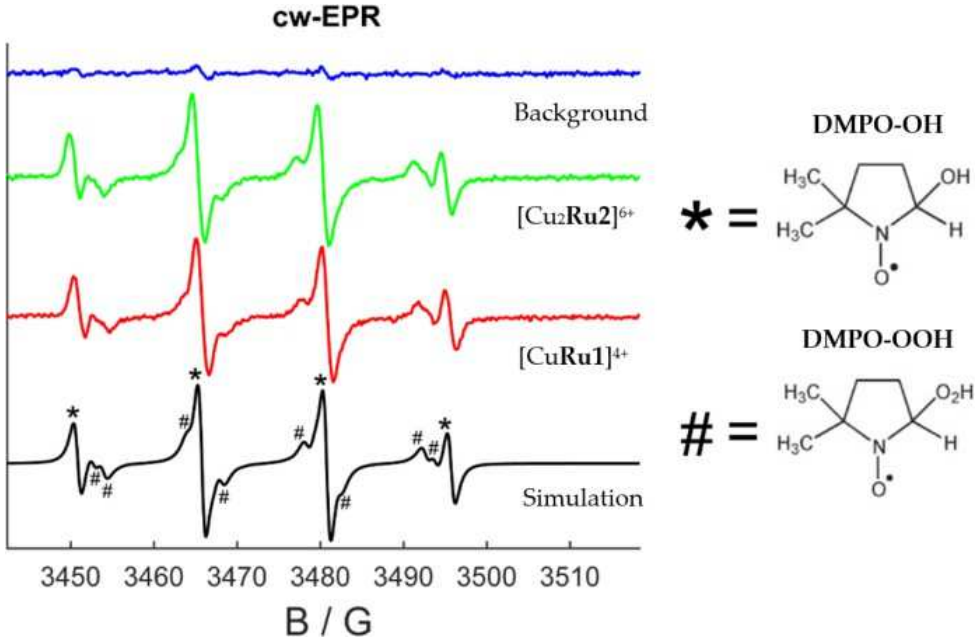

Figure 1. EPR spectra registered at 298 K of solutions containing DMPO and H_2O_2 (blue line), together with $[Cu\mathbf{Ru1}]^{4+}$ (red line) or $[Cu_2\mathbf{Ru2}]^{6+}$ (green line). The black trace is the best simulation (see text) obtained as a 50:50 mixture of hydroxide and peroxide radicals. Molecular structures of the corresponding adducts formed with DMPO are shown in the right part of the figure. The EPR lines referring to hydroxide and peroxide radicals are, respectively, labeled with symbols * and #. ([DMPO] = 750 mM, $[H_2O_2]$ = 100 mM, $[[Cu\mathbf{Ru1}]^{4+}]$ = $[[Cu_2\mathbf{Ru2}]^{6+}]$ = 5 mM).

The analysis of the narrow EPR signals can also provide useful information regarding the nature of the produced radical species. As shown by the black trace in Figure 1, the best simulation of the experimental spectra was obtained by considering the production of a 50:50 mixture of hydroxide ($OH^{\bullet}$) and perhydroxyl ($HOO^{\bullet}$) radicals (EPR lines referring to the two radical species are labeled with symbols in Figure 1, and a simulation of the single contributions is reported in Figure S7, Supplementary Materials). In analogy to other studies [23,24], these species might be the result of Fenton/Fenton-like processes mediated by the presence of reducing agents and involving the Cu(II)/Cu(I) redox cycle/s. This would be of great relevance for the biological behavior of these compounds. In fact, the cellular environment typically contains high concentrations of common reducing agents, such as glutathione, ascorbic acid and NADH, just to cite a few, which can reduce the coordinated Cu(II) ions and therefore facilitate the occurrence of Fenton/Fenton-like pathways (e.g., $Cu(I) + H_2O_2 \rightarrow Cu(II) + OH^- + OH^{\bullet}$) [23]. On the other hand, oxidation-reduction potential (ORP) measurements and cyclic voltammetry (CV) analysis of aqueous solutions of $[Cu\mathbf{Ru1}]^{4+}$ and $[Cu_2\mathbf{Ru2}]^{6+}$ confirmed that the copper centers of the two heteronuclear compounds might be reduced under these conditions (see paragraph 5 of Supplementary Materials for further details).

2.3. Internalization of Ru(II) Complexes

The human ovarian cancer cell line A2780 has been established from an untreated patient bearing an ovarian adenocarcinoma, and it is commonly used as a model for ovarian cancer in particular to test the anti-cancer potency and delivery of various drugs [25]. Preliminarily, the analysis of Ru(II) complexes' uptake in cancer versus non-cancer cells showed that, after 24 h of incubation, $\mathbf{Ru1}^{2+}$, $\mathbf{Ru2}^{2+}$, $[Cu\mathbf{Ru1}]^{4+}$ and $[Cu_2\mathbf{Ru2}]^{6+}$ complexes were finely localized in discrete areas of A2780 cells, whereas they were undetectable in C2C12 myoblasts (Figure S10, Supplementary Materials), thus demonstrating that ovarian cancer cells, but not untransformed myoblasts, efficiently internalize Ru(II) complexes.

The kinetics of internalization of Ru(II) complexes in A2780 cells as well as their intracellular distribution was therefore checked, employing laser-scanning confocal microscopy, with the purpose to set the proper time of incubation before photoactivation by exploiting the intrinsic fluorescence properties of Ru(II) compounds. As shown in Figure 2A, a localized distribution of $\mathbf{Ru1}^{2+}$ and $\mathbf{Ru2}^{2+}$ complexes was barely detectable in cells after 15 min, whereas the internalization increased at 6 h of incubation, showing a plateau at 24 h. Notwithstanding, the Ru(II)-Cu(II) complexes featured a considerably less intense fluorescence emission than $\mathbf{Ru1}^{2+}$ and $\mathbf{Ru2}^{2+}$ (Figure S6, Supplementary Materials). Their residual emission was sufficient to monitor their cellular uptake over time, which occurs with a kinetic profile similar to the ones of $\mathbf{Ru1}^{2+}$ and $\mathbf{Ru2}^{2+}$.

In parallel with confocal microscopy, fluorometric analysis was used to evaluate the kinetics of internalization of Ru(II) compounds. A2780 cells were treated with Ru(II) complexes at 10 μM for the indicated time of incubation. The results, shown in Figure 2B, are comparable with those obtained by confocal microscopy; the fluorescence signal at 600 nm increased from 6 to 18 h, reaching a plateau at 24 h of incubation. Notwithstanding, $\mathbf{Ru1}^{2+}$ and $\mathbf{Ru2}^{2+}$, almost equally emissive when administered at the same concentration, differed with regard to the intensity of fluorescence, being higher in the latter, thus suggesting an enhanced cellular internalization of $\mathbf{Ru2}^{2+}$.

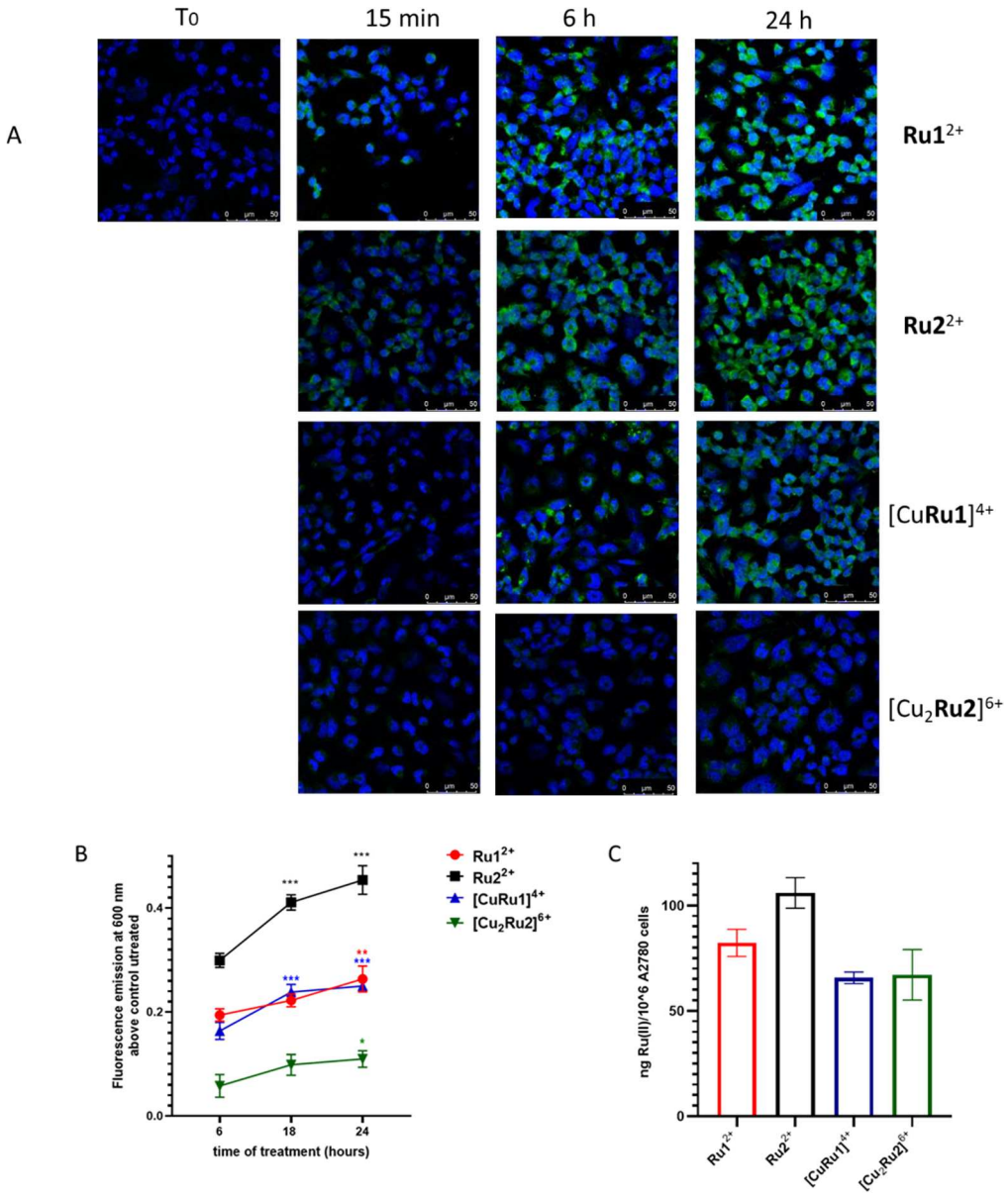

Figure 2. Internalization of Ru(II) complexes in A2780 cells. (**A**) Laser-scanning confocal microscopy was performed in A2780 cells incubated with each Ru(II) complex (10 μM) for the indicated time. DAPI (λ_{exc} = 405 nm, λ_{em} = 461 nm) was used to stain nuclei (blue spots), while the fluorescence emission in green represents that of Ru(II) complexes (λ_{exc} = 405 nm, λ_{em} = 600–640 nm). (**B**) Fluorometric analysis was performed in A2780 incubated with Ru(II) complexes (10 μM each) for 6–18–24 h. Data are reported as mean ± SD of fluorescence emission at 600 nm after subtraction of the background (untreated A2780 cells). The internalization of Ru(II) complexes was statistically significant according to one-way ANOVA followed by Bonferroni post hoc test. * $p < 0.05$, ** $p < 0.01$, *** $p < 0.001$. (**C**) Amount of internalized ruthenium after 24 h of incubation of 10^6 A2780 cells with each Ru(II) compound (10 μM). Data represent the mean ± SD of three independent experiments. The ruthenium content in the control sample, namely cells not treated with Ru(II) complexes, was not detectable.

Although the intrinsic fluorescence emission of compounds made it possible to follow their respective kinetics of internalization, it did not allow any quantitative estimation due to the different emissive properties, mainly between Cu(II)-free and Cu(II)-containing complexes. To this aim, the uptake of Ru(II) complexes in A2780 cells was also evaluated by measuring the content of ruthenium in cell lysates by ICP analysis, following 24 h incubation with a 10 μM dose of each compound (Figure 2C). As shown, **Ru1**$^{2+}$ and **Ru2**$^{2+}$

displayed higher internalization capacities compared to [Cu**Ru1**]$^{4+}$ and [Cu_2**Ru2**]$^{6+}$, the **Ru2**$^{2+}$ compound being one with the highest cellular uptake, in good agreement with confocal microscopy and fluorometric analysis.

Moreover, with the purpose of obtaining a hint on the possible internalization pathway of photosensitizers in A2780 cells, we performed immunofluorescence analysis using antibodies against Rab5, a crucial regulator of endocytosis, employed as a marker of early endosomes. Ru(II) complexes were differently localized compared to Rab5 (Figure S11A,B, Supplementary Materials), ruling out the possible involvement of a Rab5-dependent pathway in the internalization pathway of Ru(II) complexes.

Finally, based on these results, we chose to set the time of incubation with Ru(II) complexes before photoactivation at 24 h.

2.4. Effect of Ru(II) Complexes on A2780 Cell Survival after Photosensitization

The dose-dependent effect of **Ru1**$^{2+}$, **Ru2**$^{2+}$, [Cu**Ru1**]$^{4+}$ and [Cu_2**Ru2**]$^{6+}$ on dark cytotoxicity and photoactivity was evaluated through MTT assays in A2780 cells incubated for 24 h with different concentrations of Ru(II) complexes and exposed or not to photoirradiation 48 h before being analyzed. In the photoirradiation experiments, cells were irradiated with a light-emitting diode (LED, λ_{max} = 434 nm, 30 W) by employing the experimental set-up sketched in Figure S12 of Supplementary Materials.

As shown in Figure 3, under dark conditions, cell survival was only slightly affected by **Ru1**$^{2+}$ and **Ru2**$^{2+}$, at least up to a 1 μM dose of compounds. Then, beyond this value, cell viability underwent an approx. 35% decrease. An even lower cytotoxicity was displayed by the [Cu**Ru1**]$^{4+}$ and [Cu_2**Ru2**]$^{6+}$ complexes, being almost ineffective within the 0–10 μM range of concentration tested. In this respect, it can be tentatively speculated that the inferior activity of the mixed Ru(II)-Cu(II) complexed species would be associated with their lower capacity to be internalized by A2780 cells, as suggested by the internalization experiments described above.

Strikingly, the irradiation of complexes triggered a significant anti-cancer effect. Marked differences between the activities in dark and upon irradiation were indeed displayed by the good singlet oxygen sensitizers **Ru1**$^{2+}$ and **Ru2**$^{2+}$, starting from 100 nM.

Among the mixed heteronuclear complexes, [Cu**Ru1**]$^{4+}$ exhibited a sharper increase in phototoxicity when dosed at 10 μM, resulting in an approximatively 75% decrease of cell viability. Given the scarce ability of [Cu**Ru1**]$^{4+}$ and [Cu_2**Ru2**]$^{6+}$ to sensitize the formation of singlet oxygen, the anti-survival data suggest that alternative light-mediated pathways are made accessible by these systems in the cellular environment. Considering the redox activity of heteronuclear compounds (see Section 2.2), and in analogy to our previous study [16], a synergetic action between the Fenton-active copper center/s and light to generate harmful ROS species can be envisaged.

Interestingly, the effect of [Cu_2**Ru2**]$^{6+}$ was considerably less pronounced compared to the one of [Cu**Ru1**]$^{4+}$. This would suggest that, in addition to the similar cellular internalization and modes of activation of these latter two compounds, other less predictable features (such as differences in the chemical structures, chemical–physical properties, etc.) may play a role in the biological response of this typology of compounds.

Although PDT is a minimally invasive procedure, which effectively kills tumor cells, photosensitizers may have cytotoxic effects on normal cells. To study the effect of Ru(II) complexes on non-cancer cells, we performed MTT analysis in C2C12 myoblasts under dark and photoactivation conditions to assess Ru(II) complex cytotoxicity and photoactivity, respectively. As reported in Figure S13 of Supplementary Materials, Ru(II) complexes show negligible cytotoxicity and a minor photoactivity in myoblasts compared to A2780 cells, in agreement with the negligible internalization capacity of the PSs in this non-cancer cell model (Figure S10, Supplementary Materials).

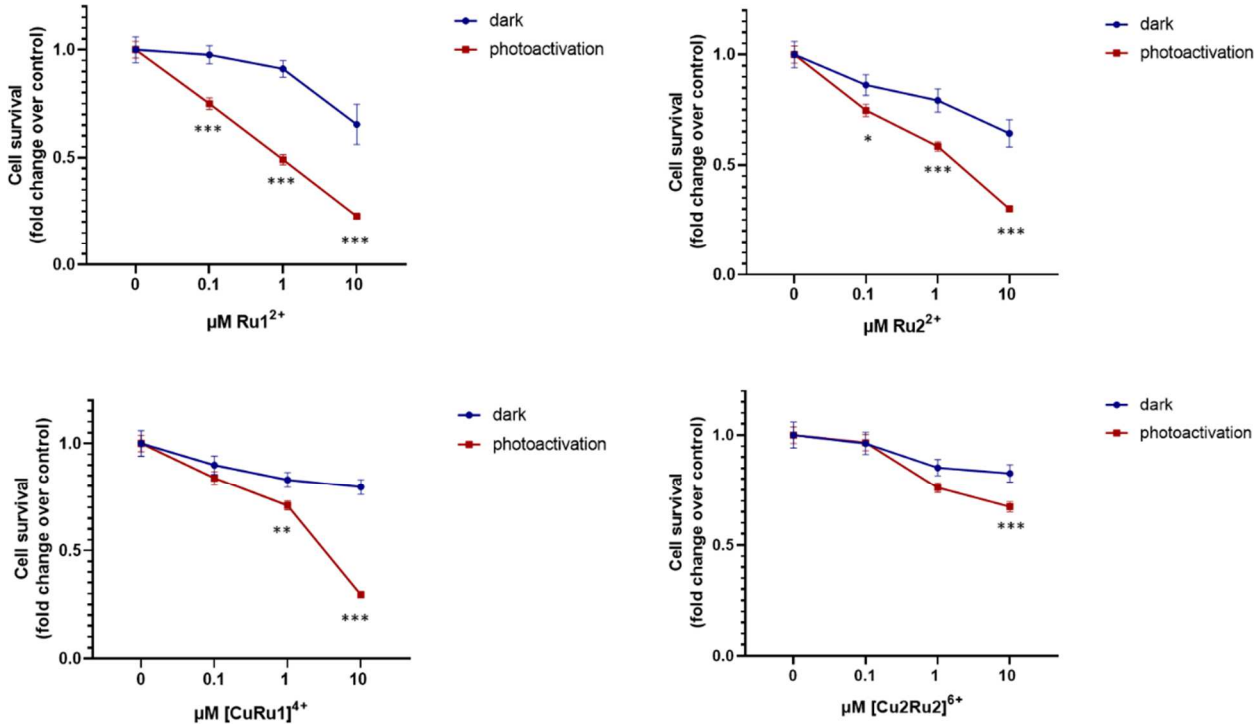

Figure 3. Dose-dependent effect of Ru(II) complexes on cell survival of ovarian cancer cells after photosensitization. A2780 were incubated for 24 h in the presence of Ru(II) complexes, **Ru1**$^{2+}$, **Ru2**$^{2+}$, [Cu**Ru1**]$^{4+}$ and [Cu_2**Ru2**]$^{6+}$ at the following concentrations (0, 0.1 μM, 1 μM, 10 μM) in serum-deprived culture media (RPMI with BSA 0.1%). Photoactivation for 20 min, as described in the Materials and Methods section. MTT reduction tests were performed in triplicate, representative of three independent experiments with similar results. Data reported are mean ± SD, fold change of absorbance at 570 nm over untreated control. The effect of photoactivation of Ru(II) complexes on the inhibition of cell survival was statistically significant according to two-way ANOVA followed by Bonferroni post hoc test. * $p < 0.05$, ** $p < 0.01$, *** $p < 0.001$.

2.5. Effect of Ru(II) Complexes on Apoptosis of A2780 Cells after Photoactivation

To dissect the molecular mechanism responsible for the selective anti-survival effect exerted by Ru(II) complexes, the involvement of apoptosis was studied by using different approaches in A2780 cells. As shown in Figure 4A, the treatment with each photosensitizer was completely ineffective on caspase 3 activity under dark conditions, whereas light irradiation of Ru(II) complexes after 24 h incubation caused a significant and potent activation of the pro-apoptotic enzyme.

Moreover, the involvement of caspase 3 in the mechanisms of action of Ru(II) photosensitizers was further investigated in dark conditions and after photoactivation employing Western blot analysis by measuring the proteolytic cleavage of the enzyme (Figure 4B). Although each Ru(II) complex was not able to induce caspase 3 cleavage under dark conditions, the cleaved form significantly increased after photoactivation, suggesting the involvement of caspase 3 in the anti-survival effect induced by photoactivation of Ru(II) complexes in A2780 cells.

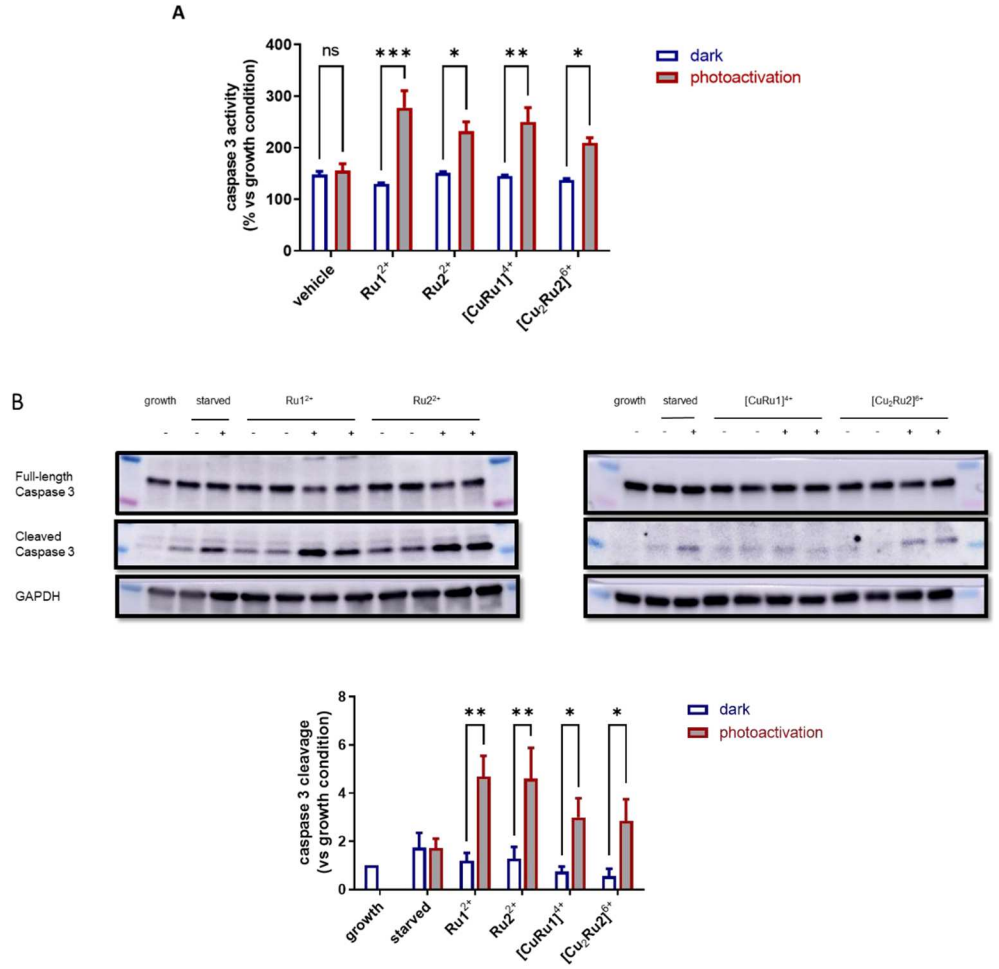

Figure 4. Effect of Ru(II) complexes on caspase 3 activation in ovarian cancer cells after photosensitization. A2780 cells were treated with each Ru(II) complex, $\mathbf{Ru1}^{2+}$, $\mathbf{Ru2}^{2+}$, $[Cu\mathbf{Ru1}]^{4+}$ and $[Cu_2\mathbf{Ru2}]^{6+}$, at 10 μM. After 24 h of incubation, cells were photoactivated (red) or not (blue), collected after 24 h of light irradiation, homogenized, and total protein concentration was analyzed in each lysate. (**A**) Caspase 3 activity assay was performed in 30 μg of total cell lysates by using a specific fluorogenic substrate Ac-DEVD-ACF (ex/em: 400/505 nm). Data are reported as mean ± SD of fluorescence compared to control cells under growth condition (10% FBS RPMI), set as 100. The effect of photoactivation was statistically significant for each Ru(II) complex tested according to two-way ANOVA analysis followed by Bonferroni post hoc test: * $p < 0.05$, ** $p < 0.01$, *** $p < 0.001$. (**B**) Western blot analysis was performed in 30 μg total cell lysates using specific anti-caspase 3 antibody. Densitometric analysis of cleaved caspase 3 was performed in three independent experiments performed in duplicate. Data are the mean ± SD and are reported as cleaved caspase 3 levels normalized to GAPDH, fold change over FBS control (growth), set as 1. Results are statistically significant according to two-way ANOVA followed by Bonferroni post hoc test: * $p < 0.05$, ** $p < 0.01$, not significant (ns).

Finally, programed cell death and its involvement in the photoactivity of Ru(II) complexes was confirmed by measuring the cleavage of poly ADP-ribose polymerase (PARP), which is one of the major hallmarks of apoptosis (Figure 5). The specific inactivation of PARP by proteolytic cleavage was undetectable under dark conditions, while it was significantly appreciable after photoactivation of each Ru(II) complex, although to a different extent.

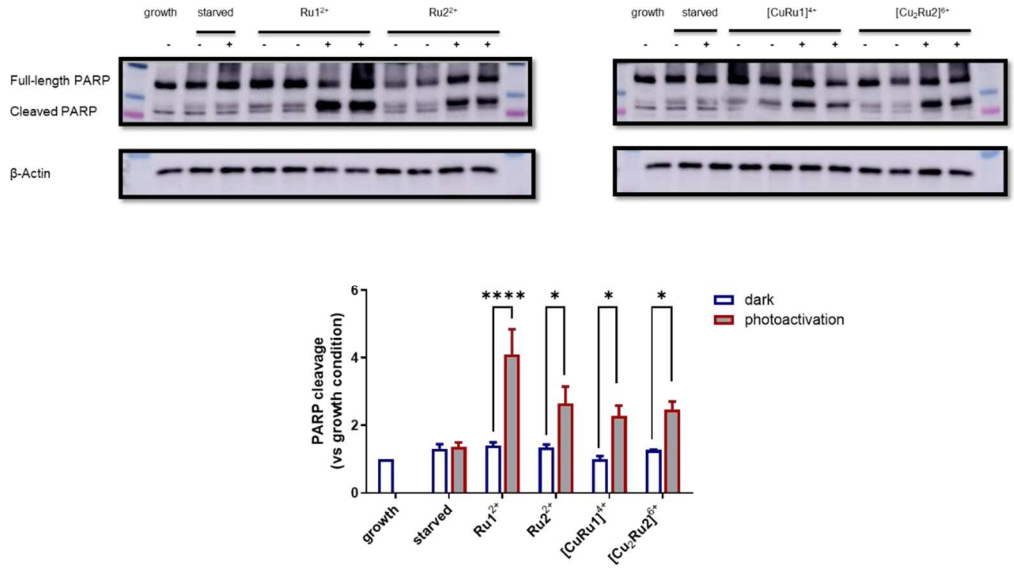

Figure 5. Effect of Ru(II) complexes on PARP cleavage in ovarian cancer cells after photosensitization. A2780 cells were treated for 24 h with each Ru(II) complex before being photoactivated and collected after 24 h of light irradiation. Western blot analysis was performed in 30 μg total cell lysates using specific anti-PARP (46D11) antibody. Densitometric analysis of cleaved form of PARP was performed in three independent experiments conducted in duplicate. Data are the mean ± SEM and are reported as cleaved protein levels normalized to β-actin, fold change over FBS control. Results are statistically significant according to two-way ANOVA followed by Bonferroni post hoc test: * $p < 0.05$, **** $p < 0.0001$.

2.6. Mitochondrial Membrane Potential Is Lost after Photosensitization of Ru(II) Complexes

Mitochondria play a key role in the intrinsic pathway of apoptosis in mammalian cells, and mitochondrial membrane potential (ΔΨm) loss is considered an early event of the apoptotic process in some cellular systems [26]. For this reason, ΔΨm was analyzed after photosensitizer administration in A2780 cells using a cationic fluorescent probe, which accumulates in the negatively charged mitochondrial matrix, by laser-scanning confocal microscopy imaging. Figure 6 illustrates the distribution of functional mitochondria in A2780 cells in the presence of Ru(II) complexes under dark conditions or after photoactivation. The administration of photosensitizers under dark conditions did not affect ΔΨm or cell morphology. However, photoactivation of $\mathbf{Ru1}^{2+}$ and $\mathbf{Ru2}^{2+}$ caused a dramatic loss of ΔΨm in almost all the cells. Remarkably, this was accompanied by the appearance of a pyknotic morphology of the nuclei, possibly representing an initial phase of chromatin condensation prior to DNA fragmentation [27]. Nonetheless, A2780 cells treated with $[Cu\mathbf{Ru1}]^{4+}$ and $[Cu_2\mathbf{Ru2}]^{6+}$ did not exhibit any mitochondrial change or decrease in ΔΨm in the presence or in the absence of photoactivation, thus ruling out the possible involvement of early loss of mitochondrial membrane potential in the pro-apoptotic effect of mixed Ru(II)-Cu(II) complexes. Given the cationic nature of Ru(II) complexes, mitochondrial localization subsequent to light-induced mitochondrial depolarization might occur. To analyze this possibility, we performed laser-scanning confocal microscopy employing a mitochondria-specific probe in A2780 cells incubated with $\mathbf{Ru1}^{2+}$, $\mathbf{Ru2}^{2+}$, $[Cu\mathbf{Ru1}]^{4+}$ or $[Cu_2\mathbf{Ru2}]^{6+}$, followed by a colocalization test, to assess the possible localization of Ru(II) complexes into mitochondria. Confocal microscopy images showed a random distribution of Ru(II) complexes compared to mitochondria (Figure S9, Supplementary Materials), thus ruling out the possibility that mitochondrial depolarization induced by photoactivation depends on Ru(II) complexes' localization in these organelles.

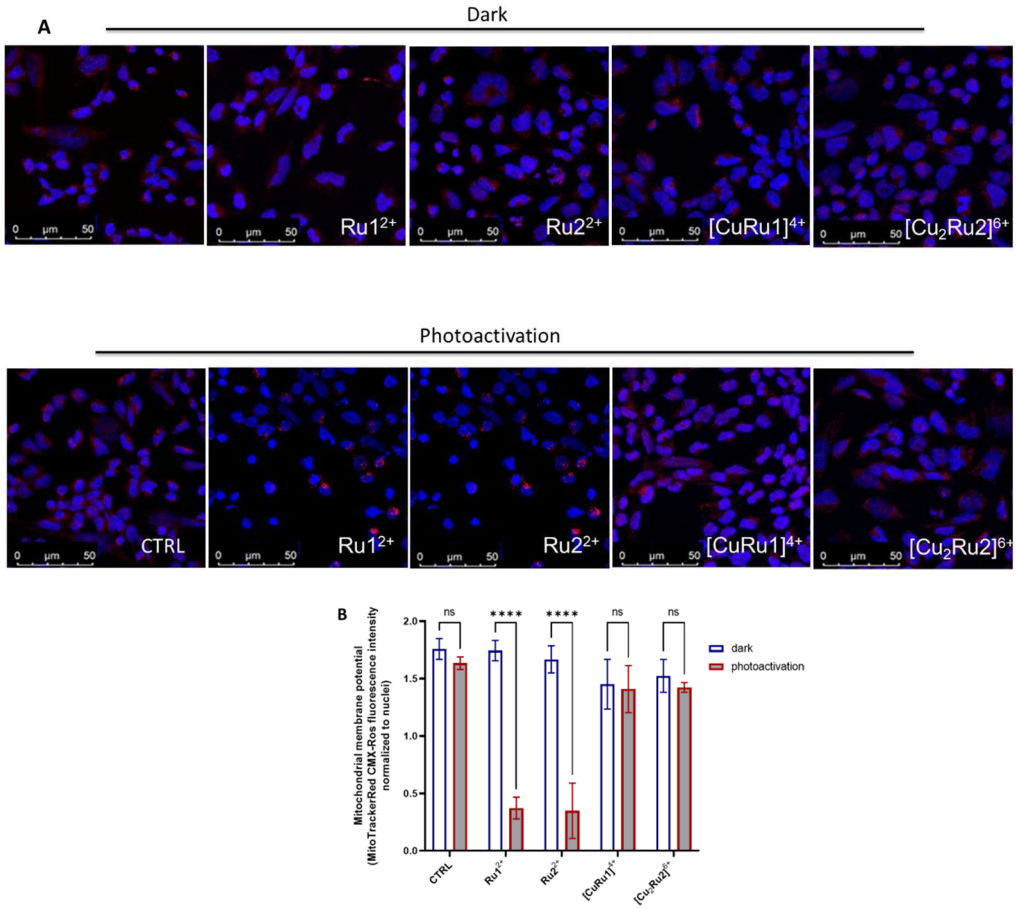

Figure 6. Effect of Ru(II) complexes on mitochondrial membrane potential after photoactivation. Mitochondrial membrane potential of A2780 cells was detected using cationic fluorescent dye Mito-Tracker Red CMXRos, which proportionally accumulates in the negatively charged mitochondrial matrix. (**A**) A2780 cells were plated in microscope slides and challenged or not (CTRL) with 10 μM of each Ru(II)-complex (**Ru1**$^{2+}$, **Ru2**$^{2+}$, [Cu**Ru1**]$^{4+}$ and [Cu_2**Ru2**]$^{6+}$). After 24 h of incubation, A2780 were subjected to photoactivation or not (dark) for 20 min, 2 h before being labeled with Mitotraker Red CMXRos and fixed in paraformaldehyde, as described in the Materials and Methods section. Confocal analysis was performed using 63X oil immersion objective. Images were representative of six fields of each condition in three independent experiments with analogous results. (**B**) Data are reported as mean ± SD of MitoTracker Red CMXRos fluorescence intensity normalized to the number of nuclei in six fields for each condition in three independent experiments by using Leica Application Software. Results are statistically significant according to two-way ANOVA followed by Bonferroni post hoc test: **** $p < 0.0001$, not significant (ns).

2.7. Cytosolic ROS Production after Photosensitization of Ru(II) Complexes Ru1^{2+} and Ru2^{2+}

With the purpose of dissecting the possible involvement of reactive oxygen species (ROS) production in the biological effect induced by **Ru1**$^{2+}$ and **Ru2**$^{2+}$ photosensitizers, confocal analysis was performed in A2780 cells employing the CM-H_2DCFDA probe to detect cytosolic ROS after **Ru1**$^{2+}$ and **Ru2**$^{2+}$ administration upon photoactivation compared to the dark conditions. As shown in Figure 7, cytosolic ROS were almost completely undetectable after each **Ru1**$^{2+}$ or **Ru2**$^{2+}$administration in A2780 under dark conditions, even if Ru(II) complexes were efficiently internalized (red fluorescence). However, as early as 2 h after photoactivation, cytosolic ROS were detected in the majority of cell populations, notwithstanding at different degrees of intensity, thus suggesting a critical role of ROS in the proapoptotic action exerted by **Ru1**$^{2+}$ and **Ru2**$^{2+}$ photosensitizers.

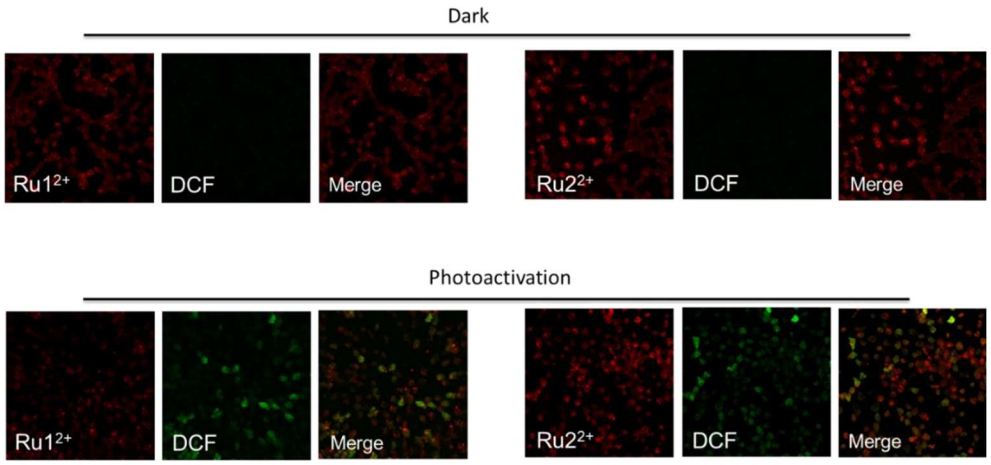

Figure 7. Effect of Ru(II) complexes, **Ru1**$^{2+}$ and **Ru2**$^{2+}$, on ROS production after photoactivation. ROS production in A2780 cells was detected using CM-H_2DCFDA. A2780 cells were plated on microscope slides and challenged with 10 μM of each Ru complex, **Ru1**$^{2+}$ and **Ru2**$^{2+}$. After 24 h of incubation, A2780 were exposed to photoactivation or not (dark) for 20 min, 2 h before being labeled with CM-H_2DCFDA (DCF) and fixed in paraformaldehyde, as described in the Materials and Methods section. Confocal analysis was performed using 63X oil immersion objective. The fluorescence of Ru(II) complexes is shown in red ($\lambda_{exc}/\lambda_{em}$: 405/600–640 nm) and DCF in green ($\lambda_{exc}/\lambda_{em}$: ~492–495/517–527 nm). Images were representative of six fields of each condition in three independent experiments with analogous results.

3. Discussion

Increasing evidence reports that platinum-based anti-cancer drugs have severe side effects, such as myelotoxicity and peripheral neuropathy [28]. Moreover, ovarian cancer recurrence less than six months after the completion of platinum-based therapy is frequent, and prognosis is extremely poor [29]. The main reason for the dramatic failure of ovarian cancer treatments [30,31] relies on the intrinsic and acquired resistance to platinum-based chemotherapy. Therefore, efforts are needed in this research field to develop other potential anti-cancer drugs. Ru(II) polypyridyl complexes have shown remarkable anti-tumor activity coupled with advantages over platinum drugs, such as higher potency, lower toxicity, minor drug resistance, and they are expected to become a new generation of clinical metal anti-cancer drugs [11,32,33].

In our study, a series of RPCs-based photosensitizers for PDT application were investigated for the capability of inducing anti-tumor effects following photoactivation with low-energy light. Their biological potential was evaluated in the A2780 ovarian cell line, which was taken as a model of ovarian cancer [25]. Since PDT activity may result from different pathways, such as the production of ROS through *type I* and *II* mechanisms, four different Ru(II) polypyridyl complexes, namely **Ru1**$^{2+}$, **Ru2**$^{2+}$, [Cu**Ru1**]$^{4+}$ and [Cu_2**Ru2**]$^{6+}$, featuring different modalities of activation, were evaluated in this study.

Among these metal complexes, **Ru1**$^{2+}$ and **Ru2**$^{2+}$ are highly luminescent and possess good (and comparable) abilities to sensitize the formation of singlet oxygen through *type II* reactions. On the other hand, the insertion of one or two Fenton-active Cu(II) ion/s in their corresponding heteronuclear Ru(II)-Cu(II) complexed species ([Cu**Ru1**]$^{4+}$ and [Cu_2**Ru2**]$^{6+}$) results in less luminescent compounds, which can mainly promote the generation of perhydroxyl and hydroxyl radicals via *type I* reactions. The coordination of Cu(II) ion/s in these latter two compounds is remarkably strong (LogK values between 15.34 and 27.6), making any transmetalation process unfavorable in conditions mimicking the cellular environment. Importantly, the peculiar polyamine frameworks confer to all these compounds excellent solubilities in water, a key requisite for their application in the biomedical field.

In a previous report, the Ru(II)-arene complex [Ru(η6-p-cymene)Cl_2] (RAPTA-C) was tested for efficacy in combination with the epidermal growth factor receptor inhibitor erlotinib, demonstrating an efficient anti-angiogenic and anti-tumor activity [34]. The therapeutic potential of these compounds and their combination was further confirmed in preclinical in vivo models of chicken chorioallantoic membrane grafted with A2780 tumors and in mice bearing A2780 tumors, highlighting the tumor growth inhibition and anti-angiogenic effect [34].

In line with the literature data, the RPCs investigated herein were found to possess negligible cytotoxicity without light irradiation in non-cancer and cancer cells, respectively, converted in turn in a tight dose-dependent and significant anti-tumor action upon photoactivation. In particular, a marked increase in the activity was observed upon light activation of $\mathbf{Ru1}^{2+}$ and $\mathbf{Ru2}^{2+}$, in agreement with the good singlet oxygen sensitizing properties of these compounds. Among the mixed heteronuclear complexes, [Cu**Ru1**]$^{4+}$ displayed the sharpest photoactivity. Interestingly, this suggests that, beyond the singlet oxygen sensitization, alternative oxidative pathways must be accessible to heteronuclear compounds, leading to similar photoinduced effectiveness compared to the one of copper-free complexes. However, further efforts will be needed to obtain further insights into these processes, which likely occur under biological conditions and appear to be hard to mimic in cell-free experiments. Moreover, the significant differences in activity observed between [Cu**Ru1**]$^{4+}$ and [Cu_2**Ru2**]$^{6+}$ suggest that other less predictable features, such as differences in the chemical structures, may play a critical role in the biological behavior of such compounds.

The investigated RPCs also displayed good capacities to be internalized by A2780 cancer compared to non-cancer cells, with $\mathbf{Ru1}^{2+}$ and $\mathbf{Ru2}^{2+}$ being the most effective. This result is of great interest, especially considering that similar RPCs-based PSs were shown to poorly penetrate the cell membrane, and additional expedients, such as ion pairing with suitable lipophilic counter-anions, were necessary to augment the cellular uptake [35]. In the present study, it is reasonable to assume that the significant cellular uptake by cancer cells is associated with the presence of the polyamino macrocyclic frameworks **L′** and **L″** of the Ru(II) compounds, which may impart optimal chemical–physical features for cellular internalization, such as hydrophilicity and total charge of the compounds. Even if the precise mechanism by which the Ru(II) compounds are internalized in A2780 cells was not investigated in detail, their uptake appears to be independent of the Rab5-dependent early endosome pathway. Nonetheless, taking into consideration the hydrophilic chemical nature of RPCs and their observed localized cellular distribution, the occurrence of an efficacious passive transport can be excluded, rather pointing at alternative endocytotic events accounting for RPC uptake. Indeed, this is in line with the literature data showing the occurrence of specific cellular transport of cytotoxic metallodrugs [36].

Apoptosis is clearly advantageous for the organism, since, during apoptosis, the cell membrane remains intact, thus preventing the release of intracellular content. Hence, the elucidation of the mechanisms that triggered cell death after the light activation of Ru(II) complexes appears to be crucial. In A2780 cells, the photoactivation of all the tested RPCs caused a potent caspase 3 activation, as well as both caspase 3 and PARP cleavage, while the RPCs were ineffective in the absence of photosensitization, pointing at a crucial role for programed cell death in the anti-tumor activity of these systems.

Mitochondria might be seen as a gatekeeper to entrap pro-apoptotic proteins and prevent the release and activation of these proteins in the cytosol [37]. In particular, the exit of pro-apoptotic proteins from the mitochondria activates caspase proteases. Of note, the opening of the mitochondrial permeability transition pore has been demonstrated to induce ΔΨm depolarization, loss of oxidative phosphorylation and release of apoptogenic factors. Thus, a distinctive feature of apoptosis can be represented by the disruption of the normal mitochondrial function, especially changes that affect the ΔΨm. In some apoptotic systems, the loss of ΔΨm may be an early event in the apoptotic process [38]. Here, using confocal microscopy, it was demonstrated that $\mathbf{Ru1}^{2+}$ and $\mathbf{Ru2}^{2+}$, but not [Cu**Ru1**]$^{4+}$ or [Cu_2**Ru2**]$^{6+}$,

caused a dramatic loss of ΔΨm depending on photoactivation and that this effect was accompanied by ROS production in the cytosol as soon as 2 h after light irradiation, thus upstream to the pro-apoptotic stimuli.

Lastly, although previous in vitro studies underlined the capacity of RPCs to effectively interact and damage plasmid DNA upon irradiation [16], in this work, we did not detect RPCs in the nucleus, at least within 24 h of incubation, since these compounds were found distributed into segregated areas of the cytosol. This finding suggests that the induced programed cell death is likely independent of the PSs–DNA interaction.

In summary, the present study demonstrates that all four synthesized Ru(II) complexes are effectively internalized into the ovarian cancer A2780 cells, and their administration, regardless of the low dark cytotoxicity, induces a specific photoactivation-dependent cell death, with the extent of cytotoxicity that varies slightly depending on the chemical structures of RPCs. Apoptosis emerged as the main mechanism of light-mediated cellular death. In particular, among the four compounds, $\mathbf{Ru1}^{2+}$ and $\mathbf{Ru2}^{2+}$ profoundly altered mitochondrial activity after photoactivation, accompanied by cytosolic ROS production.

4. Materials and Methods

4.1. Materials

All materials used for the preparation of ruthenium compounds were of reagent grade and used as received, unless otherwise specified.

4.2. Synthesis of Ru(II)-Complexes

Ruthenium compounds $\mathbf{Ru1}^{2+}$, $\mathbf{Ru2}^{2+}$, $[Cu\mathbf{Ru1}]^{4+}$ and $[Cu_2\mathbf{Ru2}]^{6+}$ were synthesized according to the procedures previously described [16,39]. Briefly, $\mathbf{Ru1}^{2+}$ and $\mathbf{Ru2}^{2+}$ were prepared by direct reaction of the intermediate $(phen)_2\mathbf{Ru}Cl_2$ with the bidentate **L′** o **L″** ligands, in ethylene glycol and under microwave irradiation. The resulting complexes were then dissolved in concentrated HCl and precipitated as their respective hydrochloride salts $[\mathbf{Ru1}]Cl_2 \cdot 5HCl \cdot 2H_2O$ and $[\mathbf{Ru2}]Cl_2 \cdot 6HCl \cdot 2H_2O$, following the addition of ethanol.

The mixed Ru(II)/Cu(II) complexes were obtained as the perchlorate salts $[Cu\mathbf{Ru1}](ClO_4)_4 \cdot 4H_2O$ and $[Cu_2\mathbf{Ru2}](ClO_4)6 \cdot 3H_2O$, by adding equimolar amounts of $Cu(ClO_4)_2$ to aqueous solutions of $\mathbf{Ru1}^{2+}$ or $\mathbf{Ru2}^{2+}$ at pH 6.5 and following the slow evaporation of the solvent at r.t.

4.3. Potentiometric Measurements

The acid-base behavior and the binding ability toward Cu^{2+}, Zn^{2+}, Ca^{2+}, Na^+ and Mg^{2+} of ruthenium complexes were investigated by means of potentiometric measurements in NMe_4Cl 0.1 M at 298 ± 0.1 K by using the equipment and methods previously described [40–43].

4.4. EPR Measurements

X-band electron paramagnetic resonance (EPR) experiments were performed by using a Bruker Elexsys E500 spectrometer. All the spectra were acquired at room temperature by using the same modulation frequency (100 kHz), modulation amplitude (1 G), microwave power (~0.2 mW, 30 dB) and receiver gain (60 dB). The magnetic field was calibrated with a crystal of DPPH.

4.5. Cell Culture

Human A2780 ovarian cancer cell culture (ECACC 93112519) was maintained in RPMI-1640 medium containing 10% fetal bovine serum (FBS), 100 μg/mL streptomycin, 100 U/mL penicillin and 2 mM L-glutamine, at 37 °C in 5% CO_2, as previously reported [44]. All cell culture reagents were purchased from Merck Life Science (Darmstadt, Germany), including phosphate-buffered saline (PBS). A2780 cells were shifted to RPMI without serum supplemented with 1 mg/mL Bovine Serum Albumin (BSA) and treated with each Ru(II) complex (0.1, 1 and 10 μM) for 24 h. After incubation, cells were photoactivated with a 30 W three-arm LED light lamp (430–470 nm emission, 30 W) for 20 min at the distance of

5 cm from the cell culture plate and then kept in the incubator at 37 °C, 5% CO_2. Cells were washed twice with PBS and then collected after photoactivation at different times, which depended on each kind of experiment.

4.6. ICP-AES Measurements

A Varian 720-ES axial Inductively Coupled Plasma Atomic Emission Spectrometer (ICP-AES) was used to determine the Ru contents in the samples. Measurements were performed in triplicate, and each sample was spiked with 1.0 ppm of Ge, used as an internal standard. The calibration standards were prepared by gravimetric serial dilution from commercial stock standard solutions of Ru at 1000 mg L^{-1} (Honeywell Fluka). For Ru determination, the 267.876 and 245.657 nm wavelengths were used, whereas the line at 209.426 nm was considered for Ge. The operating conditions were optimized to obtain maximum signal intensity, and between each sample, a rinse solution containing 2% *v*/*v* of HNO_3 was used.

4.7. MTT Reduction Assay for Cell Survival

A2780 viability was evaluated by the MTT method, as previously described [45].

4.8. Caspase-3 Activity Assay

A2780 cells were seeded in 6-well plates (100.000 cells/well) and after 24 h were incubated with 10 μM of each Ru(II) complex in serum-deprived culture media, then light-irradiated for 20 min, as described above. After 24 h of photoactivation, cells were washed twice with PBS, collected and analyzed, as previously described [46].

4.9. Western Blot Analysis

A2780 lysates were quantified for total protein content by the Bradford Protein assay, resuspended in Leammli's sodium dodecyl sulphate (SDS) sample buffer, and subjected to SDS-PAGE and transferred to PVDF membranes, as previously described [46].

4.10. Laser-Scanning Confocal Microscopy

A2780 cells were seeded on microscope slides and treated with each Ru(II) complex (10 μM). To evaluate the internalization of Ru(II) complexes, cells were incubated at three different times, 15 min, 6 h and 24 h, washed with PBS and fixed in 2% paraformaldehyde in PBS for 20 min. Ru(II) complexes excitation was performed using 405 nm laser diode, acquiring emission in the range of 600/620 nm.

MitoTracker Red CMXRos (#M7512; Ex/Em: 579/599 nm) and CM-H_2DCFDA (#C6827; Ex/Em: ~492–495/517–527 nm) probes (Invitrogen, Thermo Fisher Scientific INC, Waltham, MA, USA) were used to detect the mitochondrial membrane potential and ROS production, respectively. After 24 h incubation of Ru(II) complexes at 37 °C, cell slides were photoactivated or not for 20 min and incubated for 2 h at 37 °C, 5% CO_2 in humidified atmosphere. Probes were diluted in RPMI medium without phenol red, incubated for 30 min at 37 °C in dark and then fixed in 2% paraformaldehyde, as suggested by the manufacturer's instruction. After 30 min at room temperature, slides were incubated with a permeabilization and quenching solution, obtained by adding Triton 0.1% X-100 and ethanolamine (1:165) in PBS. The DAPI solution was administered to cell slides to detect the nuclei. Slides were mounted by using the Fluoromount Aqueous Mounting Medium (Sigma-Aldrich, Saint Louis, MA, USA), and images were obtained using a Leica SP8 laser-scanning confocal microscope (Leica Microsystems GmbH) using a 63x oil immersion objective.

4.11. Statistical Analysis

Densitometric analysis of Western blot bands was performed using the ImageJ software, and graphical representations were obtained by GraphPad Prism 5.0 (GraphPad Software, San Diego, CA, USA). Statistical analysis was performed using one-way or two-

way ANOVA analysis of variance followed by the Bonferroni post hoc test. Asterisks indicate statistical significance.

5. Conclusions

In conclusion, our study identifies Ru(II)-polypyridyl complexes as challenging tools to be further investigated in the research of new therapeutic strategies to overcome chemoresistance in epithelial ovarian cancers and provides further insights on the biological behavior of these complexes, which rely on ROS production and altered mitochondrial function to trigger pro-apoptotic effects.

Supplementary Materials: The following are available online at https://www.mdpi.com/article/10.3390/ijms232113302/s1. Refs. [47,48] are cited in Supplementary Materials.

Author Contributions: Conceptualization: C.G., L.C. and F.C.; Project administration: C.G., F.C. and L.C.; Supervision: C.G., F.C., P.B. and B.V.; Funding acquisition: L.C., C.G., P.B. and F.C.; Writing: C.G., L.C., F.C., P.B. and B.V.; Methodology: G.E.G., S.P., P.S.S., M.P. and A.P.; Investigation: G.E.G., S.P., P.S.S. and I.P., M.P. and A.P.; Data curation: L.C. and F.C. All authors have read and agreed to the published version of the manuscript.

Funding: A.P. acknowledges support from the Italian Ministry of Education and Research (MIUR) through PRIN project 2017 "Quantum detection of chiral-induced spin selectivity at the molecular level" (2017Z55KCW) The work was supported by University of Florence (Fondi Ateneo to P.B. and F.C.). The data presented in the current study were in part generated using the equipment of the Facility of Molecular Medicine and of the Department of Experimental and Clinical Biomedical Sciences "*Mario Serio*" and the Department of Chemistry "*Ugo Schiff*", funded by the Ministry of Education, University and Research of Italy–Dipartimenti di Eccellenza 2018–2022.

Institutional Review Board Statement: Not applicable.

Informed Consent Statement: Not applicable.

Data Availability Statement: All the data are reported in the manuscript.

Acknowledgments: The authors thank Mirko Severi for the ICP-AES analysis.

Conflicts of Interest: The authors declare no conflict of interest.

References

1. Siegel, R.L.; Miller, K.D.; Fuchs, H.E.; Jemal, A. Cancer Statistics, 2021. *CA Cancer J. Clin.* **2021**, *71*, 7–33. [CrossRef]
2. Coburn, S.B.; Bray, F.; Sherman, M.E.; Trabert, B. International patterns and trends in ovarian cancer incidence, overall and by histologic subtype. *Int. J. Cancer* **2017**, *140*, 2451–2460. [CrossRef]
3. Buys, S.S.; Partridge, E.; Black, A.; Johnson, C.C.; Lamerato, L.; Isaacs, C.; Reding, D.J.; Greenlee, R.T.; Yokochi, L.A.; Kessel, B.; et al. Effect of Screening on Ovarian Cancer Mortality. *JAMA* **2011**, *305*, 2295–2303. [CrossRef] [PubMed]
4. Mikuła-Pietrasik, J.; Witucka, A.; Pakuła, M.; Uruski, P.; Begier-Krasińska, B.; Niklas, A.; Tykarski, A.; Ksia¸z˙ek, K. Comprehensive review on how platinum- and taxane-based chemotherapy of ovarian cancer affects biology of normal cells. *Cell. Mol. Life Sci.* **2019**, *76*, 681–697. [CrossRef] [PubMed]
5. Simovic´, A.R.; Masnikosa, R.; Bratsos, I.; Alessio, E. Chemistry and reactivity of ruthenium(II) complexes: DNA/protein binding mode and anticancer activity are related to the complex structure. *Co-ord. Chem. Rev.* **2019**, *398*, 113011. [CrossRef]
6. Lee, S.Y.; Kim, C.Y.; Nam, T.-G. Ruthenium Complexes as Anticancer Agents: A Brief History and Perspectives. *Drug Des. Dev. Ther.* **2020**, *14*, 5375–5392. [CrossRef]
7. Kostova, I. Ruthenium Complexes as Anticancer Agents. *Curr. Med. Chem.* **2006**, *13*, 1085–1107. [CrossRef] [PubMed]
8. Liu, J.; Zhang, C.; Rees, T.W.; Ke, L.; Ji, L.; Chao, H. Harnessing ruthenium(II) as photodynamic agents: Encouraging advances in cancer therapy. *Co-ord. Chem. Rev.* **2018**, *363*, 17–28. [CrossRef]
9. Poynton, F.E.; Bright, S.A.; Blasco, S.; Williams, D.C.; Kelly, J.M.; Gunnlaugsson, T. The development of ruthenium(II) polypyridyl complexes and conjugates for *in vitro* cellular and *in vivo* applications. *Chem. Soc. Rev.* **2017**, *46*, 7706–7756. [CrossRef]
10. Monro, S.; Colón, K.L.; Yin, H.; Roque, J., III; Konda, P.; Gujar, S.; Thummel, R.P.; Lilge, L.; Cameron, C.G.; McFarland, S.A. Transition Metal Complexes and Photodynamic Therapy from a Tumor-Centered Approach: Challenges, Opportunities, and Highlights from the Development of TLD1433. *Chem. Rev.* **2019**, *119*, 797–828. [CrossRef]
11. Lin, K.; Zhao, Z.-Z.; Bo, H.-B.; Hao, X.-J.; Wang, J.-Q. Applications of Ruthenium Complex in Tumor Diagnosis and Therapy. *Front. Pharmacol.* **2018**, *9*, 1323. [CrossRef] [PubMed]

12. Mari, C.; Pierroz, V.; Ferrari, S.; Gasser, G. Combination of Ru(II) complexes and light: New frontiers in cancer therapy. *Chem. Sci.* **2015**, *6*, 2660–2686. [CrossRef] [PubMed]
13. Le Gall, T.; Lemercier, G.; Chevreux, S.; Tucking, K.-S.; Ravel, J.; Thetiot, F.; Jonas, U.; Schonherr, H.; Montier, T. Ruthenium(II) Polypyridyl Complexes as Photosensitizers for Antibacterial Photodynamic Therapy: A Structure-Activity Study on Clinical Bacterial Strains. *ChemMedChem* **2018**, *13*, 2229–2239. [CrossRef]
14. Giacomazzo, G.E.; Conti, L.; Guerri, A.; Pagliai, M.; Fagorzi, C.; Sfragano, P.S.; Palchetti, I.; Pietraperzia, G.; Mengoni, A.; Valtancoli, B.; et al. Nitroimidazole-Based Ruthenium(II) Complexes: Playing with Structural Parameters to Design Photostable and Light-Responsive Antibacterial Agents. *Inorg. Chem.* **2021**, *61*, 6689–6694. [CrossRef] [PubMed]
15. Castano, A.P.; Demidova, T.N.; Hamblin, M.R. Mechanisms in photodynamic therapy: Part one—Photosensitizers, photochemistry and cellular localization. *Photodiagn. Photodyn. Ther.* **2004**, *1*, 279–293. [CrossRef]
16. Conti, L.; Bencini, A.; Ferrante, C.; Gellini, C.; Paoli, P.; Parri, M.; Pietraperzia, G.; Valtancoli, B.; Giorgi, C. Highly Charged Ruthenium(II) Polypyridyl Complexes as Effective Photosensitizer in Photodynamic Therapy. *Chem.–A Eur. J.* **2019**, *25*, 10606–10615. [CrossRef] [PubMed]
17. Conti, L.; Mengoni, A.; Giacomazzo, G.E.; Mari, L.; Perfetti, M.; Fagorzi, C.; Sorace, L.; Valtancoli, B.; Giorgi, C. Exploring the potential of highly charged Ru(II)- and heteronuclear Ru(II)/Cu(II)-polypyridyl complexes as antimicrobial agents. *J. Inorg. Biochem.* **2021**, *220*, 111467. [CrossRef] [PubMed]
18. Conti, L.; Flore, N.; Formica, M.; Giorgi, L.; Pagliai, M.; Mancini, L.; Fusi, V.; Valtancoli, B.; Giorgi, C. Glyphosate and AMPA binding by two polyamino-phenolic ligands and their dinuclear Zn(II) complexes. *Inorg. Chim. Acta* **2021**, *519*, 120261. [CrossRef]
19. Juarranz, Á.; Jaén, P.; Sanz-Rodríguez, F.; Cuevas, J.; González, S. Photodynamic therapy of cancer. Basic principles and applications. *Clin. Transl. Oncol.* **2008**, *10*, 148–154. [CrossRef]
20. Ochsner, M. Photophysical and photobiological processes in the photodynamic therapy of tumours. *J. Photochem. Photobiol. B Biol.* **1997**, *39*, 1–18. [CrossRef]
21. Pineiro, M.; Pereira, M.M.; Gonsalves, A.M.D.R.; Arnaut, L.; Formosinho, S. Singlet oxygen quantum yields from halogenated chlorins: Potential new photodynamic therapy agents. *J. Photochem. Photobiol. A Chem.* **2001**, *138*, 147–157. [CrossRef]
22. Ding, H.; Yu, H.; Dong, Y.; Tian, R.; Huang, G.; Boothman, D.A.; Sumer, B.D.; Gao, J. Photoactivation switch from type II to type I reactions by electron-rich micelles for improved photodynamic therapy of cancer cells under hypoxia. *J. Control. Release* **2011**, *156*, 276–280. [CrossRef] [PubMed]
23. Kucková, L.; Jomová, K.; Švorcová, A.; Valko, M.; Segl'a, P.; Moncol', J.; Kožíšek, J. Synthesis, Crystal Structure, Spectroscopic Properties and Potential Biological Activities of Salicylate–Neocuproine Ternary Copper(II) Complexes. *Molecules* **2015**, *20*, 2115–2137. [CrossRef] [PubMed]
24. Haas, K.L.; Franz, K.J. Application of Metal Coordination Chemistry To Explore and Manipulate Cell Biology. *Chem. Rev.* **2009**, *109*, 4921–4960. [CrossRef]
25. Kakar, S.S.; Jala, V.R.; Fong, M.Y. Synergistic cytotoxic action of cisplatin and withaferin A on ovarian cancer cell lines. *Biochem. Biophys. Res. Commun.* **2012**, *423*, 819–825. [CrossRef]
26. Ricci, J.E.; Waterhouse, N.; Green, D.R. Mitochondrial functions during cell death, a complex (I–V) dilemma. *Cell Death Differ.* **2003**, *10*, 488–492. [CrossRef]
27. Hu, X.-M.; Li, Z.-X.; Lin, R.-H.; Shan, J.-Q.; Yu, Q.-W.; Wang, R.-X.; Liao, L.-S.; Yan, W.-T.; Wang, Z.; Shang, L.; et al. Guidelines for Regulated Cell Death Assays: A Systematic Summary, A Categorical Comparison, A Prospective. *Front. Cell Dev. Biol.* **2021**, *9*, 634690. [CrossRef]
28. Oun, R.; Moussa, Y.E.; Wheate, N.J. The side effects of platinum-based chemotherapy drugs: A review for chemists. *Dalton Trans.* **2018**, *47*, 6645–6653. [CrossRef]
29. Rocconi, R.P.; Case, A.S.; Michael Straughn, J., Jr.; Estes, J.M.; Partridge, E.E. Role of chemotherapy for patients with recurrent platinum-resistant advanced epithelial ovarian cancer. *Cancer* **2006**, *107*, 536–543. [CrossRef]
30. Au, K.K.; Josahkian, J.A.; Francis, J.A.; Squire, J.A.; Koti, M. Current state of biomarkers in ovarian cancer prognosis. *Futur. Oncol.* **2015**, *11*, 3187–3195. [CrossRef]
31. Kurman, R.J.; Shih, I.-M. The Dualistic Model of Ovarian Carcinogenesis: Revisited, revised, and expanded. *Am. J. Pathol.* **2016**, *186*, 733–747. [CrossRef]
32. Thota, S.; Rodrigues, D.A.; Crans, D.; Barreiro, E.J. Ru(II) Compounds: Next-Generation Anticancer Metallotherapeutics? *J. Med. Chem.* **2018**, *61*, 5805–5821. [CrossRef] [PubMed]
33. Zeng, L.; Gupta, P.; Chen, Y.; Wang, E.; Ji, L.; Chao, H.; Chen, Z.-S. The development of anticancer ruthenium(II) complexes: From single molecule compounds to nanomaterials. *Chem. Soc. Rev.* **2017**, *46*, 5771–5804. [CrossRef]
34. Berndsen, R.H.; Weiss, A.; Abdul, U.K.; Wong, T.J.; Meraldi, P.; Griffioen, A.W.; Dyson, P.; Nowak-Sliwinska, P. Combination of ruthenium(II)-arene complex [Ru(η6-p-cymene)Cl2(pta)] (RAPTA-C) and the epidermal growth factor receptor inhibitor erlotinib results in efficient angiostatic and antitumor activity. *Sci. Rep.* **2017**, *7*, srep43005. [CrossRef] [PubMed]
35. Yan, Z.-Y.; Chen, J.; Shao, J.; Jiao, Z.-Q.; Tang, T.-S.; Tang, M.; Sheng, Z.-G.; Mao, L.; Huang, R.; Huang, C.-H.; et al. The cell-impermeable Ru(II) polypyridyl complex as a potent intracellular photosensitizer under visible light irradiation via ion-pairing with suitable lipophilic counter-anions. *Free Radic. Biol. Med.* **2021**, *171*, 69–79. [CrossRef]
36. Spreckelmeyer, S.; Orvig, C.; Casini, A. Cellular Transport Mechanisms of Cytotoxic Metallodrugs: An Overview beyond Cisplatin. *Molecules* **2014**, *19*, 15584–15610. [CrossRef]

37. Wang, C.; Youle, R.J. The Role of Mitochondria in Apoptosis. *Annu. Rev. Genet.* **2009**, *43*, 95–118. [CrossRef] [PubMed]
38. Ly, J.D.; Grubb, D.R.; Lawen, A. The mitochondrial membrane potential (deltapsi(m)) in apoptosis; an update. *Apoptosis Int. J. Program. Cell Death* **2003**, *8*, 115–128. [CrossRef] [PubMed]
39. Conti, L.; Mummolo, L.; Romano, G.; Giorgi, C.; Giacomazzo, G.; Prodi, L.; Bencini, A. Exploring the Ability of Luminescent Metal Assemblies to Bind and Sense Anionic or Ionizable Analytes A Ru(phen)$_2$bipy-Based Dizinc Complex for Bisphenol A (BPA) Recognition. *Molecules* **2021**, *26*, 527. [CrossRef]
40. Aragoni, M.C.; Arca, M.; Bencini, A.; Caltagirone, C.; Conti, L.; Garau, A.; Valtancoli, B.; Isaia, F.; Lippolis, V.; Palomba, F.; et al. Zn^{2+}/Cd^{2+} optical discrimination by fluorescent acridine-based *bis*-macrocylic receptors. *Supramol. Chem.* **2017**, *29*, 912–921. [CrossRef]
41. Conti, L.; Giorgi, C.; Valtancoli, B.; Paoli, P.; Rossi, P.; Marchionni, A.; Faggi, E.; Bencini, A. Switching on the Fluorescence Emission of Polypyridine Ligands by Simultaneous Zinc(II) Binding and Protonation. *ChemPlusChem* **2020**, *85*, 659–671. [CrossRef] [PubMed]
42. Garau, A.; Bencini, A.; Blake, A.J.; Caltagirone, C.; Conti, L.; Isaia, F.; Lippolis, V.; Montis, R.; Mariani, P.; Scorciapino, M.A. [9]aneN3-based fluorescent receptors for metal ion sensing, featuring urea and amide functional groups. *Dalton Trans.* **2019**, *48*, 4949–4960. [CrossRef] [PubMed]
43. Becatti, M.; Bencini, A.; Nistri, S.; Conti, L.; Fabbrini, M.G.; Lucarini, L.; Ghini, V.; Severi, M.; Fiorillo, C.; Giorgi, C.; et al. Different Antioxidant Efficacy of Two MnII-Containing Superoxide Anion Scavengers on Hypoxia/Reoxygenation-Exposed Cardiac Muscle Cells. *Sci. Rep.* **2019**, *9*, 10320. [CrossRef] [PubMed]
44. Bernacchioni, C.; Ghini, V.; Cencetti, F.; Japtok, L.; Donati, C.; Bruni, P.; Turano, P. NMR metabolomics highlights sphingosine kinase-1 as a new molecular switch in the orchestration of aberrant metabolic phenotype in cancer cells. *Mol. Oncol.* **2017**, *11*, 517–533. [CrossRef]
45. Conti, L.; Ciambellotti, S.; Giacomazzo, G.E.; Ghini, V.; Cosottini, L.; Puliti, E.; Severi, M.; Fratini, E.; Cencetti, F.; Bruni, P.; et al. Ferritin nanocomposites for the selective delivery of photosensitizing ruthenium-polypyridyl compounds to cancer cells. *Inorg. Chem. Front.* **2022**, *9*, 1070–1081. [CrossRef]
46. Donati, C.; Cencetti, F.; De Palma, C.; Rapizzi, E.; Brunelli, S.; Cossu, G.; Clementi, E.; Bruni, P. TGFβ protects mesoangioblasts from apoptosis via sphingosine kinase-1 regulation. *Cell. Signal.* **2009**, *21*, 228–236. [CrossRef]
47. Stoll, S.; Schweiger, A. EasySpin, a comprehensive software package for spectral simulation and analysis in EPR. *J. Magn. Reson.* **2006**, *178*, 42–55. [CrossRef]
48. Rosen, G.M.; Beselman, A.; Tsai, P.; Pou, S.; Mailer, C.; Ichikawa, K.; Robinson, B.H.; Nielsen, R.; Halpern, H.J.; MacKerell, A.D. Influence of Conformation on the EPR Spectrum of 5,5-Dimethyl-1-hydroperoxy-1-pyrrolidinyloxyl: A Spin Trapped Adduct of Superoxide. *J. Org. Chem.* **2004**, *69*, 1321–1330. [CrossRef]

Supplementary Materials

Table of Contents

1. Acid-base properties of ruthenium compounds $Ru1^{2+}$ and $Ru2^{2+}$

A preliminary requisite for the investigation of the binding properties of the receptor in its protonated forms concerns the knowledge of its basicity properties. The protonation equilibria of both **Ru1**$^{2+}$ and **Ru2**$^{2+}$ have been studied by means of potentiometric measurements in aqueous solution at 298.1 ± 0.1 K in 0.1 mol dm^{-3} NMe_4Cl at 298.1 ± 0.1 K. The protonation constants are reported in Table S1 and in Figures S1-S2 are shown the distribution diagrams of the protonated species present in solution.

$[Ru(phen)_2\mathbf{L'}]^{2+}$ (**Ru1**$^{2+}$) and $[Ru(phen)_2\mathbf{L''}]^{2+}$ (**Ru2**$^{2+}$) are capable of binding up to five ($[H_5\mathbf{Ru1}]^{7+}$) and six ($[H_6\mathbf{Ru2}]^{8+}$) protons in overall the range of pH investigated (between 2.5-10.5). In particular, it can be highlighted that in a wide range of pH, including at physiological pH value, the predominant species of ruthenium compounds present in solution are their di- and tetra-protonated forms, $[H_2\mathbf{Ru1}]^{4+}$ and $[H_4\mathbf{Ru2}]^{6+}$, respectively.

***Table S1**. Acid-base study of ruthenium compounds*

*Protonation constants of **Ru1**$^{2+}$ and **Ru2**$^{2+}$ determined by means of potentiometric measurements in NMe_4Cl 0.1 M, at 298.1 ± 0.1 K.*

Reaction	LogK L	
	L = Ru1	**L = Ru2**
$\mathbf{L}^{2+} + H^+ = H\mathbf{L}^{3+}$	9.50(4) [a]	11.23(8)
$H\mathbf{L}^{3+} + H^+ = H_2\mathbf{L}^{4+}$	7.59(5)	9.92(7)
$H_2\mathbf{L}^{4+} + H^+ = H_3\mathbf{L}^{5+}$	5.32(5)	8.37(5)
$H_3\mathbf{L}^{5+} + H^+ = H_4\mathbf{L}^{6+}$	3.91(5)	7.27(5)
$H_4\mathbf{L}^{6+} + H^+ = H_5\mathbf{L}^{7+}$	2.37(5)	
$H_4\mathbf{L}^{6+} + 2H^+ = H_6\mathbf{L}^{8+}$	-	7.13 (6)

[a] Values in parentheses are standard deviations in the last significant figure.

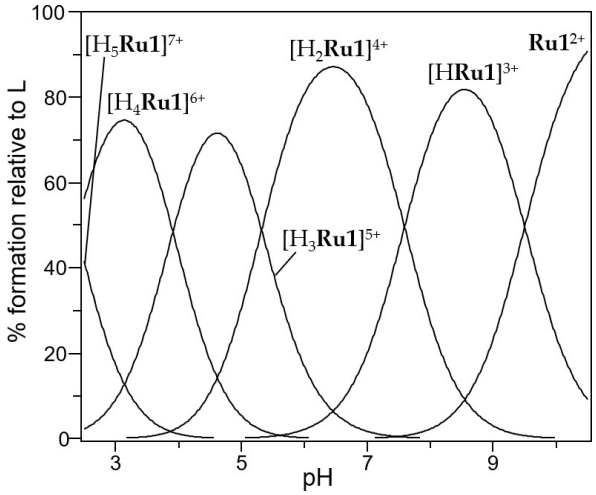

Figure S1. Distribution diagram of the protonated species of $Ru1^{2+}$

*Distribution diagram of the protonated species of **Ru1**$^{2+}$ as a function of pH ($[\mathbf{Ru1}^{2+}] = 1 \times 10^{-3}$ M, NMe_4Cl 0.1 M, 298.1 ± 0.1 K).*

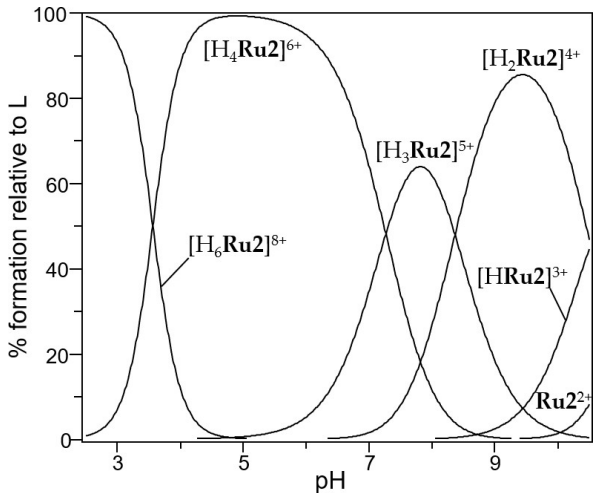

Figure S2. Distribution diagram of the protonated species of $Ru2^{2+}$

*Distribution diagram of the protonated species of **Ru2**$^{2+}$ as a function of pH ([**Ru2**$^{2+}$] = 1 x 10^{-3} M, NMe_4Cl 0.1 M, 298.1 ± 0.1 K).*

2. Metal-binding properties of $Ru1^{2+}$ and $Ru2^{2+}$

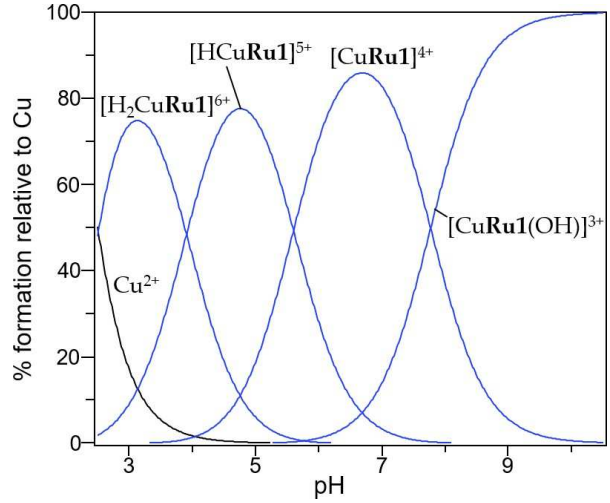

Figure S3. Distribution diagram of the Cu(II)-complexed species of $Ru1^{2+}$

*Distribution diagram of the species present in solution for the system **Ru1**$^{2+}$/Cu(II) in 1:1 molar ratio as a function of pH ([**Ru1**$^{2+}$] = [Cu(II)] = 1 x 10^{-3} M, NMe_4Cl 0.1 M, 298.1 ± 0.1 K).*

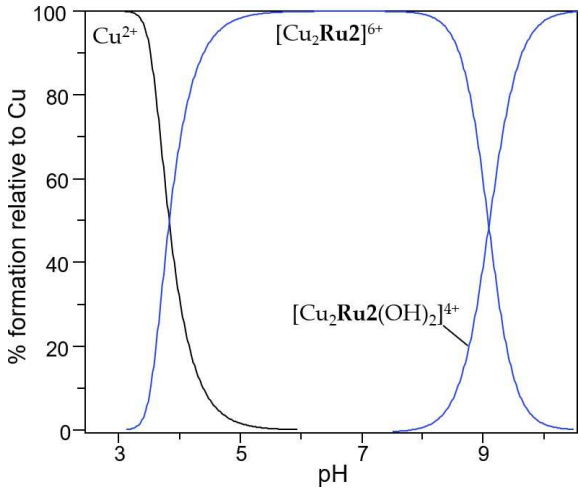

Figure S4. Distribution diagram of the Cu(II)-complexed species of Ru2^{2+}

*Distribution diagram of the species present in solution for the system **Ru2**$^{2+}$/Cu(II) in 1:2 molar ratio as a function of pH ([**Ru2**$^{2+}$] = 1 x 10^{-3} M, [Cu(II)] = 2 x 10^{-3} M, NMe_4Cl 0.1 M, 298.1 ± 0.1 K).*

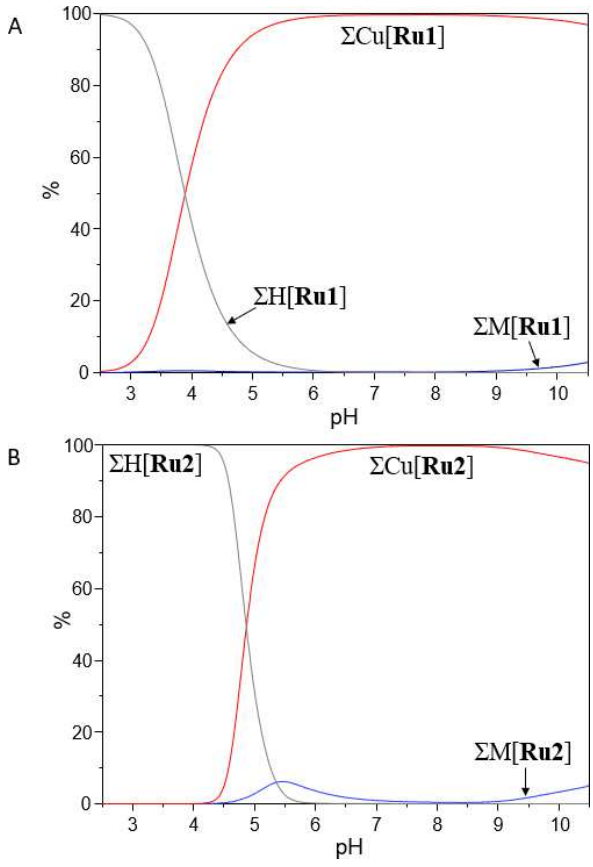

Figure S5. Selectivity diagrams with Cu(II) and other biologically relevant cations

*Overall percentages of the complexed species formed by **Ru1**$^{2+}$ (A) and **Ru2**$^{2+}$ (B) with Cu(II) (red lines), compared to the protonated forms of free ligands (grey lines) and to the metal complexed species formed with Ca(II), Zn(II) and Mg(II) (blue lines). [**Ru1**$^{2+}$] = [**Ru2**$^{+}$] = 1 μM, [Cu(II)] = 1 μM, [Zn(II)] = 15 μM, [Ca(II)] = 2.5 x 10^{-3} M, [Mg(II)] = 1.5 x 10^{-3} M.*

3. Fluorescence properties of ruthenium compounds

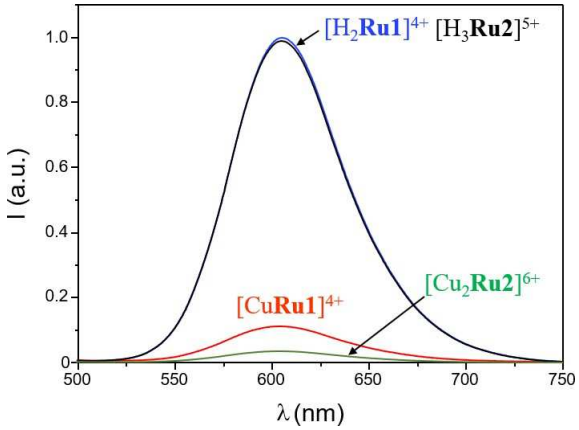

Figure S6. Fluorescence emission by Ru(II)- and mixed Ru(II)-Cu(II) complexes

Fluorescence spectra of aqueous solution of ***Ru1***$^{2+}$ *(blue line),* [Cu***Ru1***]$^{4+}$ *(red line),* ***Ru2***$^{2+}$ *(black line) and* [Cu$_2$***Ru2***]$^{6+}$ *(green line), collected at pH 7.4 (*λ_{exc} *= 411 nm, [Ru] = 3 μM).* [H$_2$***Ru1***]$^{4+}$, [H$_3$***Ru2***]$^{5+}$, [Cu***Ru1***]$^{4+}$ *and* [Cu$_2$***Ru2***]$^{6+}$ *are the main species present in solution at this pH value.*

4. ROS production and identification by [CuRu1]$^{4+}$ and [Cu$_2$Ru2]$^{6+}$

ROS production by [Cu**Ru1**]$^{4+}$ and [Cu$_2$**Ru2**]$^{6+}$ was performed by using Electron Paramagnetic Resonance (EPR) spin trapping technique. This technique involves the reaction of an initially generated short-living radical with an added organic compound, known as spin trap, to generate longer-living radical adducts with clear EPR fingerprints. Among the most common spin traps, 5,5-dimethyl-1-pyrroline-N-oxide (DMPO) efficiently captures the free radicals generated by an unstable species (H_2O_2) due to the catalysing action of a supposedly active molecule.

The spectra collected for a solution containing only H_2O_2 and DMPO, as reference sample, are reported, together with those obtained by adding [Cu**Ru1**]$^{4+}$ or [Cu$_2$**Ru2**]$^{6+}$ to this mixture, in Figure 1 of the manuscript. The acquired EPR spectra were also simulated by using the core function *pepper* of the open-source MATLAB toolbox EasySpin[1]. The simulations were obtained using an isotropic g factor = 2.0054 for both radicals and the following hyperfine constants: A = 42 MHz for both N and H nuclei in the hydroxide species and A = 32.5, 39.8, 3.4 MHz for H, N and H nuclei, respectively, according to literature[2]. The obtained results are shown in Figure S7.

It is important to notice that different concentrations of reagents (especially of the radical source, H_2O_2) can lead to different hydroxide/perhydroxyl radical ratios. All the EPR measurements reported in this paper were taken in the same experimental conditions and were therefore comparable.

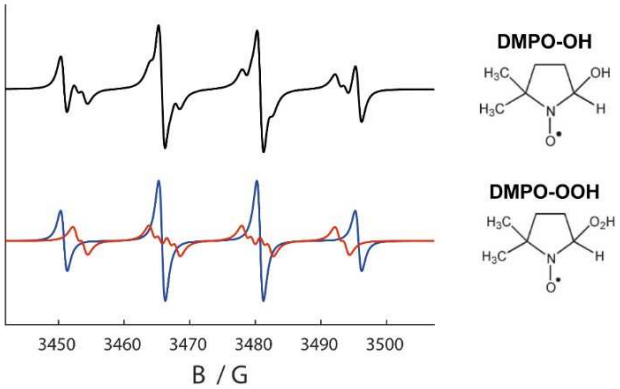

Figure S7. Simulation of the EPR spectra reported in Figure 1

The black trace is the best simulation obtained as the sum the EPR spectra of DMPO-OH (blue trace) and DMPO-OOH (red trace) radicals whose molecular structures are reported in the right part of the figure.

The lack of formation of singlet oxygen upon irradiation of the heteronuclear Ru(II)/Cu(II) complexes was confirmed through EPR measurements employing 2,2,6,6-tetramethylpiperidine (TEMP) as spin trap for single oxygen. In Figure S8 are reported the spectra obtained following irradiation of an aqueous solution of [Cu**Ru1**]$^{4+}$ at physiological pH in the presence of TEMP; similar results were also obtained for [Cu_2**Ru2**]$^{6+}$ (data not shown).

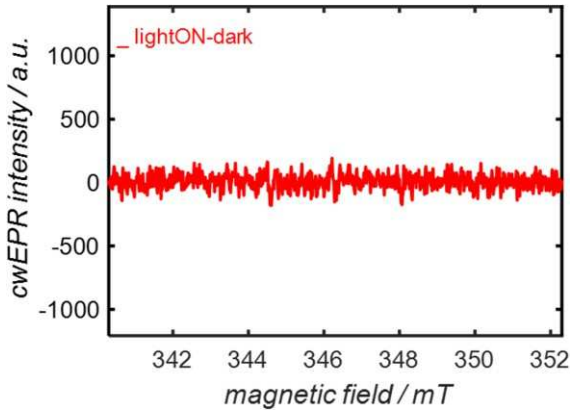

Figure S8. EPR analysis with TEMP as spin trap for singlet oxygen
*Difference between the spectra acquired under (lightON) and before (dark) light irradiation in a water solution (pH 7.4) containing [Cu**Ru1**]$^{4+}$ (5 mM) and TEMP (125 mM). For sample irradiation, a 405nm laser diode was used.*

5. Redox properties of [CuRu1]$^{4+}$ and [Cu_2Ru2]$^{6+}$

Redox potential, also known as oxidation-reduction potential (ORP), is a physicochemical parameter that can be used to measure the oxidative or reductive properties of a solution. ORPs of the [Cu**Ru1**]$^{4+}$ and [Cu_2**Ru2**]$^{6+}$ solutions were measured with an ORP electrode (HI3148B ORP, Hanna® Instruments, Padova, Italy) combined with a pH/ORP meter (HI5222 bench meter Hanna® Instruments, Padova, Italy). Before measurement, the electrode was calibrated with two redox standard solutions (HI7021 and HI7022, Hanna® Instruments, Padova, Italy). Glutathione (GSH) was obtained from Sigma-Aldrich.

Table S2. ORP analysis for heteronuclear complexes
*Oxidation-Reduction Potential (ORP) measured for 5 mL of 10 µM [Cu**Ru1**]$^{4+}$, 10 µM [Cu_2**Ru2**]$^{6+}$, and 5 mM GSH in 10 mM phosphate buffer pH 7.4.*

Sample	ORP value (mV)
[Cu_2**Ru2**]$^{6+}$	299.2 ± 4.9
[Cu**Ru1**]$^{4+}$	275.6 ± 1.3
GSH	130.0 ± 3.0

Table S2 shows the ORP values obtained for [Cu_2**Ru2**]$^{6+}$, [Cu**Ru1**]$^{4+}$ and GSH. By the analysis of these values, the ORP value of a 5 mM GSH solution turned out to be the lowest, thus confirming the higher reduction properties of this solution in comparison to both [Cu**Ru1**]$^{4+}$ and [Cu_2**Ru2**]$^{6+}$ solutions.
The redox properties of the two Cu(II)-containing complexes were also studied in cyclic voltammetry (CV) at a carbon screen-printed electrode. The redox system associated with changes in the oxidation state of copper ion is visible in the potential range from about +0.1 to -0.5 V, at a scanning rate of 50 mV/s. The potential-current parameters are reported in Table S3, including the cathodic peak potential ($E_{p,c}$), the anodic peak potential ($E_{p,a}$) and the ($E_{p,a}$+$E_{p,c}$)/2 values (the potential midway between the anodic and cathodic peaks, corresponding to the formal potential).
A lower potential value has to be reached on the cathodic wave to reduce the Cu(II) coordinated by [Cu**Ru1**]$^{4+}$ if compared to [Cu_2**Ru2**]$^{6+}$ (Table S3).

Nonetheless, given the highly reducing potential of GSH (Table S2), it cannot be excluded that the Cu(II) coordinated by **Ru1**$^{2+}$ and **Ru2**$^{2+}$ could be reduced in the cellular environment, where high concentrations of GSH are present.

Table S3. CV analysis for heteronuclear complexes

*Potential of the anodic ($E_{p,a}$) and cathodic ($E_{p,c}$) peaks measured by cyclic voltammetry for 1 mM [Cu**Ru1**]$^{4+}$ and 1 mM [Cu_2**Ru2**]$^{6+}$ in 0.1 M KNO_3; scan rate 50 mV/s. KNO_3 was chosen as non-complexing supporting electrolyte. The solutions containing the two complexes were drop-casted (45 µL) onto the surface of disposable screen-printed electrodes (Ecobioservices and Researches (EBSR), Florence, Italy) composed of a carbon working electrode (Ø 3 mm), a carbon counter electrode, and an external Ag/AgCl reference electrode filled with saturated KCl. The voltammograms were recorded using a PGSTAT12 potentiostat/galvanostat running with GPES software (Metrohm Italia).*

Sample	$E_{p,a}$ (mV)	$E_{p,c}$ (mV)	$(E_{p,a}+E_{p,c})/2$ (mV)
[Cu**Ru1**]$^{4+}$	-40	-396	-218
[Cu_2**Ru2**]$^{6+}$	+14	-340	-163

6. Analysis of ruthenium compounds' distribution in mitochondria

Taking into account that the cationic nature of ruthenium compounds may affect their cellular localization and thus photoactivation-dependent mitochondrial depolarization, we evaluated possible localization of the photosensitizers in mitochondria. A2780 ovarian cancer cells were seeded on microscope slides and treated with 10 µM of each Ru complex for 24 hours. After incubation with 20 nM MitroTracker Green FM probe (#M7514, Thermo Fisher Scientific; Ex/Em: 490/516) in RPMI without phenol red for 30 minutes at 37°C, living cells were analyzed using a Leica SP8 laser scanning confocal microscope (Leica Microsystems GmbH) by 63X oil immersion objective.

Images of A2780 cells incubated with **Ru1**$^{2+}$, **Ru2**$^{2+}$, [Cu**Ru1**]$^{4+}$ or [Cu_2**Ru2**]$^{6+}$ and MitoTracker green are shown in Figure S9A. Scatterplots of red versus green pixel intensities of the images reported in Figure S9B show that a random distribution occurs between each ruthenium compound and mitochondria.

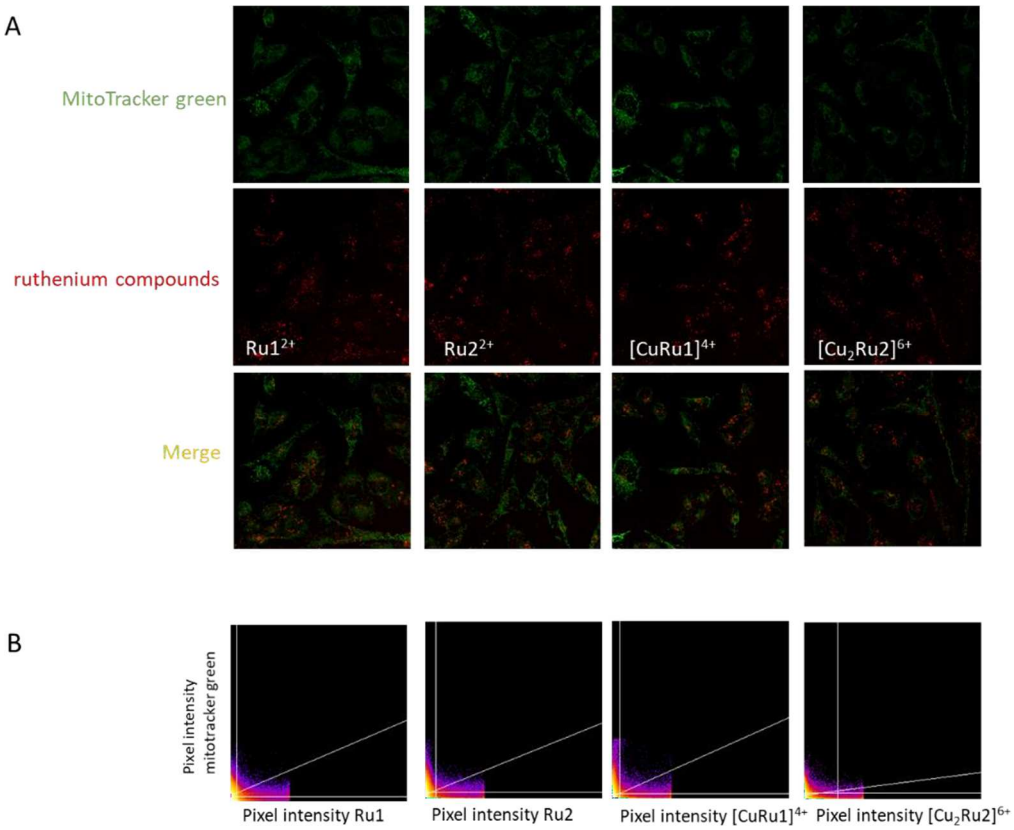

Figure S9. Localization of ruthenium compounds compared to mitochondria in A2780 cells

A) Confocal microscopy of A2780 cells following Mitotracker green (Green) staining after 24 h-incubation with ***Ru1***$^{2+}$, ***Ru2***$^{2+}$, [Cu***Ru1***]$^{4+}$ *or* [Cu_2***Ru2***]$^{6+}$ *(Red). B) Scatterplots of red and green pixel intensities for each ruthenium compound.*

7. Internalization of ruthenium compounds in cancer versus non-cancer cells

In order to analyse ruthenium compound internalization in cancer versus non-cancer cells, we performed laser scanning confocal microscopy in non-cancer cell line, namely C2C12 myoblasts (undifferentiated skeletal muscle cells), as well as A2780 ovarian cancer cells, both incubated with 10 μM of each ruthenium compounds for 24 hours. Confocal microscopy images in Figure S10 show that in C2C12 myoblasts incubated with each photosensitizer the associated red fluorescence is not appreciable. However, in A2780 cells ruthenium compounds are located in segregated areas into the cytosol thus excluding passive diffusion as possible mechanism of ruthenium compound uptake.

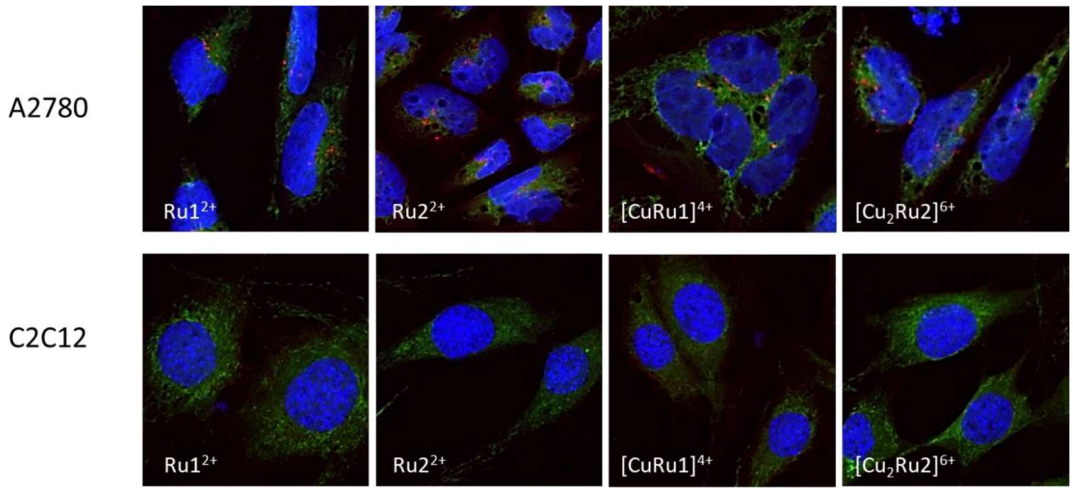

Figure S10. Internalization of Ru complexes in A2780 versus C2C12 cells.
A2780 ovarian cancer cells and C2C12 myoblasts were seeded into microscope slides, both incubated with each photosensitizer ***Ru1***$^{2+}$, ***Ru2***$^{2+}$, *[Cu**Ru1**]*$^{4+}$ *or [Cu*$_2$*Ru2]*$^{6+}$ *(Red) at a concentration of 10 μM for 24 hours and challenged with DAPI (Blue), after administration of Mitotraker CMX-Ros (Green). Confocal microscopy was performed to assess ruthenium compound internalization using Leica SP8 with a 63X objective.*

8. Analysis of ruthenium compounds' internalization in early endosomes

To evaluate the possible internalization pathways of ruthenium compounds in A2780 cancer cells, localization of **Ru1**$^{2+}$, **Ru2**$^{2+}$, [Cu**Ru1**]$^{4+}$ or [Cu$_2$**Ru2**]$^{6+}$ in early endosomes (EE) was analyzed. For this purpose, A2780 cells were seeded on microscope slides and treated with 10 μM of each Ru (II) complex for 30 minutes or 24 hours. After cell fixation using 2% paraformaldehyde, slides were incubated for 30 minutes with permeabilization and quenching solution (0.1% Triton X-100, 10 mM ethanolamine in PBS) and then with a blocking buffer (3% BSA in PBS) for 40 minutes. Subsequently, 1:100 Anti-Rab5 (E6N8S) Mouse Antibody (#46449, Cell Signaling Technology), maker of EE, was employed for 2 hours, then Fluorescein Anti-Mouse secondary antibody 1:200 (FI-2000) (Vector Laboratories, Inc., Burlingame, CA) was incubated for 1 hour at room temperature. Finally, DAPI solution (#MBD0015, Sigma-Aldrich) was administered to detect nuclei. Slides were mounted by using Fluoromount Aqueous Mounting Medium (Sigma-Aldrich, MA, USA) and images acquired using a Leica SP8 laser scanning confocal microscope (Leica Microsystems GmbH) by 63X oil immersion objective.

As reported in Figure S11, immunofluorescence analysis of Rab5 in A2780 cells after incubation with **Ru1**$^{2+}$, **Ru2**$^{2+}$, [Cu**Ru1**]$^{4+}$ or [Cu$_2$**Ru2**]$^{6+}$ for 30 minutes (A) and 24 hours (B) demonstrated negligible localization of ruthenium compounds with Rab5, ruling out the possible involvement of EE in the internalization pathway of Ru(II) photosensitizers.

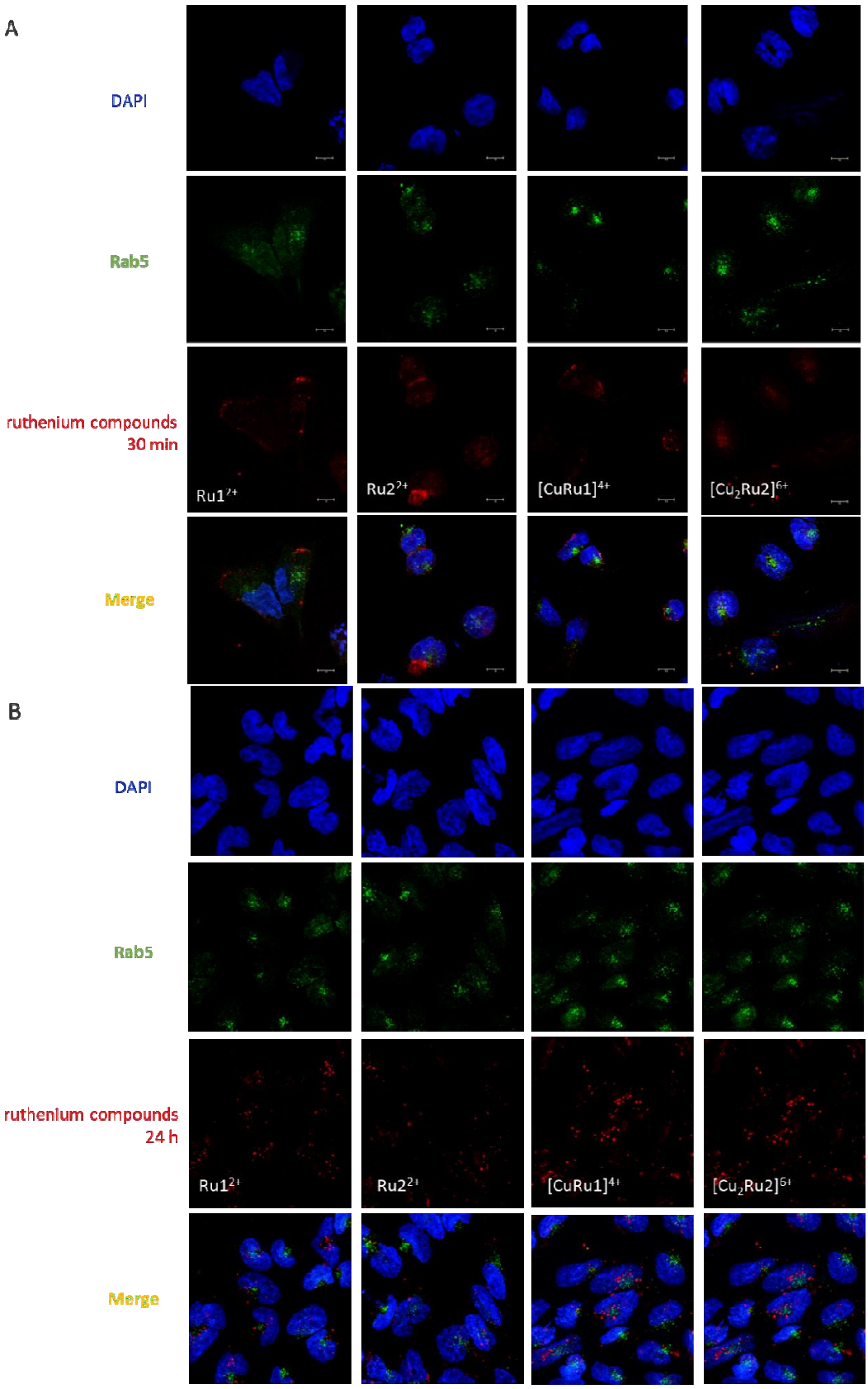

Figure S11. Localization of ruthenium compounds compared to early endosome in A2780 cells

Immunofluorescence analysis of Rab5 in A2780 cells after incubation with 10 μM ***Ru1***$^{2+}$, ***Ru2***$^{2+}$, [Cu***Ru1***]$^{4+}$ *or* [Cu$_2$***Ru2***]$^{6+}$ *for 30 min (A) or 24 h (B).*

9. Cytotoxicity and photoactivity of Ru complexes in non-cancer cells

To test cytotoxicity and photoactivity of different concentrations of **Ru1**$^{2+}$, **Ru2**$^{2+}$, [Cu**Ru1**]$^{4+}$ and [Cu_2**Ru2**]$^{6+}$ in non-cancer cells, MTT assays was performed in C2C12 myoblasts incubated for 24 hours with 0.1, 1 and 10 μM of each ruthenium compound then exposed or not to photoirradiation, 48 hours before being analysed. The photoirradiation experiments were conducted by using a low energy blue light-emitting diode (LED, λ_{max} = 434 nm, 30 W) and by employing the experimental set-up schematically represented in Fig. S12.

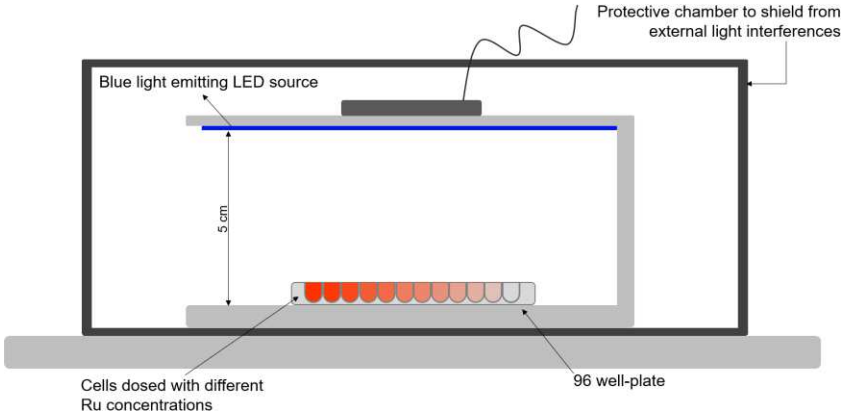

Figure S12. Experimental set-up employed for the photoirradiation experiments.

As shown in Figure S13, photosensitizers have a negligible effect on cytotoxicity of C2C12 myoblasts under dark conditions, whereas photoirradiation of **Ru1**$^{2+}$, **Ru2**$^{2+}$ or [Cu**Ru1**]$^{4+}$ shows a minor effect on cell survival of C2C12 myoblasts compared to A2780 cells that was not significant excepted for **Ru1**$^{2+}$, **Ru2**$^{2+}$, [Cu**Ru1**]$^{4+}$ at the higher (10 μM) concentration employed. The photoirradiation-induced cell death induced by [Cu_2**Ru2**]$^{6+}$ complex was not significant at all the concentrations used for MTT analysis.

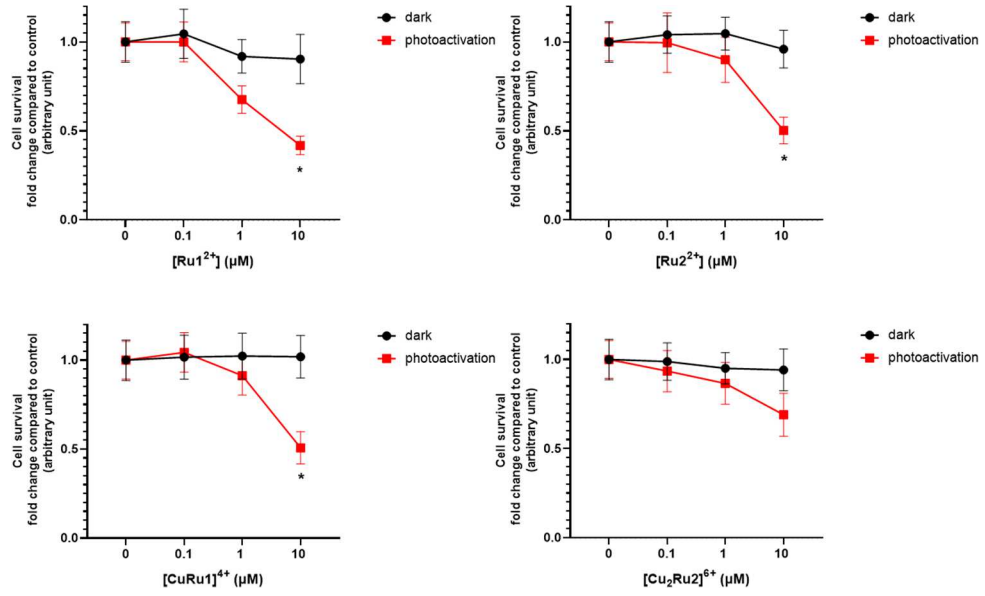

Figure S13. Cytotoxicity and photoactivity of ruthenium compounds in non-cancer C2C12 myoblasts.

C2C12 myoblasts were seeded in 96 multiwell plates and MTT reduction assay was performed under dark or photoactivation condition after challenge with 0.1, 1 and 10 μM of each photosensitizer for 24 hours. MTT analyses were performed in pentaplicate and are representative of three independent experiments. Data reported are mean ± SD of fold change above control untreated. The effect of photoactivation of 10 μM of ***Ru1***$^{2+}$, ***Ru2***$^{2+}$, *[Cu**Ru1**]*$^{4+}$ *and [Cu_2**Ru2**]*$^{6+}$ *complexes on cell survival of C2C12 cells was statistically significant by two-way ANOVA followed by Bonferroni post-hoc test; *P<0.05.*

10. List of Abbreviations.

Photosensitizer agents	PSs
Photodynamic therapy	PDT
Reactive oxygen species	ROS
Ruthenium polypyridyl complexes	RPCs
Ground-state molecular oxygen	$^3O_2$
Singlet oxygen	$^1O_2$
Superoxide	$O_2^{\bullet-}$
Hydroxyl radical	$HO^{\bullet}$
Quantum yields	φ_{Δ}
Electron Paramagnetic Resonance	EPR
2,2,6,6-tetramethylpiperidine	TEMP
5,5-dimethyl-1-pyrroline-N-oxide	DMPO
Perhydroxyl	$HOO^{\bullet}$
Cyclic voltammetry	CV
Mitochondrial membrane potential	$\Delta\psi m$
Not significant	ns
CM-H_2DCFDA	DCF
Fetal bovine serum	FBS
Bovine Serum Albumin	BSA
Inductively Coupled Plasma Atomic Emission Spectrometer	ICP-AES
3-(4,5-Dimethylthiazol-2-yl)-2,5-Diphenyltetrazolium Bromide	MTT
Sodium dodecyl sulphate	SDS
Potential of the anodic peaks	Ep,a
Potential of cathodic peaks	Ep,c
Inductively Coupled Plasma Atomic Emission Spectrometer	ICP-AES
Phosphate buffered saline	PBS

References

[1] S. Stoll, A. Schweiger, EasySpin, a comprehensive software package for spectral simulation and analysis in EPR, J. Magn. Reson. (2006). https://doi.org/10.1016/j.jmr.2005.08.013.

[2] G.M. Rosen, A. Beselman, P. Tsai, S. Pou, C. Mailer, K. Ichikawa, B.H. Robinson, R. Nielsen, H.J. Halpern, A.D. MacKerell, Influence of Conformation on the EPR Spectrum of 5,5-Dimethyl-1-hydroperoxy-1-pyrrolidinyloxyl: A Spin Trapped Adduct of Superoxide, J. Org. Chem. (2004). https://doi.org/10.1021/jo0354894.

INORGANIC CHEMISTRY
FRONTIERS

RESEARCH ARTICLE

View Article Online
View Journal | View Issue

Cite this: *Inorg. Chem. Front.*, 2023, 10, 3025

Ruthenium(II) polypyridyl complexes with π-expansive ligands: synthesis and cubosome encapsulation for photodynamic therapy of non-melanoma skin cancer†

Gina Elena Giacomazzo,‡[a] Michele Schlich, ‡[b] Luca Casula, ‡[b] Luciano Galantini, [c,d] Alessandra Del Giudice, [c,d] Giangaetano Pietraperzia,[a,e] Chiara Sinico,[b] Francesca Cencetti, [f] Sara Pecchioli, [f] Barbara Valtancoli,[a] Luca Conti, *[a] Sergio Murgia *[b,d] and Claudia Giorgi *[a]

In photodynamic therapy (PDT), Ru(II) polypyridyl complexes (RPCs) featuring the popular π-expansive benzo[*i*]dipyrido[3,2-*a*:2',3'-*c*]phenazine (dppn) ligand have attracted much attention, mainly due to the good singlet oxygen sensitizing properties imparted by this peculiar ligand. However, notwithstanding the intriguing perspectives, much remains to be explored about the use of RPC-based photosensitizing agents (PSs) with more than a dppn ligand in their scaffolds. Herein, two bis-heteroleptic RPCs of the general formula $[Ru(dppn)_2L]^{n+}$ (L = 4,4'-dimethyl-2,2'-bipyridine, $n = 2$, Ru1 or 2,2'-bipyridine-4,4'-dicarboxylate, $n = 0$, Ru2) were prepared in good yields by adopting an alternative synthetic approach to previously reported methods. The optimal singlet oxygen sensitizing properties and capabilities to interact with DNA displayed by Ru1 and Ru2 were paralleled by a potent light-triggered toxicity (λ_{max} = 462 nm) exerted on squamous epithelial carcinoma cells. To improve the biopharmaceutical properties of these compounds, Ru1 and Ru2 were encapsulated into cubosomes, soft nanoparticles with a lyotropic liquid crystalline core. *In vitro* studies probed the effectiveness of these formulations against light-irradiated cancer cells and confirmed intracellular ROS generation as the mechanism likely to be responsible for the observed PDT efficacy. This work highlights the potential of $[Ru(dppn)_2L]$-based PSs in PDT, beyond providing a general and straightforward synthetic route for the preparation of this class of compounds. To the best of our knowledge, this is also the first example of the encapsulation of a RPC into cubosome nanostructures, paving the way for the development of nano-formulations with augmented biopharmaceutical properties for PDT application.

Received 16th December 2022,
Accepted 6th April 2023

DOI: 10.1039/d2qi02678c

rsc.li/frontiers-inorganic

Introduction

Photodynamic therapy (PDT) continues to attract increasing attention thanks to the encouraging results that its application has led to the treatment of a variety of cancers, spanning from skin tumors to lung, bladder and prostate cancers,[1,2] as well as bacterial infections.[3,4] The main advantage of this therapeutic approach, which consists of the light activation of a prodrug, called a photosensitizer (PS), to produce harmful reactive oxygen species (ROS), is represented by the complete spatio-temporal control over drug activation, which provides a precious chance to limit the severe side effects normally occurring with standard chemotherapeutics.

Ruthenium(II) polypyridyl complexes (RPCs) have been largely employed in the research of suitable PSs in PDT, with the Mc Farland compound TLD1433 being the first Ru(II)-based PS to enter human clinical trials for bladder cancer.[5–8]

[a]*Department of Chemistry "Ugo Schiff", University of Florence, Via della Lastruccia 3, 50019 Sesto Fiorentino (FI), Italy. E-mail: luca.conti@unifi.it, claudia.giorgi@unifi.it*
[b]*Department of Life and Environmental Sciences, University of Cagliari, 09124 Cagliari (CA), Italy. E-mail: murgias@unica.it*
[c]*Department of Chemistry, University of Rome La Sapienza, P.le A. Moro 5, 00185 Rome, Italy*
[d]*CSGI, Consorzio Interuniversitario per lo Sviluppo dei Sistemi a Grande Interfase, 50019 Sesto Fiorentino (FI), Italy*
[e]*European Laboratory for Non-Linear Spectroscopy (LENS), Via Nello Carrara 1, 50019 Sesto Fiorentino (FI), Italy*
[f]*Department of Experimental and Clinical Biomedical Sciences "Mario Serio", 50134 Florence, Italy*

† Electronic supplementary information (ESI) available: Methods, supplementary figures and schemes, and the spectra of compounds. See DOI: https://doi.org/10.1039/d2qi02678c

‡ These authors contributed equally.

The interest towards this versatile class of compounds can be attributed to its rich chemical–physical repertoire, which includes a variety of excited-state electronic configurations accessible with light, good singlet oxygen sensitizing properties, and the capacity to interact with key biological targets (such as DNA or proteins).[9–11] Of relevance is that a fine choice of ligands in their octahedral geometries permits convenient modulation of the photophysical, photochemical, and photobiological properties of the resulting RPCs, in an effort to improve cellular uptake,[12,13] shift the absorption profiles towards red,[14] confer targeting ability,[15,16] and boost $^1O_2$ sensitization. With regard to the latter aim, as prolonged excited state lifetimes are important for efficient energy transfer to molecular oxygen to form $^1O_2$, changing the nature of the lowest-lying excited state from metal-to-ligand charge-transfer (^{3}MLCT) to long-lived intraligand ^{3}IL states represents a suitable way to endow the resulting RPCs with augmented cytotoxicity.[6,17] Following this strategy, over the past few years much interest has been devoted to the use of the π-expansive benzo[*i*]dipyrido[3,2-*a*:2′,3′-*c*]phenazine (dppn) ligand in the rational design of RPC-based PSs. Indeed, this peculiar ligand has been largely exploited not only to improve the photobiological activity of the resulting compounds, *via* the population of long-lived dppn-centered $^3\pi\pi^*$ excited states, but also to shift their ^{1}MLCT absorption towards longer wavelengths[18] and, given its known DNA-intercalating properties, to strengthen their interaction with the nucleic acid.[19–21] A recent example of this was reported by Zhao and coworkers, who showed the benefits derived from the substitution of a bpy (bipyridine) unit by a dppn ligand in their tris-heteroleptic RPC-based PSs.[22]

Notwithstanding the advantages derived from the use of dppn, it is surprising that PSs containing two dppn ligands simultaneously coordinated to a Ru(II) center have been only sparingly explored,[23,24] while numerous examples of dppn-containing RPCs for PDT are reported in the literature[25–31] (some of them have also been applied for compounds at the boundary between PDT and photoactivated chemotherapy PACT).[32,33] Such net discrepancy between RPCs containing one and two dppn units would be related to synthetic issues concerning the preparation of the latter compounds by the general procedures for bis-heteroleptic Ru(II) complexes,[34,35] involving the intermediate [(dppn)$_2$RuCl$_2$] which is scarcely soluble in most organic solvents.

In addition, the potential anticancer activity of these systems might be limited by their common hydrophobic nature, leading to poor bioavailability and compromised therapeutic outcomes. To overcome these limits, nanocarriers have been widely investigated as a formative approach to increase the water solubility of insoluble drug candidates, prevent drug degradation, and enhance their delivery.[36–38] In the midst of the innovative exploited nano-systems, great interest has arisen around cubosomes, also known as bicontinuous cubic liquid crystalline nanoparticles with a three-dimensional arrangement of the lipid bilayer forming a honeycomb-like inner structure. Compared to single-bilayer liposomes, cubosomes are characterized by an inner portion completely filled with the lipid matrix, providing a greater hydrophobic volume and thus a higher loading efficiency.[39] Despite the fact that some investigations illustrated a possible cubosome cytotoxicity,[40,41] appropriate formulation strategies and administration at lower concentrations can be used to achieve the desired therapeutic effects. In fact, recent studies have proven their useful biomedical applications for diagnostic purposes, anticancer activity, and PDT.[42–46]

Prompted by this scenario, herein we explored the potential as PSs of two Ru(II) compounds featuring two dppn ligands simultaneously coordinated to the Ru(II) centers; [Ru(dppn)$_2$(dmbpy)]$^{2+}$ (Ru1) and [Ru(dppn)$_2$(dcbpy^{2-})] (Ru2) (dmbpy = 4,4′-dimethyl-2,2′-bipyridine, dcbpy^{2-} = 2,2′-bipyridine-4,4′-dicarboxylate) (Chart 1). Besides the Ru(dppn)$_2$-core, different dmbpy and dcbpy^{2-} ancillary ligands were chosen to provide a potential synthetic platform for obtaining differently functionalized (dppn)$_2$-RPCs, to investigate their possible influence on the chemical–physical and biological properties of the resulting compounds.

Ru1 and Ru2 were prepared by adopting a straightforward synthetic route where the dppn ligands were allowed to react with Ru(II)-intermediates in the last step of the reaction, thus avoiding the use of [Ru(dppn)$_2$Cl$_2$] and leading to the production of RPCs in good yields. These systems exhibited promising features as PSs, by virtue of optimal singlet oxygen sensitizing properties and capacity to interact with DNA, and for this reason their phototoxicity and biocompatibility were tested on non-melanoma skin cancer cells *in vitro*, a model tumor selected for the feasibility of its treatment by photodynamic therapy.[47] To further ascertain their potential as PSs, Ru1 and Ru2 were also encapsulated in monoolein-based cubosomes stabilized with Pluronic F108. Following a preliminary investigation of the obtained formulations, Ru2-cubo was then selected for further development including a thorough physicochemical characterization and the assessment of its phototoxic activity against epidermoid carcinoma cells.

The results herein discussed may provide fundamental knowledge for the design of novel and highly performant PSs

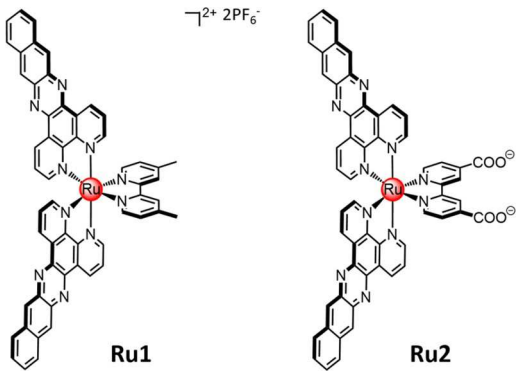

Chart 1 Chemical structures of ruthenium complexes Ru1 and Ru2 of this study.

based on $(dppn)_2$-containing RPCs. Moreover, to the best of our knowledge, this study reports the first example of the encapsulation of a RPC into cubosome nanostructures, thus paving the way for the development of pharmaceutically viable nano-formulations for PDT applications.

Results and discussion

Synthesis and characterization of ruthenium compounds

Ru(II) complexes Ru1 and Ru2 were obtained *via* stepwise ligand addition following the synthetic route shown in Scheme 1c. In this synthetic approach, the polymeric precursor $[Ru(CO)_2Cl_2]_n$ was first prepared by the reaction of the commercial $RuCl_3 \cdot nH_2O$ with paraformaldehyde in formic acid. Then, this compound was allowed to react with the bidentate ligands in refluxing methanol (dmbpy) or DMF (dcbpy), affording the *trans*-Cl[Ru(dmbpy)$(CO)_2Cl_2$] and *trans*-Cl[Ru(dcbpy)$(CO)_2Cl_2$] intermediates, with yields of 75 and 55%, respectively. In the latter case, DMF was chosen as the solvent because of the limited solubility of dcbpy in methanol.[48] Finally, two equivalents of dppn ligands were added to solutions of the *trans*-Cl[RuL$(CO)_2Cl_2$] (L = 4,4′-dimethyl-2,2′-bipyridine or dmbpy, 2,2′-bipyridine-4,4′-dicarboxylic acid or dcbpy) intermediates in 2-methoxyethanol, and in the presence of trimethylamine *N*-oxide (TMAO), to favour the detachment of the strongly coordinated CO ligands[49] and allow their replacement by the bidentate dppn ligands. The addition of aqueous KPF_6 led to the precipitation of the hexafluorophosphate salt of Ru1 whereas Ru2 precipitated as a neutral product from the reaction mixture. Ru1 and Ru2 were obtained, after purification by flash chromatography, in 78% and 50% yields, respectively. The identity of the obtained compounds was confirmed by ^1H, ^{13}C, COSY and HSQC NMR and high-resolution mass spectrometry (HR-MS) analysis (see the ESI, Fig. S1–S10†). ^1H NMR signal assignment is reported in the ESI;† recording of ^{13}C and HSQC spectra of Ru2 was prevented by its poor solubility in $(CD_3)_2SO$.

As shown in Scheme 1, it can be highlighted that, compared to the most employed synthetic approach used for the preparation of bis-heteroleptic complexes with the general formula $[Ru(NN)_2L]^{2+}$ (*N*,*N* = polypyridyl bidentate ligand)[50,51] (Scheme 1a), commonly obtained by the reaction of $[Ru(NN)_2Cl_2]$ with a third chelate ligand (L), in the method of this work the two dppn ligands are allowed to react with the Ru(II)-scaffolds only in the last step of the reaction. This would permit to overcome solubility issues arising from the use of the $[Ru(dppn)_2Cl_2]$ intermediate. A similar "*reverse*" concept was also previously applied by Turro and coworkers in the synthesis of a rare example of a $(dppn)_2$-containing RPC reported in the literature, namely $[Ru(bpy)(dppn)_2][PF_6]_2$,[24] which was indeed obtained by the reaction of dppn with $[Ru(bpy)(CH_3CN)_4]^{2+}$ in the last reaction step (Scheme 1b). However, long reaction times (in the order of 7–24 days) were required by this route to prepare the intermediate $[Ru(bpy)(CH_3CN)_4]^{2+}$ using $RuCl_3 \cdot nH_2O$ as the starting material.[52,53]

In light of these considerations, the synthetic strategy employed in this work may provide an alternative and straightforward way for the preparation of RPCs featuring the general formula $[Ru(dppn)_2L]^{n+}$ (L = variously functionalized bidentate polypyridyl chelates), in good yields and reaction times.

The electronic absorption spectra of Ru1 and Ru2 in acetonitrile are shown in Fig. 1a, whereas their molar extinction coefficients (ε) at different absorption maxima (λ_{max}) are listed

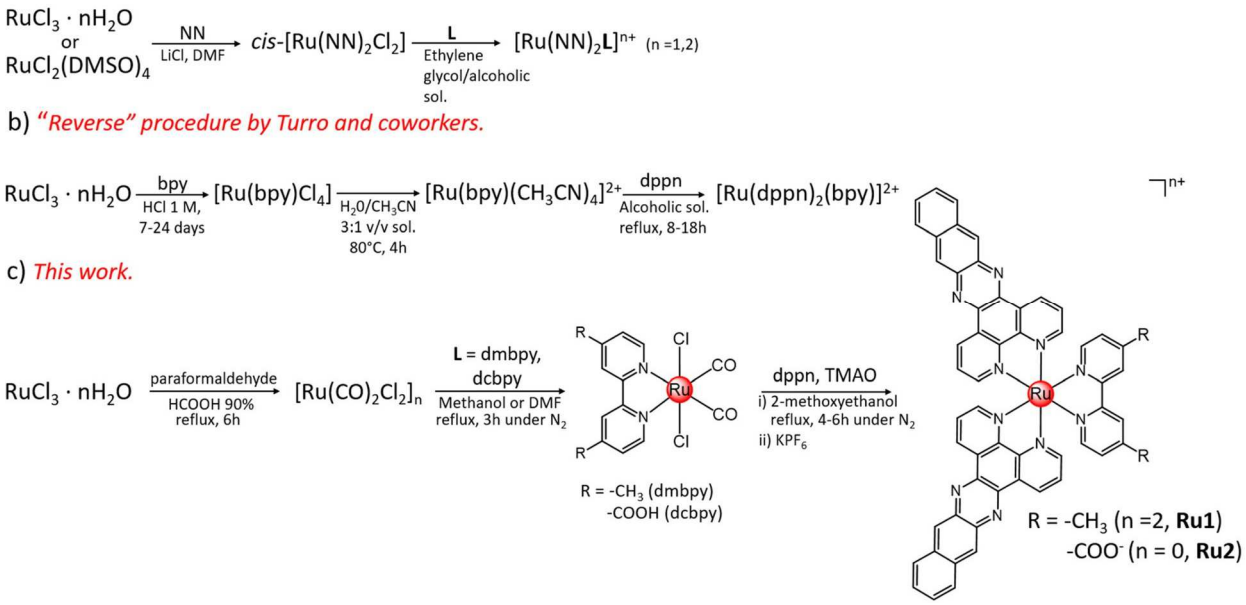

Scheme 1 Synthetic route followed for the preparation of complexes Ru1 and Ru2 of this work (3c), compared to the one generally employed for the preparation of bis-heteroleptic RPCs (3a) and to the one previously reported for the Turro's compounds $[Ru(bpy)(dppn)_2][PF_6]_2$ and [Ru(phpy)$(dppn)_2][PF_6]$ (3b).

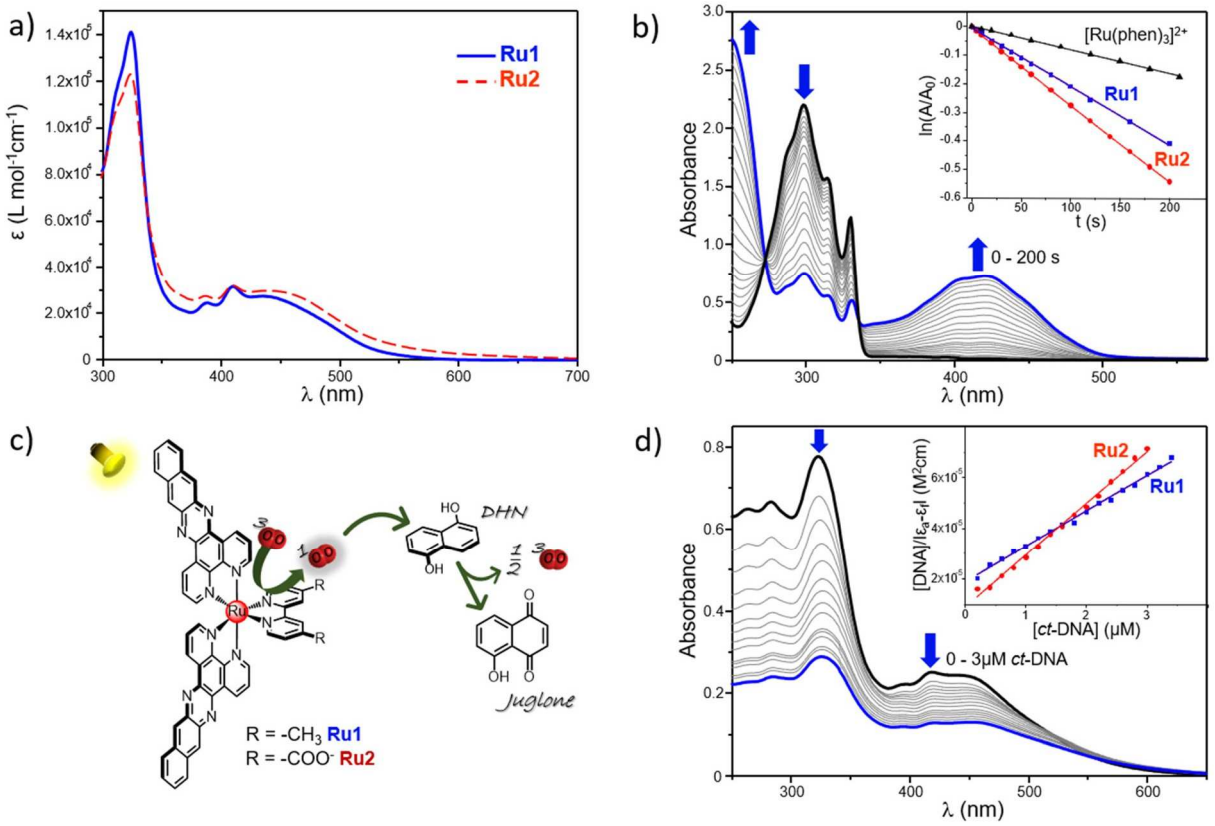

Fig. 1 Electronic absorption spectra of Ru1 and Ru2 in acetonitrile (a). Singlet oxygen determination as evaluated through UV-Vis analysis by using DHN as an indirect $^1O_2$ reporter; in the inset are compared the semilogarithmic plots of $\ln(A/A_0)$ as a function of the irradiation time registered for Ru1 and Ru2 and $[Ru(phen)_3]^{2+}$ as the reference control ([DHN] = 3.3 × 10^{-4} M, [Ru1] = [Ru2] = 10 μM) (b). Sketch of the $^1O_2$ determination by employing DHN as an indirect probe for $^1O_2$ (c). Absorption spectra of aqueous solutions of Ru1 registered in the presence of increasing concentrations of *ct*-DNA; in the inset are reported the $[DNA]/|\varepsilon_a - \varepsilon_f|$ values obtained for Ru1 and Ru2 *versus* the molar concentration of DNA ([Ru1] = [Ru2] = 10 μM, TRIS buffer pH 7.4) (d).

Table 1 Electronic absorption maxima measured in acetonitrile, rate constants K_{obs}, quantum yields for $^1O_2$ generation (ϕ_Δ) and binding constants with *ct*-DNA (K_b) of ruthenium complexes of this study

Compound	λ_{abs} nm^{-1} ($\varepsilon \times 10^3$ M^{-1} cm^{-1})[a]	K_{obs} [a]	ϕ_Δ ($^1O_2$) [b]	K_b ($\times 10^6$ M^{-1})	pK_a
Ru1	324 (146.1), 387 (25.3), 409 (32.2), 440 (26.6)	1.85×10^{-3}	0.54 ± 0.06	7.49×10^5	—
Ru2	323 (123.2), 387 (27.8), 410 (32.4), 445 (30.0)	2.71×10^{-3}	0.50 ± 0.07	2.34×10^6	pK_{a1}, pK_{a2}°3.6 ± 0.3, pK_{a2}^* 4.6 ± 0.4

[a] Determined in acetonitrile. [b] Determined for air-saturated acetonitrile solutions of Ru(II) complexes.

in Table 1. As shown, besides the intense intraligand π → π* transitions at 280–330 nm, both complexes display a double humped absorption at ~387 and ~410 nm, which is typical of the dppn centered π → π* transitions, plus a broad ^{1}MLCT absorption centered at ~445 nm, in good agreement with those of dppn-containing RPCs reported in the literature.[24,54] It can also be noted that the absorptions relative to the dppn-centered transitions of Ru1 and Ru2 are more intense than the corresponding ones reported for the parental compound [Ru(bpy)$_2$dppn]$^{2+}$,[24] as expected due to the presence of two dppn units in their Ru(II) scaffolds. On the other hand, Ru1 and Ru2 resulted to be weakly luminescent, with the highest emission being displayed by Ru2 in acetonitrile and ethanol (Fig. S11, ESI†).

Finally, given the presence of the ionizable dcbpy ligand in Ru2, the acid–base behavior of this complex in water was examined by means of spectrophotometric titrations, as described in the ESI.† Similar to what was previously reported for a parental dcbpy-containing Ru(II) complex,[55] of the two possible protonation equilibria only pK_{a2} values of 3.6 ± 0.3 and 4.6 ± 0.4, respectively, for the ground (pK_{a2}°) and the excited state (pK_{a2}^*) (Table 1) were determined by these measurements. This, along with the presence of two inflection points in the fluorescence titrations, suggested that the first

pK_a value was too low to be accurately determined. The higher value found for pK_{a2}^* relative to pK_{a2}° would be in line with the higher basicity of the complex in the excited state. It should also be noted that these data confirm that the carboxylic functions of Ru2 are likely to be fully deprotonated at neutral pH, conferring an overall total neutral charge to the complex. Therefore, along with the different nature of their ancillary ligands, it can be envisaged that the different charges of metal complexes in physiological media (+2 for Ru1, 0 for Ru2) might have an influence on their biological behavior and interaction with cubosome nanostructures (*vide infra*).

Singlet oxygen sensitizing properties of Ru(II)-complexes and DNA interaction

A crucial requisite for a candidate PS for PDT applications relies on its ability to trigger the formation of harmful reactive species under light-irradiation, such as the highly oxidant singlet oxygen $^1O_2$, the classical warhead of PDT produced as the result of *type*-II-based pathways.[56]

The singlet oxygen sensitizing properties of Ru(II) complexes Ru1 and Ru2 were first assessed spectrophotometrically, by employing 1,5-dihydroxynaphtalene (DHN) as an indirect reporter for singlet oxygen. Indeed, in the presence of $^1O_2$, DHN is promptly and quantitatively oxidized to give 5-hydroxy-1,4-naphthalenedione (Juglone), thus allowing to easily follow the photoexcitation process by monitoring the decrease of the DHN absorption band, centered at 297 nm, and the simultaneous increase of the broad Juglone band at around 427 nm (see Fig. 1c for a schematic illustration of the $^1O_2$ analysis by the DHN method for Ru1 and Ru2 complexes).

Fig. 1b shows the absorption spectra of an acetonitrile solution containing Ru1 and DHN subjected to increasing irradiation times (LED emitting at 434 nm, 160 mW), light-exposure determined the progressive decrease of the DHN absorption band along with the simultaneous increase of that of Juglone, thus clearly demonstrating the photosensitizing properties of Ru1. It should also be noted that the appearance of two clear isosbestic points in the UV-Vis titration, at ~280 and 330 nm, ruled out the formation of long-lived intermediates or byproducts. An analogous behavior was displayed by Ru2, as reported in Fig. S13 of the ESI.† Compared to [Ru(phen)$_3$]$^{2+}$, taken as a reference RPC for $^1O_2$ sensitization, both Ru1 and Ru2 exhibited remarkably higher photosensitizing features. This can be easily appreciated from the corresponding semilogaritmic plots of ln(A/A_0) over the irradiation time frame (A_0 and A are the absorbance values at 297 nm at time "*zero*" and at a generic time "*t*") reported in the inset of Fig. 1b, in which can be evidenced, for example, that a similar amount of $^1O_2$ was produced within 65–75 s by Ru1 and Ru2, and in more than 200 s by [Ru(phen)$_3$]$^{2+}$. In detail, Ru1 and Ru2 displayed a comparable potency, as denoted by the slight differences emerging between their relative rate constants for the DHN photooxidation processes (k_{obs}), of 1.85×10^{-3} and 2.71×10^{-3}, respectively (Table 1). In addition to the indirect DHN method, the $^1O_2$ sensitizing properties of Ru1 and Ru2 were further probed through direct measurement of the phosphorescence signal of $^1O_2$ at 1270 nm, induced by irradiation of air-saturated acetonitrile solutions of ruthenium complexes. This allowed us to determine the relative quantum yields of $^1O_2$ generation (ϕ_Δ), which are listed, along with the one of [Ru(phen)$_3$]$^{2+}$ for comparison (ϕ_Δ = 0.38 ± 0.06), in Table 1. As shown, ϕ_Δ values of 0.54 ± 0.06 and 0.50 ± 0.07 were respectively obtained for Ru1 and Ru2, thus confirming that the simultaneous presence of two dppn units into the Ru(II) scaffolds confers to these complexes a potent and comparable ability to sensitize the formation of singlet oxygen, in well agreement with the results of the UV-Vis analysis.

Since it is known that $^1O_2$ rapidly reacts with the surrounding biological substrates (estimated half-life <40 ns, range of action in the order of 20 nm),[57] leading to an extremely localized oxidative damage, the ability of a PS to effectively interact with a desired biological target may be important for its potential application in PDT, as it would ensure drug localization in close proximity to the target to be treated, strengthening the oxidative damage induced by ROS sensitization. This, along with the known DNA intercalating properties imparted by the π-expansive dppn ligands, prompted us to consider the affinity of the studied RPCs with the nucleic acid. The DNA-binding abilities of Ru1 and Ru2 were evaluated on *calf thymus* (*ct*-DNA) through UV-Vis analysis, by monitoring the changes in the absorption profiles of the aqueous solution of RPCs buffered at pH 7.4 induced by increasing concentrations of *ct*-DNA. As shown in Fig. 1d for a 10 μM solution of Ru1, the addition of *ct*-DNA resulted in a strong hypochromism in both the MLCT and π → π* absorption bands of the metal complex, with a reduction of approximately 50 and 65% of their relative intensities in the presence of only 3 μM DNA. No blue or red shift was observed upon the addition of DNA and a very similar trend was also observed in the case of Ru2 (see Fig. S14, ESI†). The intrinsic binding constants (K_b) of Ru1 and Ru2 were calculated from titration data (see the inset of Fig. 1d for a comparison between the two RPCs) as described in the ESI† and the resulting values are reported in Table 1. As shown, K_b values of 7.49×10^5 M^{-1} and 2.34×10^6 M^{-1} were respectively obtained for Ru1 and Ru2, thus confirming the ability of these systems to strongly interact with DNA under abiotic conditions. It can be noted that these values are in line with the ones reported for other dppn-containing ruthenium complexes (K_b in the order of 10^6 M^{-1})[54,58,59] and though not conclusive, together with the large extent of hypochromism observed, they hint at the intercalation as the most likely binding mode for these complexes. Moreover, the possible beneficial role played by the presence of a second dppn ligand in strengthening the interaction of complexes with the biopolymer is particularly evidenced by comparing Ru1 with its mono-dppn containing analogue, [Ru(dmbpy)(dppn)]$^{2+}$, for which a lower K_b, of almost 5.8-fold has been reported.[28]

Cytotoxicity and photoactivity of Ru(II)-complexes

To be qualified as a potential agent for photodynamic therapy, newly developed photosensitizers should be biologically inert in the dark, but highly cytotoxic when exposed to light of a

given wavelength.[60] This simple mechanism allows for selective action against the light-exposed area (*i.e.* the tumor), abolishing the systemic toxicity typically associated with traditional chemotherapeutic drugs.[46] Here, the anticancer activity of Ru1 and Ru2 was evaluated on A431 cells, an *in vitro* model of human epidermoid carcinoma.

As shown in Fig. 2, both compounds were found to be well tolerated by cells when no light was provided to the culture dishes. A slight difference between their *in dark* toxicities was observed, thus indicating that seemingly small modifications on the groups gathered on the bpy moieties of complexes (methyl or carboxylic functions) may influence their toxicity. In details, cell viability was reduced to 75.1 ± 4.1% and 82.4 ± 2.0% upon exposure to the highest dose of Ru1 and Ru2 (25 μM) in the dark, respectively. Conversely, 30-minutes of irradiation with an LED array (λ_{max} = 462 nm, 18 mW cm^{-2}) induced potent activation of the complexes, triggering complete cell death (viability < 10%) at concentrations of 0.25 μM (Ru1, Fig. 2a) and 5 μM (Ru2, Fig. 2b): Fig. 2c summarizes the IC_{50} values calculated from *in vitro* experiments. As shown, both Ru1 and Ru2 displayed high photo-toxic indexes (PI, defined as IC_{50} in the dark/IC_{50} upon irradiation), with values exceeding 988 and 130, respectively. From a translational point of view, higher PIs are predictive of a larger therapeutic window, with limited off-target cytotoxicity and enhanced on-target potency. Of note, notwithstanding the lack of data for the phototoxicity of dppn-containing Ru(II) complexes in A431 cells, it can be highlighted that the *in vitro* therapeutic outcomes of complexes of this study are ones of the highest among those reported in the literature for the PDT effect of dppn-containing RPCs.[23,25,61–63]

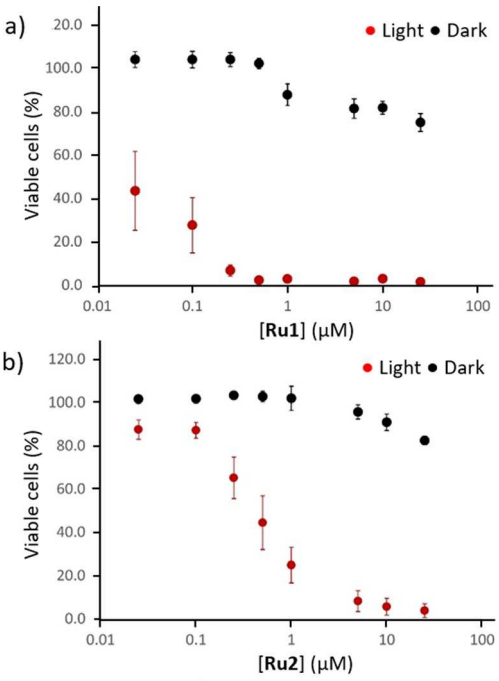

c)

	Light	Dark
IC_{50} Ru1	0.0253 ± 0.0107 μM	> 25 μM
IC_{50} Ru2	0.191 ± 0.023 μM	> 25 μM

Fig. 2 Viability of A431 epidermoid carcinoma cells assessed by MTT following treatments with Ru1 (a) or Ru2 (b), with or without exposure to light for 30 minutes (n = 5). Table summarizing the IC_{50} values (±SEM) for the different experimental groups (c).

Cubosome loading and characterization

The *in vitro* results highlighted the promising activity of the obtained systems in PDT. Nevertheless, their poor aqueous solubility would not be compatible with direct administration to a patient. In fact, self-aggregation phenomena might occur due to the high hydrophobicity of these systems, leading to low bioavailability, possible off-target activation and reduction of their photosensitivity and photophysical properties.[64] The encapsulation of PSs into nanocarriers is a well-known technique used to overcome these issues and to facilitate their biomedical application.[65] In this study, we prepared Ru1 and Ru2 cubosome-loaded formulations using monoolein (MO) as the molecular building block and PF108 as the stabilizing agent. In line with previous results,[66] the obtained samples were fluid aqueous dispersions with a milky macroscopic appearance. Cubosomes, here proposed as PS carriers, were prepared as described in paragraph 4.1 of the ESI† and characterized in terms of encapsulation efficiency and colloidal properties, namely size, size distribution and zeta potential.

Unencapsulated PSs were removed by exhaustive dialysis, then cubosomes were dissolved in methanol and the drug content was spectrophotometrically quantified. The results revealed high encapsulation values of Ru2 (60%), whereas the amount of encapsulated Ru1 was 9%. Besides their different structures, the two complexes also display different overall charges (at neutral pH Ru1 features a double positive charge whereas Ru2 is likely to be present in its neutral form) and this can be reasonably assumed to affect the encapsulation efficiency into cubosomes. Indeed, the production procedure and the excipients employed were identical for both formulations, the encapsulated PS being the sole difference.

As for the colloidal properties, DLS analysis revealed the presence of nanoparticles with an average diameter of approximately 138 and 142 nm, for Ru1-cubo and Ru2-cubo respectively (Fig. 3a). Both formulations showed a narrow size distribution with PDI values below 0.2. Concerning the nanoparticle zeta potential, we recorded a value of −9 mV for Ru1-cubo and −30 mV for Ru2-cubo, thus indicating a superior stabilization of the latter.

We monitored the average diameter, PDI and zeta potential over a period of 30 days, for a medium-term stability study of the colloidal systems (Fig. S16, ESI†). The size distribution study revealed optimal stability of Ru2-cubo, since the mean diameter did not vary appreciably during the 30 days on storage at 25 °C, with an average diameter of approximately 140 nm during the whole study. The PDI and zeta potential were almost constant, confirming the retention of the fairly narrow size distribution on storage. Conversely, the average

a)

	Composition (% w/w)					Characterization			
	MO	PF108	**Ru1**	**Ru2**	H_2O	D (nm)	PDI	ZP (mV)	EE %
Ru1-cubo	3.3	0.03	0.02	-	96.65	138 ± 2	0.11 ± 0.02	-13 ± 3	9 ± 3
Ru2-cubo	3.3	0.03	-	0.02	96.65	142 ± 1	0.13 ± 0.01	-30 ± 2	60 ± 5

b)

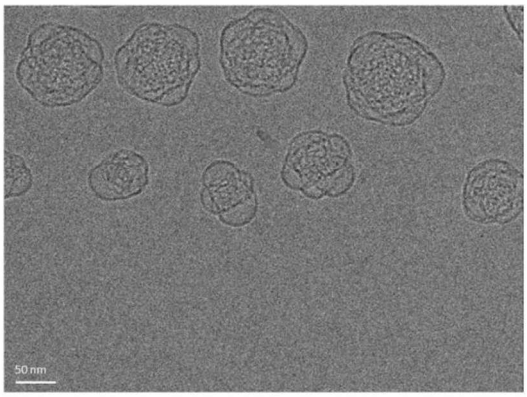

c)

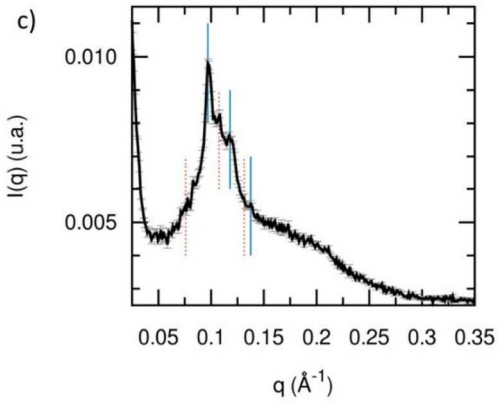

Fig. 3 Ru1-cubo and Ru2-cubo composition and characterization in terms of average diameter (*D*, nm), polydispersion index (PDI), zeta potential (ZP, mV) and encapsulation efficiency (EE%) (a). Cryo-transmission electron microscopy (b) and small angle X-ray scattering patterns of Ru2-cubo with indication of the Bragg peaks corresponding to the Im3 m (red dotted lines) and the Pn3 m (blue continuous lines) cubic bicontinuous phases (c).

diameter of Ru1-cubo increased from 138 nm (day 0) to 235 nm (day 30), the zeta potential moved to lower values, while PDI values were almost steady.

Given the obtained preliminary results of Ru1-cubo, namely, low encapsulation efficiency and an increase of the average diameter over 30 days of storage, we selected Ru2-cubo for further characterization and *in vitro* bioactivity tests. Firstly, we evaluated the nanoparticles morphology of Ru2-cubo by means of cryo-transmission electron microscopy (Cryo-TEM). As shown in Fig. 3b, cubosomes appear as spherical nanoparticles with an internal structure characterized by a dark matrix and bright spots, which represent the lipid phase and the water channels respectively. We then evaluated the inner nanostructure of Ru2-cubo through small angle X-ray scattering. Particularly, the recorded SAXS pattern shown in Fig. 3c strongly suggests the simultaneous presence of two bicontinuous cubic phases, the Pn3 m and the Im3 m, respectively characterized by lattice parameters of 92 ± 1 Å and 117 ± 1 Å and water channel radii of 38 ± 1 Å and 37 ± 1 Å. In fact, the coexistence of the two phases is often observed when MO cubosomes are stabilized with Pluronics.[66,67]

Cytotoxicity, photoactivity and ROS production of cubosomes-encapsulated Ru2

In addition to promoting solubility and stability, nanoencapsulation of photosensitizers in soft colloids has shown to improve the management of cancer in previous studies, as it allows targeted delivery and favors bio-membranes crossing.[68–71] When designing novel PS-loaded nanoparticles, it is critical to assess that the biological activity of the cargo is retained upon nano-encapsulation, and that no unspecific toxicity comes from the nanoparticle itself (*i.e.* empty vector). For such reasons, we tested the cytotoxicity (in the dark) and phototoxicity (upon LED illumination) of Ru2-cubo on the previously described epidermoid carcinoma model, comparing the results with the effect triggered by empty cubosomes (E-cubo, not loaded with PS). Ru2-cubo sensitized cancer cells to light even at a very low concentration of 0.025 μM ([Ru2]), with more than 50% reduction of cell viability at a dose of 0.25 μM (Fig. 4a). Calculated IC_{50} for Ru2-cubo was 0.268 ± 0.079 μM. The slightly higher IC_{50} of Ru2-cubo compared to free Ru2 is expected for a nano-encapsulated molecule and can be partially explained by the lower intracellular localization of ruthenium, evidenced by inductively coupled plasma atomic emission spectrometry (ICP-AES), when entrapped in the soft lipid matrix (Fig. S17, ESI†). As expected, treatment with Ru2-cubo was efficacious only when coupled with LED irradiation, as cells incubated in the dark did not show signs of sufferance. The risk of unspecific toxicity of other components of the nanoformulation (*i.e.* monoolein and PF108) was ruled out by exposing cells to E-cubo under the same conditions (Fig. 4b).

To obtain preliminary information about the mechanism of the observed phototoxicity, we first investigated the production of intracellular ROS upon PDT using the 2′,7′-dichlorodihydro-

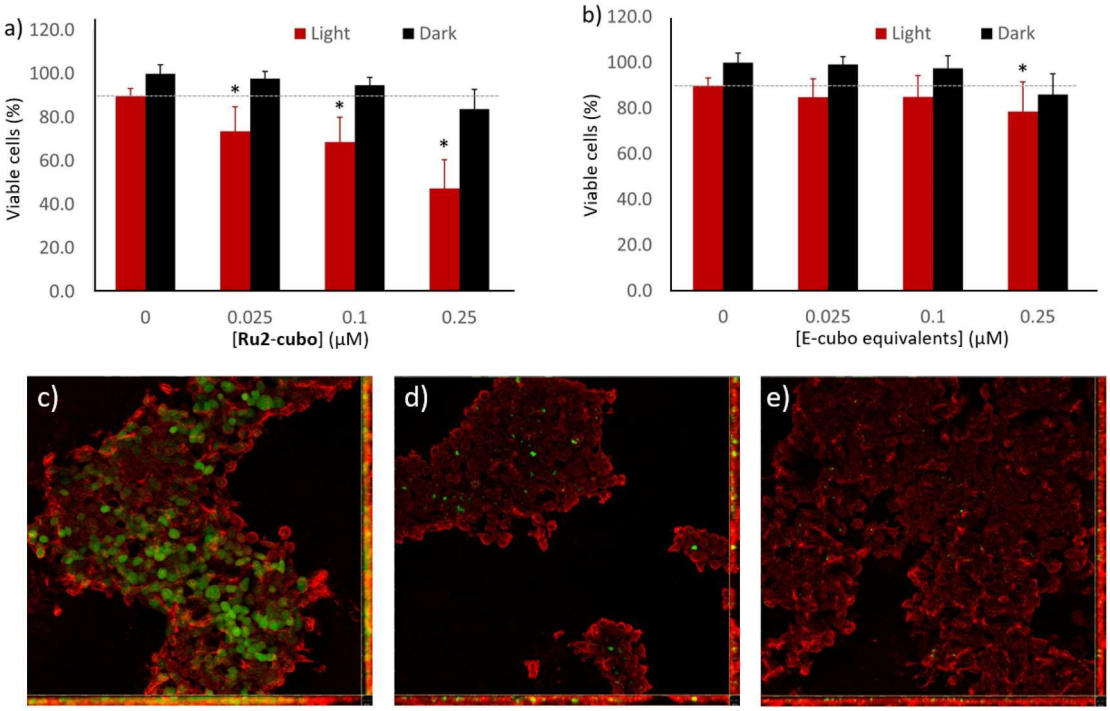

Fig. 4 Viability of A431 epidermoid carcinoma cells assessed by MTT following treatments with Ru2-cubo (a) or E-cubo (b), with or without exposure to light for 30 minutes. The dose is expressed as concentration of Ru2 in the cell culture well or the corresponding volume of E-cubo. The dashed line is a guide for the eye to highlight the viability of cells exposed to light without PS. One way ANOVA with *post-hoc* Tukey HSD test was employed to substantiate differences between cells exposed only to light (no PS, 0 μM) *vs.* cells treated with Ru2-cubo or E-cubo and exposed to light (*$p < 0.01$) ($n = 8$). Production of ROS by A431 epidermoid carcinoma cells estimated by the oxidation of the DCF-DA sensor and visualized by confocal laser scanning microscopy (c–e). Cells treated with Ru2-Cubo (100 nM) and exposed to light for 10 minutes (c) or incubated in the dark (d). Untreated cells (e). The green signal corresponds to the sensor oxidized by intracellularly produced ROS to its fluorescent derivative DCF. Red signal shows the cell membranes stained with WGA. Scalebar = 50 μm.

fluorescein diacetate (DCFH-DA) assay.[72] When applied to the cell culture, the cell permeable probe DCFH-DA crosses the cell membrane and it is deacetylated by cytosolic esterases into a non-fluorescent metabolite (DCFH). In the presence of intracellular ROS, the metabolite can be oxidized to produce highly fluorescent 2′,7′-dichlorofluorescein (DCF). The amount of ROS produced by the cells in response to PDT can be estimated by measuring the green fluorescence intensity of DCF localized within the cell body.

A431 cells were treated with Ru2-cubo, supplied with the DCFH-DA probe and exposed to light to trigger the activation of the photosensitizer. The dose of Ru2-cubo (100 nM of Ru2) was selected to allow for the observation of ROS generation, limiting the extent of cell toxicity. Immediately after irradiation, cells were fixed, and their membranes were stained with WGA for microscopy observation. Representative images acquired by confocal laser scanning microscopy allow to observe a diffuse green fluorescence in almost 87.4% of the cells exposed Ru2-cubo + light (Fig. 4c). Conversely, the treatment with Ru2-cubo in the dark did not induce significant production of ROS, as the amount of green signal detectable (Fig. 4d) was comparable to the one observed in a well of untreated cells (control, Fig. 4e). More specifically, the percentage of ROS-producing cells calculated through image analysis was 1.3% and 0.3% for Ru2-cubo in the dark and for untreated cells, respectively.

We then inspected the intracellular distribution of Ru2-cubo into A431 cells by employing laser-scanning confocal microscopy (Fig. S18, ESI†). Despite the ability of the PS to bind DNA, our results indicated a modest localization of Ru2-cubo within the nuclei, at least after 1 hour of incubation of A431 cells. This was also observed for the non-encapsulated metal complex, thus suggesting that ROS oxidation of other types of macromolecules, such as proteins or membrane lipids, rather than DNA, is likely to be the cause of the observed phototoxicity under our experimental conditions. These oxidized species, in addition to losing their function, can initiate the pro-apoptotic and pro-necrotic cascade, resulting in cell damage and death.[73]

Interestingly, it can also be noted that, in contrast to the free metal complex, which, after 1 hour of incubation, evidenced a random distribution in the cellular cytosol, after the same incubation time Ru2-cubo was rather found to be finely localized in discrete areas.

Overall, these results confirm that the cytotoxic effect observed upon PDT with Ru2-cubo would be related to the capacity of this system to effectively trigger the production of intracellular ROS, as expected due to the good singlet oxygen sensitizing properties of Ru2.

Conclusions

In this study, we explored the potential as PSs for PDT applications of two novel Ru(II) complexes, Ru1 and Ru2, characterized by two π-expansive dppn units simultaneously coordinated to their Ru(II) centers. The synthetic route followed for the preparation of these complexes may represent a valid alternative to commonly employed methods and can be potentially harnessed for the preparation of bis-heteroleptic RPCs of the general formula $[Ru(dppn)_2L]^{2+}$ (L = variously functionalized bpy ligands), whose chemical–physical and photobiological properties can be finely modulated by tuning the nature of their bidentate chelates. The simultaneous presence of two dppn ligands conferred to Ru1 and Ru2 optimal singlet oxygen sensitizing features and DNA-interaction capabilities, which were paralleled by a potent light-triggered toxicity exerted on squamous epithelial carcinoma cells, with PI values exceeding 988 (Ru1) and 130 (Ru2).

Given their scarce solubility in physiological media, which would preclude their direct administration for therapeutic use, Ru1 and Ru2 were encapsulated into cubosomes, chosen as soft nanoparticles to obtain Ru(II)-formulations with improved biopharmaceutical properties. Among the resulting hybrid systems, Ru2-cubo displayed superior encapsulation efficiency and stability as compared to Ru1-cubo, thus hinting at a subtle role played by the nature of the ancillary ligands and/or the overall charge of RPCs. For this reason, we focused our attention on the former system, which was further characterized and subjected to bioactivity investigations. Our results probed the effectiveness of Ru2-cubo, as denoted by the photoactivity observed even at a very low drug concentration, whereas mechanistic studies confirmed that intracellular ROS generation was likely responsible for the Ru2-cubo-mediated PDT efficacy.

An important aspect that deserves consideration is that soft matter nanoparticles are prone to phase transition/degradation when dispersed in fluids of biological interest.[74] However, several studies evidenced that monoolein-based cubosomes are rather stable when incubated in fetal bovine serum solution,[75,76] while when dispersed in human plasma[77] after 15 min they start to evolve towards a different kind of nanoparticle known as hexosomes, characterized by a hexagonal inner nanostructure.[78,79] Indeed, at least one investigation proved that after 10/15 min from i.v. administration in mice, cubosomes are non-altered and able to reach all the biological compartments without the release of the imaging agent they carried.

In conclusion, the results herein discussed highlight the great potential of RPCs featuring two π-expansive dppn ligands as photosensitizing agents in the blooming field of research of PDT. Going beyond providing a simple and general synthetic route for the preparation of this class of compounds, to the best of our knowledge this work also reports the first RPC to be encapsulated into cubosome nanostructures, providing fundamental knowledge about the design of pharmaceutically viable Ru(II)-cubosome formulations for PDT applications.

Author contributions

G. E. G., M. S. and L. Casula: investigation and data curation, L. G., A. D. G., C. S., G. P., F. C., S. P. and B. V.: investigation, S. M. and C. G.: supervision and project administration, L. Conti.: writing the original draft and project administration. G. E. G., M. S., L. Casula, L. Conti, C. S., B. V., C. G. and S. M. are inventors on a pending patent application pertaining to the ruthenium polypyridyl complexes described in this work. All authors have given approval to the final version of the manuscript.

Conflicts of interest

The authors declare no conflicts of interest.

Acknowledgements

The authors would like to thank Dr Annalisa Guerri, from the Department of Chemistry Ugo Schiff of the University of Florence for the Cryo-TEM measurements. UniCA-Progetti biennali di Ateneo Finanziati dalla Fondazione di Sardegna 2018 (CUP F74I19000950007) is gratefully acknowledged for (partial) financial support.

References

1 G. Gunaydin, M. E. Gedik and S. Ayan, Photodynamic Therapy for the Treatment and Diagnosis of Cancer–A Review of the Current Clinical Status, *Front. Chem.*, 2021, 9, 686303.
2 J. H. Correia, J. A. Rodrigues, S. Pimenta, T. Dong and Z. Yang, Photodynamic Therapy Review: Principles, Photosensitizers, Applications, and Future Directions, *Pharmaceutics*, 2021, 13, 1332.
3 L. Karner, S. Drechsler, M. Metzger, A. Hacobian, B. Schädl, P. Slezak, J. Grillari and P. Dungel, Antimicrobial Photodynamic Therapy Fighting Polymicrobial Infections-a Journey from: In Vitro to in Vivo, *Photochem. Photobiol. Sci.*, 2020, 19, 1332–1343.
4 G. Boccalini, L. Conti, C. Montis, D. Bani, A. Bencini, D. Berti, C. Giorgi, A. Mengoni and B. Valtancoli, Methylene Blue-Containing Liposomes as New Photodynamic Anti-Bacterial Agents, *J. Mater. Chem. B*, 2017, 5, 2788–2797.
5 L. Conti, E. Macedi, C. Giorgi, B. Valtancoli and V. Fusi, Combination of Light and Ru(II) Polypyridyl Complexes: Recent Advances in the Development of New Anticancer Drugs, *Coord. Chem. Rev.*, 2022, 469, 214656.
6 S. Monro, K. L. Colón, H. Yin, J. Roque, P. Konda, S. Gujar, R. P. Thummel, L. Lilge, C. G. Cameron and S. A. McFarland, Transition Metal Complexes and Photodynamic Therapy from a Tumor-Centered Approach: Challenges, Opportunities, and Highlights from the Development of TLD1433, *Chem. Rev.*, 2019, 119(2), 797–828.

7 Y. Wu, S. Li, Y. Chen, W. He and Z. Guo, Recent Advances in Noble Metal Complex Based Photodynamic Therapy, *Chem. Sci.*, 2022, 13, 5085–5106.
8 C. Mari, V. Pierroz, S. Ferrari and G. Gasser, Combination of Ru(II) Complexes and Light: New Frontiers in Cancer Therapy, *Chem. Sci.*, 2015, 6, 2660–2686.
9 A. Notaro and G. Gasser, Monomeric and Dimeric Coordinatively Saturated and Substitutionally Inert Ru(II) Polypyridyl Complexes as Anticancer Drug Candidates., *Chem. Soc. Rev.*, 2017, 46, 7317–7337.
10 L. Conti, G. E. Giacomazzo, B. Valtancoli, M. Perfetti, A. Privitera, C. Giorgi, P. S. Sfragano, I. Palchetti, S. Pecchioli, P. Bruni and F. Cencetti, Highly Charged Ru(II) Polypyridyl Complexes as Photosensitizer Agents in Photodynamic Therapy of Epithelial Ovarian Cancer Cells, *Int. J. Mol. Sci.*, 2022, 23(21), 13302.
11 L. Conti, A. Mengoni, G. E. Giacomazzo, L. Mari, M. Perfetti, C. Fagorzi, L. Sorace, B. Valtancoli and C. Giorgi, Exploring the Potential of Highly Charged Ru(II)- and Heteronuclear Ru(II)/Cu(II)-Polypyridyl Complexes as Antimicrobial Agents, *J. Inorg. Biochem.*, 2021, 220, 111467.
12 Z. Y. Yan, J. Chen, J. Shao, Z. Q. Jiao, T. S. Tang, M. Tang, Z. G. Sheng, L. Mao, R. Huang, C. H. Huang, Z. H. Zhang, H. M. Su and B. Z. Zhu, The Cell-Impermeable Ru(II) Polypyridyl Complex as a Potent Intracellular Photosensitizer under Visible Light Irradiation via Ion-Pairing with Suitable Lipophilic Counter-Anions, *Free Radicals Biol. Med.*, 2021, 171, 69–79.
13 S. Estalayo-Adrián, S. Blasco, S. A. Bright, G. J. McManus, G. Orellana, D. C. Williams, J. M. Kelly and T. Gunnlaugsson, Water-Soluble Amphiphilic Ruthenium (II) Polypyridyl Complexes as Potential Light-Activated Therapeutic Agents, *Chem. Commun.*, 2020, 56, 9332–9335.
14 J. Karges, F. Heinemann, F. Maschietto, M. Patra, O. Blacque, I. Ciofini, B. Spingler and G. Gasser, A Ru(II) Polypyridyl Complex Bearing Aldehyde Functions as a Versatile Synthetic Precursor for Long-Wavelength Absorbing Photodynamic Therapy Photosensitizers, *Bioorg. Med. Chem.*, 2019, 27(12), 2666–2675.
15 L. K. McKenzie, M. Flamme, P. S. Felder, J. Karges, F. Bonhomme, A. Gandioso, C. Malosse, G. Gasser and M. Hollenstein, A Ruthenium-Oligonucleotide Bioconjugated Photosensitizing Aptamer for Cancer Cell Specific Photodynamic Therapy, *RSC Chem. Biol.*, 2022, 3, 85–95.
16 M. Lin, S. Zou, X. Liao, Y. Chen, D. Luo, L. Ji and H. Chao, Ruthenium(II) Complexes as Bioorthogonal Two-Photon Photosensitizers for Tumour-Specific Photodynamic Therapy against Triple-Negative Breast Cancer Cells, *Chem. Commun.*, 2021, 57, 4408–4411.
17 A. Chettri, J. A. Roque, K. R. A. Schneider, H. D. Cole, C. G. Cameron, S. A. McFarland and B. Dietzek, It Takes Three to Tango: The Length of the Oligothiophene Chain Determines the Nature of the Long-Lived Excited State and the Resulting Photocytotoxicity of a Ruthenium(II) Photodrug, *ChemPhotoChem*, 2021, 5(5), 421–425.
18 E. C. Glazer, Panchromatic Osmium Complexes for Photodynamic Therapy: Solutions to Existing Problems and New Questions, *Photochem. Photobiol.*, 2017, 93(5), 1326–1328.
19 A. Zamora, E. Wachter, M. Vera, D. K. Heidary, V. Rodríguez, E. Ortega, V. Fernández-Espín, C. Janiak, E. C. Glazer, G. Barone and J. Ruiz, Organoplatinum(II) Complexes Self-Assemble and Recognize AT-Rich Duplex DNA Sequences, *Inorg. Chem.*, 2021, 60(4), 2178–2187.
20 L. E. Joyce, J. D. Aguirre, A. M. Angeles-Boza, A. Chouai, P. K. L. Fu, K. R. Dunbar and C. Turro, Photophysical Properties, DNA Photocleavage, and Photocytotoxicity of a Series of Dppn Dirhodium(II,II) Complexes, *Inorg. Chem.*, 2010, 49(12), 5371–5376.
21 R. N. Akhimie, J. K. White and C. Turro, Dual Photoreactivity of a New Rh2(II,II) Complex for Biological Applications, *Inorg. Chim. Acta*, 2017, 454, 149–154.
22 S. Li, J. Zhao, X. Wang, G. Xu, S. Gou and Q. Zhao, Design of a Tris-Heteroleptic Ru(II) Complex with Red-Light Excitation and Remarkably Improved Photobiological Activity, *Inorg. Chem.*, 2020, 59(15), 11193–11204.
23 L. Wang, H. Yin, M. A. Jabed, M. Hetu, C. Wang, S. Monro, X. Zhu, S. Kilina, S. A. McFarland and W. Sun, π-Expansive Heteroleptic Ruthenium(II) Complexes as Reverse Saturable Absorbers and Photosensitizers for Photodynamic Therapy, *Inorg. Chem.*, 2017, 56(6), 3245–3259.
24 B. Peña, N. A. Leed, K. R. Dunbar and C. Turro, Excited State Dynamics of Two New Ru(II) Cyclometallated Dyes: Relation to Cells for Solar Energy Conversion and Comparison to Conventional Systems, *J. Phys. Chem. C*, 2012, 116(42), 17095–17101.
25 B. A. Albani, B. Peña, N. A. Leed, N. A. B. G. De Paula, C. Pavani, M. S. Baptista, K. R. Dunbar and C. Turro, Marked Improvement in Photoinduced Cell Death by a New Tris-Heteroleptic Complex with Dual Action: Singlet Oxygen Sensitization and Ligand Dissociation, *J. Am. Chem. Soc.*, 2014, 136(49), 17095–17101.
26 C. Reichardt, S. Monro, F. H. Sobotta, K. L. Colón, T. Sainuddin, M. Stephenson, E. Sampson, J. Roque, H. Yin, J. C. Brendel, C. G. Cameron, S. A. McFarland and B. Dietzek, Predictive Strength of Photophysical Measurements for in Vitro Photobiological Activity in a Series of Ru(II) Polypyridyl Complexes Derived from π-Extended Ligands, *Inorg. Chem.*, 2019, 58(5), 3156–3166.
27 F. Haddache, A. Le Goff, B. Reuillard, K. Gorgy, C. Gondran, N. Spinelli, E. Defrancq and S. Cosnier, Label-Free Photoelectrochemical Detection of Double-Stranded HIV DNA by Means of a Metallointercalator-Functionalized Electrogenerated Polymer, *Chem. – Eur. J.*, 2014, 20(47), 15555–15560.
28 S. Vidhisha, K. L. Reddy, Y. P. Kumar, M. Srijana and S. Satyanarayana, Synthesis, Characterization, Antibacterial Activity and Investigation of DNA Binding for Ru(II) Molecular "Light Switch" Complexes, *Int. J. Pharm. Sci. Rev. Res.*, 2014, 25(1), 197–205.

29 H. Yin, M. Stephenson, J. Gibson, E. Sampson, G. Shi, T. Sainuddin, S. Monro and S. A. McFarland, In Vitro Multiwavelength PDT with 3IL States: Teaching Old Molecules New Tricks, *Inorg. Chem.*, 2014, 53(9), 4548–4559.

30 Q. X. Zhou, W. H. Lei, J. R. Chen, C. Li, Y. J. Hou, X. S. Wang and B. W. Zhang, A New Heteroleptic Ruthenium(II) Polypyridyl Complex with Long-Wavelength Absorption and High Singlet-Oxygen Quantum Yield., *Chem. – Eur. J.*, 2010, 16(10), 3157–3165.

31 C. W. Jiang, H. Chao, R. H. Li, H. Li and L. N. Ji, Syntheses, Characterization and Third-Order Nonlinear Optical Properties of Ruthenium(II) Complexes Containing 2-Phenylimidazo-[4,5-f][1,10]Phenanthroline and Extended Diimine Ligands, *Polyhedron*, 2001, 20(17), 2187–2193.

32 L. N. Lameijer, T. G. Brevé, V. H. S. van Rixel, S. H. C. Askes, M. A. Siegler and S. Bonnet, Effects of the Bidentate Ligand on the Photophysical Properties, Cellular Uptake, and (Photo)Cytotoxicity of Glycoconjugates Based on the [Ru(Tpy)(NN)(L)]2 + Scaffold, *Chem. – Eur. J.*, 2018, 24(11), 2709–2717.

33 N. Toupin, S. J. Steinke, S. Nadella, A. Li, T. N. Rohrabaugh, E. R. Samuels, C. Turro, I. F. Sevrioukova and J. J. Kodanko, Photosensitive Ru(II) Complexes as Inhibitors of the Major Human Drug Metabolizing Enzyme CYP3A4, *J. Am. Chem. Soc.*, 2021, 143(24), 9191–9205.

34 A. C. Munteanu, A. Notaro, M. Jakubaszek, J. Cowell, M. Tharaud, B. Goud, V. Uivarosi and G. Gasser, Synthesis, Characterization, Cytotoxic Activity, and Metabolic Studies of Ruthenium(II) Polypyridyl Complexes Containing Flavonoid Ligands, *Inorg. Chem.*, 2020, 59(7), 4424–4434.

35 G. E. Shillito, S. E. Bodman, J. I. Mapley, C. M. Fitchett and K. C. Gordon, Accessing a Long-Lived 3LC State in a Ruthenium(II) Phenanthroline Complex with Appended Aromatic Groups, *Inorg. Chem.*, 2020, 59(23), 16967–16975.

36 K. Sztandera, M. Gorzkiewicz and B. Klajnert-Maculewicz, Nanocarriers in Photodynamic Therapy—in Vitro and in Vivo Studies, *Wiley Interdiscip. Rev.: Nanomed. Nanobiotechnol.*, 2020, 12(3), 1509.

37 A. Q. Annu, B. Nabi, S. Kotta, J. K. Narang, S. Baboota and J. Ali, Role of Nanocarriers in Photodynamic Therapy, *Photodiagn. Photodyn. Ther.*, 2020, 30, 101782.

38 F. Lai, M. Schlich, R. Pireddu, F. Corrias, A. Fadda and C. Sinico, Production of Nanosuspensions as a Tool to Improve Drug Bioavailability: Focus on Topical Delivery, *Curr. Pharm. Des.*, 2015, 21(42), 6089–6103.

39 S. Murgia, S. Biffi and R. Mezzenga, Recent Advances of Non-Lamellar Lyotropic Liquid Crystalline Nanoparticles in Nanomedicine, *Curr. Opin. Colloid Interface Sci.*, 2020, 48, 28–39.

40 J. Barauskas, C. Cervin, M. Jankunec, M. Špandyreva, K. Ribokaite, F. Tiberg and M. Johnsson, Interactions of Lipid-Based Liquid Crystalline Nanoparticles with Model and Cell Membranes, *Int. J. Pharm.*, 2010, 391(1–2), 248–291.

41 J. C. Bode, J. Kuntsche, S. S. Funari and H. Bunjes, Interaction of Dispersed Cubic Phases with Blood Components, *Int. J. Pharm.*, 2013, 448(1), 87–95.

42 S. Murgia, S. Bonacchi, A. M. Falchi, S. Lampis, V. Lippolis, V. Meli, M. Monduzzi, L. Prodi, J. Schmidt, Y. Talmon and C. Caltagirone, Drug-Loaded Fluorescent Cubosomes: Versatile Nanoparticles for Potential Theranostic Applications, *Langmuir*, 2013, 29(22), 6673–6679.

43 F. D. Victorelli, L. Salvati Manni, S. Biffi, B. Bortot, H. H. Buzzá, V. Lutz-Bueno, S. Handschin, G. Calixto, S. Murgia, M. Chorilli and R. Mezzenga, Potential of Curcumin-Loaded Cubosomes for Topical Treatment of Cervical Cancer, *J. Colloid Interface Sci.*, 2022, 620, 419–430.

44 S. Jenni, G. Picci, M. Fornasier, M. Mamusa, J. Schmidt, Y. Talmon, A. Sour, V. Heitz, S. Murgia and S. C. Caltagirone, Multifunctional Cubic Liquid Crystalline Nanoparticles for Chemo- A Nd Photodynamic Synergistic Cancer Therapy, *Photochem. Photobiol. Sci.*, 2020, 19, 674–680.

45 U. Bazylińska, D. Wawrzyńczyk, J. Kulbacka, G. Picci, L. S. Manni, S. Handschin, M. Fornasier, C. Caltagirone, R. Mezzenga and S. Murgia, Hybrid Theranostic Cubosomes for Efficient NIR-Induced Photodynamic Therapy, *ACS Nano*, 2022, 16(4), 5427–5438.

46 U. Bazylińska, J. Kulbacka, J. Schmidt, Y. Talmon and S. Murgia, Polymer-Free Cubosomes for Simultaneous Bioimaging and Photodynamic Action of Photosensitizers in Melanoma Skin Cancer Cells, *J. Colloid Interface Sci.*, 2018, 522, 163–173.

47 M. C. F. Simões, J. J. S. Sousa and A. A. C. C. Pais, Skin Cancer and New Treatment Perspectives: A Review, *Cancer Lett.*, 2015, 357(1), 8–42.

48 M. Kubeil, R. R. Vernooij, C. Kubeil, B. R. Wood, B. Graham, H. Stephan and L. Spiccia, Studies of Carbon Monoxide Release from Ruthenium(II) Bipyridine Carbonyl Complexes upon UV-Light Exposure, *Inorg. Chem.*, 2017, 56(10), 5941–5952.

49 N. Nickita, M. J. Belousoff, A. I. Bhatt, A. M. Bond, G. B. Deacon, G. Gasser and L. Spiccia, Synthesis, Structure, Spectroscopic Properties, and Electrochemical Oxidation of Ruthenium(II) Complexes Incorporating Monocarboxylate Bipyridine Ligands, *Inorg. Chem.*, 2007, 46(21), 8638–8651.

50 A. Notaro, M. Jakubaszek, S. Koch, R. Rubbiani, O. Dömötör, E. A. Enyedy, M. Dotou, F. Bedioui, M. Tharaud, B. Goud, S. Ferrari, E. Alessio and G. Gasser, A Maltol-Containing Ruthenium Polypyridyl Complex as a Potential Anticancer Agent, *Chem. – Eur. J.*, 2020, 26(20), 4997–5009.

51 E. Wachter, D. K. Heidary, B. S. Howerton, S. Parkin and E. C. Glazer, Light-Activated Ruthenium Complexes Photobind DNA and Are Cytotoxic in the Photodynamic Therapy Window, *Chem. Commun.*, 2012, 48, 9649–9651.

52 R. A. Krause, Synthesis of Mixed Complexes of Ruthenium (II) with 2,2′-Dipyridyl, *Inorg. Chim. Acta*, 1977, 22, 209–213.

53 A. Petroni and L. D. Slep, Etchenique, R. Ruthenium(II) 2,2′-Bipyridyl Tetrakis Acetonitrile Undergoes Selective Axial Photocleavage., *Inorg. Chem.*, 2008, 47(3), 951–956.
54 H. K. Saeed, P. J. Jarman, S. Archer, S. Sreedharan, I. Q. Saeed, L. K. Mckenzie, J. A. Weinstein, N. J. Buurma, C. G. W. Smythe and J. A. Thomas, Homo– and Heteroleptic Phototoxic Dinuclear Metallo–Intercalators Based on Ru II (Dppn) Intercalating Moieties: Synthesis, Optical, and Biological Studies, *Angew. Chem., Int. Ed.*, 2017, 56(41), 12628–12633.
55 T. Shimidzu, T. Iyoda and K. Izaki, Photoelectrochemical Properties of Bis(2,2′-Bipyridine)(4,4′-Dicarboxy-2,2′-Bipyridine) Ruthenium(II) Chloride, *J. Phys. Chem.*, 1985, 89(4), 642–645.
56 C. Imberti, P. Zhang, H. Huang and P. J. Sadler, New Designs for Phototherapeutic Transition Metal Complexes, *Angew. Chem., Int. Ed.*, 2020, 59(1), 61–73.
57 A. P. Castano, T. N. Demidova and M. R. Hamblin, Mechanisms in Photodynamic Therapy: Part One - Photosensitizers, Photochemistry and Cellular Localization, *Photodiagn. Photodyn. Ther.*, 2004, 1(4), 279–293.
58 Y. Sun, L. E. Joyce, N. M. Dickson and C. Turro, Efficient DNA Photocleavage by [Ru(Bpy)2(Dppn)]2+ with Visible Light, *Chem. Commun.*, 2010, 46, 2426–2428.
59 S. P. Foxon, C. Metcalfe, H. Adams, M. Webb and J. A. Thomas, Electrochemical and Photophysical Properties of DNA Metallo-Intercalators Containing the Ruthenium(II) Tris(1-Pyrazolyl)Methane Unit., *Inorg. Chem.*, 2007, 46(2), 409–416.
60 D. Van Straten, V. Mashayekhi, H. S. de Bruijn, S. Oliveira and D. J. Robinson, Oncologic Photodynamic Therapy: Basic Principles, Current Clinical Status and Future Directions, *Cancers*, 2017, 9(2), 1–54.
61 L. M. Lifshits, J. A. Roque, P. Konda, S. Monro, H. D. Cole, D. V. Dohlen, S. Kim, G. Deep, R. P. Thummel, C. G. Cameron, S. Gujar and S. A. McFarland, Near-infrared absorbing Ru(II) complexes act as immunoprotective photodynamic therapy (PDT) agents against aggressive melanoma, *Chem. Sci.*, 2020, 11, 11740.
62 L. N. Lameijer, S. L. Hopkins, T. G. Brevé, S. H. C. Askes and S. Bonnet, D-Versus L-Glucose Conjugation: Mitochondrial Targeting of a Light-Activated Dual-Mode-of Action Ruthenium-Based Anticancer Prodrug, *Chem. – Eur. J.*, 2016, 22, 18484–18491.
63 S. Li, J. Zhao, X. Wang, G. Xu, S. Gou and Q. Zhao, Design of a Tris-Heteroleptic Ru(II) Complex with Red-Light Excitation and Remarkably Improved Photobiological Activity, *Inorg. Chem.*, 2020, 59, 11193–11204.
64 S. Moghassemi, A. Dadashzadeh, R. B. Azevedo, O. Feron and C. A. Amorim, Photodynamic cancer therapy using liposomes as an advanced vesicular photosensitizer delivery system, *J. Controlled Release*, 2021, 339(10), 75–90.
65 C. F. de Freitas, D. S. Pellosi and A. L. Tessaro, 8-Lipid-based nanoparticles in photodynamic therapy, *in Nanomaterials for Photodynamic Therapy*, 2023, 203–226.
66 M. Fornasier, S. Biffi, B. Bortot, P. Macor, A. Manhart, F. R. Wurm and S. Murgia, Cubosomes Stabilized by a Polyphosphoester-Analog of Pluronic F127 with Reduced Cytotoxicity, *J. Colloid Interface Sci.*, 2020, 580, 286–297.
67 A. M. Falchi, A. Rosa, A. Atzeri, A. Incani, S. Lampis, V. Meli, C. Caltagirone and S. Murgia, Effects of Monoolein-Based Cubosome Formulations on Lipid Droplets and Mitochondria of HeLa Cells, *Toxicol. Res.*, 2015, 4, 1025–1036.
68 J. Guo, M. Schlich, J. F. Cryan and C. M. O'Driscoll, Targeted Drug Delivery via Folate Receptors for the Treatment of Brain Cancer: Can the Promise Deliver?, *J. Pharm. Sci.*, 2017, 106(12), 3413–3420.
69 Z. Zhen, W. Tang, C. Guo, H. Chen, X. Lin, G. Liu, B. Fei, X. Chen, B. Xu and J. Xie, Ferritin Nanocages to Encapsulate and Deliver Photosensitizers for Efficient Photodynamic Therapy against Cancer, *ACS Nano*, 2013, 7(8), 6988–6996.
70 S. Demartis, G. Rassu, S. Murgia, L. Casula, P. Giunchedi and E. Gavini, Improving Dermal Delivery of Rose Bengal by Deformable Lipid Nanovesicles for Topical Treatment of Melanoma, *Mol. Pharm.*, 2021, 18(11), 4046–4057.
71 L. Conti, S. Ciambellotti, G. E. Giacomazzo, V. Ghini, L. Cosottini, E. Puliti, M. Severi, E. Fratini, F. Cencetti, P. Bruni, B. Valtancoli, C. Giorgi and P. Turano, Ferritin Nanocomposites for the Selective Delivery of Photosensitizing Ruthenium-Polypyridyl Compounds to Cancer Cells, *Inorg. Chem. Front.*, 2022, 9, 1070–1081.
72 S. Wang, A. Riedinger, H. Li, C. Fu, H. Liu, L. Li, T. Liu, L. Tan, M. J. Barthel, G. Pugliese, F. De Donato, M. Scotto D'Abbusco, X. Meng, L. Manna, H. Meng and T. Pellegrino, Plasmonic Copper Sulfide Nanocrystals Exhibiting Near-Infrared Photothermal and Photodynamic Therapeutic Effects, *ACS Nano*, 2015, 9(2), 1788–1800.
73 M. Redza-Dutordoir and D. A. Averill-Bates, Activation of Apoptosis Signalling Pathways by Reactive Oxygen Species, *Biochim. Biophys. Acta*, 2016, 1863(12), 2977–2992.
74 A. Yaghmur and H. Mu, Recent advances in drug delivery applications of cubosomes, hexosomes, and solid lipid nanoparticles, *Acta Pharm. Sin. B*, 2021, 11(4), 871–885.
75 S. Deshpande, E. Venugopal, S. Ramagiri, J. R. Bellare, G. Kumaraswamy and N. Singh, *ACS Appl. Mater. Interfaces*, 2014, 6(19), 17126–17133.
76 A. Gupta, T. Stait-Gardner, L. de Campo, L. J. Waddington, N. Kirby, W. S. Price and M. J. Moghaddam, *J. Mater. Chem. B*, 2014, 2, 1225–1233.
77 J. C. Bode, J. Kuntsche, S. S. Funari and H. Bunjes, *Int. J. Pharm.*, 2013, 448(1), 87–95.
78 C. Caltagirone, M. Arca, A. M. Falchi, V. Lippolis, V. Meli, M. Monduzzi, T. Nylander, A. Rosa, J. Schmidt, Y. Talmond and S. Murgia, *RSC Adv.*, 2015, 5, 23443–23449.
79 V. Meli, C. Caltagirone, C. Sinico, F. Lai, A. M. Falchi, M. Monduzzi, M. Obiols-Rabasa, G. Picci, A. Rosa, J. Schmidt, Y. Talmone and S. Murgia, *New J. Chem.*, 2017, 41, 1558–1565.